Fatigue Design and Behaviour of Carburized Steel

by

Wanhua Liang

A thesis
presented to the University of Waterloo
in fulfillment of the
thesis requirement for the degree of
Doctor of Philosophy
in
Civil Engineering

Waterloo, Ontario, Canada, 2022

Examining Committee Membership

The following served on the Examining Committee for this thesis. The decision of the Examining Committee is by majority vote.

External Examiner:	Dave DuQuesnay Professor, Dept. of Mechanical and Aerospace Engineering Royal Military College of Canada
Supervisor:	Scott Walbridge Professor, Dept. of Civil & Environmental Engineering University of Waterloo
Supervisor:	Albrecht Conle Adjunct Professor, Dept. of Civil & Environmental Engineering University of Waterloo
Internal Member:	Hassan Baaj Professor, Dept. of Civil & Environmental Engineering University of Waterloo
Internal Member:	Stan Potapenko Professor, Dept. of Civil & Environmental Engineering University of Waterloo
Internal-External Member:	Hamid Jahed Motiagh Professor, Dept. of Mechanical & Mechatronics Engineering University of Waterloo

Author's Declaration

I hereby declare that I am the sole author of this thesis. This is a true copy of the thesis, including any required final revisions, as accepted by my examiners.

I understand that my thesis may be made electronically available to the public.

Abstract

Steel is an essential component used in infrastructure, automobiles, machines and many other areas due to its low cost and high tensile strength. Carburization is a heat treatment process commonly used to harden and strengthen the metal. Carburizing a steel component produces a case layer with high strength and hardness and a core layer with adequate ductility and toughness. Residual stresses are generated in the component during the carburization process, which improves the fatigue behaviour of the component under certain loading conditions. However, no complete design theory has been established for carburized steel components due to the complexity of the microstructure transformation and the residual stress relaxation phenomenon under cyclic loading.

This research aims to improve our understanding of the fatigue behaviour of carburized steel components, considering the microstructural and the residual stress changes during cyclic loading. A methodology for estimating the fatigue life for carburized steel components is proposed in this study.

Extensive experimental and analytical work was performed to study the stress-strain behaviour and the fatigue performance of carburized steels.

Monotonic and fatigue tests were conducted on carburized case-hardened samples, through-carburized case samples and simulated core samples to obtain the model input parameters and to acquire data for simulation results validation. Subsurface crack initiation was observed in the long-life fatigue tests in the case-hardened axial samples. The fracture surfaces of the samples with subsurface failure were examined using Scanning Electron Microscopic (SEM). X-ray diffraction (XRD) was employed to measure the retained austenite (RA) content and the magnitude of residual stresses at different depths of the case-hardened samples before and after various loading histories.

A finite element (FE) model and a compatibility model were developed to estimate the initial residual stress formed during the carburization process. The amount of RA transformed under various cyclic loading amplitude was determined. Models for predicting the crack initiation and propagation life were developed in Fortran. A three-layer model,

assuming constant stress and material property within each layer, was employed in the crack initiation and propagation simulations for the case-hardened axial and notched samples under constant amplitude (CA) and variable amplitude (VA) loading histories. The residual stress in each layer, including the RA transformation effect, was accounted for in the fatigue life prediction.

The three-layer model adequately predicts the crack initiation location in the case-hardened sample at different CA and VA load levels. For the composite axial sample under VA loading, the predicted fatigue life using the vacuum crack growth curve is within a factor of two of the experimental data at stress levels above the fatigue limit. For the case-hardened notched samples, conservative fatigue lives were estimated at high stress levels using the models proposed in this study.

Acknowledgements

I cannot express enough thanks to my supervisors, Al Conle, Tim Topper and Scott Walbridge, for their consistently high level of guidance, support and encouragement. I am extremely fortunate to have worked with them and benefited immensely from their words and deeds.

Professor Al Conle, my advisor and friend, has not only guided me through my research. His attitude on solving problems in everyday life greatly influenced me. He showed me that it could be more efficient to tackle the problem at its root with patience rather than trying superficial solutions. During my research, he has given me enough freedom to try different innovative approaches. Without his thorough guidance on lab testing, I could not have completed all the experimental work.

Professor Timothy .H. Topper is always accessible and willing to help when I needed it the most. He patiently walked me through the history of the metal fatigue theories revolution and how the complex models were derived from the most basic mechanics rules. He has many resources and ideas to improve my computational models and simulation results. Besides research, he has offered me valuable advice on making important decisions for life.

Professor Scott Walbridge has always been enthusiastic and encouraging of my research. He has provided me with essential guidance on achieving the milestones throughout my graduate studies. Joining his research group brought me a sense of belonging in the graduate student community.

I am greatly indebted to my mother, who brought me up with unconditional love and encouragement. Without her, I could not make it to this stage.

I am fortunate to meet and have the support of my boyfriend, Longlong, during my graduate studies. Ever since he came into my life, he filled it with joy and love. He was always there for me to share my up and downs.

I am heartily thankful to my friends and colleagues in my graduate programs for their accompany and encouragement.

I am grateful for the technical support provided by Peter Volcic, Doug Hirst and Richard Morrison at the lab.

I would also like to thank James Pineault and Peter Guba for their help on measuring the microstructure and residual stresses in my samples.

Financial support for this research provided by the American Iron and Steel Institute bar steel fatigue group is gratefully acknowledged.

Table of Contents

List of Tables

List of Figures

Chapter 1

Introduction

Steel is one of the most commonly used materials in modern society. Different heat treatment techniques can alter the material properties of raw steel to give a wide range of mechanical and cyclic properties. Carburization is a heat treatment that hardens the outer layer of a steel component, increases its tensile and fatigue strength, and generates compressive residual stresses beneficial for certain loading conditions.

Even though carburization has been employed for a long time, no mature guide has been developed to enable design of carburized components due to the complexity of estimating the residual stresses induced during the carburizing process and predicting their effect on fatigue performance. In order to determine the fatigue life of a carburized component during the design process, the machined and heated prototypes have to be tested under cyclic loading. This procedure can require many iterations and is cost-inefficient and time-consuming.

1.1 Carburized steel

Carburization, a form of case-hardening, is a type of heat treatment performed on steel to improve the load-carrying capacity and durability of a component. A carburized

steel component consists of two main layers, the case and the core. The case is made of martensite with high carbon content, high strength and good wear resistance, while the core contains a low carbon content and has a lower strength but higher ductility. Carburization of steel is widely used in gears, shafts, and bearings.

Gas carburizing is one of the most commonly used carburization processes for large volume production. Firstly, the machined components are placed into a high-temperature gas carrier containing hydrocarbons and carbon monoxide molecules. At this stage, the steel transfers to an austenitic phase and the carbon atoms diffuse into the steel surface and subsequently into the interior of steel. When the desired case depth is reached, the components are taken out from the chamber and rapidly cooled by quenching in oil or water. During quenching, austenite transfers to martensite in the high carbon content case, while the core transfers to ferrite and cementite due to the low carbon content and the slow cooling rate in the interior of a steel component. A martensite core could also be produced in small components where the temperature drops rapidly throughout the sample during quenching. Tempering is usually performed at 120°C to 200°C after quenching to reduce the case brittleness and to release part of the high residual stress developed during quenching [127].

The difference in volume expansion resulting from phase changes in the case and thermal contractions in the core during cooling create residual stresses in the carburized steel. When a compressive residual stress is developed in the case layer, a balancing tensile stress is generated in the core. Under an applied load, the stress in a notch in the surface of the component is significantly reduced by the compressive residual stress in the carburized layer. Consequently, the fatigue life of the component will be prolonged. However, this beneficial residual stress is believed to relax under high-stress amplitude cyclic loading thus diminishing the improved fatigue performance.

The retained austenite (RA) in the case layer of the carburized component could transform into martensite under loading. This transformation increases the magnitude of the compressive residual stress in the case layer and enhances fatigue performance.

1.2 Fatigue design and flaw definitions

Fatigue tests are usually conducted under two types of loading: constant amplitude (CA) and variable amplitude (VA), illustrated in Figure 1.1.

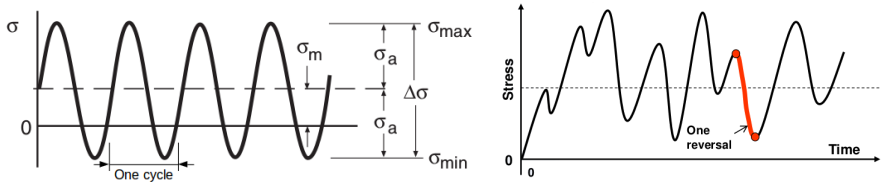

(a) CA cycling with mean stress (b) VA stress history

Figure 1.1: Constant amplitude (CA) and variable amplitude (VA) histories

The definitions of *stress range* ($\Delta\sigma$), *stress amplitude* (σ_a), and *mean stress* (σ_m) are given in Figure 1.1a. The *stress ratio*, also called the *R-ratio*, is equal to the ratio of the minimum stress to the maximum stress. The term "reversal" is often used as a synonym for "half cycle", which means the change from compressive to tensile peak or vice versa. For components with notches, the local stresses at the roots of the notches are higher than the nominal stresses. Hence, a notch is called a stress raiser. The *stress concentration factor*, K_t, is defined as the ratio of the local peak stress at the notch root divided by the nominal stress applied.

Stress-based, strain-based, and fracture mechanics approaches are the three most commonly used methods in fatigue design. This research involves working primarily with the strain-based and the fracture mechanics approaches.

The strain- and stress-life based approaches are typically employed to predict the fatigue initiation life in parts without initial flaws. The local stress and strain in a component can be obtained from (1) a Finite Element (FE) model or (2) applying a stress concentration factor to the nominal stress, along with Neuber's rule [112] or other theories if plasticity is involved. The local stress and strain range are then used to calculate the damage caused by cyclic loading. Fatigue failure can be predicted through an accumulated damage estimation under CA or VA loading.

Crack propagation models are widely used for parts containing initial flaws to characterize the crack growth behaviour. In linear elastic fracture mechanics (LEFM), the range of stress intensity factor, ΔK, is employed to correlate the stress and the crack length to the growth rate of a crack ($\frac{da}{dN}$ vs ΔK curve) [117]. The final fracture occurs when the crack length approaches a defined crack size, or K reaches the fracture toughness, K_C, of the material.

In most cases considered in this thesis, the total fatigue life is calculated as the sum of the crack initiation and propagation lives. Generally, the initiation life can be neglected in welded metals or in other situations where an initial crack exists. On the other hand, in small components or brittle materials, the crack propagation life accounts for a negligible portion of the total fatigue life compared to the initiation life; therefore, crack propagation is usually neglected in the calculation.

Impurities in the material are essential sources of the initial flaw usually as second phase inclusion or an oxidization that occurs during carburization. These flaws cause subsurface crack initiation and shorten the fatigue life of the component. Subsurface crack initiation is usually found in gigacycle fatigue tests in untreated metals and in long-life fatigue tests in the case-hardened components under axial loading. An interior crack initiation site, called a "fisheye", typically appears on the fracture surface, as shown in Figure 1.2. The centre of the "fisheye" usually contains an inclusion, a "super grain", or porosity.

1.3 Objective and scope

The ultimate objective of this study is to predict the fatigue life of the case-hardened smooth and notched samples loaded under CA and VA histories. Experimental studies were carried out to determine the input parameters and validate the simulation models. The experimental studies performed in this research include:

- CA tests on the through-carburized case, simulated core and case-hardened composite axial samples (material properties and sample design described in Sections 4.1 and 4.2) to obtain their stress-life, strain-life and cyclic stress-strain curves;

Figure 1.2: A "fisheye" on the carburized axial sample fracture surface

- CA with negative mean stress tests on through-carburized case samples to examine the effect of negative mean stress on fatigue performance of very hard steels;
- Fully reversed CA tests on case, core and composite notched plate samples to study the effect of notches on the three materials;
- Periodic overload (POL) tests on the core and case axial samples to observe the effect of overload on fatigue life;
- VA load histories tests on the composite axial and notched samples, as well as the case notched plates for simulation results verification;
- Fracture surface of the case-hardened axial and the notched samples examined via SEM and microscope pictures, especially in cases where the crack initiated from sub-surface, to determine the fisheye and inclusion sizes for the model input parameters;
- Crack growth rate measured for the core material using the core notched plates;
- Core and case axial sample testing under CA with various mean stresses at different strain amplitudes and observed the mean stress relaxation effect;

- The retained austenite content and the amount of residual stress in the composite samples measured before and after various loading histories via X-ray diffraction and use as the inputs for the fatigue model.

The simulations implemented in this study includes:

- Constructed an ABAQUS (finite element) model and a compatibility model in MATLAB to predict the residual stress in the axial and notched plate samples that included the load-induced RA transformation effect;
- Conducted initiation simulations under CA and VA loading for the three layers in the composite samples to predict the crack initiation location and fatigue life in the axial and notched composite samples;
- Compared the three subsurface elliptical shaped crack propagation methods, ASME [7], BS7910 [14] and Murakami's [104], for calculating the total life of the composite axial samples under CA loading;
- Developed a subsurface elliptical crack propagation model based on the BS7910 approach and predicted the fatigue life of the composite samples under VA loading;
- Employed corner crack propagation model from BS7910 to determine the crack propagation life in the core layer of the composite notched sample;
- Compared the total life prediction results from the effective-strain based and the multi-R-ratio crack propagation approaches.

1.4 Thesis organization

This thesis consists of seven chapters, including the current one. Chapter 2 summarizes the state-of-the-art literature pertinent to the research area. Chapter 3 compares the results of the effective-strain based and the multi-R-ratio propagation models. Chapter 4

describes the tested material and the experiment setups. The test results are also presented in the same chapter. Chapter 5 explains the studies conducted on retained austenite transformation and residual stresses in the composite samples. Chapter 6 lists the fatigue analysis conducted to predict the life of the composite axial and notched samples. Chapter 7 concludes the current study and has recommendations for future work.

Chapter 2

Literature review

This chapter provides an introduction of the concepts mentioned in this study and a review of the pertinent literature.

2.1 Coaxing effect

Coaxing refers to the phenomenon that the fatigue limit of steels increased after specimens were loaded at some stress levels below the fatigue limit for a large number of cycles. This effect could also improve the fatigue performance of the material under a VA history loading. Multiple researchers have observed the coaxing effect in different steels under various loading types.

Lu and Zheng [92] conducted single tooth bending tests for transmission cylindrical gear in 20MnCr5 steel under CA and high-low cycle loading. By preloading the samples at 75% to 95% of the fatigue limit for 200 to 400 thousand cycles, followed by a stress range around or higher than the original fatigue limit, a cumulative damage over 100% was determined using Miner's rule [99]. The coaxing effect observed in the studied material was more significant than the cyclic strengthening. By loading the sample below the fatigue limit, the fatigue life increased about 109% and the fatigue strength by 4%.

Zhao et al. [166] tested 40Cr carbon steel under torsion loading. In order to attain the coaxing effect, samples were loaded at 0.75, 0.85 and 0.95 of the fatigue limit. They proposed that the change in material microstructure, including the regulation of micro-pores and reduction of pore density, causes the observed fatigue strength improvements. By studying the fracture surface of the specimens, the authors found that the pores in the samples loaded under CA are more dense and generally interconnected compared to those being coaxed, which contain smoother, more circular and independent pores. The improvement in fatigue life caused by coaxing at the CA stress level with fatigue life at 182,175 cycles ranges from 18% to 443%.

Nakajima et al. [108] studied the coaxing effect in pre-strained 304 stainless steel under rotating bending load. The austenitic stainless steel was preloaded to 0.15, 0.30 and 0.60 of strain. The samples were initially loaded at stress levels lower than the fatigue limit for 10^7 cycles and then loading continue for 10^7 cycles at each successively increased stress levels until failure. The fatigue limit stress increased by 40% to 90% due to coaxing, and it tended to increase with the amount of pre-strain. Strain-induced martensite transformation occurred during the pre-strain process. The coaxing effect in the 304 steel is attributed to both work hardening, which decreases with increasing pre-strain, and strain-induced martensite transformation that increases with pre-strain.

Later on, Nakajima et al. [107] ran stress-incremental tests on SCM435, SNCM439 and SUJ2 steels under rotary bending loading. They suggested that the coaxing effect in SCM435 and SNCM439 is associated with strain-ageing instead of work hardening.

Akita et al. [3] studied coaxing in 316 stainless steel under rotary bending load by running stress-incremental tests. By pre-straining the material to 5% and 15% before any cyclic loading, the CA fatigue limit increased by 7% and 27%, respectively. In the stress-incremental tests, the fatigue limit increased in the 5% pre-strained and un-strained specimens, but not in the 15% pre-strained ones.

Akira [2] tested 18Cr-8Ni austenitic stainless steel using progressive stress fatigue loading. He observed strain-induced martensite transformations under fatigue loading. The coaxing effect intensified proportionally with the amount of transformation. Akira claimed

that the strain-induced martensite and the strain ageing of martensite and austenite in the 18Cr-8Ni steel contributed to coaxing. The martensite transformation occurred mostly before crack initiation. The fatigue strength increased with the number of cycles loaded at each stress level below and around the original fatigue limit. With 10^5, 10^6, 10^7 cycles loaded at each increment, the fatigue strength increased by 10.8%, 14.2% and 20.5%, respectively.

Strain-controlled axial tests were conducted on SUS304-HP plate samples, which were made of a 20 mm hot-rolled sheet with ultimate stress of 618 MPa [110]. The strain-controlled specimens were loaded to the runout limit, and coaxing effect was observed. The stress-life data and the hysteresis loops of the runout tests are plotted in Figure 2.1. The hysteresis loops in the figure are sketches only of the strain hardening effect demonstration under cyclic loading. The cyclic stress response figure [110] shows that the samples with coaxing effect have a higher stress range at the same strain range compared to those failed at the initial fatigue limit.

Based on the literature listed above, the potential causes of coaxing are material microstructure change, work-hardening and strain ageing. The austenite to martensite transformation induced by pre-straining and cyclic loading is the most commonly observed factor that evokes coaxing. Figure 2.1 shows the change in the material properties before and after the coaxing effect.

2.2 Effect of periodic overload on fatigue limit

Conle and Topper [23] observed that the small load cycles below the fatigue limit of the material could propagate a crack if they were applied following one or multiple large cycles that initiated a crack. Therefore, periodic overload (POL) tests were designed to study the damage generated by the small cycles that follow the overload cycles in a load history.

This section compares the stress-life data of the heat-treated steels loaded under CA and POL. The fatigue limits of the same material under the two loading types are reviewed.

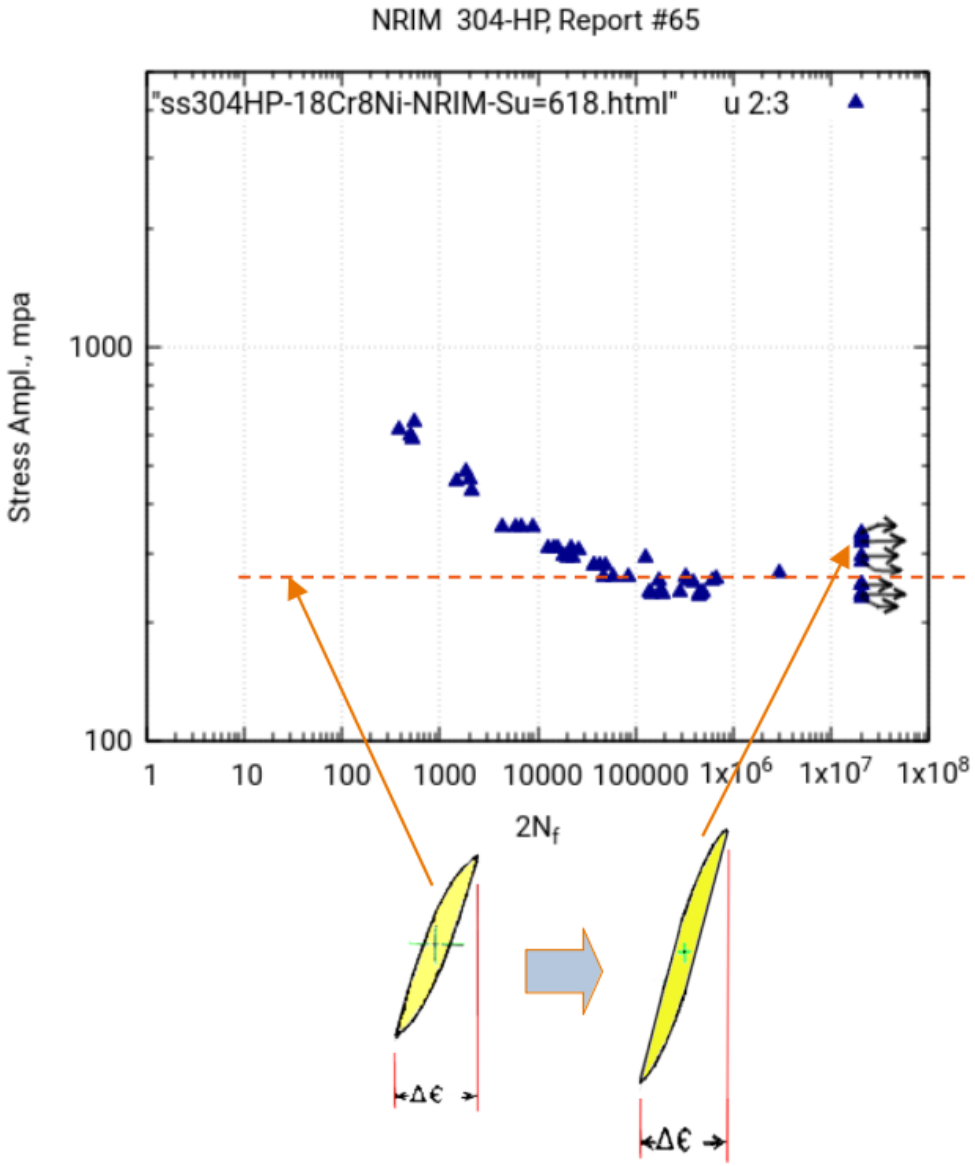

Figure 2.1: Stress-life data of SUS304-HP (18Cr-8Ni) hot rolled strainless steel [110] (hysteresis loops are sketches only, not actual data)

To study the behaviour of carburized steels, the AISI fatigue bar group [1] conducted extensive fatigue tests on the through-carburized case and the simulated core materials that

mimic the case and the core layers of the case-hardened sample. For some parts of this project, POL and CA tests were performed on the same material to study the overload effect on the fatigue limit. Table 2.1 lists the test information, including the iteration number, carburization type, material, hardness and loading history of the paired POL and CA experiment data [1].

Table 2.1: AISI POL and CA tests for simulated case and core materials [1]

Iteration#	Type	Material	Hardness [HRC]	Load His.
101	Case	8822	58	CA
105	Case	8822	58	POL
137	Case	20MoCr4	59	CA
138	Case	20MoCr4	59	POL
141	Case	20MoCr4	60	CA
142	Case	20MoCr4	60	POL
165	Case	8620	62	CA
166	Case	8620	62	POL
168	Case	9310	60	CA
169	Case	9310	60	POL
119	Core	8620	32	CA
143	Core	8620	32	POL
120	Core	8620	38	CA
144	Core	8620	38	POL
121	Core	8620	41	CA
145	Core	8620	41	POL
125	Core	9310	29	CA
149	Core	9310	29	POL
126	Core	9310	31	CA
152	Core	9310	31	POL
127	Core	9310	38	CA
151	Core	9310	38	POL

The first part of the table lists the tests conducted on the through-carburized case material, whose hardness ranges from 58 to 62 HRC. The simulated core for 8620 and 9310 steel are listed in the latter part of the table. The core materials were heat-treated differently in each iteration which results in a hardness ranges from 29 to 41 HRC.

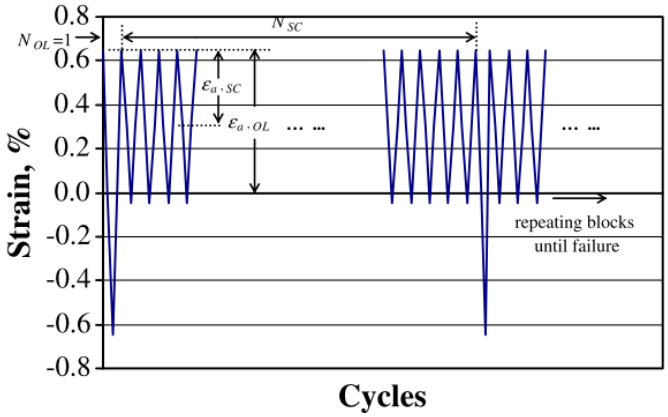

Figure 2.2: Schematic figure of the POL test [163]

For the POL tests carried out by the AISI group, the maximum stress was kept constant for both the overload and the small cycles, and the minimum stress of the small cycles increased to reduce the stress range. The overload in the POL tests was chosen as the stress level at a 10,000-cycle fatigue life in the fully reversed CA test. The small cycles are usually loaded under CA with positive mean stresses. To obtain a reasonable percent damage generated by the small cycles, the interval between the overloads changes with the stress amplitude of the small cycles. A schematic figure of the POL sequence is plotted in Figure 2.2.

The Smith-Watson-Topper (SWT) [139] model was applied to calculate the equivalent stress amplitude of the small cycles in the POL tests. Fully elastic deformation was assumed in the small cycles in the POL histories while calculating the equivalent stress amplitude accounting for the mean stresses in the test using the SWT rule ($S_a^{eq} = \sqrt{S_{max} * S_a}$).

Figures 2.3 to 2.6 compare the paired CA and POL stress-life tests. The CA (square) stress-life data points are plotted with the original POL data (star) on the left figures, and on the right are the CA with the SWT modified POL data (solid circle). The CA and POL iterations for the same material with the same hardness were plotted in the same colour. The arrows in the figures indicate the runout tests.

Due to the high positive mean stress at the levels with a low stress range in the small load cycles, the equivalent stress amplitude for the POL data increased considerably after

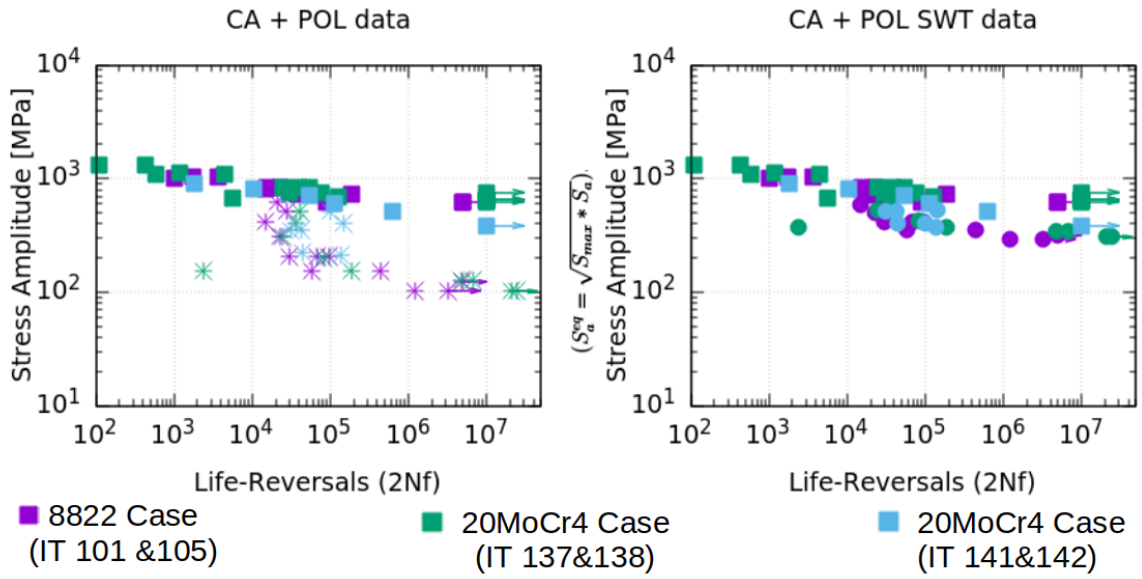

Figure 2.3: CA, POL and SWT modified POL Stress-life data for 8822 and 20MoCr4 case samples (Squares: CA data, Stars: POL data, Circles: POL SWT modified data)[1]

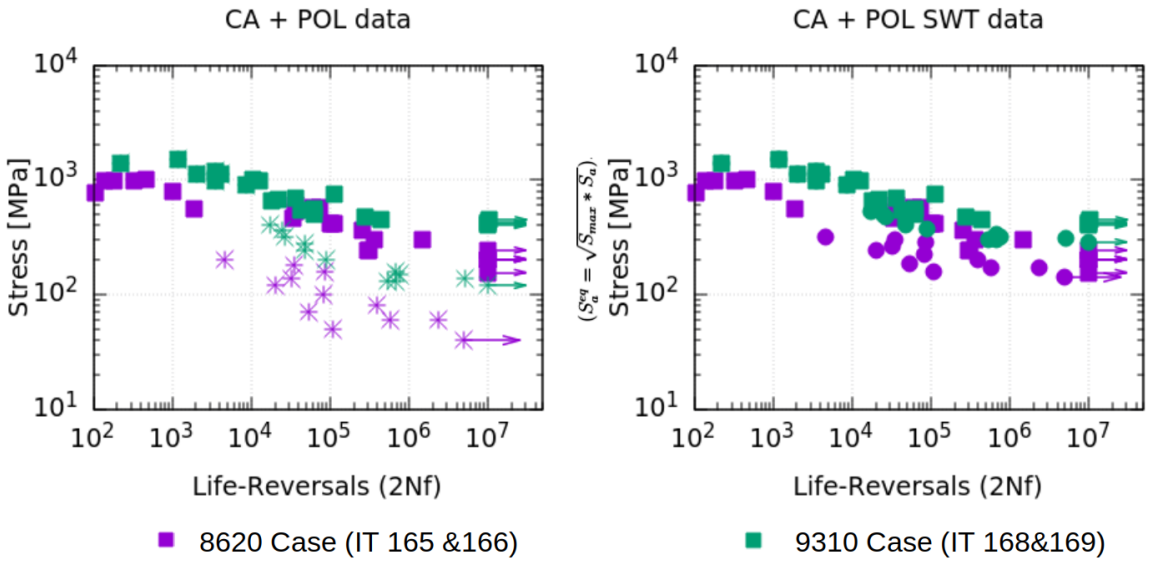

Figure 2.4: CA, POL and SWT modified POL Stress-life data for 8620 and 9310 case samples (Squares: CA data, Stars: POL data, Circles: POL SWT modified data)[1]

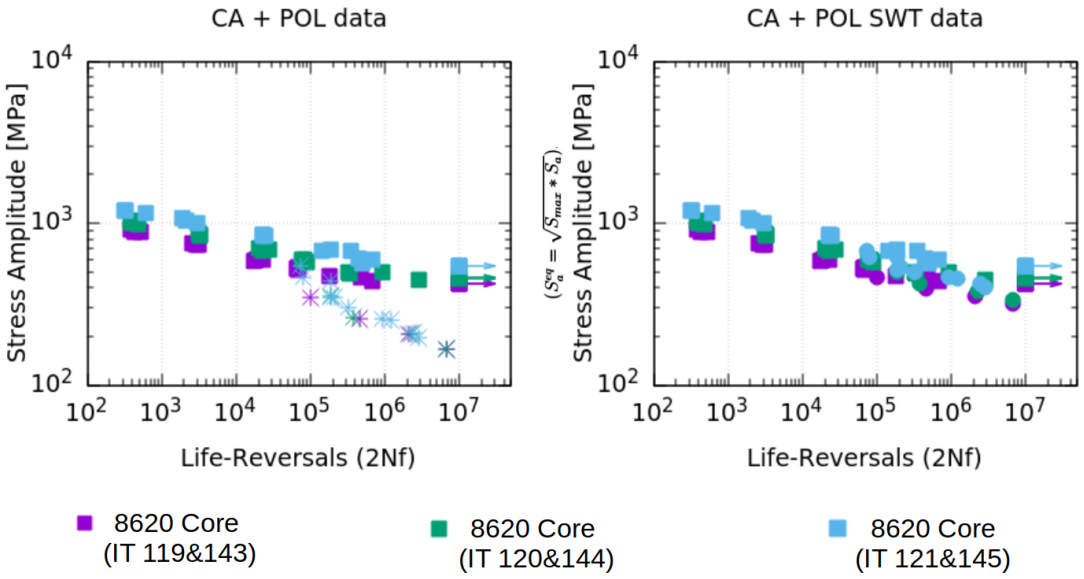

Figure 2.5: CA, POL and SWT modified POL Stress-life data for 8620 core samples (Squares: CA data, Stars: POL data, Circles: POL SWT modified data)[1]

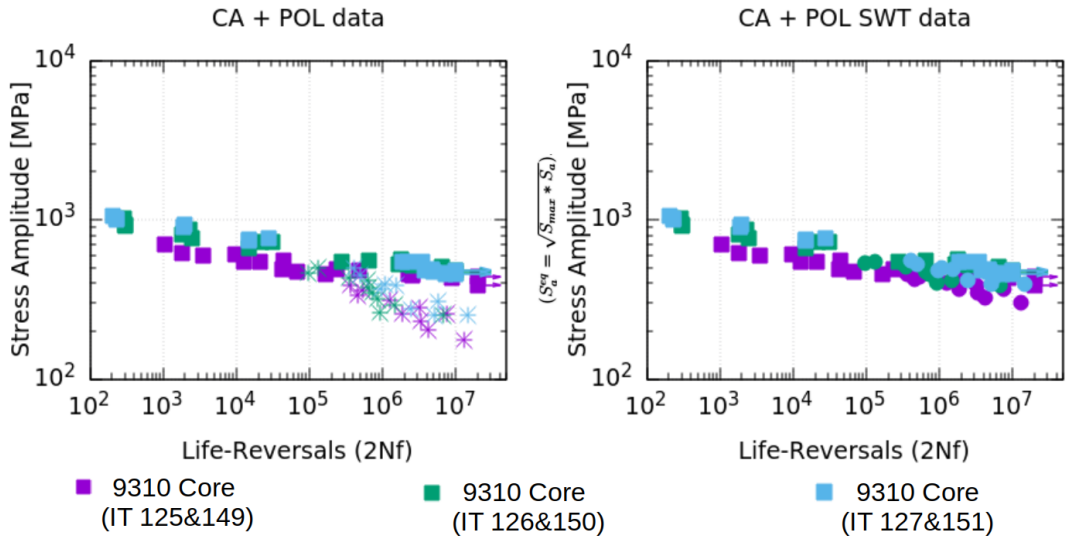

Figure 2.6: CA, POL and SWT modified POL stress-life data for 9310 core samples (Squares: CA data, Stars: POL data, Circles: POL SWT modified data)[1]

the SWT adjustment in the long-life region.

Figure 2.3 shows that the SWT adjusted POL data for the 8822 and the 20MoCr4 simulated case materials are below the CA curve, while, for the 8620 and the 9310 simulated case material in Figure 2.4, the difference between the SWT adjusted POL and the CA data are not as obvious.

Compared to the case material, the stress-life data for the 8620 and 9310 core materials, plotted in Figure 2.5 and 2.6, show much less scatter, even between sets of tests with different hardnesses. Moreover, the additional damage on fatigue performance caused by the POL cycle seems to be negligible after mean stress adjustments. The points in the same colour plotted in circles and squares are located in almost the same scatter band.

Yin et. al. [163] conducted strain-controlled fatigue tests on case-hardened 8620 under three loading histories: 1) fully reversed CA; 2) POL with constant maximum strain; 3) POL with fully reversed small cycles. In the same study, the 4320 case-hardened samples were tested under histories 1) and 2). Figures 2.7 and 2.8 plotted the results the data mentioned in the above study.

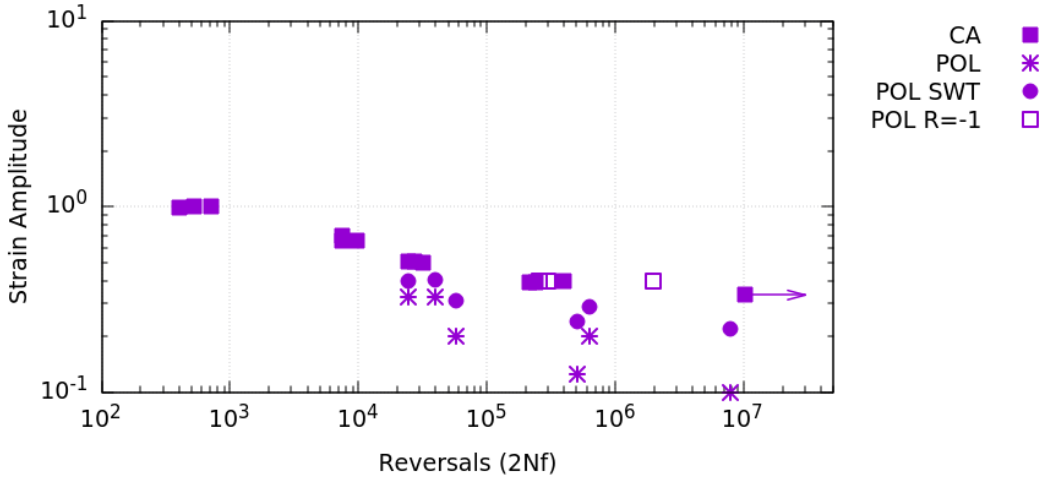

Figure 2.7: CA, POL and SWT modified POL strain-life data for 8620 composite samples [163]

From Figure 2.7, one can observe that the data points of the POL tests with fully

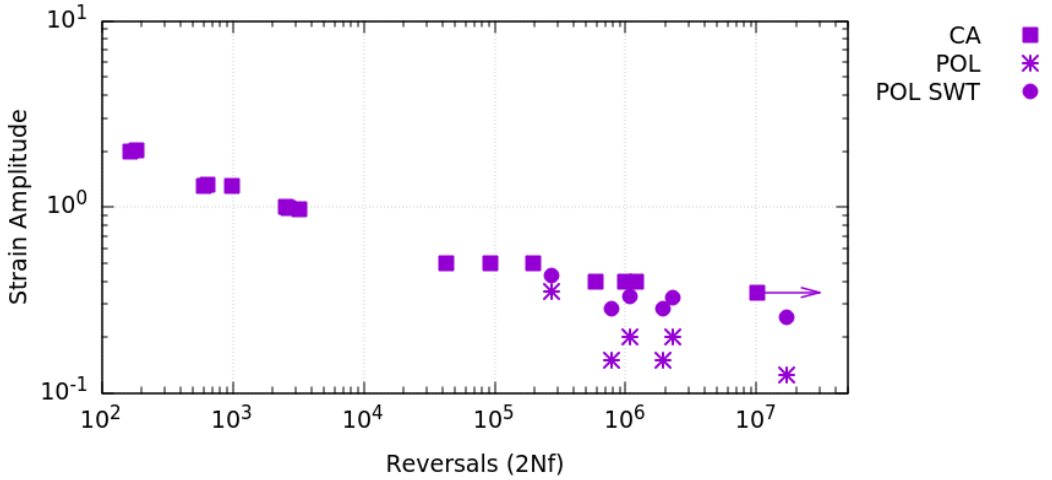

Figure 2.8: CA, POL and SWT modified POL strain-life data for 4320 composite samples [163]

reversed small cycles landed on the same level as the CA results for the 8620 material. While the POL with tensile mean stresses in small cycles performs worse than the CA test in both the 8620 and 4320 composite samples even after SWT adjustments.

Yin et al. [163] suggested that the detrimental effects in the POL tests are not only caused by the tensile mean stresses in the small cycles. The high minimum stress in the small cycles in load history 2) keeps the crack fully open, which contributes to the additional damage in this type of POL tests compared to load history 3), might consist of a partially opened crack in the fully reversed small cycles.

2.3 Residual stress developed during carburization

The residual stresses in carburized steel are developed from two processes: thermal shrinking strains and transformation-induced strains [127]. Therefore, the final metallurgical phase and the volume change resulting from a phase transformation during carburization must be determined in order to estimate the residual stress in a carburized component. Reti [127] suggested the following procedure to determine the volume change resulting from

transformation-induced strains:

- Simulate the diffusion process during carburization to establish the carbon profile of the carburized steel;
- Estimate the temperature field during quenching;
- Determine the phase transformation based on the temperature field and the metal alloy;
- Calculate the volume change during the phase transformation.

2.3.1 Carbon diffusion

When the steel components are placed in a furnace with high carbon content for a certain amount of time, the carbon transferring mechanism occurs in three stages: from the atmosphere to the steel surface; through a chemical reaction on the steel surface; via carbon diffusion from the steel surface to the interior [70].

The carbon diffusion in steel follows Fick's Second Law:

$$\frac{\partial C(x,t)}{\partial t} = \frac{\partial}{\partial x}[D(C,T)\frac{\partial C(x,t)}{\partial x}] \tag{2.1}$$

where $C(x,t)$ is the carbon concentration at a carburizing time t and a distance x from the surface, D is the diffusion coefficient for carbon atoms which depends on the carburizing temperature T and the carbon concentration. Carbon diffusion from the atmosphere to the steel surface is dominated by the carbon potential in the carrier and the mass transfer coefficient of carbon from air to the steel surface. The boundary condition is described in Equation 2.2:

$$D\frac{\partial C}{\partial x}|_{x=0} = \beta(C_p - C) \tag{2.2}$$

where β is the mass transfer coefficient and C_p is the carbon potential in the furnace. Tibbetts [148] proposed an empirical relationship for calculating the diffusion coefficient

in austenitic steel:

$$D = 0.47 \exp(-1.6C) \times \exp[\frac{37000 - 6600C}{RT}] \tag{2.3}$$

Equation 2.3 is valid for steel at high temperatures with a carbon content of up to 1.3% weight percent carbon [148]. Steel in a carburizing furnace falls into the applicable range of the above equation.

2.3.2 Heat transfer during quenching

During the quenching process, heat transfer occurs via conduction, convection and radiation. Convection and radiation remove the heat from the steel surface, and conduction drives the heat flow within the steel [62].

The steel during carburizing, is usually heated far above the boiling point of the quenchant and when the metal is dropped into the quenchant, a vapour blanket forms around the submerged part and impedes the heat transfer between the surface of the component and the quenchant initially. It is then followed by the nucleate boiling stage characterized by violent boiling of the quenchant. When the temperature of the parts has dropped enough to dissipate the vapour blanket barrier, the cooling rate starts to increase. Convection and conduction propel the last stage of heat transfer in quenching, the heat is then carried further away from the part [118].

The transient heat transfer within the steel during quenching is characterized in the form of Fourier's heat conduction shown in Equation 2.4:

$$\rho(T)c_p(T)\frac{\partial T}{\partial t} = \nabla \cdot (k(T)\nabla T) + g(r) \tag{2.4}$$

In this equation, the density, ρ, specific heat, c_p, and thermal conductivity, k, are the material properties of steel as a function of temperature, T; $g(r)$ is the latent heat released due to a phase transformation.

The boundary condition that describes the heat transfer between the submerged surface

and the quenchant can be expressed as:

$$k\frac{\partial T}{\partial x}|_{x=0}= h(T_\infty - T) \tag{2.5}$$

where h is the heat transfer coefficient dependent on T; and T_∞ is the quenchant temperature surrounding the submerged surface.

The effect of temperature and steel chemistry on the density of austenite was investigated by Miettinen [97], who proposed an empirical calculation as described in Equation 2.6:

$$\begin{aligned}\rho^\gamma = {} & 8099.79 - 0.5060T + (-118.26 + 0.00739T)C^\gamma_C \\ & + (-7.59 + 3.422\times 10^{-3}T - 5.388\times 10^{-7}T^2 - 0.0014271C^\gamma_{Cr})C^\gamma_{Cr} \\ & + (1.54 + 2.267\times 10^{-3}T - 11.26\times 10^{-7}T^2 + 0.062642C^\gamma_{Ni})C^\gamma_{Ni} \\ & - 68.24C^\gamma_{Si} - 6.01C^\gamma_{Mn} + 12.45C^\gamma_{Mo}\end{aligned} \tag{2.6}$$

Hasan [53] developed the relationships between specific heat and temperature for different steel alloys with the aid of software $MTDATA$. Equation 2.7 was derived for steel in the austenite phase with an alloy composition of 0.16 wt%C, 0.16 wt%Si and 0.67 wt%Mn [53].

$$c_p = 478.3 + 0.141T \tag{2.7}$$

Liscic [90] studied how temperature and the alloying content in steels affect their conductivity. He observed the trends plotted in Figure 2.9. The thermal conductivity of steel varies with the alloying content percentage at low temperatures and approaches around 30 $\frac{W}{mK}$ at high temperatures.

Later on, Peet et al. [120] applied the neural network model to simulate the thermal conductivity of different alloy steel over a wide range of temperature. The results are shown in Figure 2.10 . Similar to Liscic's results [90], Figure 2.10 showed that the thermal conductivity approaches 30 $\frac{W}{mK}$ at temperatures above 800°C regardless of the alloy variation.

The heat transfer coefficient, h, is strongly dependent on the quenchant type and temperature. Hasan [53] presented the heat transfer coefficients for Micron GP460 mineral oil

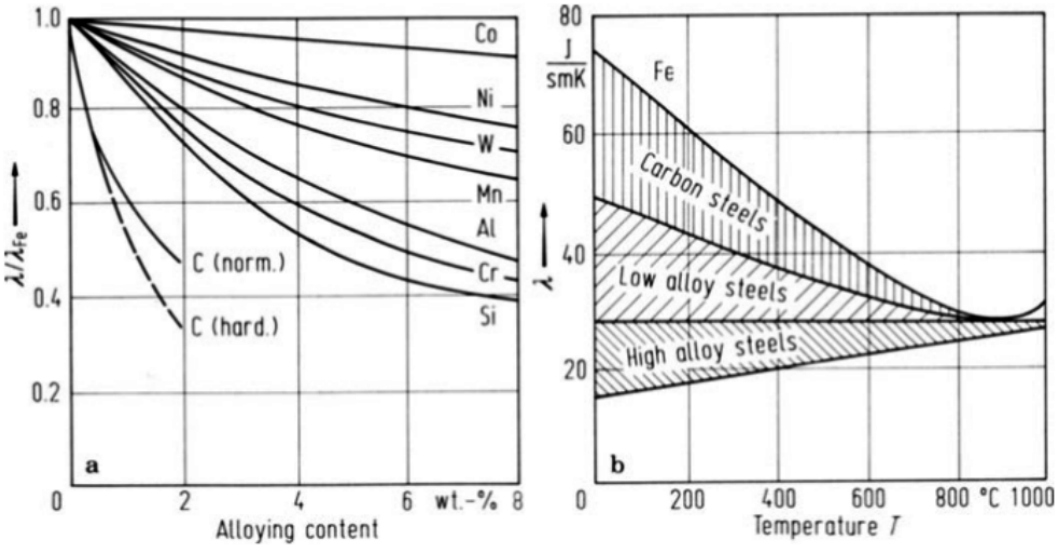

Figure 2.9: Influence of alloying elements and temperature on thermal conductivity of iron based alloys [90]

quench at a temperatures of 150°C, 85°C and 20°C, as shown in Figure 2.11.

2.3.3 Phase transformation

Martensite transformation begins when the temperature of austenite drops below the martensite start temperature, M_s. The transformed martensite percentage increases with continuous cooling below this temperature. The modified Koistinen and Marburger's equation is widely used to calculated the volume fraction of martensite after quench [76]:

$$f = 1 - exp[-\alpha_m(M_s - T)] \tag{2.8}$$

where α_m is the rate parameter that controls the kinetics of the martensite formation which depends on the steel chemistry. Through extensive experimental data collection and analysis, Bohemen [153] proposed Equations 2.9 and 2.10 to determine the rate parameter

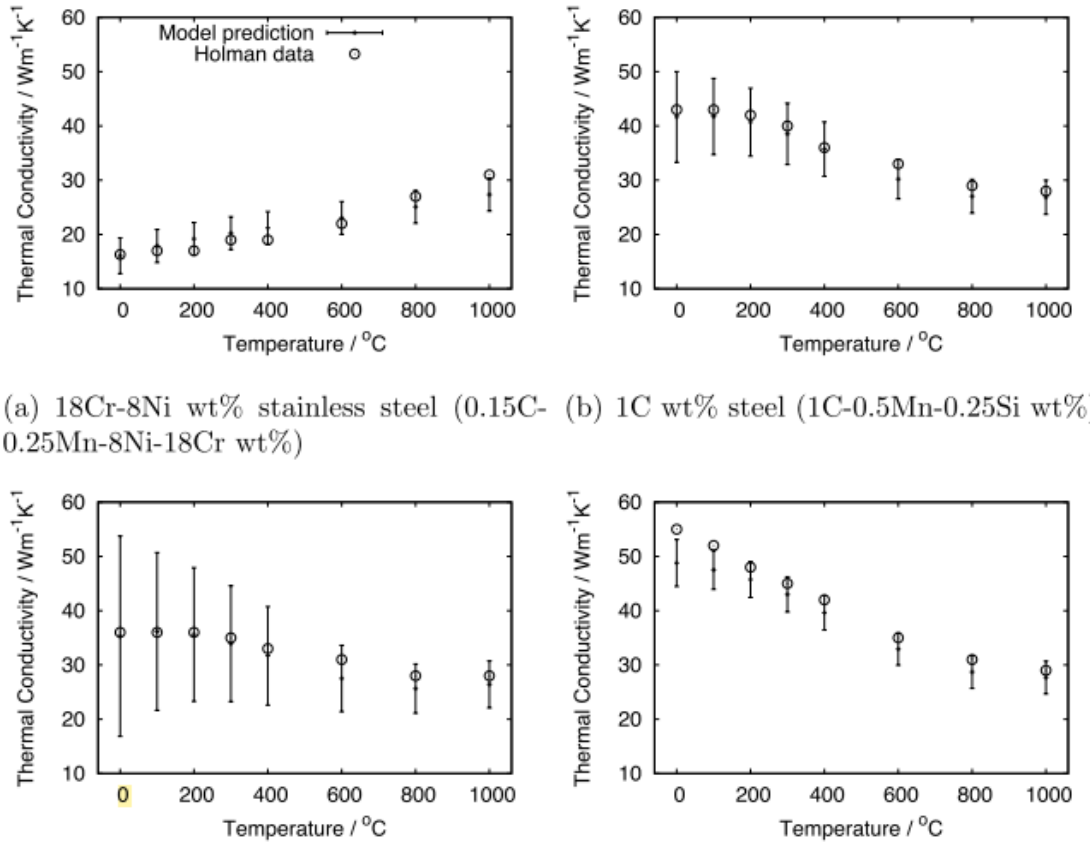

(a) 18Cr-8Ni wt% stainless steel (0.15C-0.25Mn-8Ni-18Cr wt%)

(b) 1C wt% steel (1C-0.5Mn-0.25Si wt%)

(c) 1.5C wt% steel (1.5C-0.5Mn-9,25Si wt%)

(d) 0.5C wt% steel (0.5C-0.5Mn-0.25Si wt%)

Figure 2.10: Thermal conductivity predictions and experimental values for different steel alloys [120]

and the martensite start temperature based on the alloy content in the iron-based metal:

$$\alpha_m = 27.2 - \sum_i S_i x_i - 19.8[1 - exp(-1.56x_C)] \tag{2.9}$$

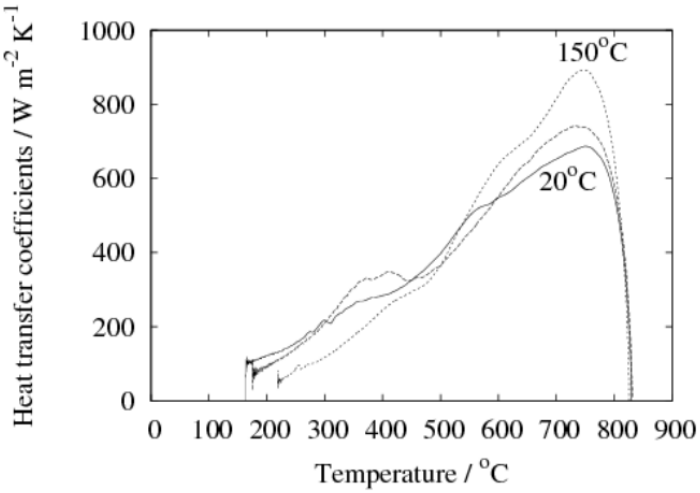

Figure 2.11: Heat transfer coefficient as a function of surface temperature during quenching at different quenchant temperatures [53]

with $\sum_i S_i x_i = 0.14x_{Mn} + 0.21x_{Si} + 0.11x_{Cr} + 0.08xNi + 0.05x_{Mo}$ (α_m is in $\times 10^{-3} K^{-1}$).

$$M_s = 565 - \sum_i K_i x_i - 600[1 - exp(-0.96x_C)] \tag{2.10}$$

with $\sum_i K_i x_i = 31x_{Mn} + 13x_{Si} + 10x_{Cr} + 18x_{Ni} + 12x_{Mo}$.

2.3.4 Phase change induced volume expansion

The volume expansion during a phase transformation is a significant contributor to residual stress formation. In this study, three methodologies from different literatures were examined.

The ASM handbook in Heat Treating [6] presented two approaches, proposed by Thelning [146] and Cohen [17] respectively, to find the volumetric changes associated with martensite formation.

Thelning [146] related the volumetric changes occurring during quenching to the carbon

content and the percentage of different phases in the steel by Equation 2.11:

$$\frac{\Delta V}{V} = (\frac{100 - V_c - V_a}{100})(1.68 \times C) + \frac{V_a}{100}(-4.64 + 2.21 \times C) \tag{2.11}$$

where V_c is the percent by volume of undissolved cementite, V_a is the percent by volume of austenite, $100 - V_c - V_a$ is the volume percent of martensite, and C is the percent weight of carbon dissolved in austenite and martensite, respectively.

Cohen [17] determined the volumetric expansion for martensitic steels using the X-ray diffraction (XRD) approach and found that it increases linearly with the carbon content as shown in Figure 2.12.

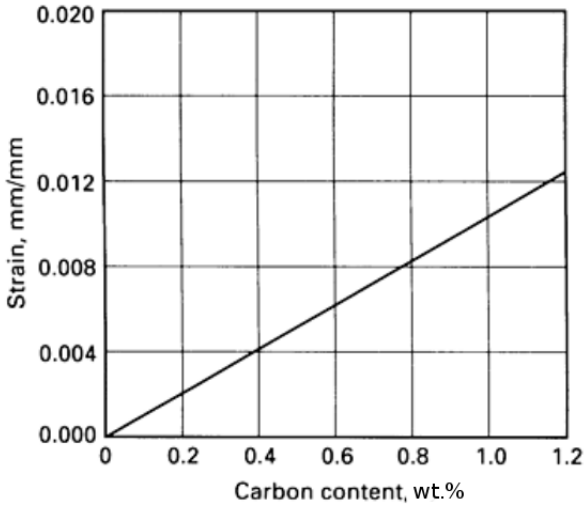

Figure 2.12: Linear expansion in steel after quenching to produce fully martensitic microstructures [17]

Additionally, Moyer [102] conducted a dialatometric study to estimate the effect of carbon content on the the martensite transformation induced volume expansion in iron-carbon alloys. He found that the volume expansion increases with carbon content mainly due to the lowering of M_s temperature and the lattice parameters altered by the carbon atoms. He proposed a polynominal fit, Equation 2.12, to the volume expansion data collected during the austenite to martensite transformation at room temperature in the

iron-based alloy with different carbon content.

$$\frac{\Delta V_{\gamma\to\alpha}}{V_\gamma} = 3.216 + 0.859(C) - 0.343(C)^2 \tag{2.12}$$

2.3.5 Thermal shrinkage

The thermal expansion coefficients of martensite, β_M, and austenite, β_γ, in K^{-1}, are linearly correlated to the atomic carbon content. These relations are presented in Lee's [86] and Warke's [157] papers:

$$\beta_M = (14.9 - 1.9 \times C_M) \times 10^{-6} \tag{2.13}$$

$$\beta_\gamma = (24.9 - 0.5 \times C_\gamma) \times 10^{-6} \tag{2.14}$$

where C_M and C_γ are the atomic percents of carbon in martensite and austenite respectively. The thermal expansion coefficients for martensite and austenite are plotted in terms of atomic carbon percentage in Figure 2.13.

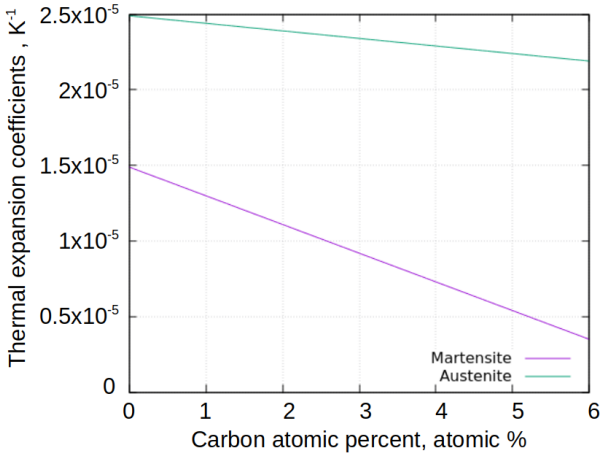

Figure 2.13: Comparison of thermal expansion coefficients of martensite and austenite

Assuming a temperature drop from 843 ^oC (quenchant boiling temperature) to 30^oC (room temperature), the strain caused by thermal shrinkage can be found.

2.4 Compatibility and force balance calculations

According to static force equilibrium and the compatibility conditions, in a multi-layer model, the sum of forces acting on all layers must equal zero, and the final deformations of all layers are the same. With these assumptions, the equilibrium equation contains only one unknown, the final deformation.

Equation 2.15 demonstrates the calculation for the sum of forces acting on all layers :

$$\sum F = E_1 A_1 \epsilon_1 + E_2 A_2 \epsilon_2 + \ldots + E_n A_n \epsilon_n = 0 \tag{2.15}$$

where E_i is the elastic modulus of layer i, A_i is the cross-sectional area of layer i, n is the total number of layers, and ϵ_i is the strain in layer i and calculated as:

$$\epsilon_i = \epsilon_f - \epsilon_i^Q \tag{2.16}$$

ϵ_f is the final strain, which is the same in all layers, and ϵ_i^Q is the strain caused by phase transformation and thermal shrinkage during quenching.

After solving Equation 2.15 for ϵ_f, the stress in each layer can be found from the following equation:

$$\sigma_i = E_i(\epsilon_f - \epsilon_i^Q) \tag{2.17}$$

In a carburized component, the carbon content decreases as the depth increases. The RA content in each layer differs as the carbon content and the quenching speed varies, which causes a deviation in the volume expansion in each layer. Additionally, the thermal expansion coefficient of RA varies from that of martensite. During quenching, the volume shrinkage of the layers differs as well. The layers in a carburized steel constrain movement from each other, thereby causing residual stresses in between layers.

With the strain change calculated based on the methodology introduced in Section 2.3,the residual stress generated during the carburization process can be estimated using the compatibility model.

2.5 Stress-induced retained austenite (RA) transformation

During the carburization and quenching process, the high carbon content in the surface layer impedes the austenite to martensite transformation. Consequently, RA can be found in the case layer of the carburized steel. RA can transform to martensite given other forms of energy input, such as mechanical loading. The strain-induced transformation of RA leads to volume changes in the case layer and alters the initial residual stress.

Researchers have previously observed asymmetric tensile and compressive behaviour in the through-carburized steels [111, 128]. Neu and Sehitoglu [111] studied the RA transformation and the stress-strain behaviour in 4320 steel for which the specimens were carburized for 18 hours and contained 35% initial RA. The tensile yield stress of the samples was much lower than the compressive yield due to RA transformation. A high stress-induced volumetric transformation strain was observed in tensile tests, while under the compressive loading there was little transformation. However, the XRD measurements of RA content after the tension and compression tests, as well as some cyclic tests, all showed an RA content of around 28%. The volumetric changes observed in their study indicated that additional RA transforms when a loading reversal has a higher stress than the previous histories under cyclic loading. Neu and Sehitoglu [111] measured directly volumetric changes that agreed with stress-strain behaviour and also obtained x-ray measurements that did not agree with the stress-strain measurements.

It has also been found that RA transforms under plastic deformation [116, 135, 147, 103] and that a high initial RA content in the material leads to a low tensile yield stress [128, 66, 52, 27, 16].

2.6 Stress relaxation

Mean stress and the initial residual stresses in a component can be alleviated under loading, this process is known as "stress relaxation" [91, 167]. Relaxation of residual stress

in a case-hardened component could affect the fatigue performance.

Several researchers have investigated the residual stress relaxation after various treatments, including case-hardening [162], induction hardening [29], cold working [167] and shot-peening [85].

Yin and Fatemi [162] built a finite element analysis (FEA) model to study residual stress relaxation in the case-hardened samples strained at three different amplitudes: 0.3%, 0.5% and 1.0%. They compared the initial residual stress profile of the case-hardened samples with those loaded by one cycle and ten cycles of fully reversed CA histories. At a strain amplitude of 0.3%, both the case and core deform elastically, and the model predicted no residual relaxation. At ±0.5% strain, the model predicted an elastic case and a plastic core; the residual stresses in both the case and the core relaxed partially. At 1.0% strain, both layers deformed plastically, and the post-loading residual stress profile is similar to that of the specimen loaded under 0.5% strain .

Dindinger et al. [29] tested induction hardened SAE1045 under different strain levels. They found that the residual stress relaxation is negligible for a plastic strain over total strain ratio, $\frac{\epsilon_{plas}}{\epsilon_{total}}$, upto 0.05; if $\frac{\epsilon_{plas}}{\epsilon_{total}}$ is greater than 0.05, the residual stresses relax swiftly during cyclic loading.

Zhuang and Halford [167] suggested the three factors that have the most significant impact on residual stress relaxation: 1) the initial residual stress profile; 2) the characteristics of the applied load, including the stress amplitude, the mean stress and the number of load cycles; 3) the cyclic response of the materials, i.e. softening or hardening behaviour. They proposed Equation 2.18 that includes the amount of cold work, the yield stress of the material, the stress amplitude and other material properties in the process of estimating the residual stress relaxation.

$$\frac{\sigma_N^{re}}{\sigma_0^{re}} = A\left(\frac{2\sigma_a^2}{(1-R)(C_W\sigma_y)^2}\right)^m (N-1)^B - 1 \tag{2.18}$$

where A is a material constant which is dependent on cyclic stress and strain response, B is a constant controlling the relaxation rate vs loading cycles, σ_0^{re} is the initial residual stress, σ_N^{re} is the residual stress after N cycles of loading, C_W is a parameter that accounts

for the degree of cold working, and m is a material constant depends on cyclic stress and strain response. This equation was fitted to the data collected on the cold-worked samples and generated reasonable predictions in Zhuang and Halford's study [167].

Holzapfel et al. [59] studied the residual stress relaxation on quenched and tempered AISI 4140 steel samples with a shot-peen treatment under axial and bending cyclic loads. The tests were run under load control. The axial tests were loaded under either pure tension or pure compression. Residual stress was measured by XRD on the surface of the sample at various fatigue cycles. The residual stress vs. cycle number plot shows that most of the residual stress relaxed after the first cycle. The amount of relaxation increases with stress amplitude.

Landgraf and Chernenkoff [85] proposed that relaxation does not depend on the magnitude of the mean stress. On the other hand, the material hardness and the applied strain amplitudes are the critical parameters that influence the amount of relaxation. They introduced the following equation to evaluate the cyclic mean stress relaxation rate:

$$\sigma_{oN} = \sigma_{ol}(N)^r \tag{2.19}$$

where σ_{oN} is the mean stress at Nth cycle, σ_{ol} is the mean stress at the 1st cycle, r is the relaxation exponent, which is dependent on the material hardness and strain amplitude of the test.

Arcari and Dowling [5] conducted multiple VA experiments on 7075-T6511 Aluminum. The cyclic and monotonic stress-strain curves of the chosen material overlapped, which indicates that there is no cyclic hardening or softening under fatigue loading. The load histories applied in this study include a two-level test, a three-level test, a two-block test and a random loading history. Continuous and repetitive mean stress relaxation was observed in the multiple-level VA tests. Additionally, mean stress relaxation occurred in the service loading as well.

Lu et al. [91] studied the residual stress relaxation phenomenon in shot-peened 35NCD16 steel during cyclic loading. In this cyclic softening material, the initial residual stress relaxes with an increasing number of cycles until a stabilized state is reached. Relaxation is

a dominant phenomenon when loaded under high cyclic stresses.

Evidence has shown that a RA transformation alters the initial residual stress in different loading conditions [101, 65]. RA transformation and residual stress relaxation are two competing phenomena in the material [101].

Morris et al. [101] conducted fully reversed shear tests at three stress levels on case-hardened carburized AISI 8620 steel with 35% RA on the surface of the specimens. They found that when the samples were sheared at a $0.4S_{us}$ stress level, RA transformed gradually throughout life and compressive residual stress in the case layer increased initially but stabilized after 1,000 cycles. At 0.6 and $0.8S_{us}$ stress levels, most of the RA decomposition occurred in the first cycle. The compressive residual stress at the $0.6S_{us}$ increased mostly in the first cycle and became stable afterwards; while under $0.8S_{us}$, the compressive residual stress increased in the first cycle and then dropped back to the initial value shortly thereafter. In another group of tests, they ran a sample at $0.8S_{us}$ for the first cycle followed by the two smaller load cycles. They found that in these tests, the first cycle consumed most of RA.

Jeddi [65] et al. tested notched samples made of carburized 14NiCr11 under a bending fatigue load. The surface compressive residual stresses changed from -269 MPa to -321 MPa and from -205 MPa to -465 MPa with 6% and 9% of RA transformation, respectively, during the 10^6 loading cycles.

2.7 Initiation predictions for carburized steels

Multiple researchers have developed models to predict the crack initiation location and the fatigue life for heat-treated components under various types of loading. Some studies on crack initiation in a vacuum environment were also reviewed to supplement the subsurface crack initiation theories.

Yin and Fatemi examined the stress-strain behaviour of case-hardened carburized steel and predicted the fatigue life for the axial samples under CA and VA loadings [162, 161, 163].

The stress-strain and fatigue behaviour of the through-carburized case, the simulated core and the case-hardened SAE8620 axial samples loaded under fully reversed CA histories were studied. The strain-life curves for the same material with the three different heat treatments intersect at one point, and this point differentiates surface and subsurface crack initiation in the case-hardened carburized axial sample. The crack initiation location was predicted using a four-layer model along with the strain-life approach that accounted for mean stresses with SWT. A comparison between the lower and upper bound predictions and the experimental data was presented. The upper bound method generated predictions closer to the experiment results, while the lower bound approach was conservative. The sensitivity study on residual stress shows that adding the residual stress relaxation model into consideration does not affect the fatigue life prediction significantly [161].

Yin et al. [163] proposed a model to predict the fatigue life for the case-hardened carburized SAE8620 and SAE4320 axial samples under POL and service loading using the linear damage rule with the effective strain-life curves derived from the POL test data. They found that the fatigue curves for the case-hardened material under POL lie below the CA curve even after a SWT mean stress correction (Figures 2.7 and 2.8). They attributed this phenomenon to the fully open crack under POL, whereas the crack in the fully reversed CA test is partially closed.

Deng et al. [28] tested carburized 12Cr steel alloy under CA at R=-1 and R=0 and observed internal failure for both R-ratios. They established a model to predict the fatigue limit based on the inclusion sizes.

Zhang et al. [165] predicted the fatigue life of SAE 1045 induction-hardened shafts by summing the cycles spent in the initiation and the crack propagation phases in a 5-layer model. The local strain-life approach was applied to determine the crack initiation life and initiation location in the 3-point bending specimen.

Baumel and Seeger [10] estimated the fatigue life of the 0.15% carbon steel axial samples loaded under CA and VA loading. The specimens were nitrided with a case depth of 0.9 mm. A two-layer model that implements the Miner's rule [99] and the Masing [95] memory model was developed for fatigue life prediction. The local stress in each layer was

derived from the total strain, which is the sum of the initial residual strain and the loaded strain. They mentioned that the two main differences between surface and subsurface crack initiation are: 1) the crack tip stress intensity factor is lower for an internal crack than a surface crack; 2) the vacuum environment in the subsurface results in longer initiation life than in air.

Wadsworth [156] conducted axial CA fatigue tests on 0.5% carbon steel in a vacuum and an air environment to study the effect of a vacuum testing environment on the crack initiation life. He found that at high strain amplitudes, cycling in the vacuum atmosphere increases the fatigue life by around ten times compared to testing in air, and the fatigue limit improves by about 25%.

On the other hand, Kujawski and Ellyin [82] showed that for ASTM A516 Gr.70 steel, the fatigue lives of the samples tested in vacuum are only about two times longer than those tested in air. Testing in vacuum improved the fatigue limit by 10%.

2.8 Case-hardened carburized steel stress-life data

The AISI fatigue bar group [1] conducted fatigue tests on the through-carburized case, simulated core, and case-hardened composite axial samples made out of SAE8620, 4320 and 9310 steels. The stress-life data for the fatigue tests of the three materials with different heat-treatments are plotted in Figure 2.14. Unfortunately, the presence of fisheyes on the fracture surface of the composite samples was not documented in the reports.

For the SAE8620 steel shown in Figure 2.14a, the simulated case samples were heat-treated to two different hardnesses, 59 HRC and 56HRC. A considerable amount of variance can be observed between the stress-life data of the case material with the two different hardnesses. The case sample with a hardness of 59HRC, which is the same as the surface hardness of the composite SAE 8620 samples, has a similar fatigue limit as the composite sample. However, the 56HRC case sample has a lower fatigue limit than the 59HRC case and the composite sample.

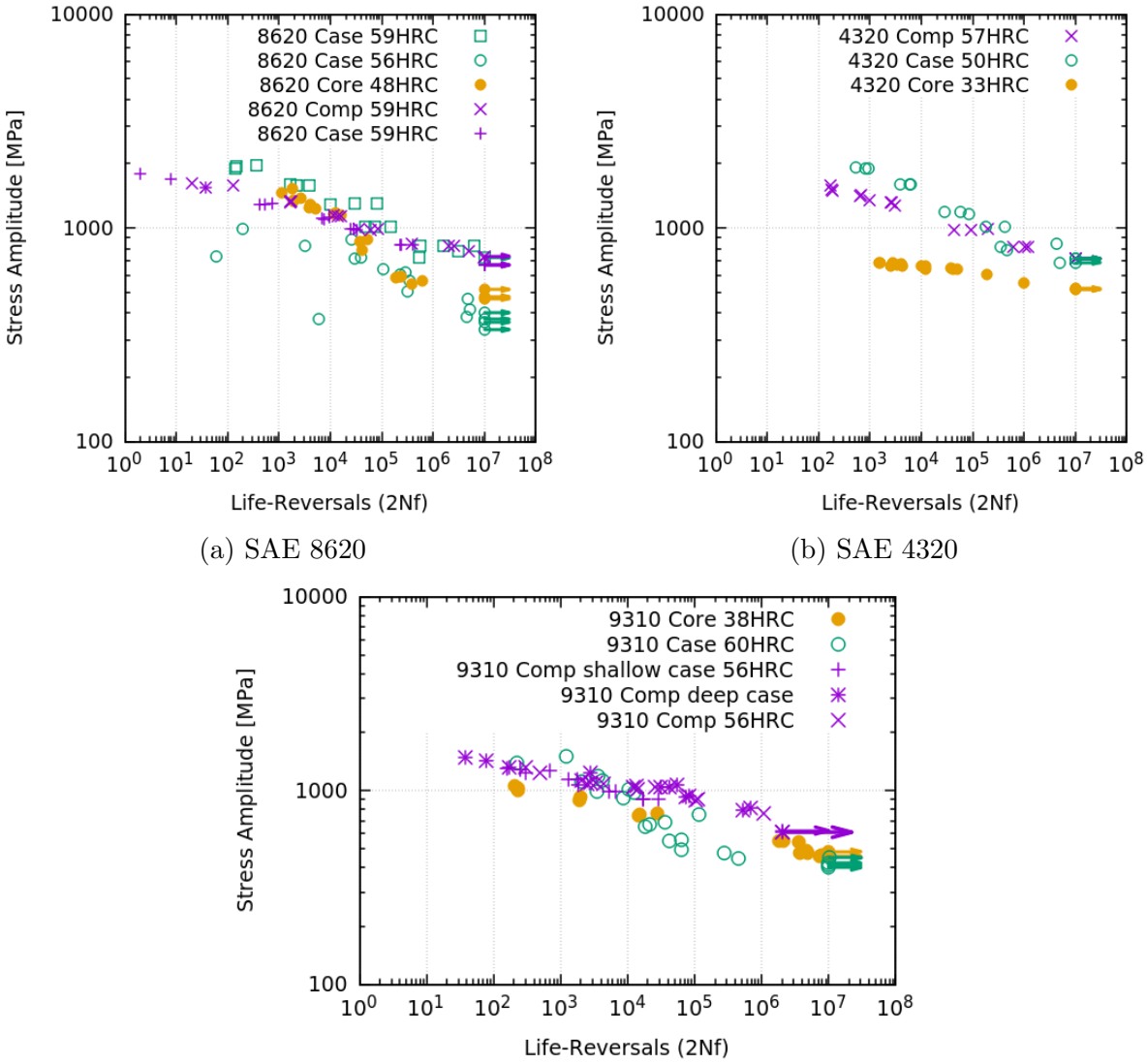

(a) SAE 8620

(b) SAE 4320

(c) SAE 9310

Figure 2.14: Stress-life data for the through-carburized case, simulated core and the case-hardened composite axial sample tests [1]

The core materials in both the SAE 8620 and 4320 steels have lower fatigue limits than the case-hardened composite of those materials. Tensile residual stress is expected in the core layer of the composite sample due to the carburization. This should cause the

composite sample to fail earlier in the core layer than the simulated core samples without a tensile mean at a low-stress amplitude. However, the opposite phenomenon was observed from the test results. The possible factors contributing to the improved fatigue performance in the core layer of the composite sample could be: 1) the vacuum environment and 2) the physical constraint by the surrounded crystals, which prevents flaw initiation driven by cross-slip.

Unfortunately, in the data set for SAE 9310 steel plotted in Figure 2.14c, the runout tests of the case-hardened sample were only run to 1 million cycles, which is ten times shorter than the standard. With the available test data for 9310, the simulated case material has the lowest stress amplitude at the fatigue limit among all three heat treatments, and the composite material has the highest stress at the fatigue limit. The depth of the case layer does not cause a visible difference in fatigue performance for the composite material plotted in purple.

In general, the stress-life data for the case material shows more scatter than the core and the composite samples, and it seems to be very sensitive to the sample hardness. The fatigue limit of the case material is similar to the composite; yet, the core samples have a lower fatigue limit.

2.9 Effects of a stress raiser

In the stress concentration zone of a component, such as at a notch, the local stress at the hot-spot zone can be significantly higher than the nominal stress applied across the plane. The theoretical elastic stress concentration factor, K_t, is defined as:

$$K_t = \frac{\sigma}{S} \tag{2.20}$$

where σ is the local elastic peak stress at the stress concentration zone, and S is the nominal stress.

A collection of stress concentration factors which characterize the local stress at different

stress raisers are recorded in the *Stress Concentration Handbook* [121]. The K_t for a plate with a circular hole under uniaxial load can be estimated as:

$$K_{tg} = \frac{2 + (1 - d/w)^3}{1 - d/w} \tag{2.21}$$

where K_{tg} stands for the stress concentration factor K_t applied to the stress on the gross cross-section area, d is the hole diameter, and w is the plate width. Equation 2.21 is an empirical formula proposed by Heywood for a circular hole [58] applicable to a wide range of d/w. This estimation agrees closely with Howland's theoretical solution [60] when $d/w < 1/3$.

If the material behaves fully elastically at the stress concentration zone, the local stress is K_t times the nominal stress. However, if the material undergoes plastic deformation, Neuber's rule [112] should be applied to determine the local stress and strain at the notch:

$$\sigma\epsilon = \frac{(K_t S)^2}{E} \tag{2.22}$$

where ϵ is the local strain and can be determined from the stress-strain curve using the local stress σ, and E is the material elastic modulus.

Conle and Nowack [21] conducted crack initiation tests for unnotched and notched 2024-T3 aluminum specimens and measured the local strain at the notch root. They found that under CA loading, the fatigue notch factor, K_f, decreases as the stress level increases. An equation for K_f that fits the CA fatigue-life data, was established as a function of the local stress and strain ranges. Both the constant and varying K_fs were applied to calculate the theoretical Neuber factor, $\sqrt{\frac{(K_f \Delta S)^2}{E}}$, at various stress ranges in the increment-step tests. While the local stress and strain were measured to obtain the experimental Neuber factor, $\sqrt{\Delta\sigma\Delta\epsilon}$. By comparing the calculated and measured Neuber factor, the authors found that the estimation generated using constant K_f was conservative, and that of the varying K_f overpredicted the local stress and strain.

Molski and Glinka [100] proposed the equivalent strain energy density (ESED) method as an alternative approach for calculating the local stress and strain at a notch in the

elastic-plastic region:

$$K_t = \frac{\sigma}{S} = (\frac{W_\sigma}{W_S})^{0.5} \tag{2.23}$$

where W_σ, calculated as $\int_0^\epsilon \sigma(\epsilon)d\epsilon$ is the strain energy per unit volume due to local stress and strain at the notch root, and W_S, $\int_0^e S(e)de$ is the elastic strain energy per unit volume due to the nominal remote stress. The ESED model predicts lower local stress and strain at the notch compared to Neuber's rule.

Knop et al. [73] compared the Neuber and the ESED approaches and concluded that the Neuber rule works better for plane stress cyclic loading, while ESED performs better for plain strain conditions. The ESED method also improves with increasing K_t value.

2.10 Crack closure theories

Since Elber's [41] proposal, the concept of crack closure, multiple effective-strain and effective-stress based models have been developed to predict the crack propagation life for samples loaded under VA loading histories with and without a stress raiser. With the hope of being able to collapse the scattered crack growth curves, which depend on the R-ratio and material properties into a single curve, many researchers have observed the crack closure behaviour and plotted crack growth rates in terms of the effective stress or strain range during which a crack is open for different types of steels.

To investigate the factors influencing the crack closure behaviour, an extensive literature search was carried out to collect the experimental crack opening and effective crack growth rate (da/dN vs ΔK_{eff}) data. A summary of the related findings for steels is presented . The crack growth data points collected from different sources were plotted in one graph to visualize the scatter in the measurements. An effective crack growth rate curve, which was best fitted through the collected data, was used in the crack propagation simulations for part of this study.

Paris and Erdogan [117] established a log-linear relationship between the stress intensity

factor range, ΔK, and the crack growth rate, $\frac{da}{dN}$, as stated in Equation 2.24:

$$\frac{da}{dN} = C(\Delta K)^m \tag{2.24}$$

C and m in Equation 2.24 are material constants, derived as per ASTM E-647 [8].

2.10.1 Effective-strain based theories

Elber [41], later on, noticed that the cracks in aluminum are not fully open under small tensile loads. He believed that this crack closure effect was caused by the compressive stress at the crack tip and that the closed portion of the stress intensity cycle did not cause damage or propagate the crack. He proposed an effective stress intensity factor, ΔK_{eff}, to account for crack closure and replaced the ΔK in Equation 2.24 for crack growth prediction:

$$\frac{da}{dN} = C(\Delta K_{eff})^m = C(U\Delta K)^m \tag{2.25}$$

where U is an effective stress range ratio defined as:

$$U = \frac{S_{max} - S_{op}}{S_{max} - S_{min}} = \frac{\Delta S_{eff}}{\Delta S} \tag{2.26}$$

Elber also suggested a linear relationship between U and the stress ratio, $R = \frac{S_{min}}{S_{max}}$, for the aluminum he tested. Since then, several researchers [12, 55, 34, 83, 134] have proposed alternative U calculations for various materials at different stress ratios. Most of these methods were developed based on the crack closure behaviour in long cracks with small scale crack-tip yielding.

Theories for effective-strain based crack growth are also well developed and can account for the behaviour of short cracks in a stress concentration zone with elastic-plastic behaviour.

Vormwald and Seeger[155] studied the crack closure in short cracks and found that the cracks closed and opened at a specific strain. Thus the crack opening and closing stresses

are different if plasticity is involved, as shown in Figure 2.15. The crack opens at Point B and closes at D.

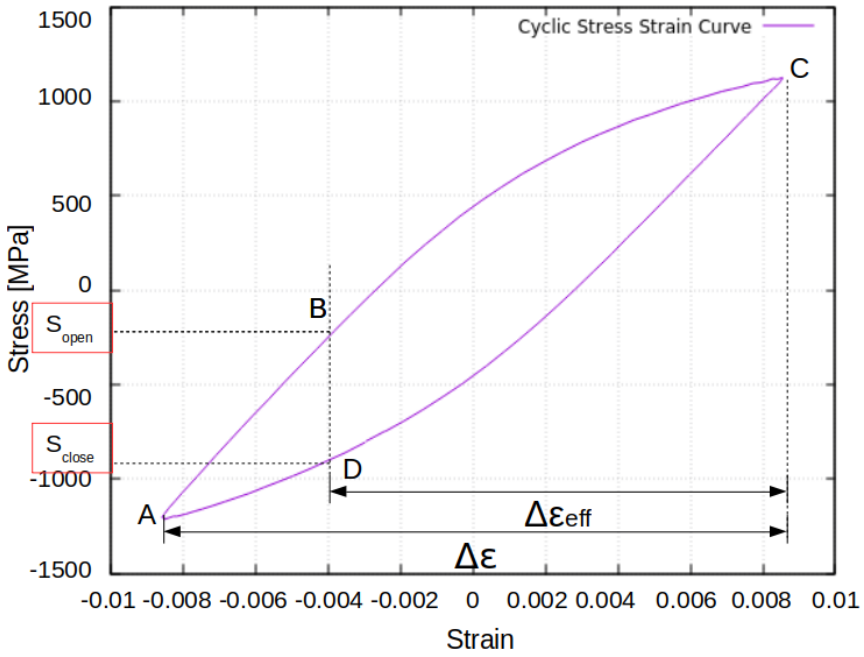

Figure 2.15: Effective strain range in a hysteresis loop

Evidence has shown that short cracks initiated from a stress concentration zone with high local stresses have a higher growth rate than the long crack with the same stress intensity factor. In order to consider the elastic-plastic effect at the crack tip in short cracks, Haddad et al. [38] proposed a modified calculation for an effective stress intensity factor by including an intrinsic crack length, a_{int}, to accommodate the fast growth rate in short cracks:

$$\Delta K_{eff} = FE\Delta\epsilon_{eff}\sqrt{\pi(a_{int}+a)} \tag{2.27}$$

where F is the geometry factor, E is the elastic modulus, $\Delta\epsilon_{eff}$ is the effective strain range, as labeled in Figure 2.15, and a_{int} is the intrinsic crack length which can be obtained from Equation 2.28.

As the crack grows, the effect of a_{int} on ΔK_{eff} dwindles and eventually a_{int} has little

effect on long cracks growth rates. a_{int} is an imaginary initial flaw in a material. It is dependent on the material properties, including the threshold stress intensity factor, ΔK_{th}, and the strain range at the fatigue limit, $\Delta\epsilon_i$ [37]:

$$a_{int} = (\frac{\Delta K_{th}}{FE\Delta\epsilon_i})^2 \frac{1}{\pi} \tag{2.28}$$

The geometry factor in Equation 2.27 is a product of two parameters: $F = SHF \times F_w$, where SHF is the crack shape factor (equals to 1 for a centre through crack, 0.7 for an elliptical crack front [154], and 1.12 for an edge flaw), F_w is the finite width correction factor. An estimation of F_w for through-thickness flaws in a centre-cracked plate was proposed by Feddersen [43] and adopted by BS7910 Section M.3.1 [14] as:

$$F_w = [sec(\pi a/W)]^{0.5} \tag{2.29}$$

where W is the total width of the plate.

2.10.2 Crack opening stress and effective strain range

The crack opening stress, S_{op}, changes in a VA history. The effective strain range, $\Delta\epsilon_{eff}$, is calculated differently depending on the crack opening stress level with respect to the maximum and minimum stresses (S_{max} and S_{min}) in the corresponding reversal. The following three conditions are applied:

1. If $S_{max} < S_{op}$, the crack is fully closed: $\Delta\epsilon_{eff} = 0$

2. If $S_{min} < S_{op} < S_{max}$, the crack is partially open during part of load cycle:

$$\Delta\epsilon_{eff} = \Delta\epsilon - \Delta\epsilon_{op} = \Delta\epsilon - (\frac{S_{op} - S_{min}}{E}) \tag{2.30}$$

   Assuming the material deforms elastically from the point of S_{min} (Point A in Figure 2.15) to S_{open} (Point B).

3. If $S_{op} < S_{min}$, the crack is fully open: $\Delta\epsilon_{eff} = \Delta\epsilon$

Much evidence [63, 78, 80, 9, 45, 74, 114, 64, 68] has proved that the crack opening stress stabilizes after several cycles under CA loading.

DuQuesnay et al. [33] proposed a model to calculate the steady-state crack opening stress:

$$S_{opss} = \theta\sigma_{max}[1 - (\frac{\sigma_{max}}{\sigma_{cy}})^2] + \varphi\sigma_{min} \tag{2.31}$$

where σ_{max} and σ_{min} are the local maximum and minimum stresses in a notched sample or the nominal stresses in an un-notched specimen, σ_{cy} is the cyclic yield stress, θ and φ are two material constants determined by experiments for a given material.

In Equation 2.31, the crack opening stress is linearly related to the minimum stress and dependent on the ratio of maximum stress to the cyclic yield stress. It has been observed that the steady-state crack opening stress drops after a compressive underload or a tensile overload near the cyclic yield stress. This steady-state crack opening stress estimation predicts the crack closure behaviour induced by the plasticity around the crack tip and by asperities on the crack surface [149].

The material constants in Equation 2.31 can be derived from the strain-life data of CA and periodic overload (POL) tests done using smooth specimens. Assuming the POL tests were designed to generate fully open cracks, while the cracks in the CA tests are partially closed depending on the R-ratio, from the fitted CA and POL strain-life curves, the effective portion of the cycle in the CA tests can be determined at different strain ranges [84]. The steady-state crack opening stress in the CA cycles can be calculated at a specific strain-range using Equation 2.32 [149]:

$$S_{op} = S_{min} + E(\Delta\epsilon_{CA} - \Delta\epsilon_{eff}) \tag{2.32}$$

Where $\Delta\epsilon_{CA}$ and $\Delta\epsilon_{eff}$ are the strain ranges of the CA and POL tests at the same fatigue life. By fitting Equation 2.31 to the results obtained from Equation 2.32, the material constants, θ and φ, can be determined.

An example of the application of this method will be described in Section 3.3. The S_{op} points plotted in Figure 3.8 are derived from the fitted strain-life curves shown in Figure 3.7.

Under VA loading, S_{op} changes with S_{opss} at each load reversal. S_{op}, at reversal i can be determined by the following rules:

1. If $S^i_{opss} \leq S^{i-1}_{op}$, then $S^i_{op} = S^i_{opss}$
2. If $S^i_{opss} > S^{i-1}_{op}$, then

$$S^i_{op} = S^{i-1}_{op} + \Delta S_{op} = S^{i-1}_{op} + m(S_{opss} - S^{i-1}_{op}) \tag{2.33}$$

Equation 2.33 proposed by Vormwald and Seeger [155] illustrates the recovery behaviour of the crack opening stress. The recovery constant, m, varies between materials. El-Zeghayar et al. [40] showed the dependency of the recovery factor on material hardness.

2.10.3 Local stress and strain at crack tip

Since the crack growth model proposed by Haddad et al. in Equation 2.27 is applicable to both short and long cracks, the traditional fatigue life estimation containing separated crack initiation and propagation stages can be incorporated into a single crack propagation phase.

Since cracks tend to initiate at notches or other stress raisers, the stress raising effect must be included when calculating the effective strain range in short cracks. Therefore, Neuber's rule was applied to calculate the local stress and strain ranges at the crack tip near a notch as described in Equation 2.34 [112]:

$$\Delta\sigma\Delta\epsilon = (K_p\Delta S)(K_p\Delta e) \tag{2.34}$$

where K_p is the stress concentration factor at the crack tip.

Xu et al. [158] compared the crack-tip stress concentration factor, K_p,with the geometric factor ($F = \frac{K_I}{\sigma\sqrt{\pi a}}$) in centre notched plates and found a good agreement between the two. Therefore, the local crack-tip stress in short cracks near a notch can be calculated using the shape factor (F).

The stress intensity factor for short cracks near a notch has been widely studied. Multiple solutions for calculating the stress intensity factor of a crack propagating away from a centre notched plate were proposed [133, 150, 140, 71, 129, 93, 81]. The solutions proposed by different authors yield similar results. In this project, the geometric factor developed by Schijve [133] for short cracks growing from an elliptical notch is applied together with the general long crack geometric factor:

$$F_{short}^{Schijve} = K_t \times [1.1215 - 3.21(\frac{a}{\rho}) + 5.16(\frac{a}{\rho})^{1.5} - 3.73(\frac{a}{\rho})^2 + 1.14(\frac{a}{\rho})^{2.5}] \quad for \quad \frac{a}{\rho} \leq 1 \tag{2.35a}$$

$$F_{long} = \sqrt{\frac{a+\rho}{a}} \quad for \quad \frac{a}{\rho} > 1 \tag{2.35b}$$

where ρ is the radius of the notch and K_t is the stress concentration factor at an elliptical notch dependent on the notch depth, a_o:

$$K_t^{ellipse} = 1 + 2 \times \sqrt{\frac{a_o}{\rho}} \tag{2.36}$$

For other types of 2D or 3D notches suitable concentration factors would need to be derived from the literature or by a finite element analysis.

A sudden shift in local stress caused by a discontinuous K_p curve can generate an unrealistic mean stress shift in the simulation. Therefore, a smooth K_p (or F) transition is desired for a stable memory event. The transition of F from short to long cracks happens at the point where $F_{short}^{Schijve}$ and F_{long} meets in the region of $\frac{a}{\rho} \leq 1$. In this case, the

transition occurs around $\frac{a}{\rho}$ of 0.6. An example of the K_p factor applied in the program is illustrated in Figure 2.16. The geometric dimensions of the elliptical notch are listed in Table 3.2 in Section 3.3.

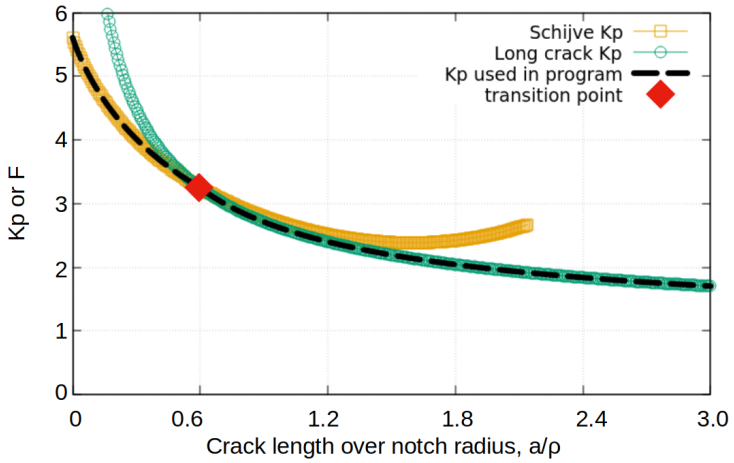

Figure 2.16: Stress concentration factor at a crack tip near an elliptical notch with geometric dimensions listed in Table 3.2

Since the geometric factors are almost equivalent to the stress concentration factors in the cracks propagating from a notch, the F factors, shown in Equation 2.35 and Figure 2.16, are used as the stress concentration factor, K_p, in Equation 2.34.

2.10.4 Effective ΔK crack growth rates and the influencing factors

The crack growth rates in terms of the effective stress intensity range for a wide variety of steels were measured by multiple researchers. Multiple factors, including crack length, sample thickness, and test method, could affect the crack closure behaviour and the shape of the crack growth curves . On the other hand, material hardness and stress-ratio appear to play limited roles on crack growth in terms of ΔK_{eff} as will be discussed in this section.

Short cracks

Previous researchers [119, 145, 132, 30, 38] have found that short cracks have higher crack growth rates and lower thresholds than the long cracks in various metals. Elmaki Aloui et .al. [39] confirmed this finding in S355NL steel. A lower threshold on the da/dN vs. ΔK_{eff} was observed in short cracks than that in long cracks. They also found that the effective growth rate was independent of the load ratios.

Ishihara et al. [63] studied the crack propagation in tool steels, in which cracks were initiated from the carbide defects near the surface at an early stage of the fatigue life; thus, most of the life was spent on crack propagation. A log-linear relationship between $(\Delta K_{eff} - \Delta K_{eff,th})$ and da/dN was proposed to fit the experimental data.

By measuring the crack growth in three types of steels at various crack lengths, Kondo et al. [77] concluded that $(\Delta K_{eff})_{th}$ in short cracks decreases with a shallow crack depth and a high R-ratio. They proposed a parameter $(\Delta K_{eff})_{th,a}$ to account for the change in effective stress intensity factor threshold for different crack lengths. Furthermore, a higher K_{op} was observed in harder materials under a low R-ratio loading in short cracks.

Sample thickness

Stress conditions, which change from plane stress to plane strain with increasing sample thickness, influence the crack closure behaviour.

In a plane-stress condition, the crack opening stress increases linearly with the applied stress range; however, in a plane strain condition, the crack opening stress stays constant over a wide range of applied stress [9, 45]. The crack closure in thin plates is caused by the lateral contraction at the crack tip point due to plasticity, therefore, a linear relationship was found between the crack opening stress and the applied stress range. On the other hand, roughness induced crack closure dominates in thick specimens[9].

Fleck and Smith[45] found that the crack closure stress in thin specimens was about 10% greater than that in the thick samples under both CA and VA loading histories.

To account for the crack closure variation with the sample thickness, Costa and Ferreira [24] proposed a modified model to calculate the crack opening ratio, U. In their model, U is dependent on t/W, $R-ratio$ and ΔK.

Although plane stress and plane strain conditions affect crack closure behaviour, the da/dN vs. ΔK_{eff} curves taken from samples made of the same material with different thicknesses do not vary from one another[9, 45, 24].

Test method

The most commonly used method for measuring the crack opening stress is the compliance approach with the strain reading from a back-face strain gauge. Kobayashi et al. [74] used an ultrasonics approach to measure the crack opening in addition to the back-face strain gauge method. However, the measurements from the ultrasonics yielded higher crack opening stresses in tests ran at R = 0.7 and R = 0.3, and resulted in more conservative da/dN vs. ΔK_{eff} curve in the threshold region. The da/dN vs. ΔK_{eff} data presented in their paper measured by ultrasonics deviate from the rest of the data. Therefore, it is excluded in the general trend in Figure 2.17a.

The compression precracking test method was developed by Pippan et al. [123] to generate auto arrested short cracks in notched samples without producing plastic zones with compressive residual stress at the crack tip that affect the crack closure behaviour in positive R-ratio testing. Newman [114] compared the compression precracking test results with those from the traditional ASTM load-reduction test, and concluded that the compression precracking method produces more conservative results than the load reduction approach. The difference is minimal, thus, both measurements are kept in the da/dN vs. ΔK_{eff} data collection in Figure 2.17a.

Hardness and other factors

Nakai et al. [106, 105], Korda et al. [80] compared the effective crack growth rate in different steels and in the same steels with different heat treatments. All evidence shows

that the da/dN vs. ΔK_{eff} curves are independent of material hardness and load ratio.

Yamabe and Matsui [159] examined the crack closure in steels with retained austenite and found that the crack closure is increased by a retained austenite transformation. The effective crack growth data presented in this paper involving retained austenite transformation do not fit in the collected pool and therefore, they are excluded in Figure 2.17a.

da/dN vs. ΔK_{eff} data collection

Figure 2.17a is a collection of da/dN vs. ΔK_{eff} curves for various steels [151, 130, 105, 106, 98, 80, 79, 74, 75, 69, 64, 45, 42, 24, 9, 39, 109, 77, 63, 57, 114, 68, 50, 122, 125, 142, 144, 164, 160]. The colour of the point indicates the hardness of the test samples. The spectrum for hardness is shown on the right of the plot. The multi-R-ratio da/dN curves presented by Hasegawa et al. [55] (Detailed description in Section 2.14) are plotted in the background and labeled with the corresponding R-ratios. The data points included in Figure 2.17a were tested in an air environment, at different R-ratios and crack lengths; those tested in hydrogen or vacuum environment or at a weld were excluded.

Visually fitted upper and lower bounds are also drawn in Figure 2.17a. The lower bound lies on the $R = 0$ multi-R-ratio da/dN curve. No apparent hardness effect on the crack growth curve can be observed from the collection. At high values of ΔK_{eff}, the data collapse into a narrow band; yet more scatter is shown near the threshold. Some of the scatter is caused by the short crack tests mentioned in the previous section.

The conservative measurements in short cracks might be generated by the high local stress near the stress raiser, the ΔK_{eff} value would be underestimated if it is calculated from nominal stress.

From the same literature [151, 130, 105, 106, 98, 80, 79, 74, 75, 69, 64, 45, 42, 24, 9, 39, 109, 77, 63, 57, 114, 68, 50, 122, 125, 142, 144, 164, 160], da/dN vs. ΔK data for R-ratios ranged from -2 to 0.95 were also collected in the tests, and the data are plotted in Figure 2.17b.

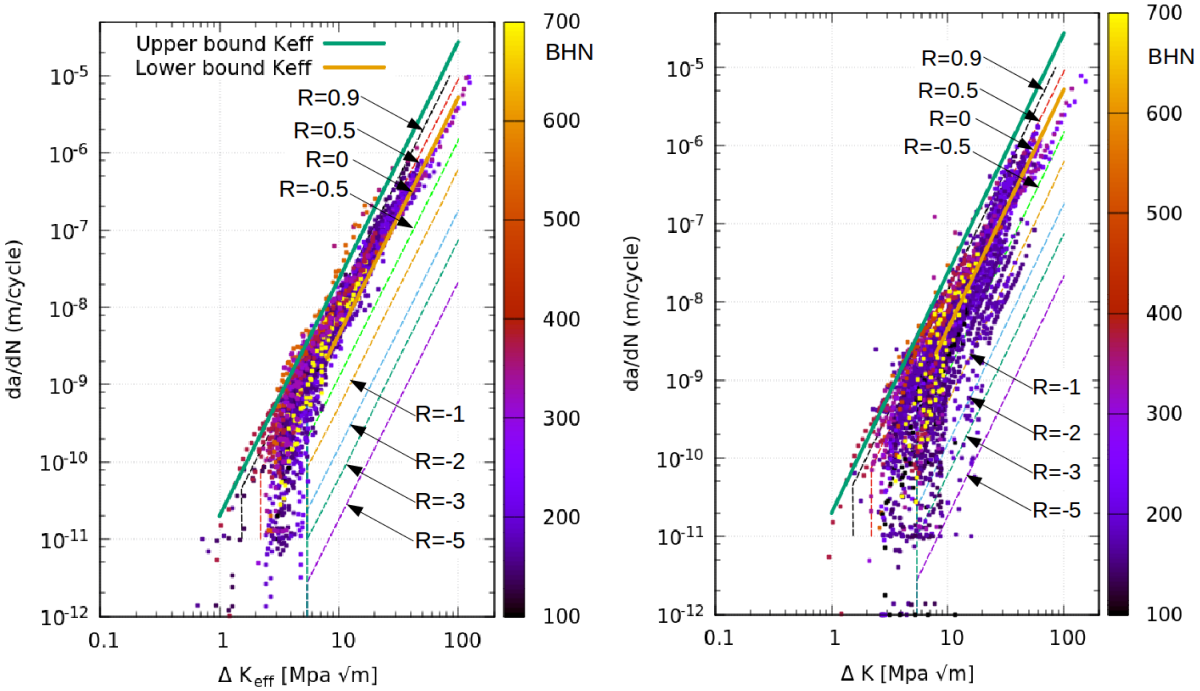

(a) da/dN vs. ΔK_{eff} data (b) da/dN vs. ΔK data for R=-2 to 0.95

Figure 2.17: Collections of crack propagation data (Note that the points in the two figures are from the same tests)

By comparing Figure 2.17a and Figure 2.17b, it can be noticed that the ΔK_{eff} plot collapses data into a single scatter band quite well.

2.11 Stress intensity factor for cracks near a centre circular notch

The stress intensity factor (SIF) is required in a crack propagation estimation. In this study, crack growth data were collected from the core plate samples with a circular centre notched . In order to compare the collected data with the others, the SIF value for the center notched plate is needed.

BS7910 [14] adopted Equation 2.37 for SIF estimation of a through crack in the first mode:

$$\Delta K_I = F_w K_p \Delta\sigma \times \sqrt{\pi a} \tag{2.37}$$

where F_w is defined in Equation 2.29, and the K_p for short and long through cracks initiated from a center notch can be calculated using Equations 2.35 with a K_t of 3.

The K_p value vs. the crack length over notch radius ratio for short and long cracks growing out of a circular notch are plotted in Figure 2.18. The final K_p value switched from short to long crack at around $0.2(l/\rho)$ ratio.

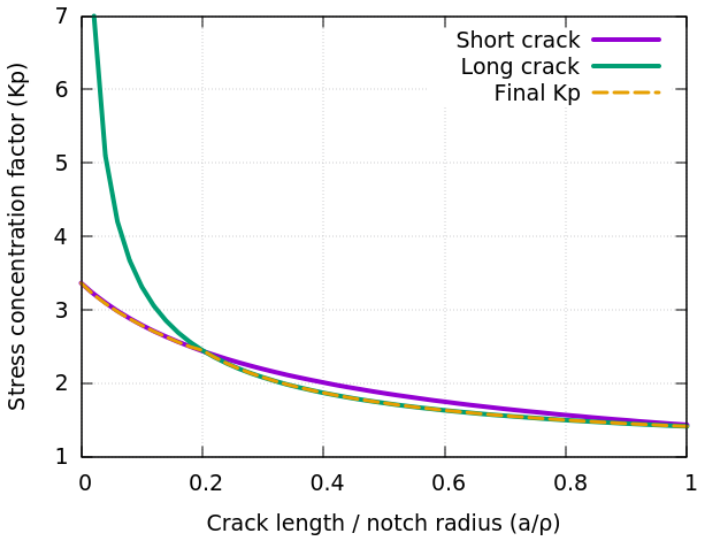

Figure 2.18: K_p values for short and long cracks

2.12 Subsurface crack propagation model

Many researchers observed subsurface failure in carburized steels [161, 163, 28, 165, 10]. Therefore, subsurface crack propagation initiated from elliptical inclusions was studied and three of the available subsurface crack propagation models are reviewed here.

2.12.1 Based on ASME Code

An estimation for the first mode SIF, K_I, of subsurface flaws was recommended in Section XI of the ASME Boiler and Pressure Vessel Code [7]. The analytical evaluations for different types of flaws, including the subsurface elliptical flaw, are listed in the non–mandatory Appendix A.

In ASME, K_I is calculated based on a crack in a flat plate using linear elastic fracture mechanics (LEFM). The subsurface elliptical crack geometry defined in the subsurface elliptical crack section of the ASME code is illustrated in Figure 2.19.

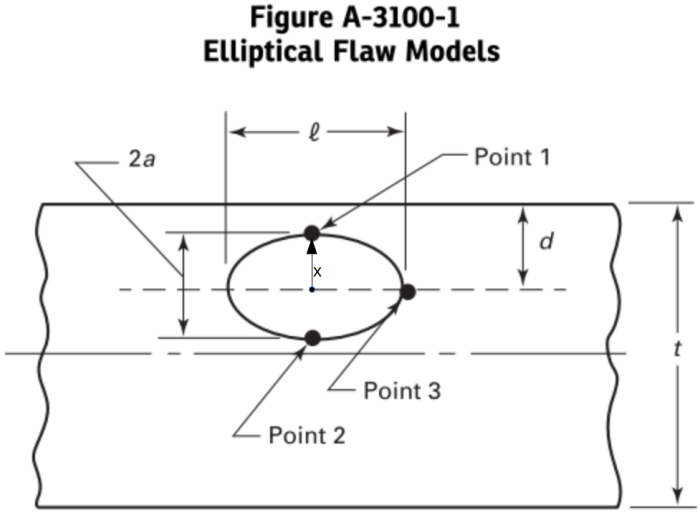

Figure 2.19: ASME elliptical flaw model [7]

In the ASME code, the local stress over the full crack depth and normal to the plane of the flaw is fitted into a polynomial equation:

$$\sigma = A_0 + A_1(\frac{x}{a}) + A_2(\frac{x}{a})^2 + A_3(\frac{x}{a})^3 + A_4(\frac{x}{a})^4 \tag{2.38}$$

where a is the half crack depth of a subsurface flaw; x is the distance from the center point of the ellipse towards the nearest surface, as indicated in Figure 2.19. A_is are the fitting constants. In the composite axial sample, it was assumed that the stress across each layer

is constant; therefore, $\sigma = A_0$, and A_1 to A_4 equal to 0.

In section A-3300 of the ASME code [7], the K_I for subsurface flaws are described using a polynomial equation dependent on the crack local stress expression:

$$K_I = (C_0G_0 + C_1G_1 + C_2G_2 + C_3G_3 + C_4G_4)\sqrt{\pi a/Q} \tag{2.39}$$

where the C_is are functions of A_is, the parameters used to fit the stress profile in Equation 2.38:

$$\begin{aligned}
C_0 &= A_0 - A_1(\tfrac{d}{a}) + A_2(\tfrac{d}{a})^2 - A_3(\tfrac{d}{a})^3 + A_4(\tfrac{d}{a})^4 \\
C_1 &= (\tfrac{t}{a})[A_1 - 2A_2(\tfrac{d}{a}) - 3A_3(\tfrac{d}{a})^2 + 4A_4(\tfrac{d}{a})^3] \\
C_2 &= (\tfrac{t}{a})^2[A_2 - 3A_3(\tfrac{d}{a}) + 6A_4(\tfrac{d}{a})^2] \\
C_3 &= (\tfrac{t}{a})^3[A_3 - 4A_4(\tfrac{d}{a})] \\
C_4 &= A_4(\tfrac{t}{a})^4
\end{aligned} \tag{2.40}$$

where t is the thickness of the plate and d is the distance from the center of the crack to the nearest surface, as shown in Figure 2.19. It is worth noting that if the local stress across the crack is constant, A_1 to A_4 are 0, and thus the only non-zero C_i value would be C_0 which is equal to A_0.

The flaw shape parameter, Q, is defined as:

$$Q = \phi - q_y \tag{2.41}$$

where q_y is the plastic zone correction factor calculated as:

$$q_y = [C_0G_0 + C_1G_1 + C_2G_2 + C_3G_3 + C_4G_4)/\sigma_{ys}]^2/6 \tag{2.42}$$

With l as the length of the major axis of the flaw as shown in Figure 2.19, σ_{ys} as the

material yield strength, factor ϕ can be determined with Equation 2.43:

$$\phi = 1 + 4.593(a/l)^{1.65} \tag{2.43}$$

Equations 2.41 to 2.43 are applicable when the aspect ratio of the crack, a/l, ranges between 0 and 0.5.

The G factors, G_0, G_1, G_2, G_3, G_4, are the K_I coefficients provided in tabular format in Tables A-3610-1 through A-3610-6 of the code. The G_i factors depend on multiple factors, including the crack aspect ratio, the a/d and d/t ratios, as well as the crack tip location of the K_I value. The point numbers for the corresponding locations at the crack tip are labeled in Figure 2.19) G_i factors for K_I locations at Points 1, 2 and 3 are given in the tables.

2.12.2 Based on BS7910 Code

The BS7910 code [14] adopted the K_I calculations for a subsurface crack in 3D finite bodies subjected to tension and bending loads proposed by Newman and Raju [113]. The geometry of the embedded elliptical crack described in BS7910 Section M.4.3 is shown in Figure 2.20 with the parameter labeled.

The general equation for calculating ΔK_I in BS7910 is shown in Equation 2.44 [14].

$$\Delta K_I = Y(\Delta\sigma)\sqrt{\pi a} \tag{2.44}$$

The factor, $Y(\sigma)$, for the primary stress contribution is calculated using Equation 2.45:

$$(Y\Delta\sigma) = M f_w\{k_{tm}M_{km}M_m\Delta\sigma_m + k_{tb}M_{kb}M_b[\Delta\sigma_b + (k_m - 1)\Delta\sigma_m]\} \tag{2.45}$$

The k_{tb}, k_{tm} and k_m factors in Equation2.45 are included to account for the misalignment effects. The M_{km} and M_{kb} are the coefficients for the local stress concentration in weld joints. Since this study of carburization steel does not anticipate any application in misalignments or weld joints, the aforementioned factors are neglected.

Figure M.8 **Embedded flaw**

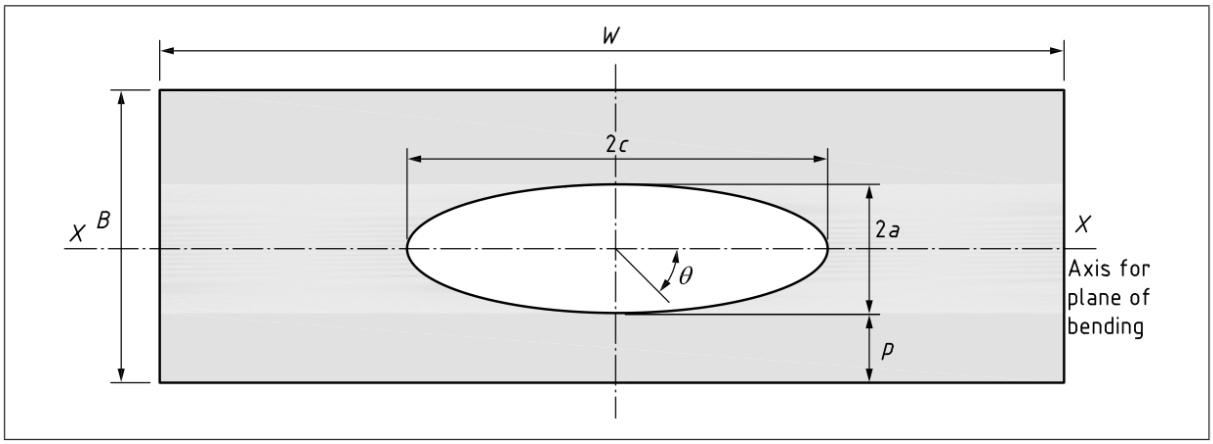

Figure 2.20: BS7910 embedded elliptical flaw demonstration[14]

The width correction factor, f_w, for subsurface elliptical crack in Equation 2.45 is defined in Equation 2.46.

$$f_w = \{sec[(\frac{\pi c}{W})(\frac{2a}{B'})^{0.5}]\}^{0.5} \tag{2.46}$$

The plate width, W, the half crack length along the major axis, c, and the half crack length along the minor axis, a are labelled in Figure 2.20. B', is the effective plate thickness calculated as $2a + 2p$; The width correction factor, f_w, is applicable up to $2c/W = 0.8$.

M, M_m and M_b in Equation 2.45 are the geometry factors. M_m accounts for membrane loading and M_b for bending. Since no bending load is applied in the experiments in this study, the calculations for M_b will not be explained in detail. For subsurface elliptical cracks, M =1 and M_m can be calculated in Equation 2.47.

$$M_m = [M_1 + M_2(\frac{2a}{B'})^2 + M_3(\frac{2a}{B'})^4]\frac{gf_\theta}{\phi} \tag{2.47}$$

where

$$
\begin{aligned}
&M_1 = 1 \quad for \qquad 0 < a/2c \leq 0.5; \\
&M_1 = (c/a)^{0.5} \quad for \quad 0.5 < a/2c \leq 1.0; \\
&M_2 = \tfrac{0.05}{0.11+(a/c)^{1.5}}; \\
&M_3 = \tfrac{0.29}{0.23+(a/c)^{1.5}}; \\
&g \quad = 1 - \{\tfrac{(2a/B')^4[2.6-4(4a/B')]^{0.5}}{1+4(a/c)}\}|cos\theta|; \\
&f_\theta \ = [(a/c)^2 cos^2\theta + sin^2\theta]^{0.25} \quad for \quad 0 < a/2c \leq 0.5; \\
&f_\theta \ = [(c/a)^2 cos^2\theta + sin^2\theta]^{0.25} \quad for \quad 0.5 < a/2c \leq 1.0; \\
&\phi = [1 + 1.464(\tfrac{a}{c})^{1.65}]^{0.5} \quad for \quad 0 \leq a/2c \leq 0.5 \\
&\phi = [1 + 1.464(\tfrac{c}{a})^{1.65}]^{0.5} \quad for \quad 0.5 \leq a/2c \leq 1.0
\end{aligned}
\tag{2.48}
$$

The applicable conditions for the membrane loading calculations in BS7910 [14] are:

$$
\begin{aligned}
&a/B' < 0.625(a/c + 0.6) \quad for \quad 0 < a/2c \leq 0.1 \\
&0 < a/2c \leq 1.0 \\
&2c/W < 0.5 \\
&-\pi \leq \theta \leq \pi
\end{aligned}
\tag{2.49}
$$

2.12.3 Based on Murakami's theories

Murakami et al. [104] conducted extensive quantitative analyses to study the effects of non-metallic inclusions on fatigue performance in high-strength steels. They proposed that the maximum SIF along a crack front of an elliptical internal crack on a plane parallel to the applied uniform tensile stress of an infinite solid is related to the area of the inclusion. It can be approximated using Equation 2.50.

$$K_{I\,max} \cong 0.5\sigma_o(\pi\sqrt{area})^{1/2} \tag{2.50}$$

where σ_o is the remote tensile stress. A maximum of 5% error could be expected by calculating the $K_{I\,max}$ using Equation 2.50 for an elliptical crack. When the elliptical crack aspect ratio, c/a, as indicated in Figure 2.20, is in between 0.2 and 5, Equation 2.50 generates reasonable results without overestimating $K_{I\,max}$.

2.12.4 Other studies

Zhang et al. [165] tested SAE1045 steel in the form of a round bar with a diameter of 35 mm under a bending load. The round bar was induction hardened to get a case depth of 6 mm. An intrinsic crack of 0.1 mm was estimated using Equation 2.51.

$$a_{intrinsic} = \frac{1}{\pi}(\frac{\Delta K_{th}}{\Delta\sigma_f F})^2 \tag{2.51}$$

where ΔK_{th} is the threshold SIF; $\Delta\sigma_f$ is the stress range at the fatigue limit; F is the function for crack geometry. In this study, the subsurface elliptical crack is assumed to be fully open. Superposition was applied to determine the local SIF to include both the loaded stress and the residual stress: $K = K(\sigma_b) + K(\sigma_{rs})$. A K solver software was employed to calculate the values of the geometric parameters that incorporate the location and the shape of the elliptical crack. From experiments, the authors measured the threshold SIF, ΔK_{th}, for core and the case materials, they are 3.5 MPa$\sqrt{m}$ and = 2.4 MPa$\sqrt{m}$, respectively. For the K_I calculation, Mode I growth is assumed to dominate, and each

point on the crack front is independent from the other. Only the positive part of the ΔK_I range, labeled as ΔK_{eff}, is assumed to contribute to crack growth. The failure criterion set in the simulations include: 1) $K_{max} + K_{res} > K_Q$, $K_Q = 59$ MPa$\sqrt{m}$ for core, and 38 MPa$\sqrt{m}$ for case; 2) $\Delta K_{eff} > 40$ MPa$\sqrt{m}$ for core material ; 3) the crack is less than 2 mm from the surface. It was found that 90% of fatigue life was spent on growing the crack from 0.5 mm to 1.0 mm. The ratios of the predicted over the experimental fatigue lives in two tests are 0.64 and 0.83.

Masuda et al. [96] examined the subsurface fatigue crack growth behaviour in D2 tool steel (JIS SKD11). This tool steel has a hardness of 784 HV (61.9 HRC), a Young's Modulus of 230 GPa, a yield stress of 2970 MPa, and the measured fracture toughness, K_{IC}, ranges from 28 to 38 MPa$\sqrt{m}$. The carbide inclusions in the material have a density of 7078 inclusions/mm^2, the maximum area of each inclusion is 200 μm^2. Rotation bending hourglass specimens with a K_t of 1.04 were tested. Compressive residual stress with a magnitude of 317 MPa was found on the surface, which was believed to be caused by the final grinding process. The authors employed a two-step stress amplitude test procedure to measure the subsurface crack growth rate. The stress amplitude at the second stage of the loading doubled that of the initial step. By examining the fracture surface using SEM, the crack length (or area) and the crack shape of the point at which the stress amplitude is changed could be determined. Therefore, the da/dN value for subsurface crack growth can be estimated. These data were plotted with other vacuum crack growth data in Figure 2.26. Equation 2.50 was applied to calculate the SIF for the subsurface crack with a local tensile stress under a bending load. The crack growth data for the subsurface crack and surface crack for this material lay on the same curve. They observed that the crack tends to grow inwards due to the compressive residual stress on the surface. In the total fatigue life calculation, the crack initiation portion was negligible compared to the propagation life.

Marines-Garcia et al. [94] applied the Paris-Hertzberg-McClintock crack growth rate law (Equation 2.52) for subsurface fisheye crack propagation.

$$\frac{da}{dN} = b(\frac{\Delta K_{eff}}{E\sqrt{b}})^3 \tag{2.52}$$

where b is the Burger's vector. The proposed threshold corner of the da/dN curve is at the intersection of $\frac{da}{dN} = b$ and $\frac{\Delta K_{eff}}{E\sqrt{b}} = 1$. The total fatigue life was calculated for three different stages: (1) crack initiation; (2) crack growth from inclusion to fisheye; (3) crack growth from fisheye to final failure. Equation 2.50 was deployed to calculate the ΔK_I value for fisheye. The authors found that in the gigacycle fatigue life region, the load ratio, R, has an insignificant effect on the subsurface crack growth rate.

Nguyen et al. [115] conducted numerical simulations of fisheye fatigue crack growth in the very-high-cycle-fatigue region. They calculated the total life as the sum of the interior crack nucleation and fisheye crack growth. Equation 2.52 was used to calculate the fisheye crack growth. The threshold on the da/dN curve is the same as that used in Marines-Garcia's paper [94]. They found that for eccentric planar circular crack, SIF is not distributed regularly along the crack front. Instead, the maximum value is located at the crack front closest to the specimen surface. Short to long crack transition was not considered in their study. The authors noticed that the difference produced by only using short crack growth and by including the short to long crack transition for the crack propagation stage is negligible.

Li et al. [87] studied the interior fracture mechanism in surface-hardened gear steel under axial loading. The low alloy Cr-Ni steel was machined into axial samples with a minimum diameter of 4.5 mm and then carburized for 8 hours to generate a 0.8 - 1.2 mm case layer. They found that the depth of subsurface inclusion failure does not depend on the fatigue life of the tests.

2.13 Propagation model for corner flaws at a hole

Section M.5.2 of BS7910 [14] listed the parameter calculations for corner flaws at a hole. These values can be substituted into Equations 2.44 and 2.45 to determine the ΔK_I for the corner flaws.

The geometry for the corner flaws at a hole is demonstrated in Figure 2.21.

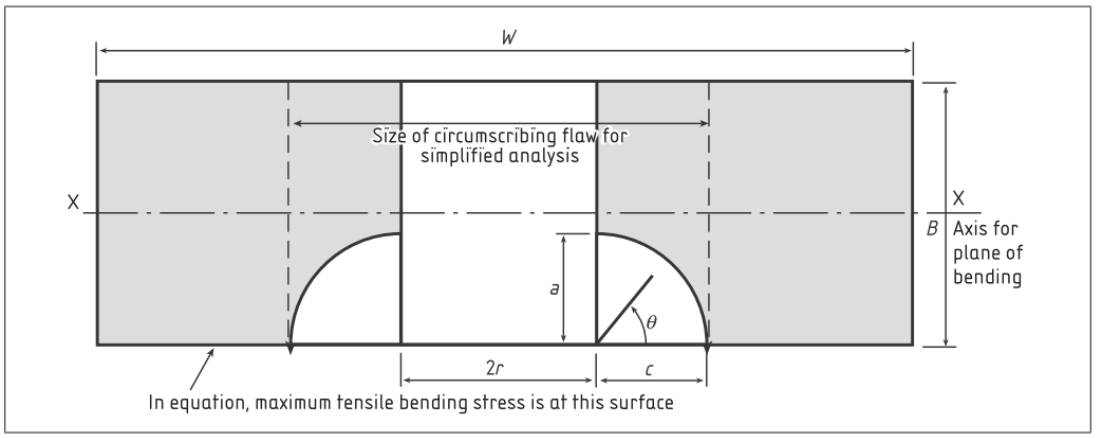

Figure 2.21: Geometry for corner flaws at hole in BS7910 [14]

For corner flaws at a hole, the M factor in Equation 2.45 equals 1, and f_w is calculated as:

$$f_w = \{\sec(\frac{\pi r}{W})\sec[\frac{\pi(2r+nc)}{4(W/2-c)+2nc}\sqrt{(a/B)}]\}^{0.5} \tag{2.53}$$

where $n = 1$ for a single flaw, and $n = 2$ for two symmetric flaws. The geometry parameters are labeled in Figure 2.21.

The membrane loading geometry factor, M_m, for the corner cracks is defined in Equation 2.55 and it is applicable when geometry of the cracks satisfy the following conditions:

$$\begin{aligned} &0.2 \le a/c \le 2 \\ &a/B < 1 \\ &0.5 \le r/B \le 2 \\ &2(r+c)/W \le 0.5 \\ &0 \le \theta \le \pi/2 \end{aligned} \tag{2.54}$$

$$M_m = [M_1 + M_2(\frac{a}{B})^2 + M_3(\frac{a}{B})^4]\frac{g_1 g_2 g_3 g_4 f_\theta}{\phi} \tag{2.55}$$

where

$$\begin{aligned}
&M_1 = 1.13 - 0.09(a/c) \quad for \qquad 0.2 < a/c \leq 1;\\
&M_1 = [1 + 0.04(c/a)]\sqrt{(c/a)} \quad for \quad 1 < a/c \leq 2;\\
&M_2 = -0.54 + 0.89/(0.2 + a/c) \quad for \qquad 0.2 \leq a/c \leq 1;\\
&M_2 = 0.2(c/a)^4 \quad for \quad 1 < a/c \leq 2;\\
&M_3 = 0.5 - 1/(0.65 + a/c) + 14(1 - a/c)^{24} \quad for \qquad 0.2 \leq a/c \leq 1;\\
&M_3 = -0.11(c/a)^4 \quad for \quad 1 < a/c \leq 2;\\
&g_1 = 1 + [0.1 + 0.35(a/B)^2](1 - sin\theta)^2 \quad for \qquad 0.2 \leq a/c \leq 1;\\
&g_1 = 1 + [0.1 + 0.35(c/a)(a/B)^2](1 - sin\theta)^2 \quad for \quad 1 < a/c \leq 2;\\
&g_2 = \frac{1 + 0.358\lambda + 1.425\lambda^2 - 1.578\lambda^3 + 2.156\lambda^4}{1 + 0.13\lambda^2}
\end{aligned} \tag{2.56}$$

where

$$\lambda = \frac{1}{[1 + (\frac{c}{r})\cos(\mu\theta)]} \quad and \quad \mu = 0.85$$

$$g_3 = [1 + 0.04(\tfrac{a}{c})][1 + 0.1(1 - \cos\theta)^2][0.85 + 0.15(\tfrac{a}{B})^{0.25}] \quad for \qquad 0.2 < a/c \leq 1;$$

$$g_3 = [1.13 - 0.09(\tfrac{c}{a})][1 + 0.1(1 - \cos\theta)^2][0.85 + 0.15(\tfrac{a}{B})^{0.25}] \quad for \quad 1 < a/c \leq 2;$$

$$g_4 = 1 - 0.7(1 - \tfrac{a}{B})(\tfrac{a}{c} - 0.2)(1 - \tfrac{a}{c}) \quad for \qquad 0.2 \leq a/c \leq 1;$$

$$g_4 = 1 \quad for \quad 1 < a/c \leq 2;$$

$$f_\theta = [(\tfrac{a}{c})^2\cos^2\theta + \sin^2\theta]^{0.25} \quad for \qquad 0.2 \leq a/c \leq 1;$$

$$f_\theta = [(\tfrac{c}{a})^2\sin^2\theta + \cos^2\theta]^{0.25} \quad for \quad 1 < a/c \leq 2; \tag{2.57}$$

2.14 Crack growth rate

To predict the crack propagation life under VA and CA histories with residual stresses, the crack growth curves for various stress ratios are needed. Since the crack in the carburized axial samples under certain loading conditions initiated in the subsurface layer, vacuum crack growth rate data were also collected for reference.

Bloom [12] compared multiple available models for calculating the effective stress range ratio U (defined in Equation 2.26) for ferritic steels in an air environment, and proposed the following:

$$\begin{aligned} U &= 1.92/(2.88 - R) \quad for \quad 0 \leq R \leq 1 \\ U &= 0.6667/(1 - R) \quad for \quad -5 \leq R < 0 \end{aligned} \tag{2.58}$$

The crack propagation rate in mm/cycle can be calculated by substituting the U factor determined in Equation 2.58 into Equation 2.25, in which, the C and m factors are 1.317×10^{-8} and 3.07 respectively for ΔK in units of MPa$\sqrt{m}$. This crack growth rate estimation was adopted by ASME [7] for R-ratio ranges from -2 to 0.9 with the threshold stress intensity factors, ΔK_{th}, listed below:

$$\begin{aligned} \Delta K_{th} &= 5.5 \text{ MPa}\sqrt{m} && for \quad R < 0 \\ \Delta K_{th} &= 5.5(1 - 0.8R) \text{ MPa}\sqrt{m} && for \quad 0 \leq R < 1.0 \end{aligned} \tag{2.59}$$

Hasegawa et al. [55] extended the applicable range of Equation 2.58 to R-ratio of -5 and compared the proposed curves with some experimental data[83, 56, 13]. The trends from the experimental data show an overall consistency with the analytical curves. The crack growth curves for R-ratio ranges from -5 to 0.9 are plotted in Figure 2.22. This set of da/dN curves is referred to as "Hasegawa1" in this thesis. When these curves were proposed, the amount of data for crack growth near the threshold at negative R-ratios was scarce.

Hasegawa et al. [54] continued their studies on crack growth near the threshold region and determined a trend for ΔK_{th} vs. stress ratio in ferritic steels and aluminum alloys . They summarized and compared the ΔK_{th} values adopted by BS7910, ASME and WRD with some experimental data. An equation that calculates ΔK_{th} based on the R-ratios was proposed:

$$\begin{aligned} \Delta K_{th} &= 5.5(1 - 0.8R) && for \quad R < 0.8 \\ \Delta K_{th} &= 2.0 && for \quad 0.8 \leq R < 1.0 \end{aligned} \tag{2.60}$$

Equation 2.60 was plotted with the data presented by Dowling and Thangjitham [31] and Hasegawa et al. [54] in Figure 2.23.

Most of the ΔK_{th} vs. stress ratio data points collected have a positive R-ratio. The Hasegawa ΔK_{th} line, Equation 2.60, is a reasonably conservative fit to the data shown in Figure 2.23. The multi-R-ratio crack growth curves with the modified ΔK_{th} values, named as "Hasegawa2" in this thesis, are plotted in Figure 2.24.

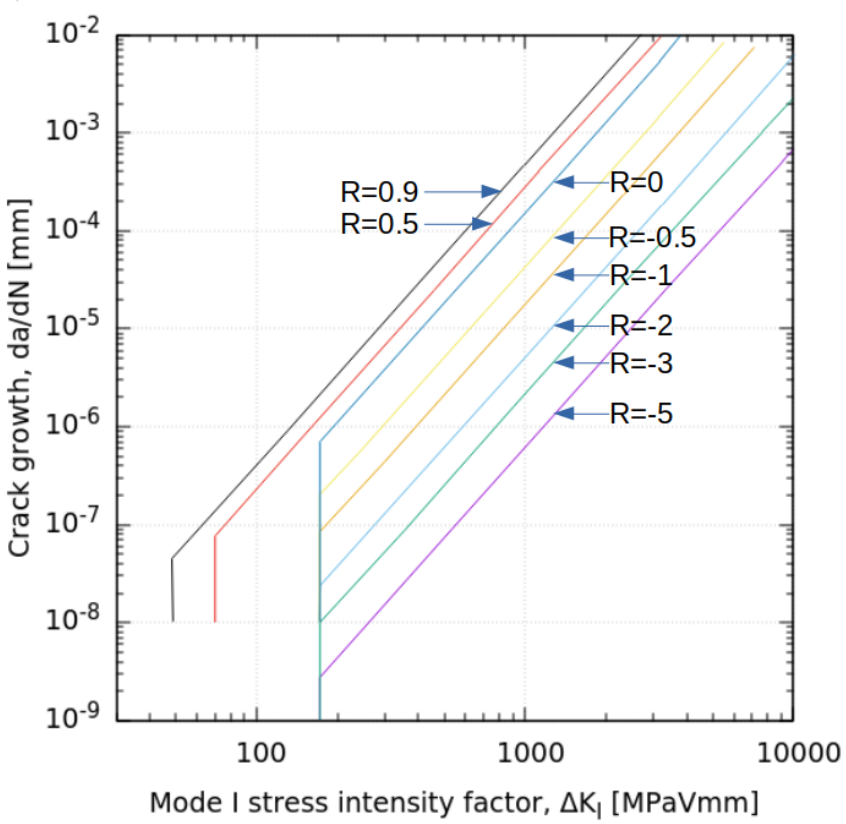

Figure 2.22: multi-R-ratio crack growth curves for R-ratios range from -5 to 0.9 [55] ("Hasegawa1" da/dN curves)

Some crack growth data for steels with hardness ranges from 126 BHN to 700BHN at stress ratios of -0.7 to -1.0 were collected from various credible sources [25, 72, 35, 36, 61, 69, 67, 46, 15, 79, 11]. The collected crack growth data were plotted with the "Hasegawa2" da/dN curves with modified ΔK_{th} in Figure 2.25. Similar plots for crack growth data for various R-ratios can be plotted at a web page developed by Conle and Liang [20]. The colour of the data point indicates the hardness of the tested samples. The hardness colour scale is presented on the right of the plot.

A considerate amount of scatter can be observed in the crack growth data for R of -0.7 to -1. However, the difference in the material hardness does not affect the crack growth

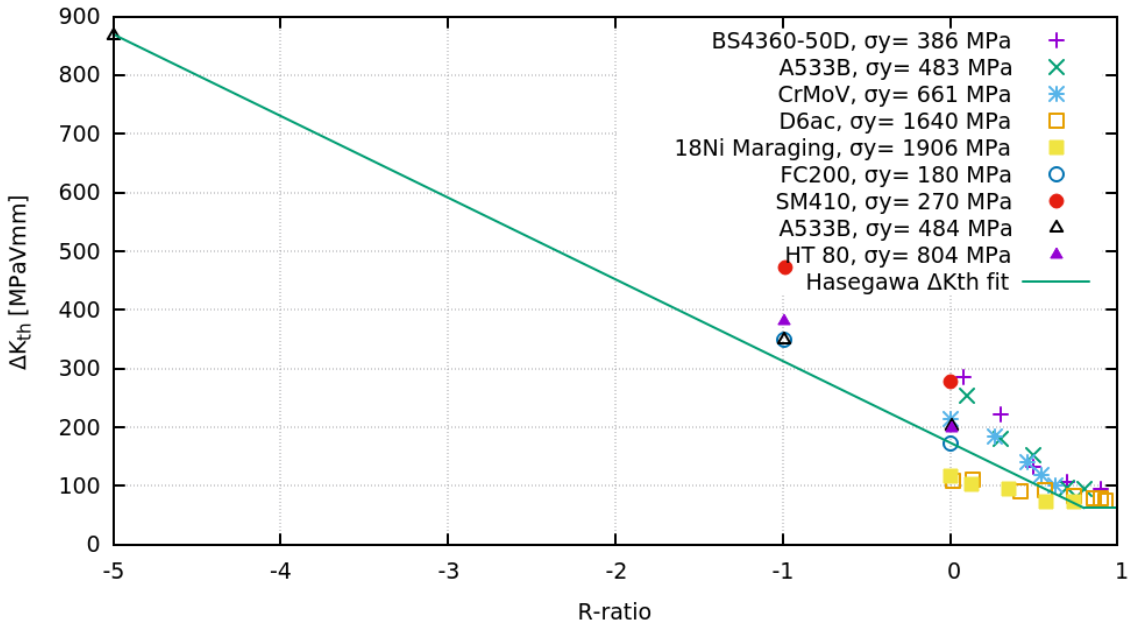

Figure 2.23: Fatigue crack growth threshold, ΔK_{th}, vs R-ratio data [31, 54] with ΔK_{th} estimate described in Equation 2.60

rate. The majority of the collected data lay between the R=-0.5 and R=-1 multi-R-ratio da/dN curves. At the threshold region, the R=-1 da/dN curve is relatively conservative compared to the collected data.

Allen et al. [4] proposed a modified crack growth rate vs SIF relationship to accommodate the region near the threshold:

$$da/dN = B(\Delta K_{eff})^n \tag{2.61}$$

where the effective SIF is defined as $\Delta K_{eff} = \Delta K - \Delta K_{th}$. Therefore, to convert the crack growth rate relationship from ΔK_{eff} to ΔK, the threshold SIF is added. This method generates da/dN curves that are rounded at the threshold region.

Shinko et al. [136] measured the fatigue crack growth rate in hydrogen, air and vacuum environment in an Armco iron with a yield stress of 170 MPa. They found that cracks grow the fastest in hydrogen and the slowest in a vacuum.

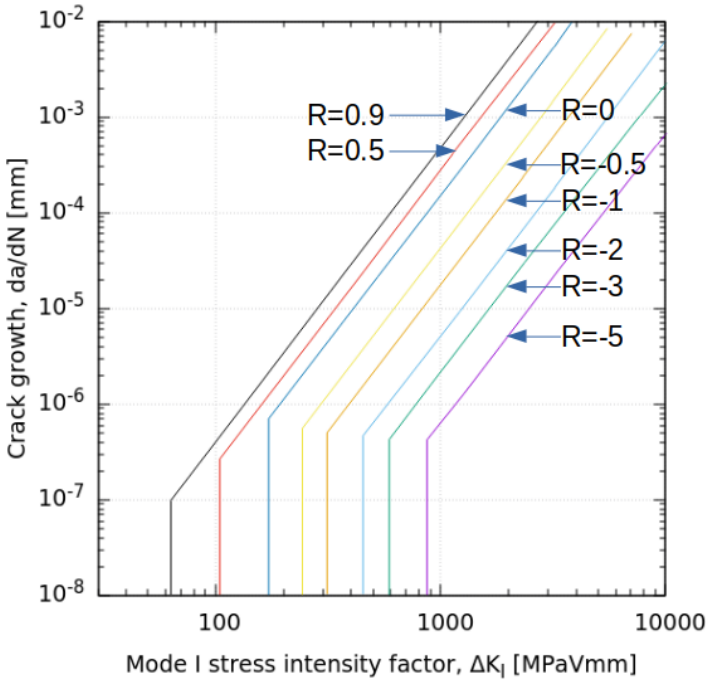

Figure 2.24: Modified ΔK_{th} multi-R-ratio crack growth curves [54, 55] ("Hasegawa2" da/dN curves)

Stewart et al. [141] studied the influence of environment and stress ratio on fatigue crack growth in normalized and tempered NiCrMoV steels. The vacuum and air crack growth rates were obtained at R=0.1.

Grinberg [51] examined the effect of vacuum on fatigue crack growth at different stress ratios. He measured the crack growth rate in air and vacuum environments at stress ratios of 0.2, 0.3, and 0.6-0.7 in high-strength martensitic En24 steels. The data show that ΔK_{th} in vacuum is independent of R-ratios.

Sarazin-Baudoux et al. [131] measured the fatigue crack propagation in gaseous hydrogen, air and vacuum environments at a stress ratio of 0.1. The material examined is 3.5Ni-1.5Cr-0.5MoV steel that was quenched and tempered. Their study shows that in the low SIF region, the crack growth is slower in a vacuum environment than that in air; yet, at high SIF, the two crack growth curves merged.

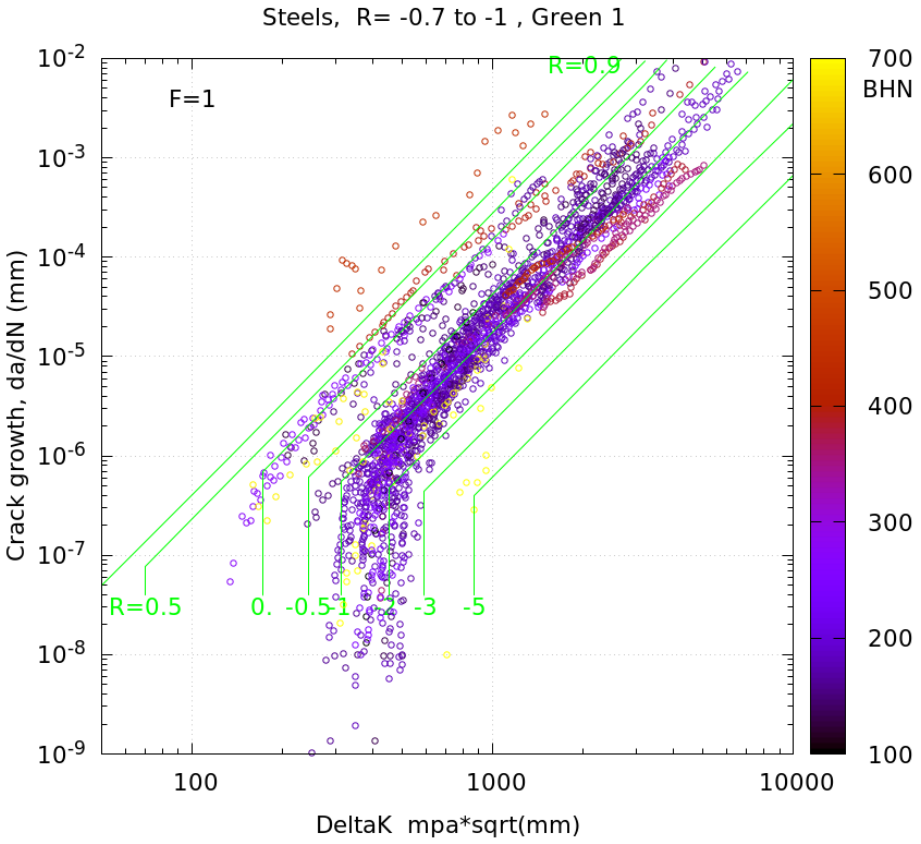

Figure 2.25: Crack growth data for R=-1 to R=-0.7 plotted with the "Hasegawa2" da/dN curves [25, 72, 35, 36, 61, 69, 67, 67, 46, 15, 79, 11]

The air and vacuum crack growth measurements are plotted in Figure 2.26 with the multi-R ratio curves.

Excluding the Masuda [96] data in Figure 2.26, the stress ratios have a limited effect on the rest of the vacuum crack growth data. Most of the vacuum crack growth data lay in between the R=-0.5 and R=-1 curves. Both the surface and subsurface crack growth data measured by Masuda at fully reversed loading show a higher threshold SIF than the rest of the vacuum data at higher stress ratios.

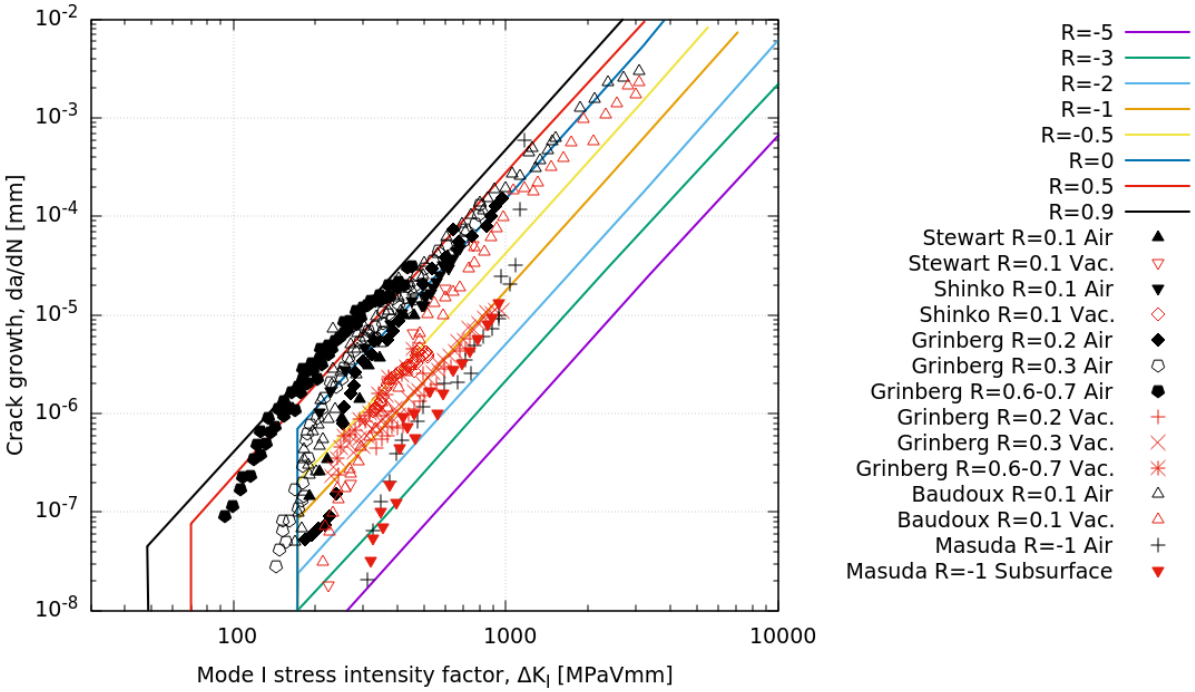

Figure 2.26: Vacuum (red points) and air crack growth data on the "Hasegawa1" crack growth curves [136, 141, 51, 131, 96]

Chapter 3

Effective-strain based and multi-R-ratio crack propagation models comparison

This study reviews the theories and methodologies for running simulations with effective-strain and effective-stress based crack propagation models and compares the simulated fatigue life results for constant amplitude (CA) and service load histories with the experimental data.

A reversal based effective-strain crack propagation model was employed in this study. Instead of counting the crack growth after a cycle is closed under the rainflow counting standard, the fatigue damage is added at each reversal. As the crack propagates away from the stress-concentration zone, the SIF decreases. In service load histories, the tensile half-cycles that occur at the beginning of the load histories are often not matched by their compressive halves to form a complete cycle. Therefore, the large half-loops in the beginning of the history may not be matched with any of the following load cycles as the crack grows. The damage caused by those half-loops would not be counted, since only the damage in the closed hysteresis loops would be considered. The reversal based method eliminates this problem. Moreover, in a service load history, there are usually numerous

small cycles between the two big half-cycles. This can cause a delay in damage count if an instantaneous rainflow counting method is used, and generate inaccurate predictions.

3.1 Crack initiation and multi-R-ratio crack propagation model

Using the multi-R-ratio crack propagation approach, the total fatigue life of the notched plate is the sum of the initiation and propagation lives.

The crack initiation life in the stress concentration zone was calculated with the strain/stress-based initiation model using a constant stress concentration factor, K_t, together with Neuber's rule (Equation 2.34). For the initiation simulation, the Rainflow counting method is employed for VA load histories, and Miner's rule is applied to account for the accumulated damage. To include the effect of overloads under VA history, the strain-life curves derived from POL or small load omission tests [18] are used.

The multi-R-ratio crack propagation model is employed starting at an initial crack length of 2 mm. With a notch radius of 1.191 mm (listed in Table 3.2), the a/ρ ratio is 1.68, and it is outside of the stress concentration zone as shown in Figure 2.16. Therefore no stress raiser effect is considered in the propagation phase. The program uses a material memory model to estimate crack propagation and computes crack advance using the crack growth curves in Figure 2.22 based on the R-ratio calculated as $\frac{K_{min}}{K_{max}}$ in each half-cycle.

The memory model embedded in this program was developed by Conle et al. [22], and the stress intensity factor in each reversal is the controlling factor of the memory event. The general rules for when to use the monotonic or the stabilized cyclic stress-strain curves, as well as the application of the push-down counting list, are identical to those described in reference [22]. The stress intensity factor is calculated in the traditional way:

$$K = FS\sqrt{\pi a} \tag{3.1}$$

It should be noted that in this program, any reversals with a negative maximum stress are assumed to cause no damage.

3.2 Effective-strain based crack growth model

A reversal-based crack propagation program applying the effective strain intensity factor theories was developed in FORTRAN for a through-thickness crack in a centre notched plate.

The material memory model used in the program is also based on the one developed by Conle et al. [22]. Instead of controlling the memory by strain as in the original paper, the memory event in the new program is controlled by Neuber stress, named *neusts* in the program, and $neusts = K_p \times S_{nom}$.

At high R-ratios, it is believed that the damage is not only caused by $\Delta\epsilon_{op}$, but also the tensile mean stress. Thus, the Smith, Watson, Topper (SWT) model [139] was modified to account for the positive mean stress in the effective-strain based model:

$$\Delta\epsilon_{eff}^{SWT} = 2 \times \sqrt{\frac{\sigma_{max}}{E} \times \frac{\Delta\epsilon_{eff}}{2}} \tag{3.2}$$

If $R > -1$ in a half cycle, and $\Delta\epsilon_{eff}^{SWT}$ calculated from Equation 3.2 is greater than $\Delta\epsilon_{eff}$ from Equation 2.30, then $\Delta\epsilon_{eff}$ in Equation 2.27 is substituted by $\Delta\epsilon_{eff}^{SWT}$.

The general procedure for calculating the crack propagation at each reversal in the model for VA histories is as follows:

1. Determine the stress concentration factor K_p, or F from Equation 2.35 or Figure 2.16.

2. Calculate the change in nominal stress, ΔS_{nom}, from the previous reversal to the current reversal, and use Neuber's rule (Equation 2.34) to calculate the local stress and strain (σ and ϵ) in the current reversal.

Note: Initial loading uses the cyclic stress-strain curve, while the doubled (Masing's) curve is used for post initial deformation paths.

3. Estimate the steady-state crack opening stress, S_{opss}, at the current reversal (Equation 2.31); If $\sigma_{max} < 0$, the steady-state crack opening stress is assumed to be 0.

4. Determine the crack opening stress, S_{op}, from Equation 2.33 or from the corresponding condition.

5. Calculate the effective strain range, $\Delta\epsilon_{eff}$, from Equation 2.30 or based on the other conditions described in Section 2.10.2. If a positive mean stress is present, compare $\Delta\epsilon_{eff}$ with $\Delta\epsilon_{eff}^{SWT}$ from Equation 3.2, and use the larger value of the two.

6. Obtain the width correction, F_w, from Equation 2.29.

7. Use a shape factor (SHF) of 0.7 for elliptical crack front if the ratio of the crack length over plate thickness is less than 0.5; else use SHF of 1.0 for centre through crack.

8. Calculate ΔK_{eff} from Equation 2.27.

9. Determine the crack growth for the current reversal from the da/dN vs. ΔK_{eff} curve and add it to the current crack length.
   Note: the crack growth for a half-cycle is half of the value determined from the da/dN curve.

As described in reference [22], a memory event is created if the controlling variable (in this case $neusts$) in the current reversal is smaller in magnitude than that in any of the previously recorded loop tip values in the "TLIM" or "CLIM" arrays. Then, some variables from the current reversal are stored into the "TLIM" and "CLIM" arrays. In addition to the local stress and strain being stored in the original program, variables including the crack length, crack growth, $neusts$, S_{op} and S_{nom} are also stored.

If a loop is closed ($|neusts^i| > |neusts^{i-1}|$ in the "TLIM" or "CLIM" array), then the crack growth at half cycle $(i-1)$ stored in the array is subtracted from the total crack

length, while the new crack growths are added. As demonstrated in Figure 3.1, the half cycle TLIM 3 (from D to E) closed the loop in CLIM2 (from point C to Point D) and continued on the older cyclic curve from point B. *Damage 1*, *Damage 2*, and *Damage 3* are the crack increments done by half cycles BC, CD (or DC), and BE respectively. When the stress-strain path closes loop CDC at memory event C and continues on the old path BC to E, *Damage 1* (BC) is subtracted from the total damage, while *Damage 2* (CD) and *Damage 3* (BCE) are added.

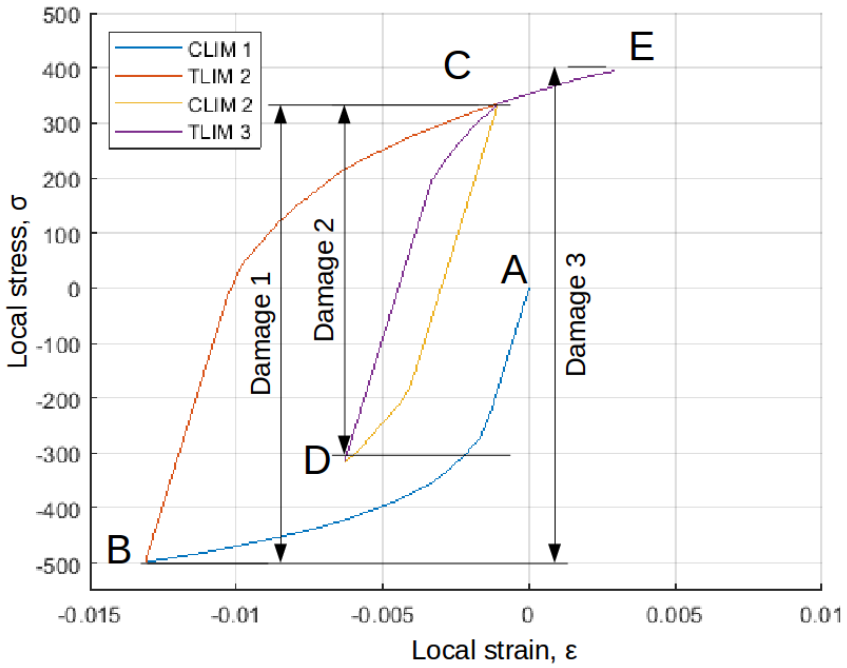

Figure 3.1: Memory event demonstration

3.2.1 Influence of discontinuous Kp

Initially, the K_p value was calculated based on Topper and Haddad's suggestion [150] for short crack when $\frac{a}{a_o} \leq 0.3$, and the general long crack expression (Equation 2.35b) for $\frac{a}{a_o} > 0.3$. This approach generates a jump in K_p at the short to long crack transition point,

therefore, the K_p values plotted in Figure 2.16 were employed in the updated simulation. Figure 3.2a shows a comparison between the original and the updated K_p factors. Even though the two K_p factors yield similar results, the jump at $\frac{a}{a_o} = 0.3$ in the original K_p caused an arbitrary mean stress shift in the local history, as illustrated in Figure 3.2b.

The sudden shift in local stress under the CA history caused by the jump in K_p generated an artificial mean stress in the simulation and therefore leads to an inaccurate life prediction.

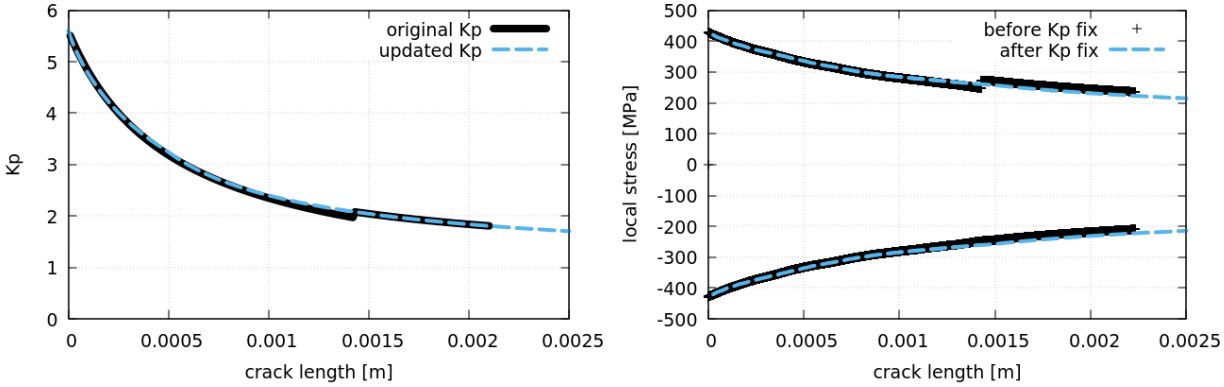

(a) K_p before and after updating (b) Local stress before and after K_p updated

Figure 3.2: Discontinuous K_p and the resulted local stress

3.2.2 Effect of K_p induced local mean stress shift under VA loading

After a da/dN vs. ΔK_{eff} curve was chosen, the simulation results for the CA loads matched those of the experiment closely, as shown in Figure 3.11 in Section 3.3.4. However, the life prediction for VA loads were still too conservative.

For the Bracket load history (Figure 3.10) with a mean stress around zero, the local stress in the initial simulation shifted to a positive mean after a few blocks of the history.

Unsymmetrical changes in the maximum and minimal local stresses (Figure 3.5a) were

found to be caused by the combined effect of the memory event and the change in crack length.

The stress concentration factor, K_p, is calculated based on the crack length. When the maximum or minimum stress reversals in the service load history occur, usually multiple small cycles get closed, and the local stress and strain in the maximum stress reversal is based on the previous minimum stress reversal memory in the history. However, between the maximum and the minimum stress events, the cracks might have grown, which therefore leads to a different K_p between the current reversal and the one used to calculate the previous memory event.

In the case of the Bracket history, shown in Figure 3.3, a minimum stress of -207 MPa occurs in the 1st reversal, while the maximum stress of 152 MPa occurs at the 131st reversal. The Bracket history consists of nearly 6000 reversals. Therefore, the crack growth from the minimum to the maximum stress reversal ($dcrack1$) could be significantly less than that from the maximum to the minimum in the next block ($dcrack2$).

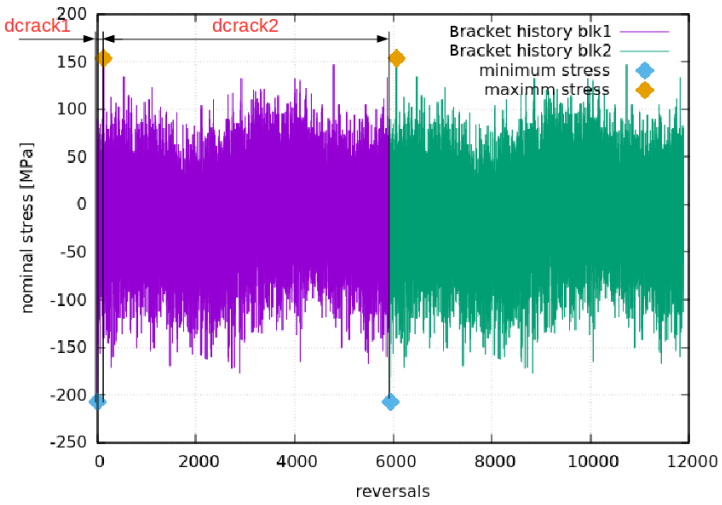

Figure 3.3: Two blocks of Bracket history with the maximum and minimum stress labeled

An exaggerated simulation was run to imitate the mean stress drift observed in Figure 3.6a. Assuming the crack grew 0.1 mm ($dcrack1 = 0.1$mm) from the minimum (-207 MPa) to the maximum (152 MPa) reversal, and 50 mm ($dcrack2 = 50$ mm) from the maximum

to the minimum reversal. Figure 3.4 shows the results caused by the exaggerated difference in crack growth effect. A similar phenomenon to that exhibited in the Bracket local stress history (Figure 3.6a), where the maximum stress stays constant and the minimum stress drifts up, can be observed.

The change in the local stress between two reversals, $\Delta\sigma$, is calculated from Neuber's rule based on the K_p factor and the crack length. Assume K_{p1} was applied for the half cycle loaded from the minimum to the maximum stress in block 1 (Point A to B in Figure 3.4a), while K_{p2} and K_{p3} were applied for reversals from Point B to C and Point C to B, respectively. The difference between K_{p1} and K_{p2} is proportional to $dcrack2$; and that between K_{p2} and K_{p3} is proportional to $dcrack1$. Since $dcrack1 \approx 0$ and $dcrack2$ is much greater than $dcrack1$, $K_{p2} \approx K_{p3}$ and $K_{p1} > K_{p2}$, and therefore, the local maximum stress stays at Point B and the local minimum stress drifts up.

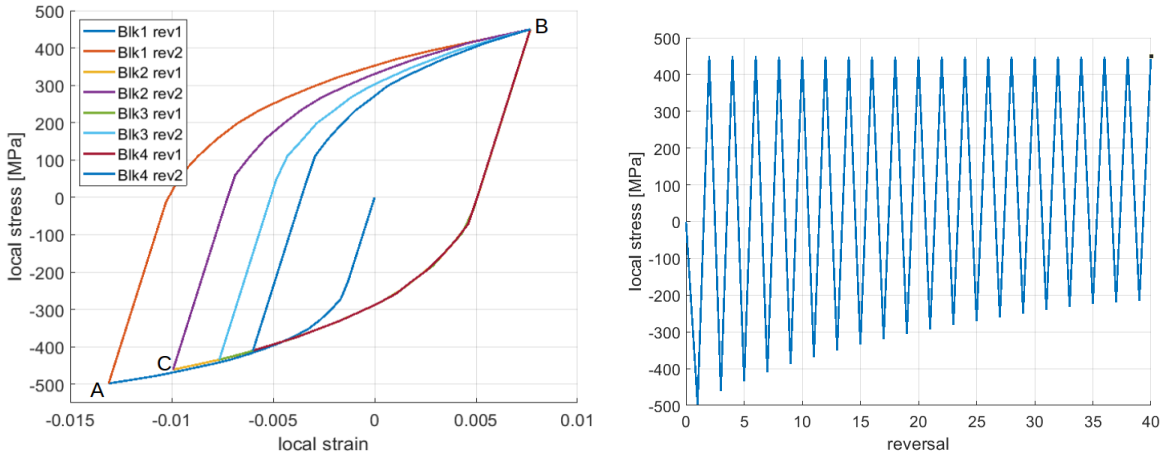

(a) hysteresis loops for the first 4 blocks

(b) local stress vs.reversal

Figure 3.4: Simulation of the mean stress drift caused by crack growth difference between max-to-min and min-to-max reversals

To address this issue, the local stress calculation based on the previous memory event is modified if the crack grew more than 0.01 mm between the two active reversals in a memory event.

For example, to calculate the local stress and strain in Blk2 rev1 (S_{nom}=-207 MPa),

the following procedure is applied (Figure 3.5b):

1. Extract the stress and strain for Blk1 rev 1 (σ_1, ϵ_1 in Figure 3.5b) from the memory array.

2. Calculate the temporary local stress and strain ($\sigma_{temp}, \epsilon_{temp}$) using the average of the initial and the current crack lengths for K_p.

3. Calculate the current local stress and strain using the current crack length.

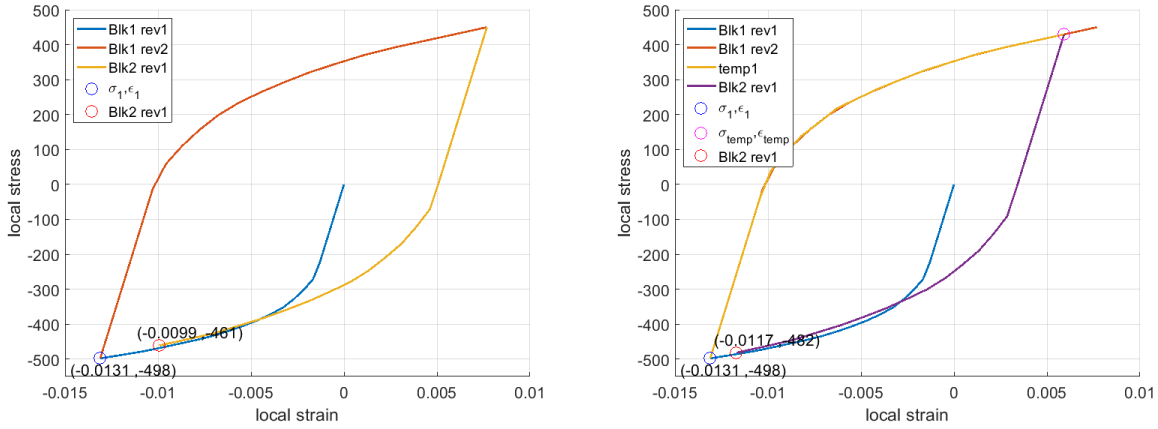

(a) Before fix

(b) Fix procedure and results after the fix

Figure 3.5: Hysteresis loops and the local stress,strain values of Blk2 rev1 before and after fix

From the comparison in Figure 3.5, the increase of stress in Blk2 rev1 from Blk1 rev 1 in Figure 3.5b is less than that in Figure 3.5a. The local stress values in the fixed simulation for the Bracket history shown in Figure 3.6b produces a stabilized local stress without a shift in mean stress.

Figure 3.6a shows the local stress and the crack opening stress in the first 65 blocks for the Bracket history simulation before the fix. In this figure, the maximum stress stays constant while the minimum stress moves up as the crack propagates with an increasing number of blocks.

In contrast, both the maximum and minimum local stresses after the fix (Figure 3.6b) decrease in magnitude symmetrically, and thus, the mean stress shift effect is avoided.

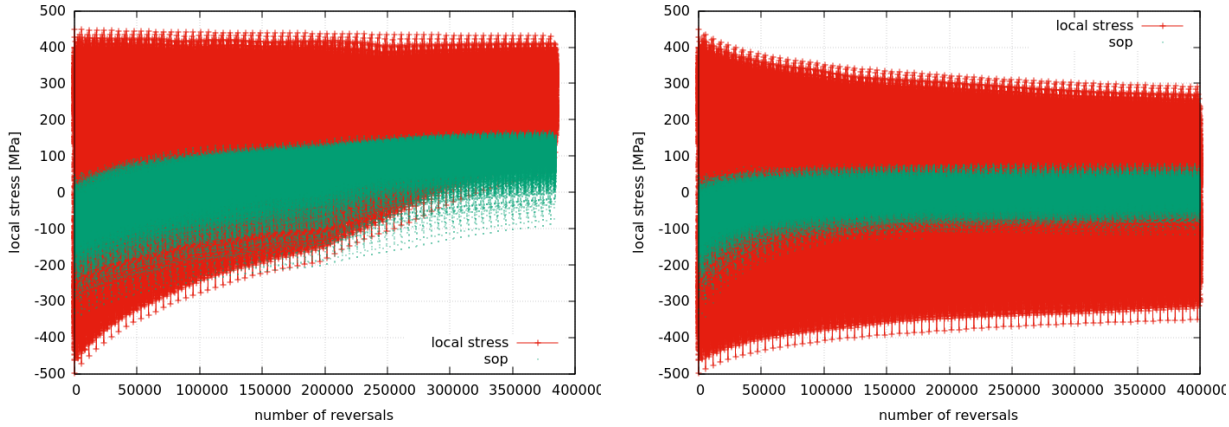

(a) Before updating

(b) After updating

Figure 3.6: Simulated local stress and crack opening stress under Bracket history before and after updating

3.3 Simulations and results

The parameters used in the multi-R-ratio and the effective-strain based models will be presented and the simulation results are compared with the experimental data.

3.3.1 Material properties and experiment details

Conle [18] conducted CA and VA loading tests on centre notched plate specimens cut from G40.21-50A steel. The material properties of G40.21-50A and the geometry of the specimen are listed in Table 3.1 and Table 3.2.

The intrinsic crack length, $a_{int} = 0.135$mm, was used in Equation 2.27. The a_{int} was calculated from Equation 2.28 assuming a ΔK_{th} of 2.5 MPa$\sqrt{m}$ for steels [84], and $F = 0.7$ for an elliptical crack front in the smooth specimen test.

Table 3.1: Material properties of G40.21-50A steel [18]

Property Name	Unit	Value
Elastic Modulus, E	MPa	206800
Cyclic Yield Stress, σ_{cy}	MPa	368
Yield Stress, σ_y	MPa	365
Ultimate Stress, σ_u	MPa	538
Reduced Area	%	66.9
Hardness	BHN	160

Table 3.2: Specimen geometry [18]

Geometry	Unit	Value
Width, W	mm	63.5
Thickness, t	mm	2.54
Notch width, d	mm	9.525
Notch radius, ρ	mm	1.191

The effective strain-life data in reference [18] was obtained from the small load omission tests. Figure 3.7 shows the raw data and the fitted strain-life curves for the CA test at $R = -1$ and the small loads omission tests.

The strain-range data from the two fitted curves were substituted into Equation 2.32 to generate the crack-opening stress points plotted in Figure 3.8. The steady-state crack opening stress parameters in Equation 2.31 were determined by fitting the curve to the data points. The fitted results are shown in Figure 3.8. The equation for the fitted curve is $S_{opss} = 0.7\sigma_{max}[1 - (\frac{\sigma_{max}}{368})^2] + 0.39\sigma_{min}$. The lower limit of the maximum stress one could use to calculate the crack opening stress accurately from the strain-life curve is the stress above the CA run-out level. It should be noted that, the cracks in the the omitted small cycles in the VA histories might not be fully open, and therefore, the effective strain-life curve fitted to the small load mission test data might lay above an ideal fully effective curve. The estimated effective strain-life curve might cause inaccuracy in the steady-state crack opening stress fitting and small errors in the coefficients in the S_{spss} equation.

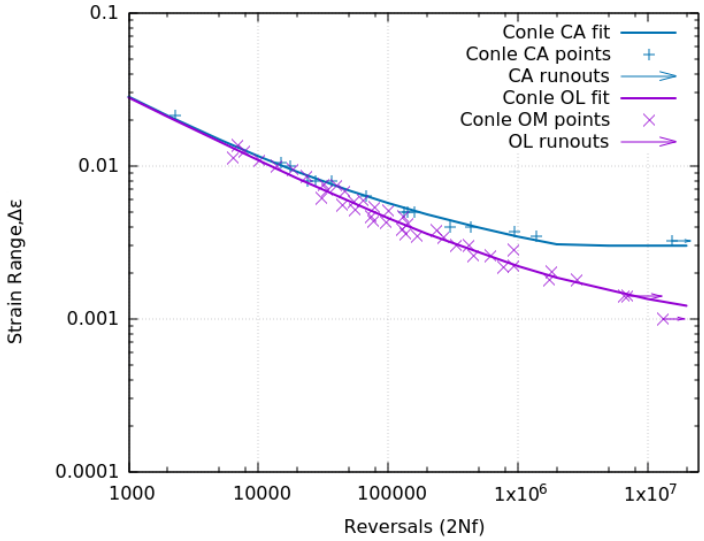

Figure 3.7: Strain-life curves from CA and POL tests[18] (OM: omission test; OL: overload)

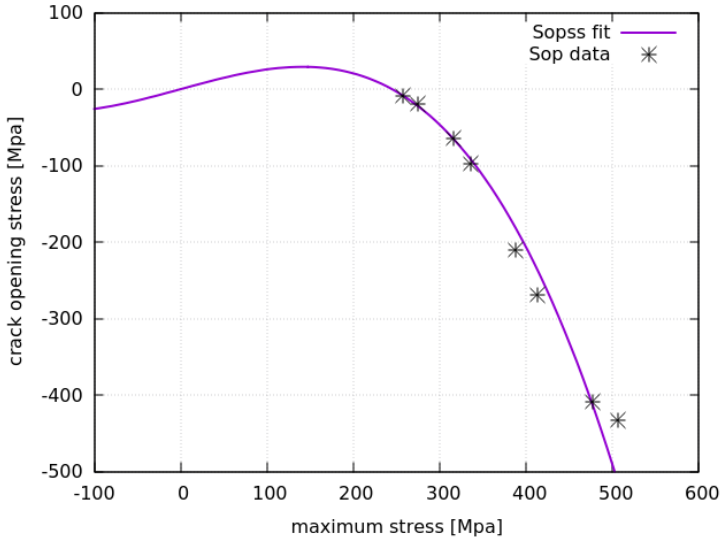

Figure 3.8: Steady-state crack opening stress fitting (Equation 2.31)

3.3.2 da/dN vs. ΔK_{eff} curve used in the simulation

Ghahremani et al. [50] and Newman et al. [114] reported the da/dN vs. ΔK_{eff} data points for G40.21 and A36 steels, respectively. The two materials are structural steels with properties similar to the G40.21-50A steel that Conle [18] tested. A da/dN vs. ΔK_{eff} curve was drawn based on Ghahremani's and Newman's data. Figure 3.9 highlights Newman's A36 and Ghahremani's G40.21 data points and shows the da/dN curve employed in the simulations.

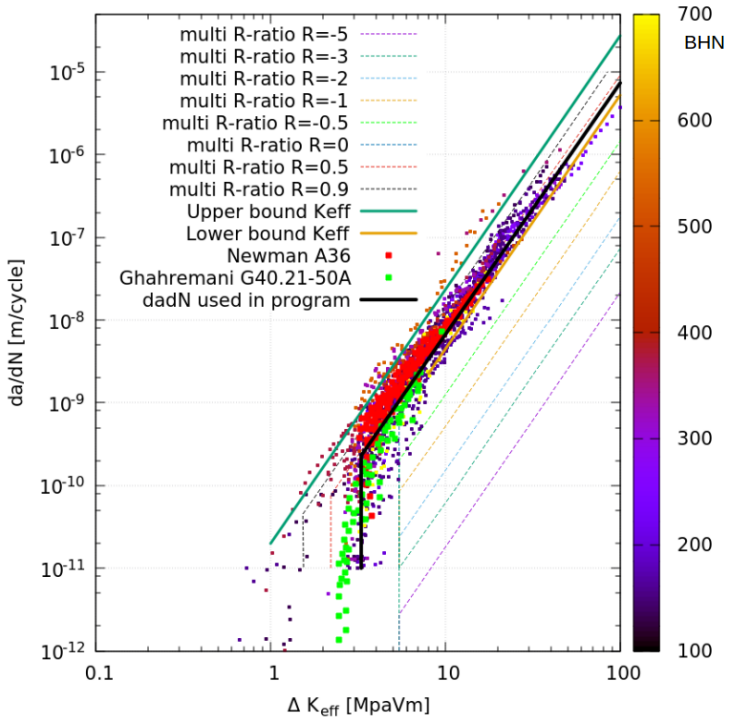

Figure 3.9: da/dN vs. ΔK_{eff} points for A36 [114] (red), G40.21-50A [50] (green), and the curve used for effective-strain based simulation (black line)

3.3.3 Load histories

Crack propagation under three VA load histories (Bracket,Transmission, and Suspension) [152] were simulated and compared with Conle's [18] experimental data at several stress ranges. The load histories are shown in Figure 3.10.

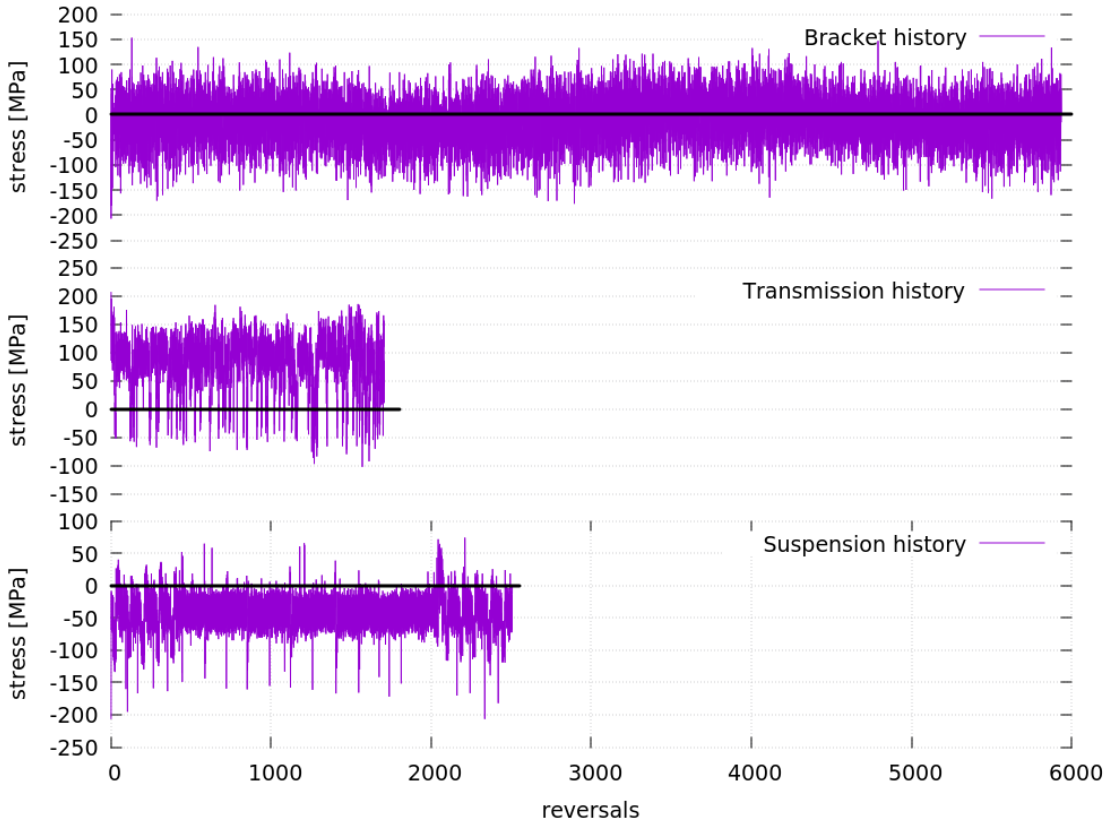

Figure 3.10: Variable amplitude load histories (Bracket, Transmission and Suspension)[152]

The Bracket history has a mean load close to zero, most cycles in the Transmission history consist of positive mean stresses but there are occasional compressive overloads, the Suspension history is composed of mostly negative load cycles. The different features in these three load histories can challenge various aspects of the program.

The absolute maximum stresses in the three VA load histories were scaled to a different

level for each test. The Bracket history was scaled to $|S_{max}|$ of 172 MPa and 207 MPa; transmission history to 155 MPa, 190 MPa, and 207 MPa; suspension history to 207 MPa.

3.3.4 Results

Before running the simulations for the VA load histories, two CA tests were simulated to check the crack growth curves and the basic concepts of the model. As shown in Figure 3.11, the effective-strain based model predicted reasonably accurate crack growth results for the CA tests with stress ranges of 206 MPa and 276 MPa, while the initiation plus multi-R-ratio propagation model predicted relatively unconservative results.

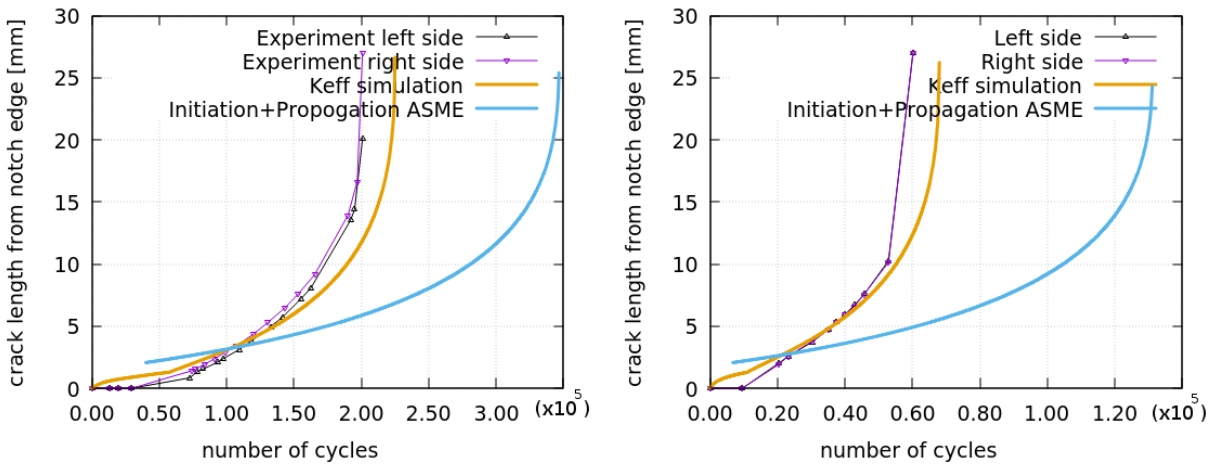

(a) Stress Range of 206 MPa

(b) Stress Range of 276 MPa

Figure 3.11: CA load histories simulations and experimental results (Purple and black lines: experiment results; yellow line: effective-strain based simulation; blue line: multi-R-ratio simulation)

The VA simulations from both the effective-strain based crack growth model and the multi-R-ratio model are plotted with the experimental results in Figure 3.12. It should be noted that the experiment ran under the suspension load history, shown in Figure 3.12f, was stopped before fracture.

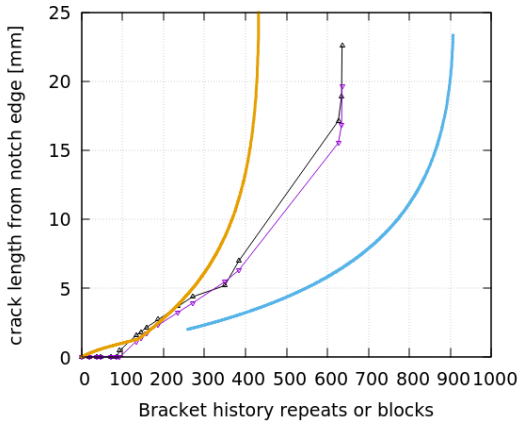

(a) Bracket history
$|S_{max}| = 172$ MPa

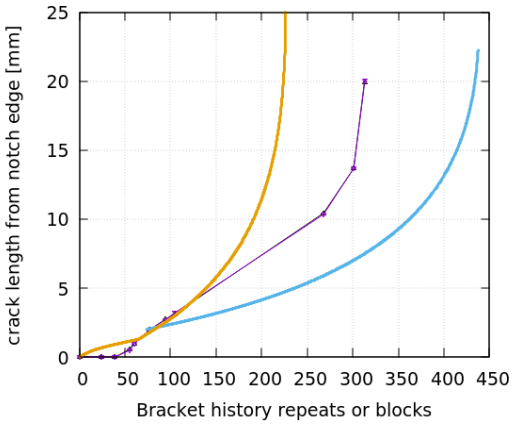

(b) Bracket history
$|S_{max}| = 207$ MPa

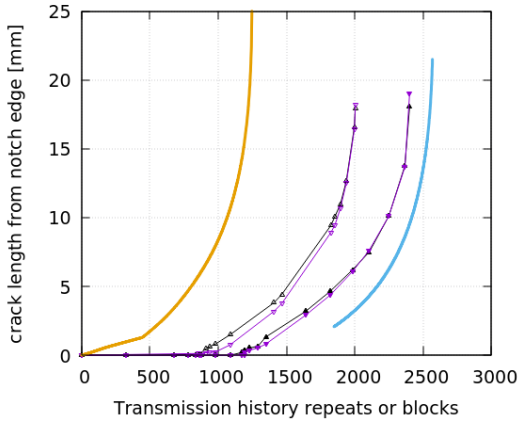

(c) Transmission history
$|S_{max}| = 155$ MPa

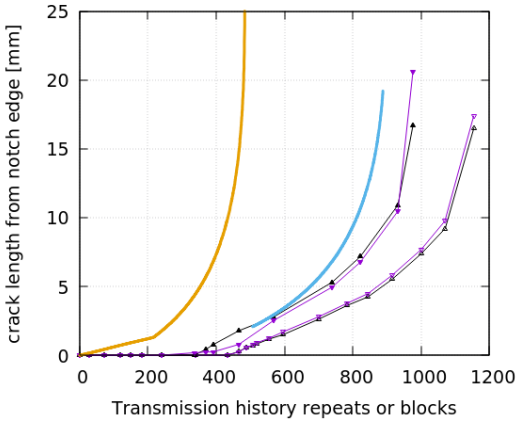

(d) Transmission history
$|S_{max}| = 190$ MPa

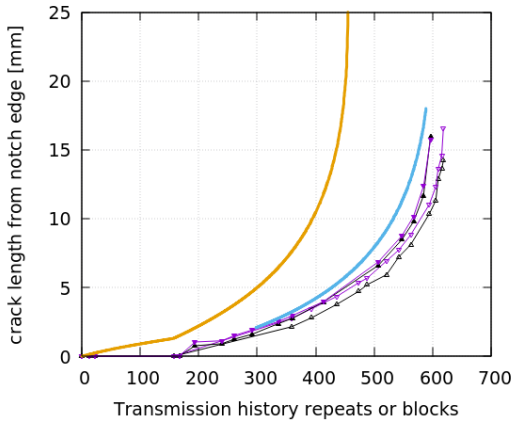

(e) Transmission history
$|S_{max}| = 207$ MPa

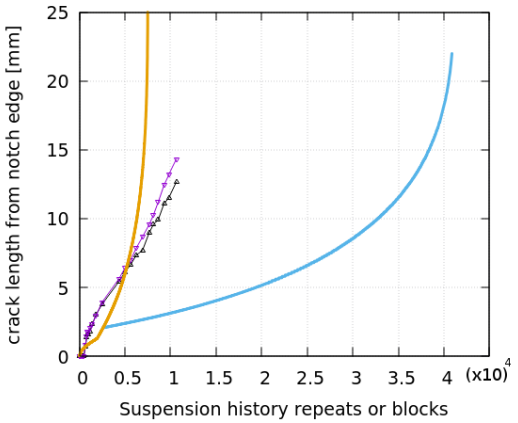

(f) Suspension history
$|S_{max}| = 207$ MPa

Figure 3.12: Simulation vs. experimental results for variable amplitude load histories (Purple and black lines: experiment results; yellow line: effective-strain based simulation; blue line: multi-R-ratio simulation)

The fatigue life results from the experiment and the two simulations, including the initiation predictions, are plotted against the stress levels for the CA, Bracket and Transmission load histories in Figure 3.13.

Both the initiation plus multi-R-ratio model and the effective strain-based model predicted the final life under VA loading within a factor of two of the experimental results, except for the Suspension history.

3.3.5 Discussion

Reasonable accuracies of the crack propagation vs. cycle results and the final life predictions were produced by both the effective-strain based and the multi-R-ratio approaches, which indicates that the crack opening stress and the assumed effective crack growth curve used in the effective-strain based approach are sensible for this given material, and the multi-R-ratio crack growth curves for different R-ratios are also applicable to this tested material.

The initiation plus multi-R-ratio propagation model predictions are generally less conservative partly due to the crack propagation starting at the initiation predicted life. The shape of the crack length vs. cycles simulation curve itself is a good match to the experiments except for the Suspension history. The long predicted life by the multi-R-ratio simulation in the suspension history might be caused by the unconservative assumption that the half-cycles with negative maximum stress generate no damage.

On the other hand, in the effective-strain based model, even though $S_{opss} = 0$ when $\sigma_{max} < 0$, the crack can still grow in the half-cycle if S_{op} is below σ_{max}. Figure 3.14 shows the local stress and the crack opening stress in the effective strain-based simulation at the 1st, 500th, and 5000th blocks of suspension history.

The local stress decreases with the K_p factor as the crack grows away from the notch in the later blocks. Due to the high K_p factor at the beginning of the test, plastic behaviour occurred in a significant part of the history and diminished the effect of the negative mean stress in the nominal stress history. As the crack grows out of the stress concentration

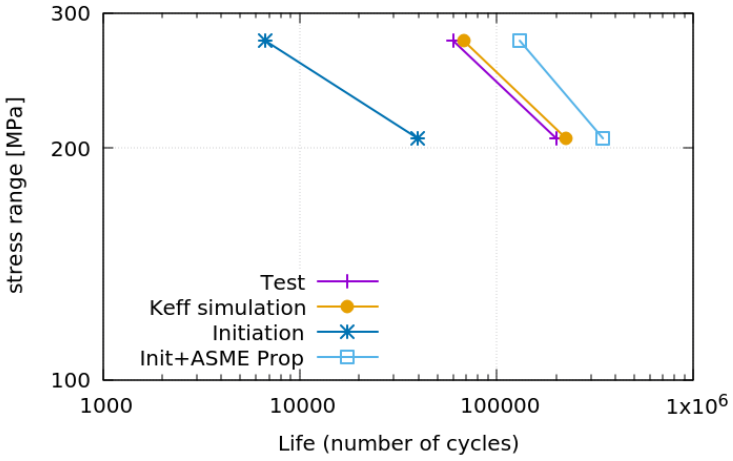

(a) CA load histories

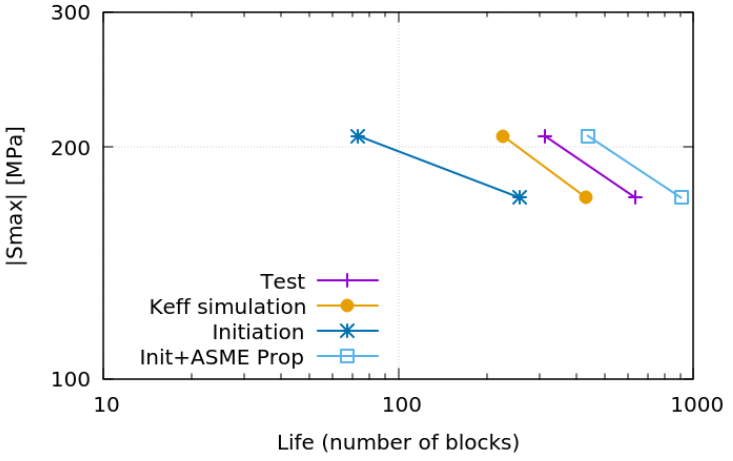

(b) Bracket load histories

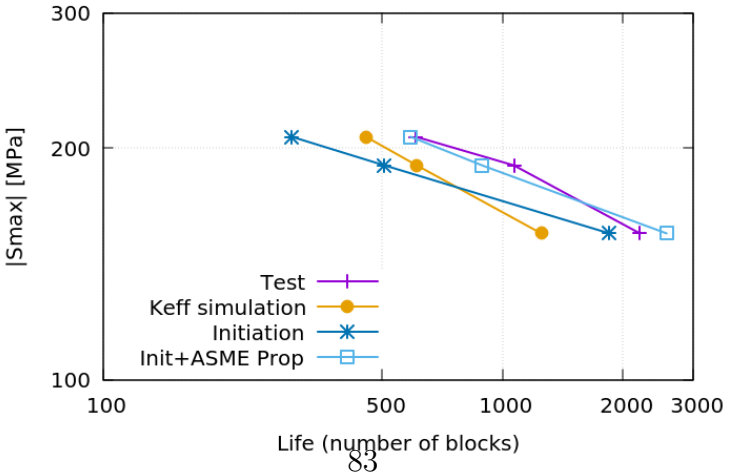

(c) Transmission load histories

Figure 3.13: Comparison of final lives for CA, Bracket and Transmission load histories

zone, the negative mean in the local stress becomes more obvious, and a larger part of the cycles become ineffective. However, even in block 5000, the crack opening stress, shown in green, does not stay constant at 0 MPa. It drops down after a compressive overload, and recovers slowly. Therefore, some of the half-cycles with maximum stress above the crack opening stress can still cause damage.

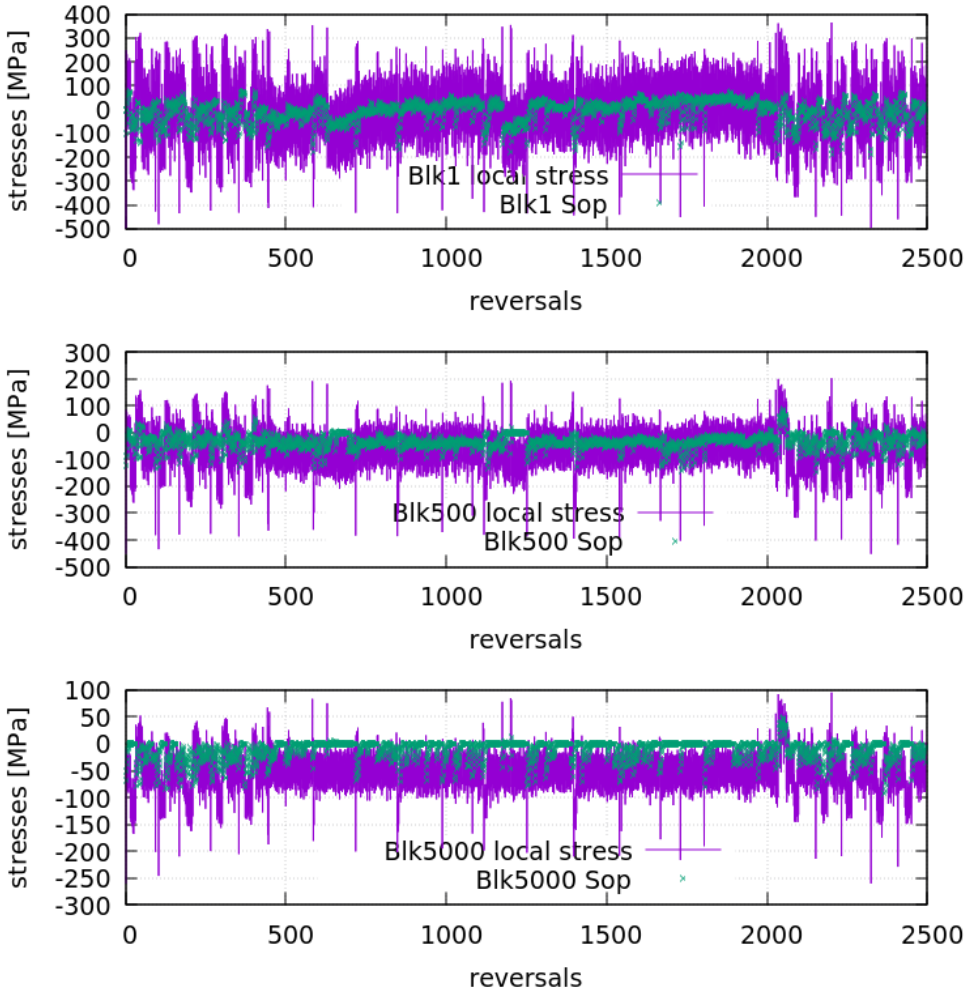

Figure 3.14: The local stress (purple line) and crack opening stress (green points) in the effective-strain based simulation under Suspension history at the 1st, 500th, and 50000th block

The multi-R-ratio crack growth curves designated for different R-ratios do not account for the change in crack opening stress under VA load histories. Judging by the suspension simulation results, depending on the crack opening stress at the half-cycle, large compressive cycles can still propagate cracks. Further details on the crack growth behaviour under fully compressive loads with periodic overloads should be studied and implemented into the multi-R-ratio model.

Chapter 4

Material properties and experimental testing

This chapter describes the experimental methodology and presents the test results obtained from the study.

CA and POL tests were conducted on the through-carburized case and the simulated core axial specimens made out of 16MnCr5 steel to obtain the material properties inputs for the analysis. In addition, crack growth rate data were collected from the core notched plate specimen. The case notched plate was tested under CA and VA. However, no crack length data was collected in the case plate due to the fast crack growth in the case material.

The composite axial and notched samples were loaded under CA and bracket VA load histories to acquire data for model validation. The fracture surfaces of the samples were examined using a scanning electron microscope (SEM) and a light microscope.

The material properties for the transition layer of the composite sample were derived based on the experimental data of the through-carburized case and the simulated core samples.

4.1 Material properties and heat treatment

The specimens used in this study were machined out of 16MnCr5 steel. The chemistry of the raw steel bar was measured by Fiat Chrysler Automobiles (FCA) as given in Table 4.1.

Table 4.1: Chemical Weight Percent for 16MnCr5 Steel

C	Mn	P	S	Si	Cr	Ni	Mo	Cu	Al
0.14	1.23	0.011	0.035	0.21	1.04	0.21	0.06	0.19	0.021
V	Cb	Ti	Zr	Co	Sn	B	Pb	Ca	W
0.028	0.01	ND	ND	0.01	0.01	0.0019	ND	0.003	0.01

"ND" = Not Determined

The specimens, machined and polished from the 16MnCr5 raw steel bar, were divided into 3 batches for different heat treatments: case-hardened composite, through-carburized case, and simulated core. The temperature and duration of the heat treatments are specified in Table 4.2.

Table 4.2: Heat Treatments

Sample	Temp. 1	Time 1	Temp. 2	Time 2	Carbon potential
Composite	927 ^{o}C	90 min	843 ^{o}C	10 min	0.85
Case	927 ^{o}C	1800 min (30 hr)	843 ^{o}C	10 min	0.85
Core	927 ^{o}C	90 min	843 ^{o}C	10 min	Neutral

The through-carburized case and the simulated core samples were treated to mimic the metallurgy of the case and the core layers in the case-hardened sample. Carburization for all specimens was carried out by FCA and conducted in a furnace containing air. After carburization, all samples were quenched in agitated oil at 66 ^oC and then tempered at 177 ^{o}C for 90 minutes. The case-hardened heat treatment aimed to produce a case layer that is 10% of the diameter of the composite sample. Deep-freeze treatments were performed in dry ice for an hour at approximately -78.5^oC on some of the through-carburized case samples to induce a complete RA to martensite transformation.

Tensile tests were conducted on the case, core and composite samples to obtain the material properties. The true stress-strain curves of the tensile tests are plotted in Figure 4.1. For the core material, the curve beyond the ultimate stress point obtained in the test was eliminated. The only point available past the ultimate stress is the point at the true fracture stress and strain.

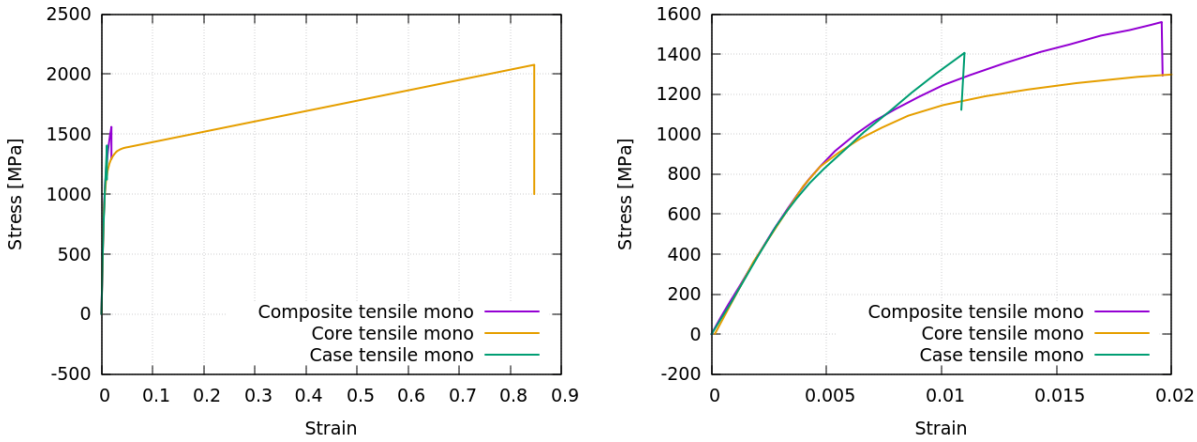

(a) Full strain range

(b) Strain range up to 0.02

Figure 4.1: Tensile stress-strain curves for the case, core and composite materials

The core material has the largest fracture strain among all indicating a high ductility. The case material has the lowest fracture strain which means that it is brittle.

The properties for the three materials are listed in Table 4.3 with the standard deviation percentages for the values. The elastic modulus was measured at the beginning of every fatigue test and during the tensile tests. The average of all the elastic modulus values collected for each specific material is listed in the table. The cyclic yield strength was determined by best fitting the cyclic stress-strain curve of the material using the least-square method. It should be noted that the cyclic yield strength of the case material was extrapolated. The rest of the values were determined from the tensile tests and they are taken as the average of the value of the two tests conducted on each material.

Figure 4.2 shows the hardness profile of the through-carburized case, the simulated core and the case-hardened composite axial samples. These hardness measurements were

Table 4.3: Material properties of the through-carburized case, simulated core and case-hardened 16MnCr5 samples

Material Property	Unit	Case	Core	Composite
Average tensile elastic modulus, E	MPa	204918 ±3.90%	208686 ±2.11%	204992 ±3.55%
0.2% offset Yield Strength, S_y	MPa	1076 ±5.65%	1024 ±3.25%	1153 ±4.23%
Ultimate Tensile Strength, S_u	MPa	1422 ±1.64%	1402 ±0.45%	1575 ±1.12%
Strain at Su, eu		0.011 ±3.75%	0.051 ±4.11%	0.020 ±3.52%
% Elongation over 8 mm gauge length		1.3% ±3.78%	23.2% ±1.96%	1.9% ±3.29%
True Fracture Stress	MPa	1412 ±1.21%	1957 ±8.68%	1631 ±4.82%
% Reduction in Area		0.4% ±67.17%	54.7% ±6.34%	2.30% ±25.26%
Cyclic Yield Strength (0.2% offset)	MPa	3018	892	1240

provided by FCA. The average hardness for the through-carburized case and the simulated core samples is 61.1 HRC and 37.3 HRC, respectively. Based on the hardness profile, the composite sample is classified into three zones: the case, the transition and the core as shown in the figure.

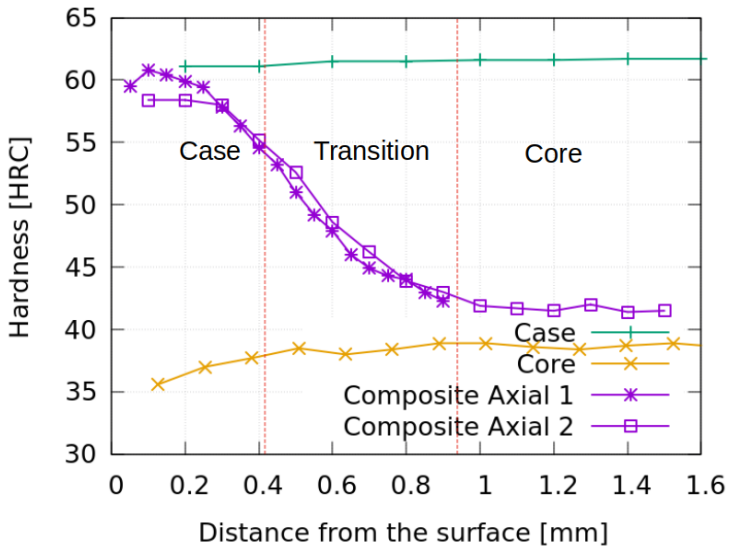

Figure 4.2: Hardness of the case, core and composite axial samples

The hardness of the through-carburized case and the simulated core samples reasonably represent the composite samples' case and core layers, respectively. The transition layer

has a hardness in between that of the case and the core layers.

Carburization in an endothermic gas atmosphere leads to an inter-granular oxidization (IGO) zone on the surface of heat-treated samples. To observe the IGO zone in the specimens, the samples were mounted in Bakelite, ground and polished following the ASTM E3 guide for preparing a metallographic specimen. Before taking the micrographic photos, the polished surface was etched with a 3% Nital solution. Figure 4.3 are the microstructure photos of the surface area of the case, core and composite samples taken by FCA. The depth of the IGO zone can be measured from these figures.

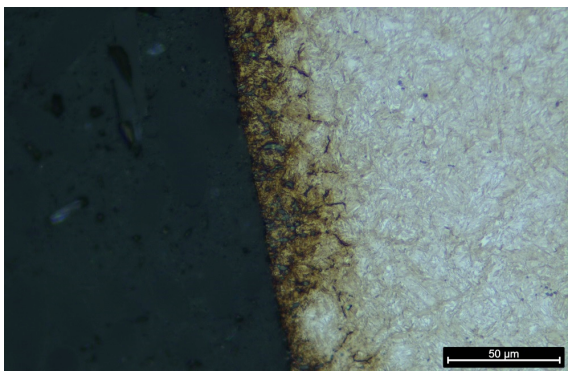

(a) Case surface taken at 500x

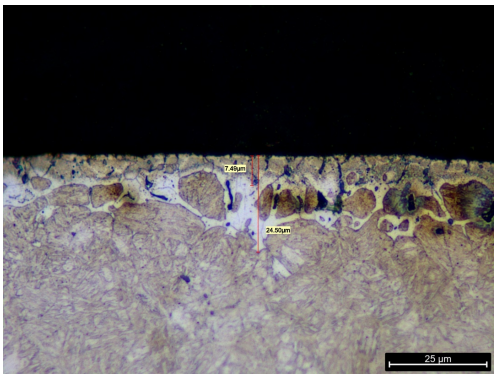

(b) Core surface taken at 1000x

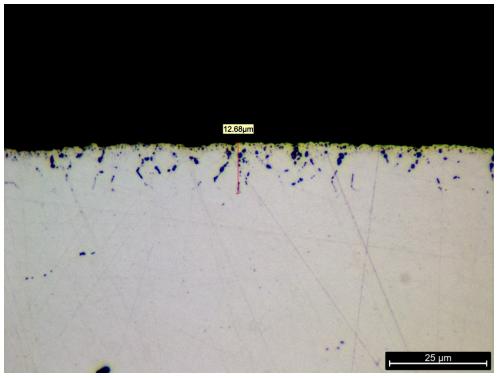

(c) Composite IGO taken at 1000x

Figure 4.3: Microscopic pictures of the heat-treated sample surfaces

The average depths of the IGO layer for the case and the composite samples are 35.7 μm and 12.7 μm, respectively.

The simulated core specimens were heat-treated in air. The surface of the sample exhibited ferrite with carburization and decarburization. The depth of the decarburization and the re-carburization layers are 24.5 μm and 7.5 μm, respectively.

4.2 Specimen design

The geometries of the smooth axial samples and the notched plate specimens are drawn in Figures 4.4 and 4.5.

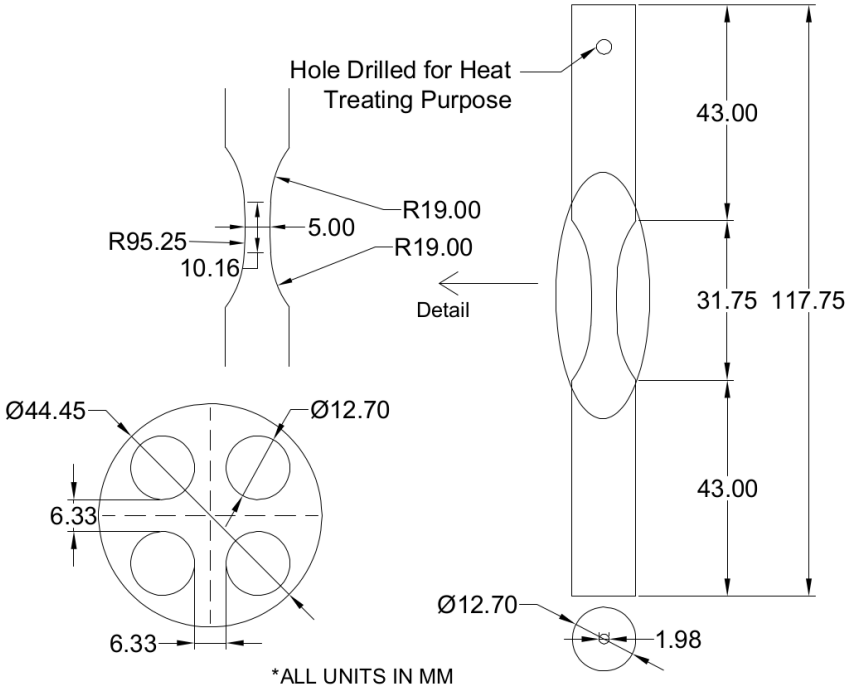

Figure 4.4: Specimen geometry of the smooth axial samples

All samples in this study were machined from a steel bar with a diameter of 44.45 mm. Only the centre of each quarter of the steel bar, as illustrated in Figure 4.4, was used for making the specimens. This was done to avoid the impurity in the core and the surface of the raw steel bar in the machined specimens. The 1.98 mm indentation at the ends of

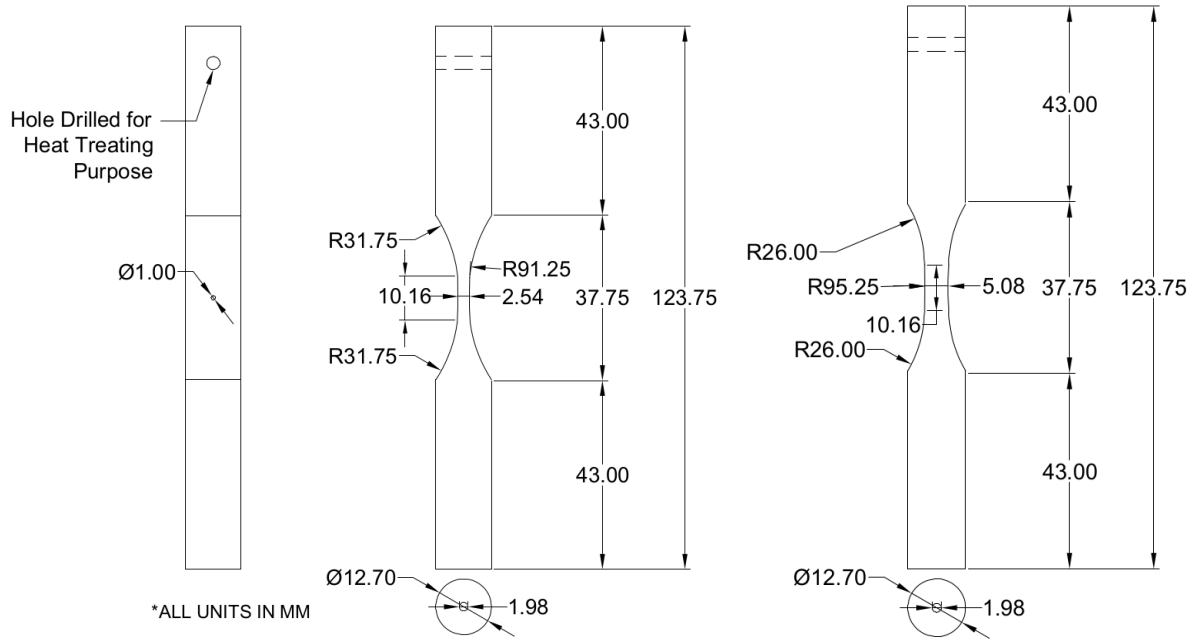

(a) Thin plate of case and core

(b) Thick plate for Composite

Figure 4.5: Specimen geometries of the notched plate specimens

the sample were dilled for polishing purpose so that the sample could be spun around the central axis on a lathe.

The composite notched plate (Figure 4.5b) is twice as thick as the case and the core plate (Figure 4.5a) to ensure a case thickness consistent with the axial sample while still having a reasonable case over core ratio in the plate sample.

After machining and prior to carburization, the specimens were polished with 240 and 400 grit Emery paper followed by a final polish in the loading direction using 600 grit paste. The carburized samples were polished again with 600 grit paper to remove the surface graphite before testing at room temperature.

4.3 Constant amplitude (CA) tests

The through-carburized case, simulated core, and case-hardened composites axial samples were loaded under a fully reversed CA history. In the short-life region, the tests were run under strain control at loading frequencies ranging from 0.5 Hz to 10 Hz. The tests were switched from strain to load control in the long-life region after the cyclic behaviour stabilized at around 100,000 cycles. The test frequencies under load control are between 2 Hz and 50 Hz. Uniaxial strain controlled tests were performed using an MTS extensometer with a gauge length of 8 mm.

Figures 4.6 and 4.7 show the strain-life and stress-life data points and the fitted curves for the case, core and composite materials. The composite samples that failed from subsurface, distinguished by the presence of fisheye on the fractures surface, are labeled in the figures. The CA fatigue test data are given in Appendix A, as well as the experimental results obtained from the rest of the tests described in this chapter.

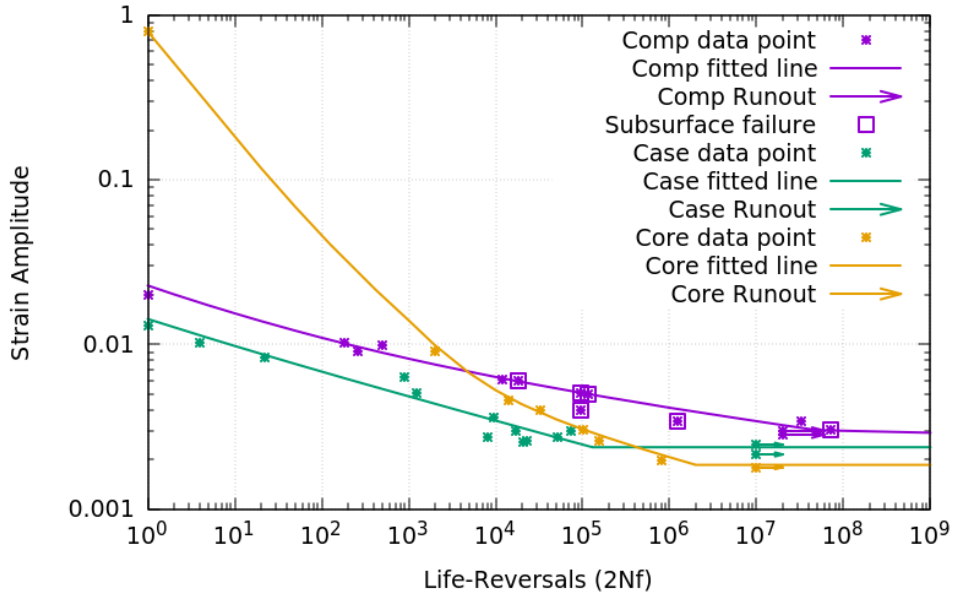

Figure 4.6: Strain-life data for the case, core and composite axial samples with fitted curves

As expected the harder carburized case material in Figure 4.6 falls below the softer

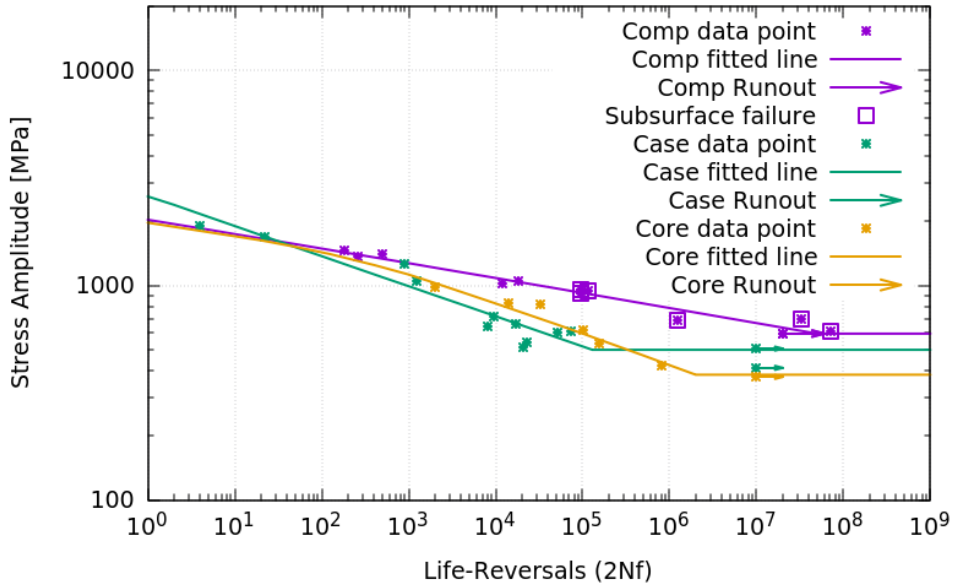

Figure 4.7: Half-life stress vs. fatigue life data for the case, core and composite axial samples with fitted curves

core material in the short fatigue life region because of its lower ductility and consequent lower resistance to plastic strain. Also at long lives it falls above the core curve because of its greater resistance to elastic straining.

The case material in the composite specimen, because it has a compressive residual stress, falls above the case curve at short lives. In the long life region, failure in the composite samples initiated from fisheye cracks in the core layer. Although the core layer in the composite specimen had tensile residual stresses and starter cracks, both of which are detrimental in fatigue, its fatigue life curve falls not only far above the simulated core material curve but also above the base curve for the harder simulated case material.

Similar to sets of carburized steel fatigue tests performed by AISI fatigue bar group plotted in Figure 2.14, the composite material has a higher fatigue limit than the simulated core. This could be attributed to the vacuum and fully constrained environment in the core layer of the composite sample, which impedes nucleation and retards the crack growth. On the other hand, the decarburized layer on the surface of the simulated core sample,

exhibited in Figure 4.3b, can lead to early crack initiation and impair the fatigue limit of the simulated core material. It suggests that the constant amplitude fatigue data of the simulated core material does not perfectly describe the fatigue behaviour of the core material in the composite specimen.

The cyclic stress-strain data for all three materials are shown in Figure 4.8 with the fitted cyclic stress-strain curves.

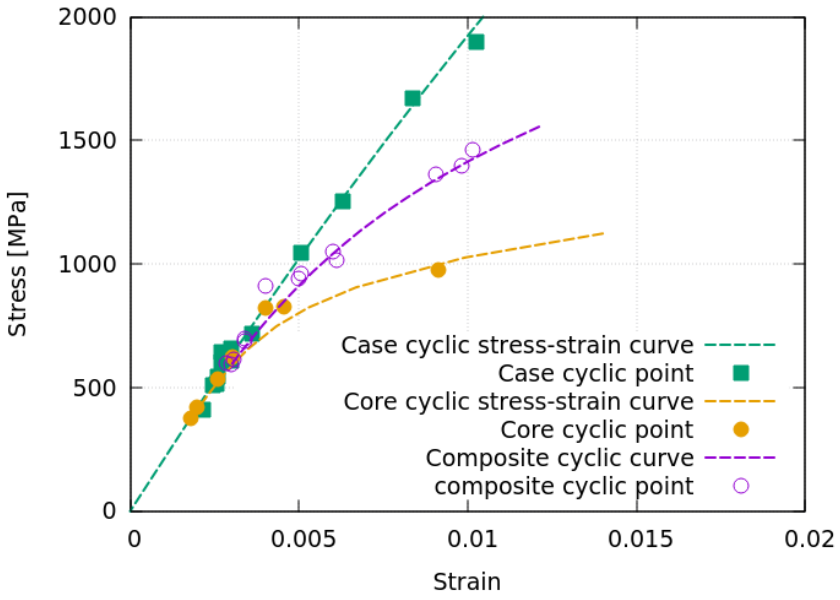

Figure 4.8: Cyclic stress-strain data for the case, core and composite materials with fitted curves

Figure 4.9 plots the fitted cyclic and monotonic stress-strain curves for the case, core and composite materials. The figure also includes the compressive monotonic stress-strain curves for the case and the composite materials.

The cyclic stress-strain curve of the core material is below that of the monotonic curve, which indicates that the simulated core material experiences cyclic softening. Due to RA transformation, the compressive stress-strain curves for the through-carburized case and the composite materials are higher than the corresponding tensile curves. The case material's cyclic and compressive stress-strain curves are similar, meaning that RA transforma-

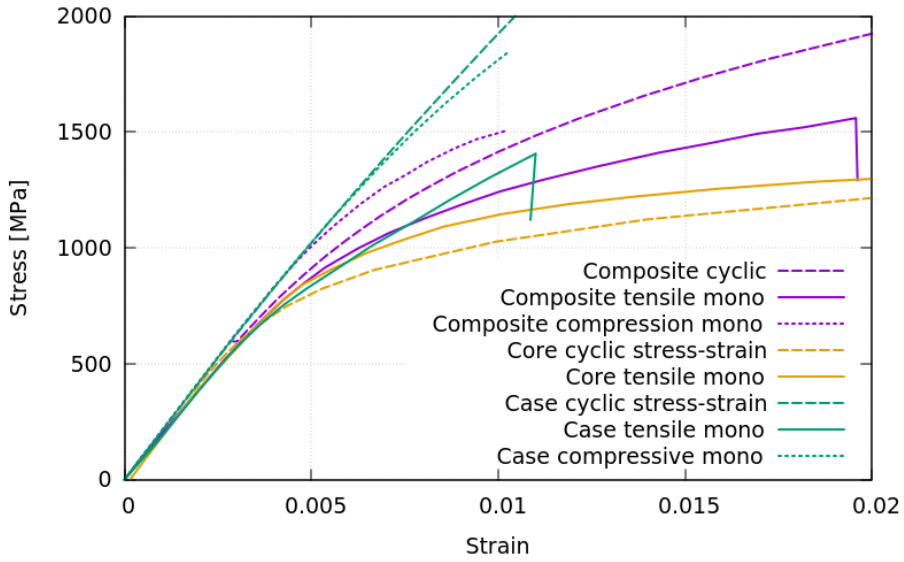

Figure 4.9: Fitted cyclic stress-strain curves compared with tensile (solid lines) and compressive (dotted lines) monotonic curves for case, core and composite materials

tion is completed in the cyclic stabilized case material. The difference between the tensile and compressive monotonic curves in the composite material is much less than that in the case material because the core layer that softens under cyclic loading holds a significant volume ratio in the composite.

Even though the digitized stress-strain-life curves instead of the cyclic parameters were used in this study to simulate the material behaviour, the stress-strain-life data were still fitted to the Coffin-Manson and Ramberg-Osgood equations to obtain the cyclic parameters. The detail of the fitting process and the parameters are listed in Appendix B.

Negative mean stress tests were conducted on the through-carburized case axial samples to validate the phenomenon proposed by Gaia Da Silva et al. [47] that when the maximum stress in a fatigue stress cycle is maintained at the value of the peak tensile stress at the fully reversed CA fatigue limit, the fatigue life for all negative stress ratios remains at the fully reversed fatigue limit.

CA load with negative mean stresses was applied on the through-carburized case axial

samples. Figure 4.10 shows the maximum and minimum stresses of the case runout tests under CA at various R-ratios.

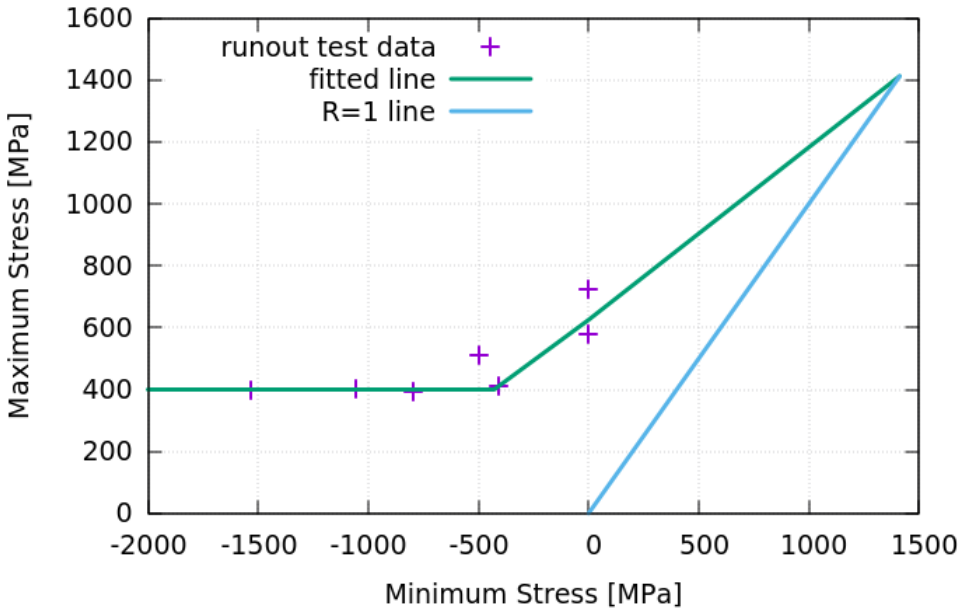

Figure 4.10: Maximum stress vs minimum stress for CA runout tests of the case material

The fitted line plotted in the figure was obtained from Morrow's mean stress rule ($\frac{\sigma_a}{\sigma_{ar}} + \frac{\sigma_m}{\sigma_u} = 1$) in the positive mean stress region and drawn flat in the negative region. The flat line was drawn near the maximum stress at 400 MPa, which is around 90% of the CA fatigue limit of the case sample.

The test data obtained from the negative mean stress tests in this study confirmed the theory proposed by Gaia Da Silva et al. [47]: when the maximum stress in the load cycle is near or below the fatigue limit under fully reversed loading, decreasing the minimum stress in the test does not cause additional damage in the very hard steel.

Due to the limited number of the notched plate specimens available, only three fully reversed CA tests were conducted on the case notched plate, two on the composite notched plate and one on the core notched plate. The tests data are compared with the smooth sample CA tests in Figure 4.11.

The stress concentration factor, K_t, at the circular notch of the plate can be calculated using Equation 2.21. With a hole diameter of 1 mm and a plate width of 12.7 mm, the K_{tg} was determined to be 3.02, which can be approximated to 3. The lines fitted to the smooth sample CA tests were divided by 3 to get a reference for the notched CA test data.

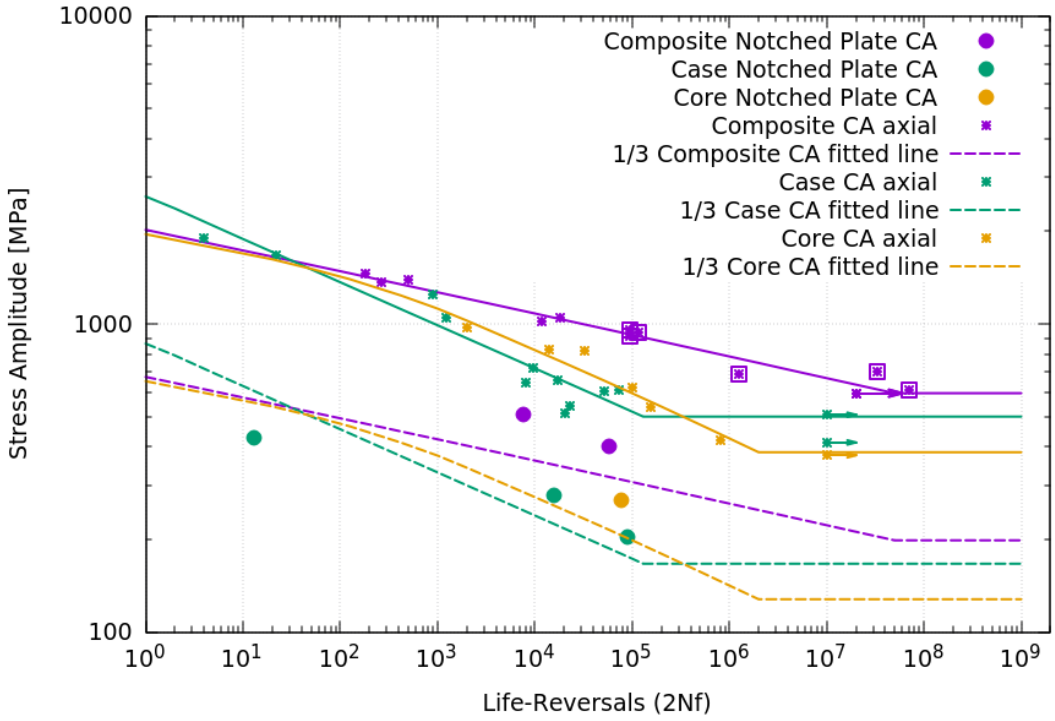

Figure 4.11: Stress-life data for the notched and axial case samples under CA loading of the case material

The green dashed line, for which the stress amplitude is 1/3 of the case axial fitted line, shows a reasonably good fit for the case notched CA test data points. However, both the scaled fitted lines for the core and the composite samples (yellow and purple dashed lines) are conservative compared to the CA notched data points. The crack propagation life might have taken up a significant portion of the total life in the core notched sample and the core layer of the composite notched sample, which leads to the longer observed fatigue life compared to the prediction using just the initiation curve in the core and composite notched plate tests.

4.4 Variable amplitude (VA) tests

Periodic overload (POL) tests were conducted on the core and the case axial samples to study the overload effect. The stress amplitude of the overload cycle equals that at a 10,000 cycles fatigue life under fully CA loading. The maximum stress was kept constant throughout the POL test, while the minimum stress of the small cycle was adjusted to obtain the desired stress amplitude. Miner's rule was applied to calculate the equivalent life of the small cycles.

Assuming the small cycle is fully elastic, the SWT equation was applied to calculate the equivalent fully reversed stress amplitude for the small cycles.

The POL contributes to 12% to 27% of the total damage in all the failed POL tests for the core material. Figure 4.12 compares the POL stress-life data with the CA data for the core material before and after a SWT correction.

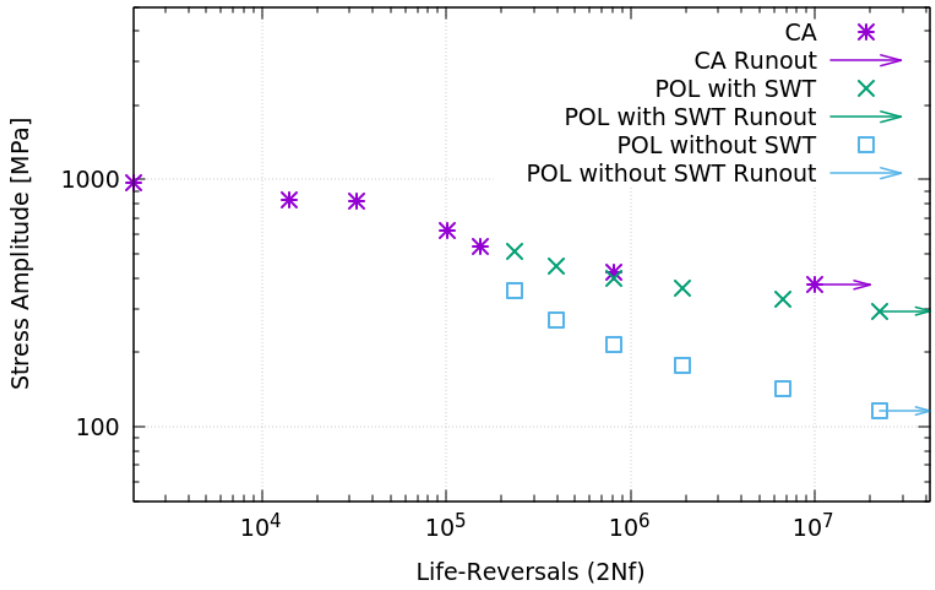

Figure 4.12: CA and POL stress-life data for core material

The green and purple points at the long-life region show that the underload does not

significantly impair the fatigue performance of the core material after a SWT correction. One could speculate that the effect of crack closure is negligible in the core material.

Figure 4.13 shows the POL and the CA stress-strain data for the case material before and after a SWT correction. Due to a limited number of samples, the run-out samples were retested at a higher stress level. The left figure in Figure 4.13 shows the POL tests ran with new samples, and the right figure plots those re-tested with previously runout samples.

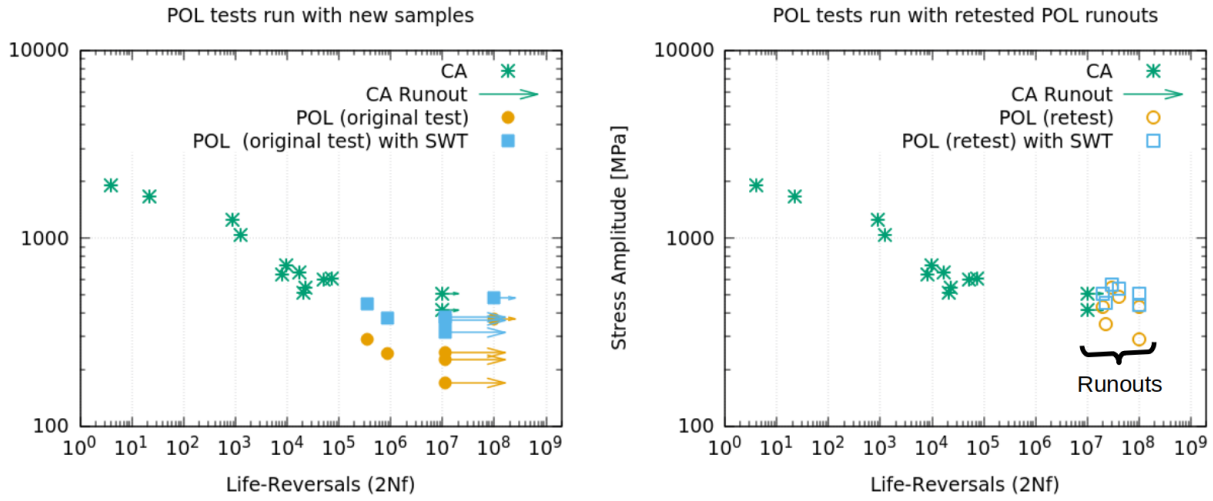

Figure 4.13: CA and POL stress-life data for case material

For the two POL tests that failed in the case sample, 3% and 13% of the total damage was caused by the overload cycles.

The results generated from the previously tested runout samples show a POL fatigue limit higher than the CA history. This coaxing effect may play a role in the high fatigue limit in the POL tests. Also, more RA might have transformed under POL than under fully reversed CA loads. The fatigue limit of martensite could be higher than that of austenite. A similar effect was observed in Figure 2.1 [110].

The smooth and the notched composite samples were tested under the bracket VA load history that was scaled to different stress levels. The bracket VA history is shown in Figure 4.14.

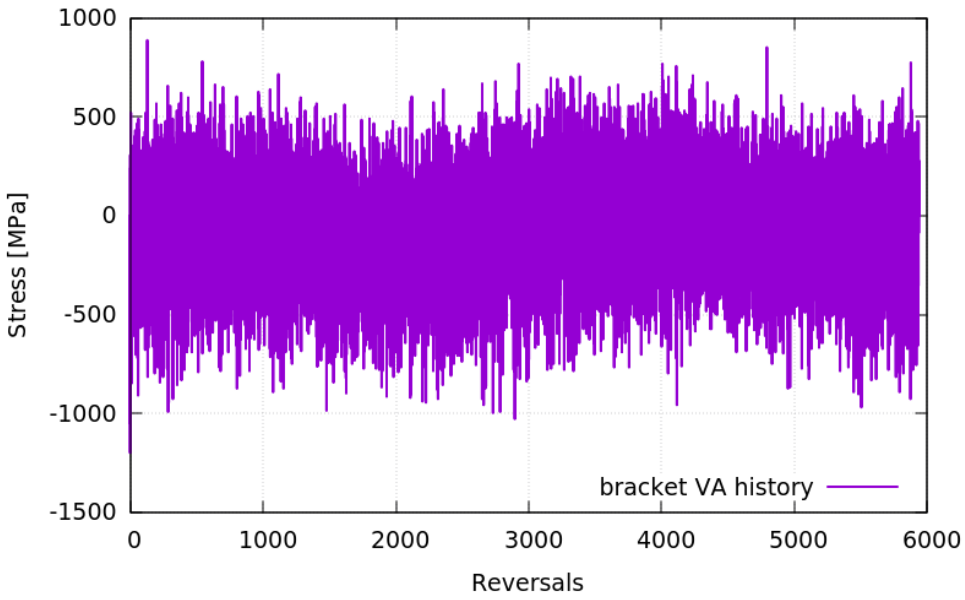

Figure 4.14: Bracket VA history

To determine the damage contributed by the small load cycles, the bracket load history was filtered to eliminate the cycles with stress ranges less than the composite material fatigue limit in a rainflow counting based process. Figure 4.15a shows the filtered history on top of the full history. The rainflow counted cycles of the two histories are plotted in Figure 4.15b.

Smooth composite samples were loaded under the full and the filtered bracket VA histories, while the notched plates were loaded under the full bracket history. The maximum stress vs the fatigue life results generated from the tests mentioned above are plotted in Figure 4.16.

It is important to note that the fracture surfaces of all the smooth composite samples that failed under VA loading contain at least one fisheye. However, no sign of subsurface failure was observed in the composite notched plates.

The smooth composite samples loaded under the full and the filtered bracket histories failed at similar fatigue lives, which suggests that the small load cycles with stress range

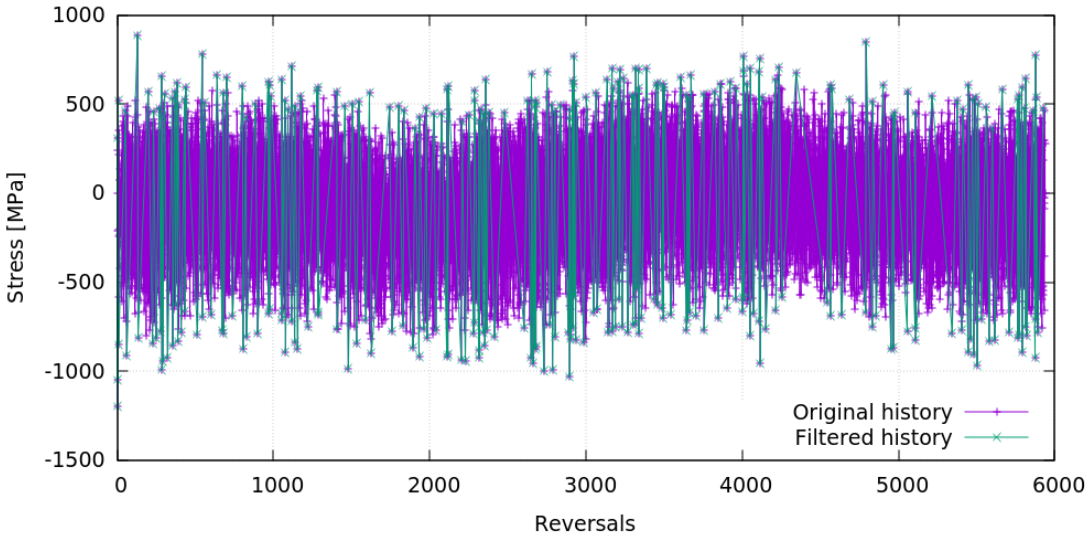

(a) Load cycle history view

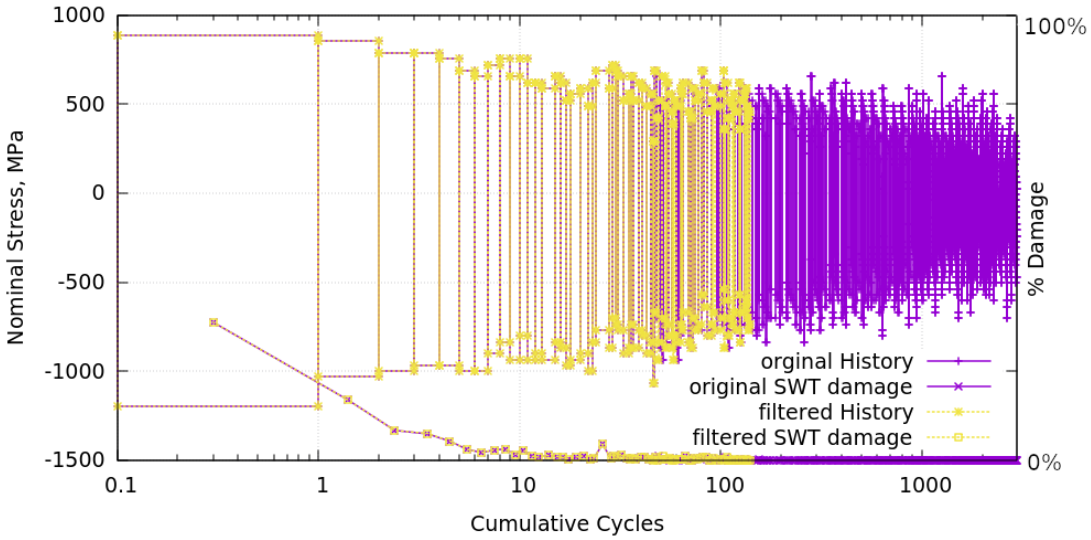

(b) Cumulative Rainflow counted stress ranges (sorted by largest to left side) and percent damage per Rainflow counted range (right side Y axis)

Figure 4.15: Comparison of the filtered and the full bracket VA histories

smaller than the fatigue limit do not cause damage.

Four of the notched case samples were tested under the full bracket VA history. The

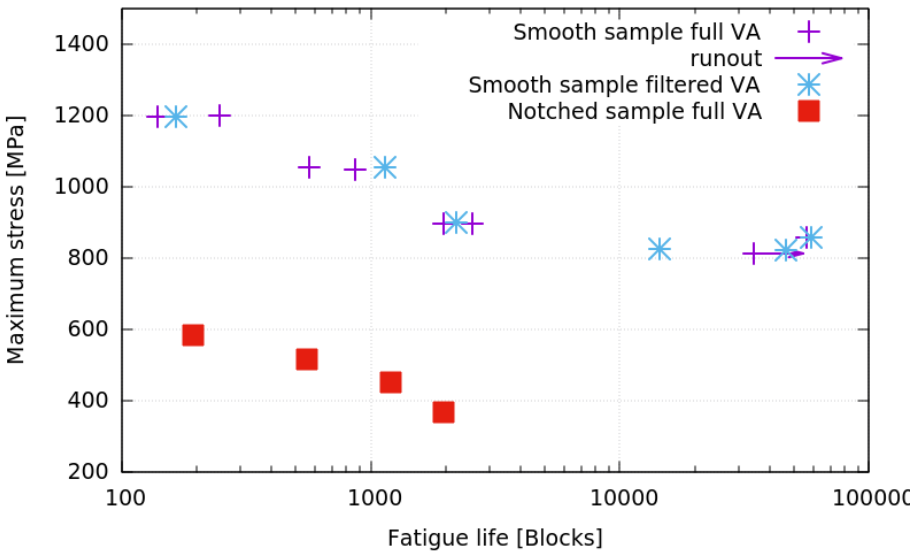

Figure 4.16: Maximum Stress vs fatigue life data for composite smooth samples loaded under full and filter VA histories, and for the notched samples loaded under full VA history

tested data of the notched case samples are compared with the composite sample in Figure 4.17.

It is expected that the compressive residual stress in the case layer of the notched composite samples will improve the fatigue performance, when compared to the notched case sample lives that have no residual stress. This difference is indicated in the test results.

The load and the strain were measured in some of the VA tests on the smooth composite samples. The hysteresis loops of the two VA tests are shown in Figure 4.18. Figure 4.18a shows the hysteresis loop at the 15th block in a test that lasted for 139 blocks of the bracket history, and Figure 4.18b shows the 23rd block in a 34,395 blocks test.

Plasticity can be observed in the hysteresis loop plotted in Figure 4.18a, which is for a short life test that lasted for 139 blocks. On the other hand, the hysteresis loop in Figure 4.18b is primarily elastic.

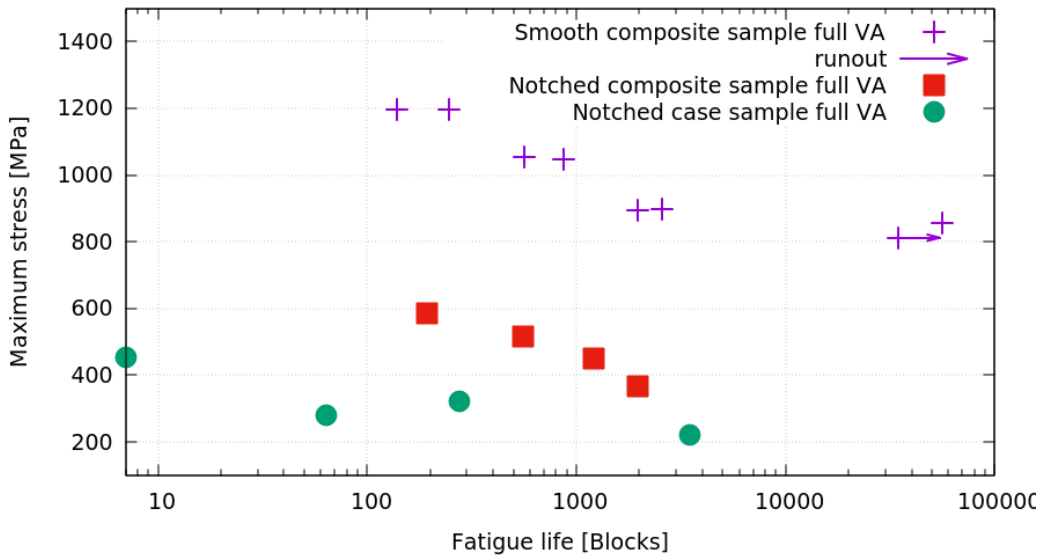

Figure 4.17: Maximum Stress vs fatigue life data for composite smooth samples and notched plate, and for case notched plate under full VA history

4.5 Fracture surfaces of the composite samples

Fisheye cracks were observed in the fracture surfaces of the axial composite samples loaded under VA loading at all stress levels and CA loading in the long-life region.

4.5.1 Fracture surfaces of composite samples loaded under VA histories

Figure 4.19 shows the typical fracture surfaces of the composite axial samples loaded under VA histories that failed at different fatigue lives.

Two fisheyes with different sizes are shown on the fracture surfaces in Figure 4.19a and 4.19b. The small fisheye in Figure 4.19a is on a different plane from the rest of the fracture surface. The fatigue life of the samples increases from Figures 4.19a to 4.19d. As the fatigue life increases, the area of the final fisheye tends to increase. Figures 4.19b to

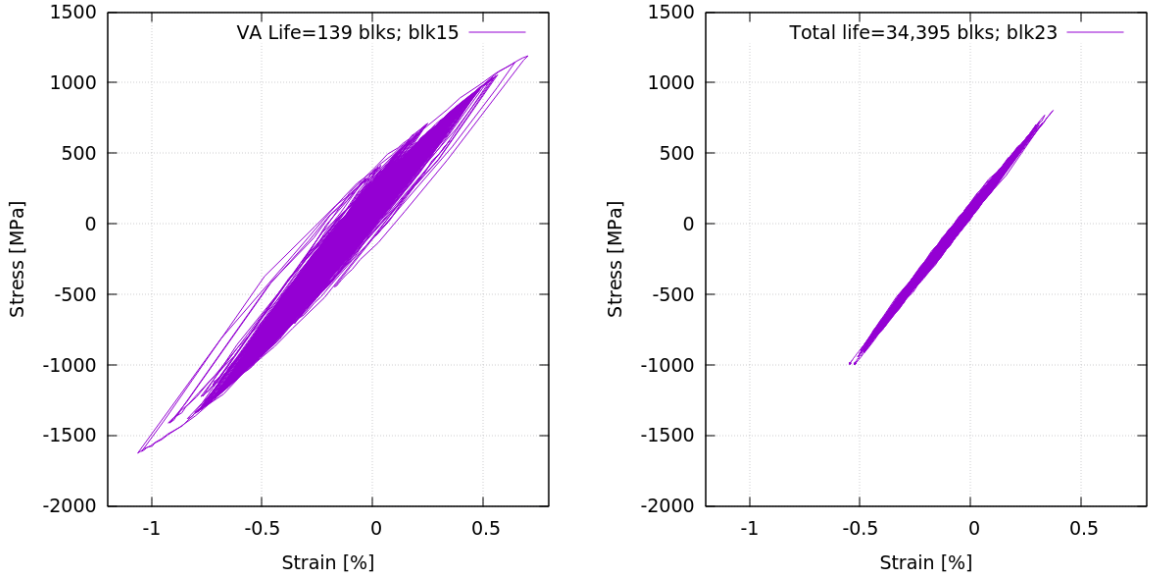

(a) Life = 139 blks, Max. Stress = 1197 MPa (b) Life = 34,395 blks, Max. Stress = 812 MPa

Figure 4.18: Hysteresis loops of the composite smooth samples under VA loading

4.19d show a failure mechanism that started from a fisheye and extended to a through crack before the final fracture. The fisheye initiation location is independent of the fatigue life in the tests, and it is somewhat random and might depend on the inclusion location.

On the other hand, no fisheye was found on the fracture surfaces of the composite notched plate samples. A typical notched plate fracture surface is displayed in Figure 4.20. This notched plate was loaded under bracket VA history and failed after 1,205 blocks of loads.

The wrinkles or rivermarks along the notch suggest multiple crack initiation points. The semicircular contour on the fracture surface implies that the cracks grew in a shape of a corner crack started on the bottom surface at the notch.

(a) Filtered history, life =116 blks

(b) Full history, life =869 blks

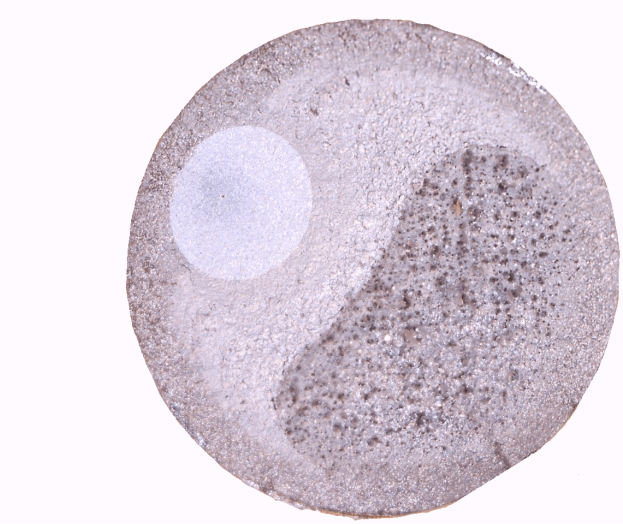

(c) Full history, life = 2,568 blks

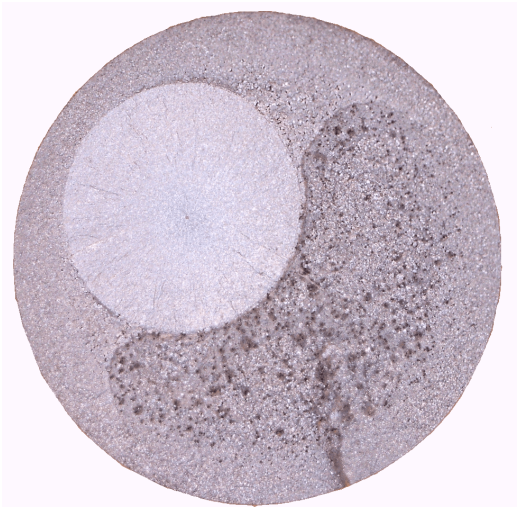

(d) Filtered history, life =46,223 blks

Figure 4.19: Fracture surfaces of the composite axial samples under bracket VA history

4.5.2 SEM images of the composite sample fracture surface

SEM images were taken on the fracture surfaces of several composite and case axial samples loaded under CA histories. Two of the fracture surfaces of the composite samples

Figure 4.20: Fracture surface of a notched composite sample under full bracket VA history

were examined closely. The sizes of the inclusions and the fisheyes were measured using an image processing tool, ImageJ, and are listed in Table 4.4.

Table 4.4: Test data for composite samples loaded under CA histories

Sample ID		cComp3	cComp4
Strain amplitude	%	0.4	0.34
Stress amplitude	MPa	908	684
Fatigue life	cycles	47,755	620,994
Measured inclusion area	μm^2	872.4	1072
Inclusion diameter convert from measured area	μm	33.3	36.9
Measured inclusion diameter	μm	34	37.6
Measured fisheye area	mm^2	5.038	2.148
Fisheye diameter convert from measured area	mm	2.53	1.65
Distance from edge of fisheye to sample surface	mm	0.575	0.426

Specimen cComp3 was loaded at a higher strain amplitude than cComp4 and thus failed in a shorter life. The inclusion and fisheye areas were measured using the elliptical selection tool in ImageJ. The average of three area measurements was recorded. The inclusion diameter was taken as the average of five measurements at different orientations across the inclusion. The difference between the diameter converted from the measured area, and that measured directly is reasonably small.

Figures 4.21 and 4.22 show the SEM for the fracture surfaces of cComp3 and cComp4.

The zoomed-in views for the fisheye and the inclusions are displayed.

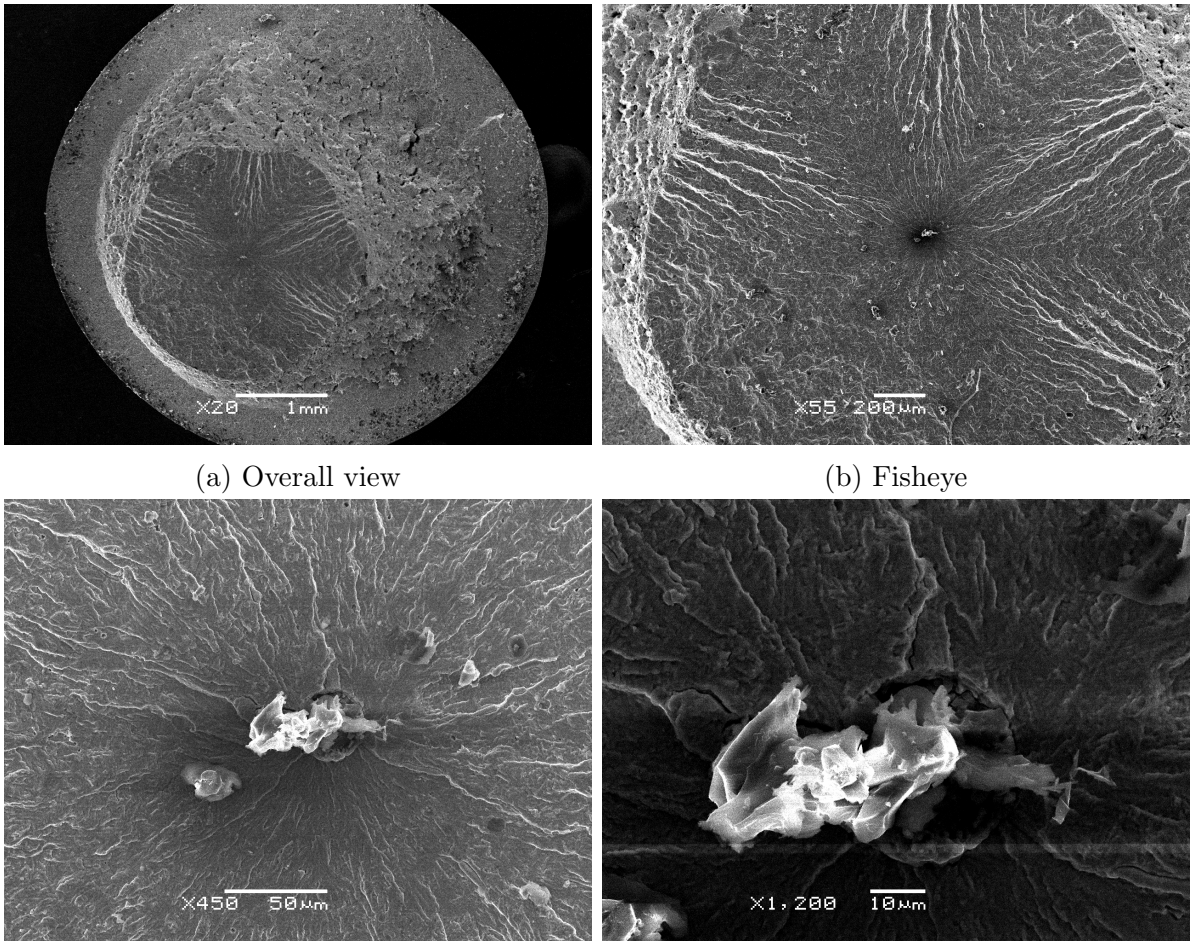

(a) Overall view (b) Fisheye

(c) Inclusion (d) Inclusion zoomed

Figure 4.21: SEM images of the fracture surface of cComp3

The fracture surface of cComp3 has two layers at different heights; one forms an outside ring surface crack, while the fisheye crack is on a higher plane in the specimen, as shown in Figure 4.21a. This suggests that in cComp3, cracks are initiated simultaneously from the surface and internally. When the subsurface crack reached the case layer, the surface crack formed on a different plane also contributed to the final fracture.

The fracture surface of specimen cComp4 is relatively smooth, as shown in Figure 4.22a,

which indicates that the crack initiated from the subsurface inclusion and propagated outwards. Once the crack reaches the case layer and propagates around the circumference, a final fracture occurs.

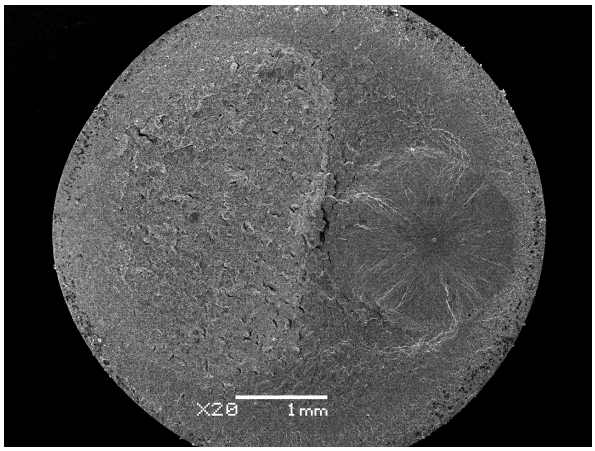

(a) Overall view

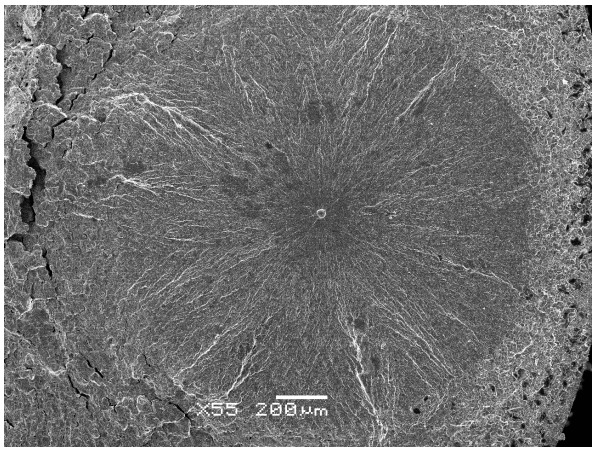

(b) Fisheye

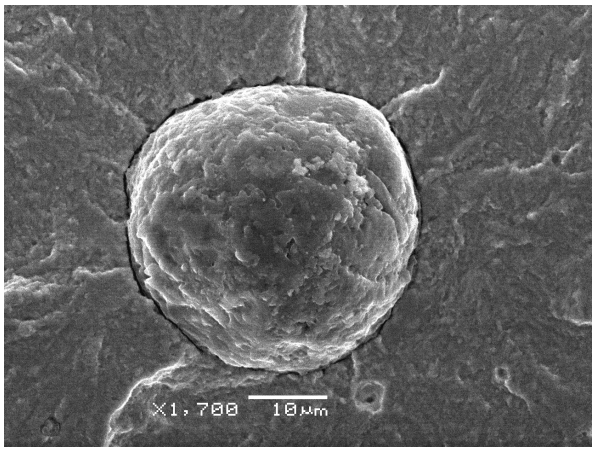

(c) Inclusion

Figure 4.22: SEM images of the fracture surface of cComp4

Since specimen cComp3 was cycled under a higher load than cComp4, which induces more plasticity in the interior layers that drops the tensile mean stress, the tensile mean stress in the hysteresis loop of cComp3 should be smaller than that in cComp4. Fisheyes were only observed in the low stress level cyclic tests, while surface failures were found in

the high stress levels. It is expected that the subsurface crack initiation sites shift closer to the surface layer at higher load levels. However, by reading the data from Table 4.4 and by comparing Figure 4.21a and Figure 4.22a, one can observe that the inclusion in cComp3 is further away from the surface than that in cComp4. Therefore, the subsurface failure initiation, or the inclusion, locations seem to be randomly distributed and independent from the stress distribution in the subsurface layers.

4.6 Crack growth rate measurements

Crack growth measurements for R = -1 and R = -3 were collected on the core notched plate samples. A 50x travelling microscope, as shown in Figure 4.23, was used to watch the crack. The length of the crack was measured using an LVDT for the horizontal movement of the travelling microscope.

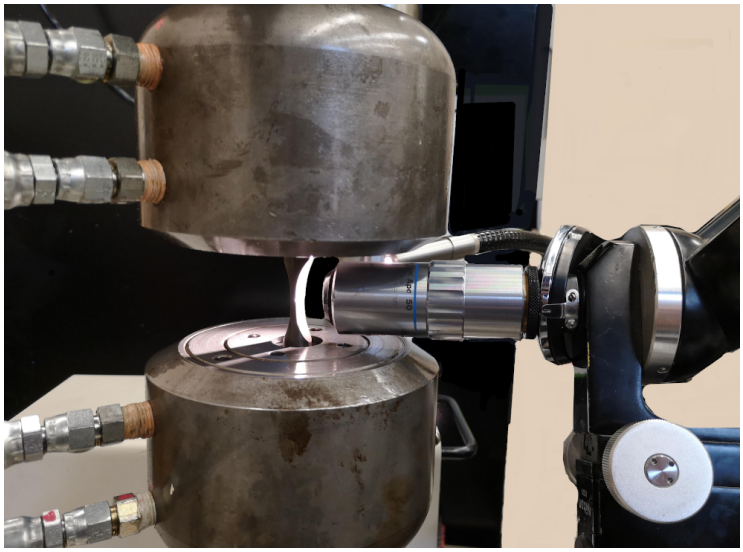

Figure 4.23: A picture of the microscope used for crack length measurement

Fully compressive cyclic loading was applied on the core notched plates to start a crack. Observations were made after every 10,000 cycles to see if a crack had been started near the notch. If no crack was found, the magnitude of the minimum load was increased by

about 10% for another 10,000 cycles of loading. This procedure was repeated until a crack was found. The lengths of the starter cracks range from 0.10 mm to 0.23 mm after 10,000 cycles of CA loading at nominal stress at 0 MPa to around -510 MPa.

An estimated stress range was chosen to run for around 400,000 cycles to measure the crack growth near the threshold SIF. If no crack growth was measured, the stress range was increased; otherwise, the stress range was reduced to obtain a point closer to the threshold.

The SIF for different crack lengths were calculated following the methods described in Section 2.11.

The average of the previous crack length and the current crack length was used to determine the SIF calculations with the current set of stress ranges.

Due to the small notch radius of 0.5 mm, the short cracks, defined in Figure 2.18, in this case, are cracks with lengths up to 0.1 mm. All crack lengths measured in the core notched plate crack growth study are long cracks.

The crack growth rate results measured in the core plate samples are plotted with the "Hasegawa1" da/dN curves in Figure 4.24.

The crack growth rate data measured in the core notched plate at a stress ratio of -1 scatter around the R = -0.5 da/dN curve, and those for R = -3 spread around the R = -3 curve. However, the threshold SIF values measured at these two stress ratios do not differ significantly from each other. They are both slightly higher than the "Hasegawa1" da/dN curve threshold value for $R > 0$.

Some representative fracture surfaces of the core notched plate samples are included in Figure 4.25.

The striations on the fracture surfaces reveal the different crack geometry during crack propagation in each sample. One common feature that all fracture surfaces show is multiple simultaneous crack initiation sites (near rivermarks) along the notch at both sides of the plate.

CorePlate1 in Figure 4.25a consists of almost a through crack that is the most uniform among all the core notched plate samples in Figure 4.25. The crack growth data, plotted in

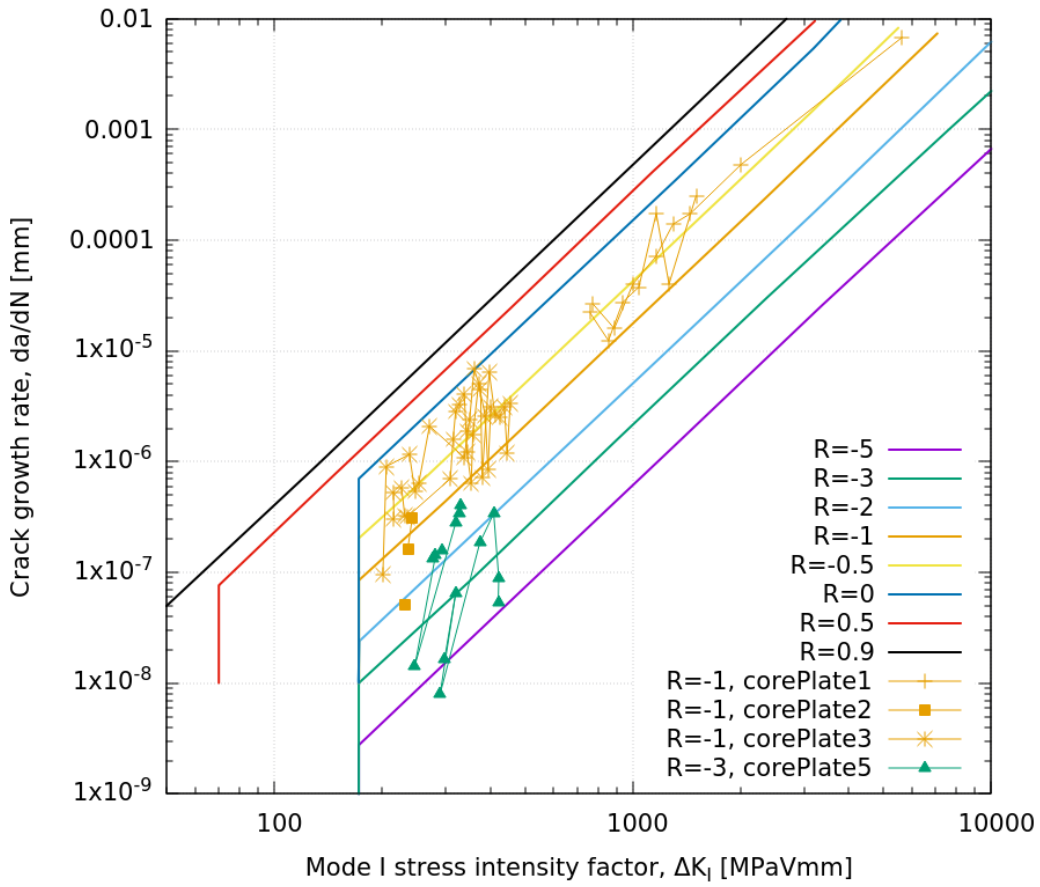

Figure 4.24: Measured crack growth data of the core plates compared with the "Hasegawa1" da/dN curves

Figure 4.24, obtained from corePlate1, contains significantly less scatter than the rest. The fracture toughness of the core material was found to be 5626 MPa$\sqrt{mm}$ or 178 MPa$\sqrt{m}$. This was calculated based on the final crack length observed from Figure 4.25a and the applied stress range. The corresponding crack growth point is also plotted in Figure 4.24.

In both CorePlate3 and CorePlate5, the cracks seem to propagate much faster on one specimen face surface than the other.

The fracture surface of CorePlate6 shows a crack through the width of the plate before

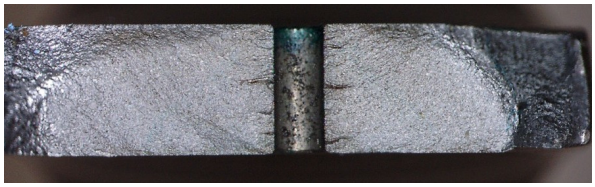

(a) CorePlate1, R=-1, $\Delta S = 536$ MPa

(b) CorePlate3, R = -1, pre-cracked in compression, near threshold measurements

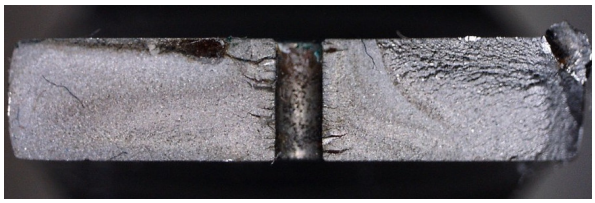

(c) CorePlate5, R = -3, pre-cracked in compression, near threshold measurements

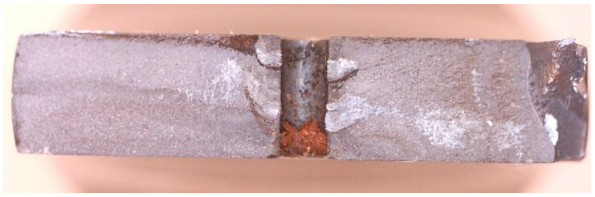

(d) CorePlate6, R = -5, pre-cracked in compression found through crack on one side

Figure 4.25: Fracture surfaces of the core notched plate samples

propagating into the thickness. This observation matches the crack measurements under the microscope, where a through crack was found on the left half of the sample at the earlier stage of the test. Therefore, the data collected from CorePlate6 is inappropriate.

Since the ΔK_I for the crack growth measurement was calculated assuming the cracks are through the thickness, those collected from CorePlate3 and CorePlate5 might not be as accurate as that from CorePlate1. The core notched plate might be too thick for crack propagation tests considering the small sample size.

4.7 Middle layer properties assumptions

The hardness profile of the composite axial sample in Figure 4.2 shows that there is a transition layer in between the case and the core layers. In order to accurately predict the stress-strain behaviour and the fatigue performance of the composite samples, a middle layer was added between the case and the core layers in the simulations.

The fatigue and the stress-strain behaviour of the material in this transition zone were

derived by digitally fitting the curves based on the case and the core material. The derived middle layer material curves are the inputs for the residual stress estimation, the initiation location predictions and crack propagation models of the composite axial samples.

Figure 4.26 demonstrates the derived cyclic stress-strain curves of the middle layer with the fitted cyclic stress-strain curves of the case, core and composite samples under CA tests. Figure 4.27 shows the strain-life and the stress-life curves of the middle layer compared with the fitted CA fatigue curves for the case, core and composite samples.

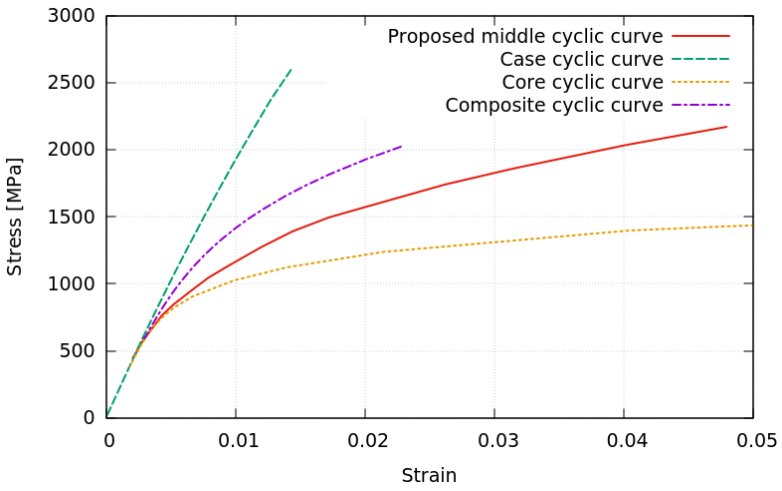

Figure 4.26: Proposed middle layer cyclic stress-strain curve compared with the case, core and composite fitted cyclic stress-strain curves

4.8 Mean stress relaxation

CA loadings with various mean stresses at different strain amplitudes were applied to the case and the core axial samples to study the mean stress relaxation phenomenon in these materials.

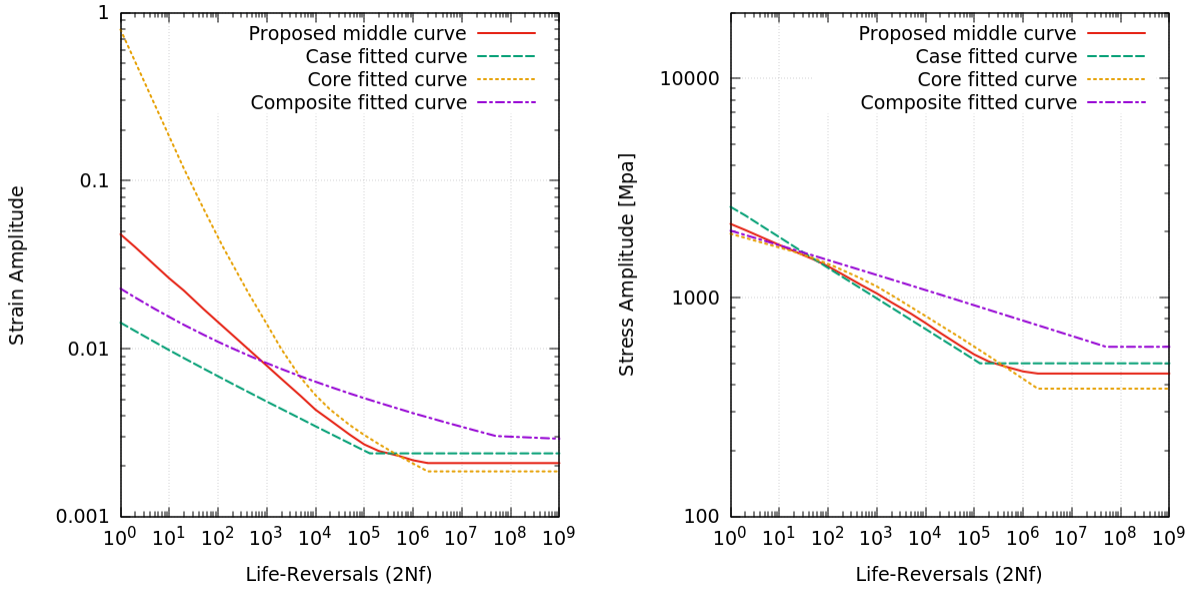

(a) Strain-life curves

(b) Stress-life curves

Figure 4.27: Proposed strain-life and stress-life curves of the middle layer compared with the fitted CA curves of the case, core and composite samples

4.8.1 Simulated core material

The strain and stress histories of a typical strain-controlled stress relaxation test are plotted in Figure 4.28. Two strain amplitudes, ±0.6% and ±0.7%, were applied sequentially to this one sample.

To minimize the cyclic softening effect while examining the mean stress relaxation, five cycles of +-1.0% strain were applied at the beginning of a test followed by a tapered load, as shown in Figure 4.28a. When changing the strain amplitude in the test on one sample, the original strain amplitude is ramped down to 0% with the initial mean strain. Then, three cycles of +-1% strain are applied, followed by a tapered loading.

Cyclic softening can be observed in the ±1% preloading cycles in Figure 4.28b. In the first session of the stress-relaxation test at ±0.6% strain, the maximum stress dropped rapidly at the beginning of the test. A moderate amount of softening occurred continuously

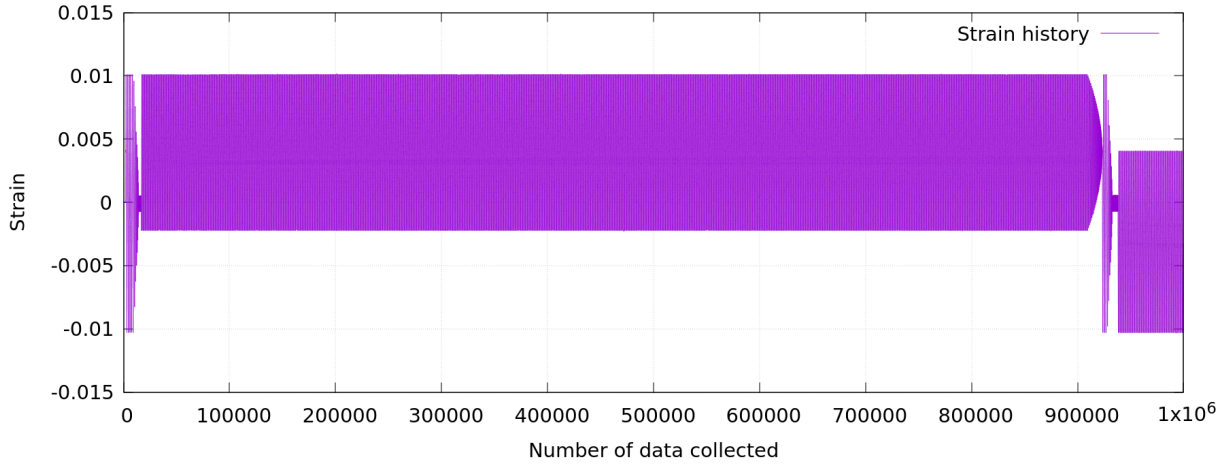

(a) Strain history

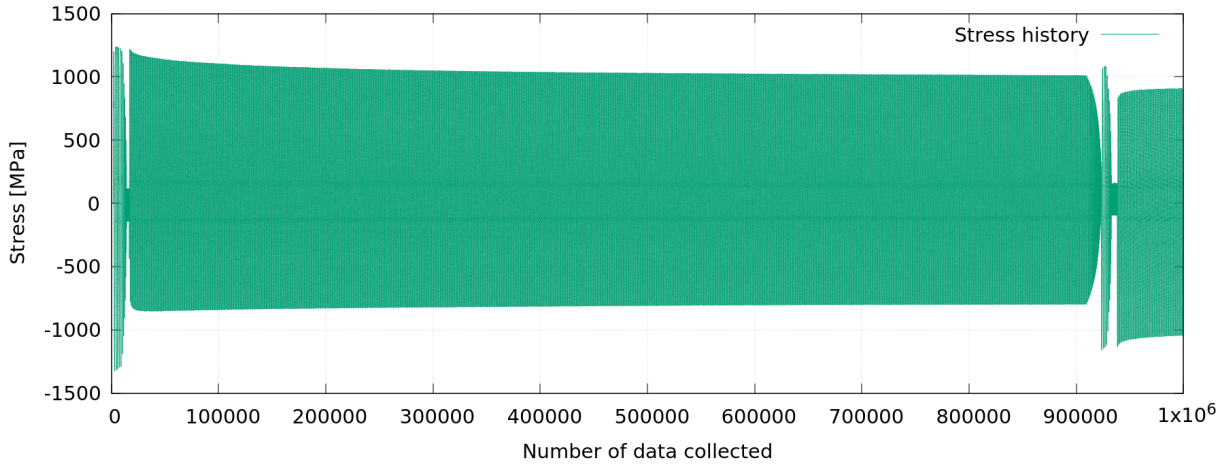

(b) Stress history

Figure 4.28: A typical strain and stress load histories of the mean stress relaxation tests

throughout the test. At the beginning of the ±0.7% strain test, the mean stress relaxes promptly, with both the maximum and minimum stress shifted towards positive stress.

The hysteresis loops for four mean stress relaxation tests at strain amplitudes ranging from 0.31% to 0.41% are plotted in Figure 4.29.

The hysteresis loops in Figure 4.29 for all tests show the mean stress shifting while

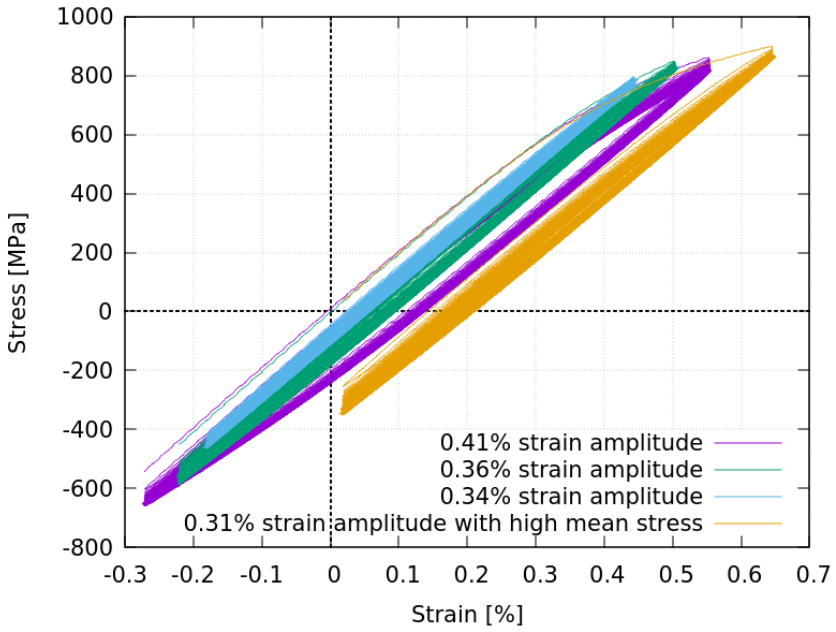

Figure 4.29: Hysteresis loops of the stress relaxation tests for the core at strain amplitudes of 0.41%, 0.36%, 0.34 and 0.31% with a high mean stress

the specimen is cycled between constant strain limits, even for the ±0.31% test where the stress-strain response is fully elastic.

The maximum and minimum strains applied in each of the core material stress relaxation tests are listed in Table 4.5 with the initial mean stress and sample number. Note that at the low strain ranges, one sample was loaded under multiple strain levels.

Normalized mean stress relaxation curves for all the tests conducted on the axial core samples are plotted in Figure 4.30. The y-axis of the plot is the ratio of the mean stress in the corresponding reversals over that of the initial mean stress. Data for the tests conducted on Core specimen 16 (five relatively low strain amplitude levels) are presented as dashed lines. The sample number and the loaded strain are labeled for the corresponding line colour.

Regardless of whether a test was started with a tensile or compressive mean stress, a continuous drop in the magnitude of the mean stress can be observed in Figure 4.30.

Table 4.5: Core stress relaxation tests strain peaks and initial mean stress

Strain amplitude	Min strain	Max strain	Initial mean stress	Sample number
0.31%	-0.18%	0.44%	322	Core16
0.34%	-0.02%	0.65%	191	Core16
0.36%	-0.22%	0.50%	199	Core16
0.41%	-0.27%	0.55%	159	Core16
0.51%	-0.36%	0.66%	110	Core16
0.62%	-0.23%	1.01%	219	Core17
0.72%	-1.03%	0.40%	-148	Core17
0.82%	-0.63%	1.01%	148	Core18
0.92%	-1.03%	0.82%	33	Core19
1.01%	-0.82%	1.19%	33	Core16

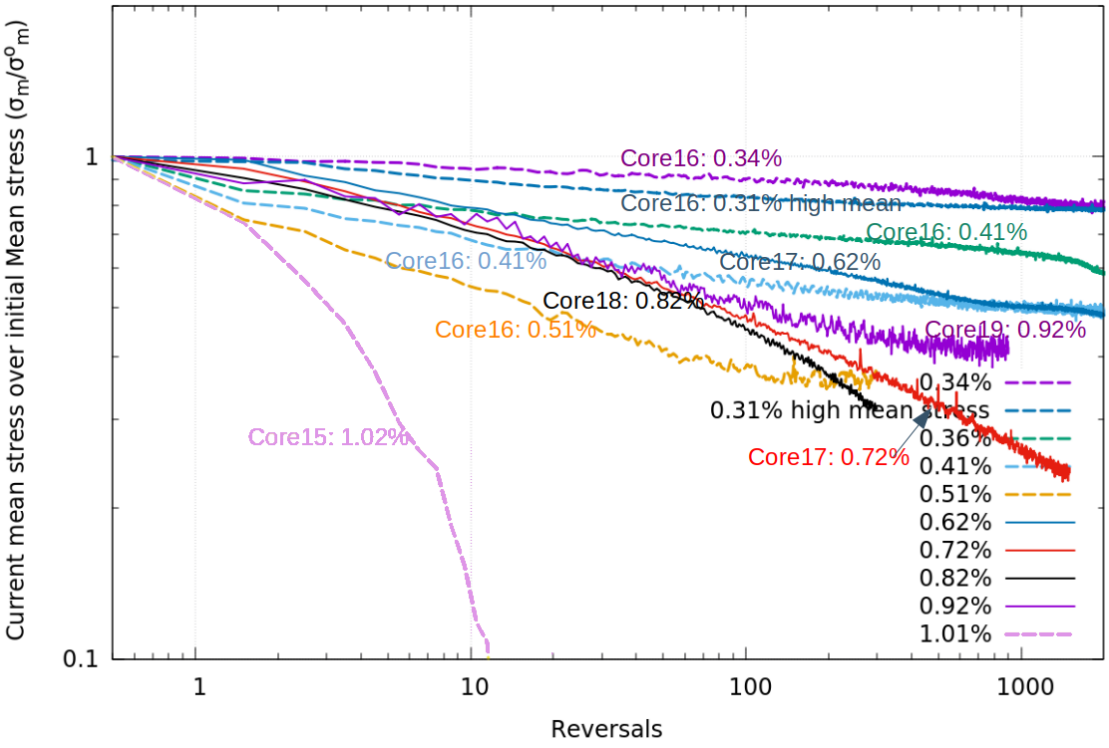

Figure 4.30: Normalized mean stress relaxation in the core samples

For all tests conducted on sample core 16 (dashed lines), the mean stress relaxation rate increases with an increase in the applied strain amplitude, except for those at 0.34% and 0.31%, where the 0.31% strain test started with higher mean stress than the 0.34% test.

Variations on the mean stress relaxation rates were found between samples, while consistency was obtained for tests conducted with the same sample.

The relaxation data in this section were converted to plastic strain vs the number of reversals required to reach a 50% mean stress decrease. The plastic strain is defined as the width of the stress-strain hysteresis loop. For the tests with strain amplitude below 0.41%, no plastic strain was perceived.

Figure 4.31 shows the converted plastic strain amplitude vs. the 50% mean stress drop reversals data obtained in this study together with other data collected by Conle [19] from several published articles. The data points in the plot are colour-coded by the material hardness. Our core material is one of the harder ones on the list.

A considerable amount of scatter is shown in the data from this study, yet it still falls into the scatter band of the collected data. A trend can be observed from Figure 4.31: the harder material tends to relax at a slower rate at the same amount of plastic strain compared to the soft material.

4.8.2 Through-carburized case material

Six stress relaxation tests at different strain amplitudes were conducted on three case samples, Case40, Case41 and Case42. Table 4.6 lists the test information in the order of which the tests were run. Each of the samples was loaded under two different strain amplitudes, a lower strain first followed by a higher strain amplitude. Since the case material failed at a tensile strain of around 0.8% under monotonic loading, all tests were started with negative initial residual stresses to avoid failure in the first cycle and to maximize the observation period.

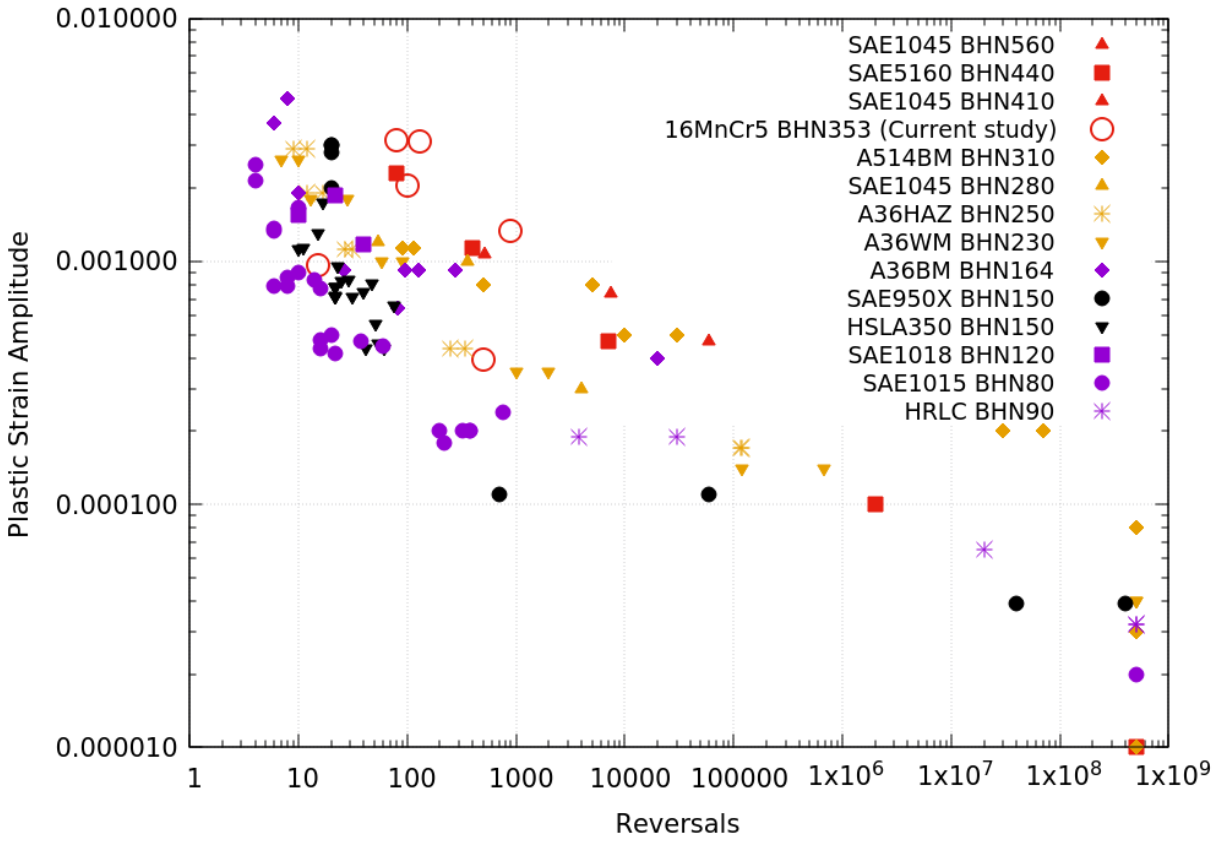

Figure 4.31: 50% strain amplitude drop vs number of reversals [19]

Figure 4.32 shows the normalized mean stress change in linear scale of the mean stress ratio versus loading reversals.

Little plasticity was observed in the stabilized hysteresis loops even at the largest strain amplitude tested at ±0.82%. The mean stress further shifted towards negative values despite the initial negative mean stress indicating that significant RA transformation always occurs at the beginning of the first test on a new case sample.

For case specimen 40, RA transformed in the first test loaded at ±0.41% and slowed down at around 500 reversals. The mean stress then started to relax. In the second test at a strain amplitude of 0.52%, the mean stress continued to relax at a fast rate. A similar

Table 4.6: Case stress relaxation tests strain peaks and initial mean stress

Strain amplitude	Min strain	Max strain	Initial mean stress	Sample
0.41%	-0.72%	0.10%	-856	Case40
0.52%	-0.85%	0.18%	-679	Case40
0.42%	-0.73%	0.11%	-846	Case41
0.52%	-0.85%	0.18%	-768	Case41
0.72%	-1.09%	0.34%	-774	Case42
0.82%	-1.19%	0.45%	-790	Case42

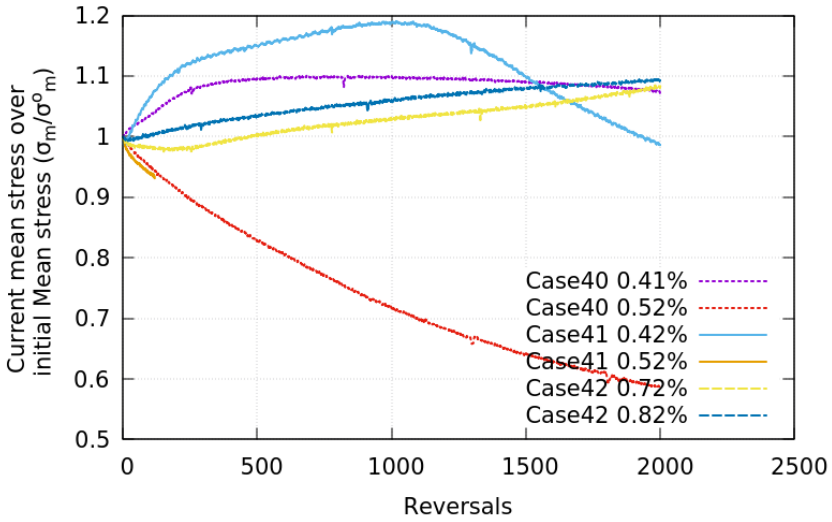

Figure 4.32: Normalized mean stress relaxation in the case samples

phenomenon can be noticed in case specimen 41. A greater amount of negative mean stress was induced at the beginning of the test, presumably by RA transformation, and then in the next phase of the test the relaxation rate increased. The second test at ±0.52% failed early. Case specimen 42 was loaded at a higher strain amplitude. In this case, the magnitude of the mean stress increases continuously in both tests.

Due to the interference of the RA transformation effect with mean stress relaxation, independent stress relaxation measurements cannot be obtained in the through-carburized case material. Unfortunately, implementing the core material mean stress relaxation behaviour into the fatigue model was complicated. Therefore, the mean stress-relaxation

model was not applied to fatigue life prediction.

Chapter 5

Retained austenite (RA) transformation and residual stress estimations

In order to predict the fatigue life of the case-hardened 16MnCr5 composite samples, residual stresses at different depths of the sample have to be determined.

A three-layer FE model and a compatibility model were developed to estimate the initial residual stress in the composite sample generated during the carburization and quenching process based on the carbon profile, temperature field, and final metallurgy phases in the carburized sample.

Quantitative analyses for the strain-induced RA transformation under different types of loading were carried out. A relationship between the cyclic strain applied to the composite sample and the strain expansion imposed in the case layer of the composite sample was determined.

A methodology for including the RA transformation expansion into the residual stress estimate was explored, and the simulated results were compared with the measured residual stress profiles.

Experimentally, the RA content and the residual stress profiles in the composite samples were measured via X-ray diffraction (XRD) techniques using a PROTO LXRD instrument[124]. The XRD beam has a diameter of about 1 mm. The XRD beam consists of a target source of Cr (Kαavg 2.291 Angstroms), and a target power of 25kV, 30mA. The gain material is Beta titanium and the gain power is 24kV, 17mA. No filter was used.

To obtain subsurface measurements, the specimens were electropolished to each targeted depth. After each polish, the depths were measured using a Mitutoyo CV-2000 contracer. All the XRD work was performed by PROTO Manufacturing Ltd.

5.1 Initial residual stress generated by the carburization process

During the carburization process, residual stresses are developed throughout the treated part. In previous studies [89, 88, 126], an ABAQUS subroutine software, DANTE, was used for the prediction of the final microstructure and residual stress in a heat-treated part. Due to financial limitations and the focus of this research, a simplified method was used to determine the final metallurgical phase and estimate the volume change in the finite layers of the sample. Residual stresses in a carburized plate and an axial sample were then estimated using a multi-layer compatibility model and a multi-layer FE model. The strains caused by thermal shrinkage during cooling and by the phase change during transformation were taken into consideration.

The specimens used in this research were carburized at the Material Engineering Lab at Chrysler Technical Center. The retained austenite and volume expansion in the case-core composite plate, as shown in Figure 4.5b, will be analyzed in this section. The carburization process for the composite plate is described in Table 4.2.

Two 25-layer compatibility models, containing a rectangular and a circular cross-section respectively, were developed by applying the force balance rules and compatibility conditions to determine the longitudinal residual stresses in the plate and the smooth specimens. Each layer in the model consists of a unique strain change caused by quenching.

Alternatively, 3-layer FE models were built in ABAQUS to estimate the longitudinal and hoop residual stresses in the plate and the smooth sample.

To validate the simulated results, PROTO[124] measured the longitudinal residual stresses across the depth for the plate and the axial samples, as well as the hoop residual stresses on the surface of the plate at several locations in the stress concentration zone.

In the FE model, the residual stresses at the corresponding areas were evaluated and then compared with the measurements. The longitudinal stress results from the compatibility and FE models were also checked with the measurements.

5.1.1 Carbon profile during carburization

Since the carbon potential values were provided by FCA, and these values can be directly used to model the carbon diffusion process in the component, the chemical reaction at the steel surface can be skipped in this research. The finite difference method (FDM) inspired by the BASIS program in *Surface Hardening of Steels* [26] was applied to estimate the carbon profile of the specimens. A MATLAB program was developed to implement FDM into Equation 2.1 with the boundary condition described in Equation 2.2 and the diffusion coefficient presented in Equation 2.3.

The assumptions made in this analysis include:

1. the carburized surface is flat and infinite in size;
2. the carbon atoms diffuse only in the direction perpendicular to the surface (1D diffusion);
3. the carbon potential in the atmosphere surrounding the steel surface stays constant;
4. the properties in the steel are constant throughout each finite layer;
5. the plate is symmetric along the plane parallel to the flat surface, so that a model of half of the plate thickness is sufficient;

6. the core surface in the model is insulated; and

7. the initial carbon content is the carbon percentage in the steel chemistry shown in Table 4.1.

With the symmetry assumption, half of the plate thickness, 2.5 mm, is modelled in the MATLAB program. Since the carbon content depends on both the carburization time and the depth from the surface, progression with a time step of 15 seconds and layers of 0.1 mm was assigned in the finite difference analysis. Therefore, 360 steps (90 minutes) and 25 segments (2.5 mm) are required to complete the simulation. Figure 5.1 demonstrates the simulated carbon profile results, including the surface carbon content during the carburization process up to 90 minutes (Figure 5.1a) and the carbon profile at various carburizing times (Figure 5.1b).

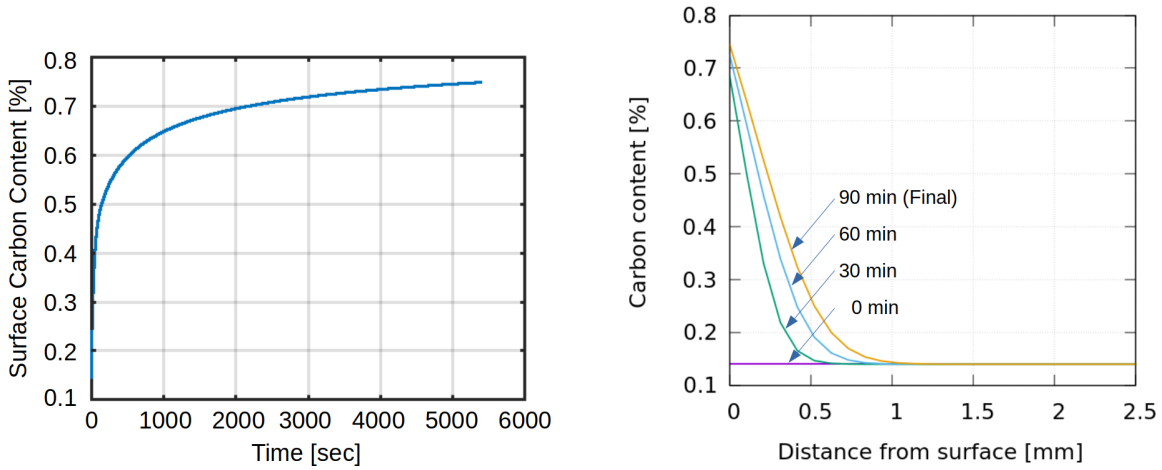

(a) Surface Carbon Content vs. Carburizing Time

(b) Carbon Profile vs. Depth from Surface

Figure 5.1: Simulated carbon profile results using the finite difference model

5.1.2 Temperature field during quenching

FDM was applied to implement Equations 2.4 and 2.5 to model the temperature drop throughout the plate during quenching. The first six assumptions made for the FD model

in Section 5.1.1 also apply in the quenching simulation. An initial part temperature of 843°C (Temp. 2 in Table 4.2) throughout the sample is assumed.

Assuming the temperature in the steel part drops mostly at the quenchant nucleate boiling stage, the flash point temperature of the quenchant is used as the surrounding temperature, T_∞, listed in Equation 2.5. The flash point is usually at least 90°C above the oil temperature being used [44]. Consequently, a T_∞ of 156°C was assumed.

The density and specific heat inputs of 16MnCr5 are dependent on the temperature. They were obtained from Equations 2.6 and 2.7.

The density of the part was calculated based on the initial steel chemistry. Even though the carbon content in the steel changes across the thickness, it was found that the difference in density between a carbon content of 0.14 wt% and 0.7 wt% is less than 1%. Therefore, a constant density is applied across the plate thickness at each time step.

From Figures 2.9 and 2.10, one can conclude that the alloy content in the steel has a significant impact on the thermal conductivity at low temperatures. However, at a temperature above 800°C, the thermal conductivities for most alloys approach to 30 $\frac{J}{mK}$. As a result, an approximated constant conductivity of 28 $\frac{J}{mK}$ is applied in this analysis.

To estimate the heat transfer coefficient, h, as the surface temperature drops, a polynomial equation was fitted to Hasan's experimental heat transfer vs. temperature relationship at a quenchant temperature of 85°C, as shown in Figure 2.11. The fitted curve is plotted with some digitized points on the original curve displayed in Figure 5.2.

The polynomial equation shown in Figure 5.2 was used in the simulation to estimate the surface heat transfer at each time step. At temperatures above 820°C, the polynomial function predicts a negative h. At such temperatures, the heat transfer coefficient was set to 0.0003 $\frac{W}{m^2K}$. This number was calibrated with the transformation diagram system of a quenched shaft presented by Gergely [49]. The simulated results from the FDM are shown in Figure 5.3.

As shown in Figure 5.3a, the surface temperature barely dropped for the first 0.3 second. This corresponds to the missing heat transfer coefficient above 820°C, which is likely related

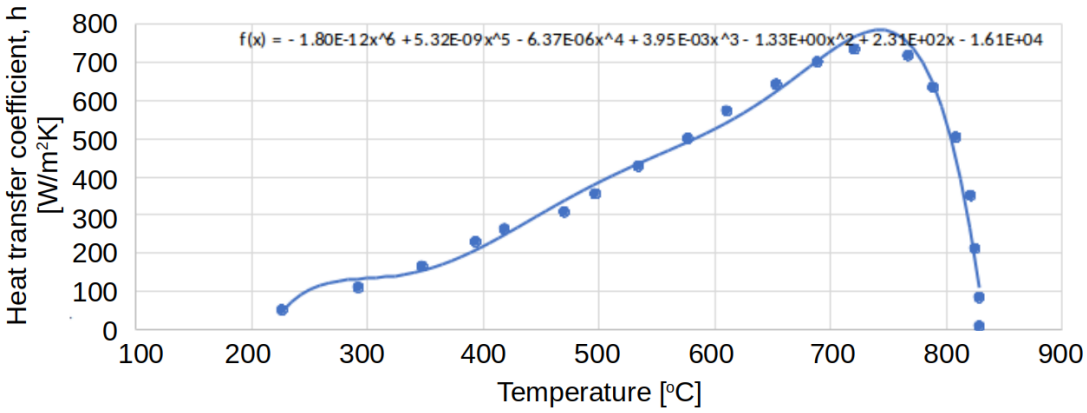

Figure 5.2: Best fitted polynomial for heat transfer coefficient

to the vapour blanket stage. As the steel temperature passes the critical point, a rapid drop occurs. The cooling slows down again as it approaches the quenchant temperature.

From the simulated temperature profile of the sample during quenching, shown in Figure 5.3b, it can be concluded that the temperature throughout the sample drops to the quenchant temperature within two seconds.

5.1.3 Final microstructure in the carburized sample

In order to determine the microstructure phases in the final product, a continuous cooling transformation (CCT) diagram of the original material is required. Figure 5.4 shows a CCT developed by Suwanpinij et al. [143] for 16MnCr5 steel.

Figure 5.4 reveals that the first Bainite particle forms when the Austenite drops below 500°C in over 12 seconds. However, due to the small specimen size, the temperature drops rapidly across the thickness of the researched sample. The temperature in the entire sample dropped below M_s within 2 seconds; therefore, only martensite exists in the final phase after quenching based on the simulated results.

A picture of the core microstructure of the carburized sample was provided by FCA (Figure 5.5) and shows the martensite core, which validates the results from the simulation.

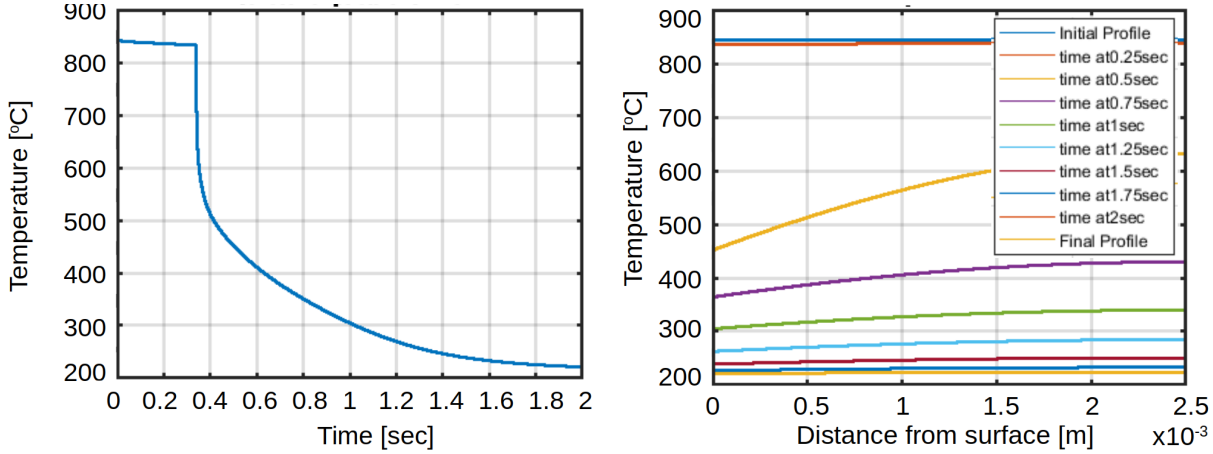

(a) Surface temperature vs. quench time (b) Temperature profile vs. depth from surface

Figure 5.3: Simulated temperature profile results

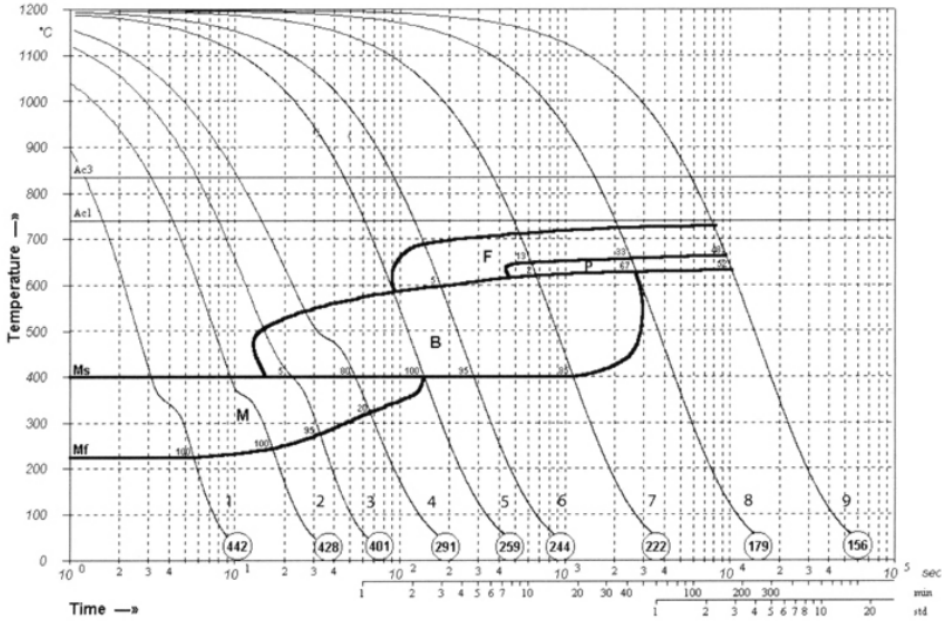

Figure 5.4: CCT diagram of 16MnCr5 steel [143]

The martensite and RA volume fractions after quenching were calculated based on

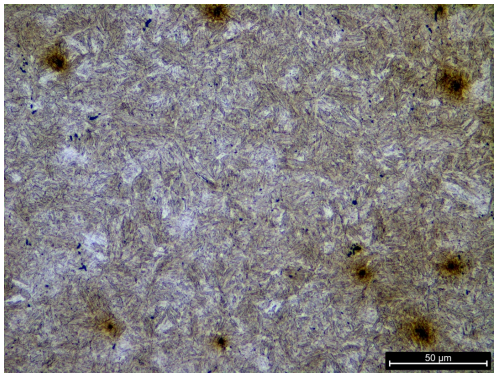

Figure 5.5: Microstructure of the centre core of the carburized sample

Equations 2.8, 2.9, and 2.10 at each layer depth with varying carbon content. The simulated martensite start temperature, M_s, in the material at each layer and the martensite volume fraction across the plate are shown in Figure 5.6. The high carbon content in the case layers reduces the martensite start temperature and causes the core to transfer before the case layer of the composite sample. This results in a compressive residual stress in the case and a balancing tensile stress in the core [127].

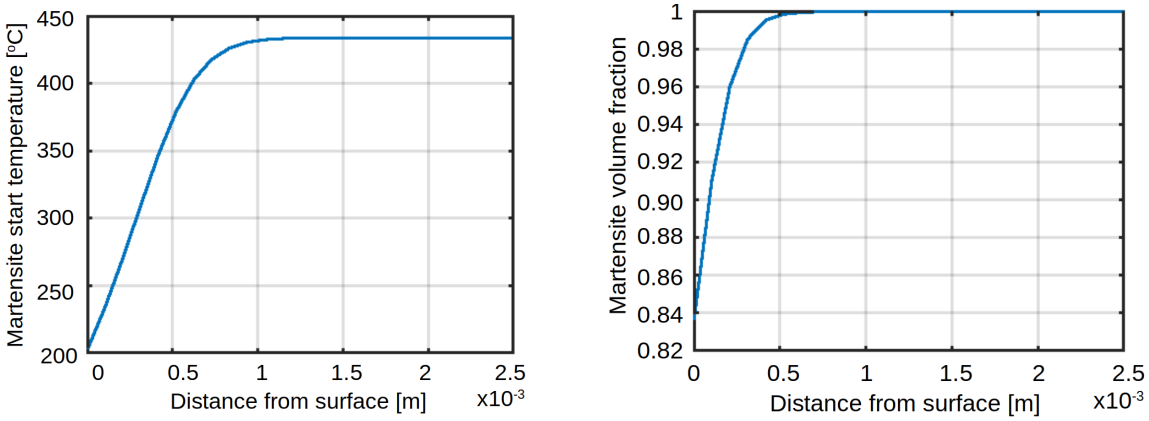

(a) Martensite start temperature profile

(b) Martensite volume fraction profile

Figure 5.6: Simulated martensite fraction

The results shown in Figure 5.6 assumed a quench temperature of 66°C (oil temperature). The martensite volume fraction on the surface is susceptible to the quench tem-

perature; which means that a small change in the quenchant temperature can result in a significant change in surface martensite volume fraction.

Figure 5.7 presents the RA volume fraction comparison of the simulated result and the measurements on the plate sample performed by PROTO. The simulation shows the same trend as the measured data.

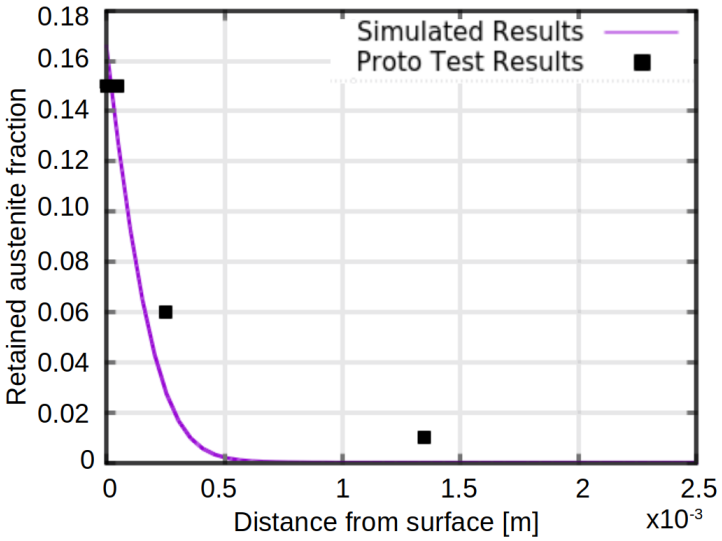

Figure 5.7: Simulated retained austenite data compared with measured data from PROTO

The volume expansion in carburized steel increases with carbon content and the martensite fraction.

5.1.4 Three-layer axial and plate models description

A three-layer compatibility model and a FE model were developed to estimate the residual stress in the carburized plate and smooth specimens.

The carbon content profile and the volume percentage of martensite throughout the carburized plate were determined in the previous sections. To simplify the analysis for the axial samples, the same carbon content profile was employed, while the martensite volume fraction was linearly extrapolated from the PROTO measurements.

In the compatibility model, fully elastic deformation was assumed. In the FE models, the plastic portion of the stress-strain curves were also included as inputs. The material properties for the case and the core layers (listed in Tale 4.3) were obtained from the monotonic tests of the through-carburized case and the simulated core samples. It is worth noting that the compressive and tensile stress-strain curves of the case material show a significant difference. Since the case layer of the sample is mostly under a compressive residual stress, the compressive stress-strain curve was used in this analysis.

In the compatibility models, the plate sample (Figure 4.5b) was simplified as a three-layer plate with a cross-section illustrated in Figure 5.8a, and Figure 5.8b demonstrates the cross-section of the axial sample (Figure 4.4). Table 5.1 lists the input parameters of the three-layer compatibility models. The values of depths and areas indicated in Figure 5.8b and Figure 5.8a correspond to the layer depths and areas shown in Table 5.1.

Table 5.1: Input properties of the 3-layer models

		Layer 1	Layer 2	Layer 3
Plate layer depth	mm	0.31	0.83	-
Plate cross-section area	mm^2	10.73	16.13	37.66
Axial layer depth	mm	0.42	0.94	-
Axial cross-section area	mm^2	6.04	5.97	7.69

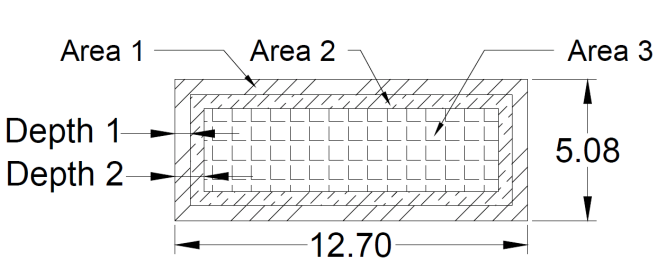

(a) Plate sample model

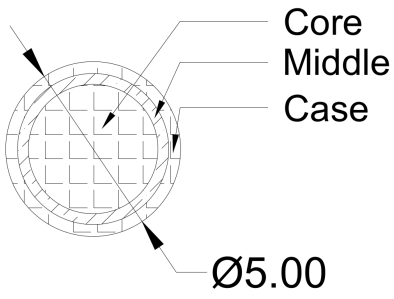

(b) Smooth sample model

Figure 5.8: Cross-section of the three-layer models

5.1.5 Strain change in each layer during carburization

The three approaches introduced in Section 2.3.4 for estimating the strain change induced by phase transformation were examined with the parameters determined in this study. The model that produces the best fitted results to the experimental data was selected for detailed calculations.

Comparison of models for phase transformation induced volume expansion

To test the different volume expansion models for phase transformation, a two-layer compatibility model was applied. A case depth of 0.55 mm was determined at the point of 50 HRC in the case-hardened sample. The carbon contents at two points, 0.208 mm and 2.342 mm from the surface plotted as the final profile in Figure 5.1b, were applied in the residual stress analysis to represent the case and the core layers.

To estimate the residual stresses in the case and the core layers, the changes in strain caused by thermal shrinkage and phase change must be determined. The thermal shrinkage strain magnitudes were subtracted from the expansions caused by phase transformation to obtain the total strain.

In order to compute the thermal expansion coefficient, the carbon content was converted from a weight percentage to an atomic percentage based on the chemical composition of the material. Table 5.2 shows the thermal strain calculated based on the methodology discussed in section 2.3.5.

Table 5.2: Thermal strains of the case and the core layers

		Case 0.208 mm depth	Core 2.342 mm depth
Carbon content	wt. %	0.526	0.140
Carbon content	at. %	2.399	0.648
Thermal expansion coefficient (Eq. 2.13)	K^{-1}	1.03×10^{-5}	1.37×10^{-5}
Thermal strain	mm/mm	-0.0112	-0.0148

Table 5.3: The strain and residual stress results from the three models for phase change induced volume expansion

Source		Thelning (Eq. 2.11)		Cohen (Fig. 2.12)		Moyer (Eq. 2.12)	
Layer		Case	Core	Case	Core	Case	Core
Carbon content	wt. %	0.526	0.140	0.526	0.140	0.526	0.140
Volume expansion	%	71.2	23.4	-	-	3.57	3.33
Phase change strain	mm/mm	0.196	0.0727	0.0062	0.0015	0.0118	0.0110
Quenching Strain	mm/mm	0.185	0.058	-0.0050	-0.013	0.00054	-0.0039
Residual stress	MPa	-16,909	6,720	-1,106	439	-585	232

The three approaches mentioned in section 2.3.4 were attempted and the strain results are listed in Table 5.3. Note that only Thelning's method takes into consideration the retained austenite content. The total strain and the residual stress determined as described in section 2.4 are also included in the table.

By comparing the results in Table 5.3 with the residual stress measurements in the composite sample, it was found that Thelning's approach over predicts the phase change strain, while Cohen's chart under predicts it. The residual stress predicted using the expansion strain calculated by Moyer's equation best matches the measurements. Figure 5.9 compares the calculated residual stress using Moyer's model and the compatibility rule with the measured data.

Total strain change calculation

The strain generated during the quenching process after carburization consists of two mechanisms: thermal shrinkage during cooling and expansion due to phase transformation.

Based on the model comparison described in the last section, Moyer's equation (Eq. 2.12) was selected to calculate the phase transformation expansion. In this analysis, it is assumed that the volume expansion is only caused by the austenite to martensite transformation.

The carbon content and the martensite volume fraction profiles obtained from the previous analysis are the inputs of the quenched strain calculations. For the axial sample

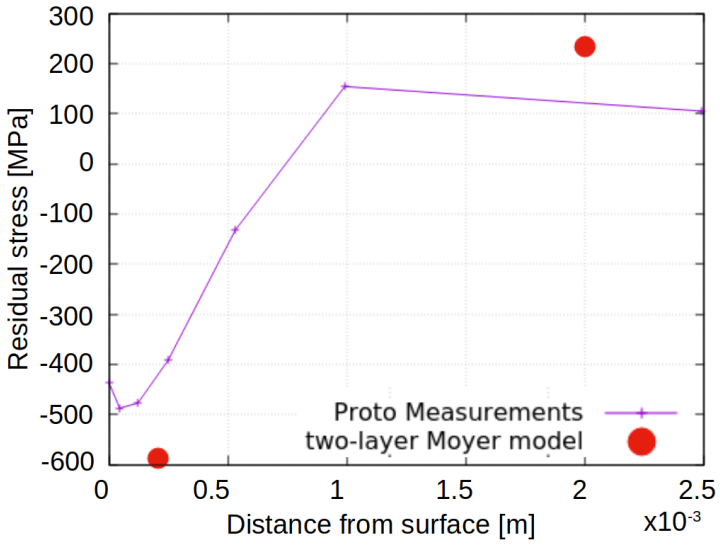

Figure 5.9: Residual stress results comparison for carburized 16MnCr5 plate sample

analysis, the carbon content profile obtained for plate sample was employed, and the retained austenite fraction was linearly extrapolated from PROTO's measurements. Figure 5.10 shows the simulated austenite volume fraction profile for the plate sample and the measured RA volume fraction in the plate and axial samples.

Equation 5.1 calculates the total quenched strain caused by the thermal shrinkage and phase transformation volume expansion. The strain change in each layer depends on austenite and martensite volume fractions. From the carburization microstructure analysis, martensite and austenite are the only two phases that exist in the final stage of the sample after the heat-treatment conducted in this study. The RA profiles of the plate and axial samples are plotted as the blue and green lines in Figure 5.10. The martensite volume fraction can be obtained by subtracting the RA profile from 1.

$$\epsilon_i^Q = [f_M^i \times \beta_M^i + (1 - f_M)^i \times \beta_\gamma^i] \times \Delta T + \sqrt[3]{(f_M^i \times \frac{\Delta V_{\gamma\to\alpha}}{V_\gamma}^i /100 + 1)} - 1 \tag{5.1}$$

where f_M^i is the volume fraction of martensite in layer i, β_M^i and β_γ^i are the thermal

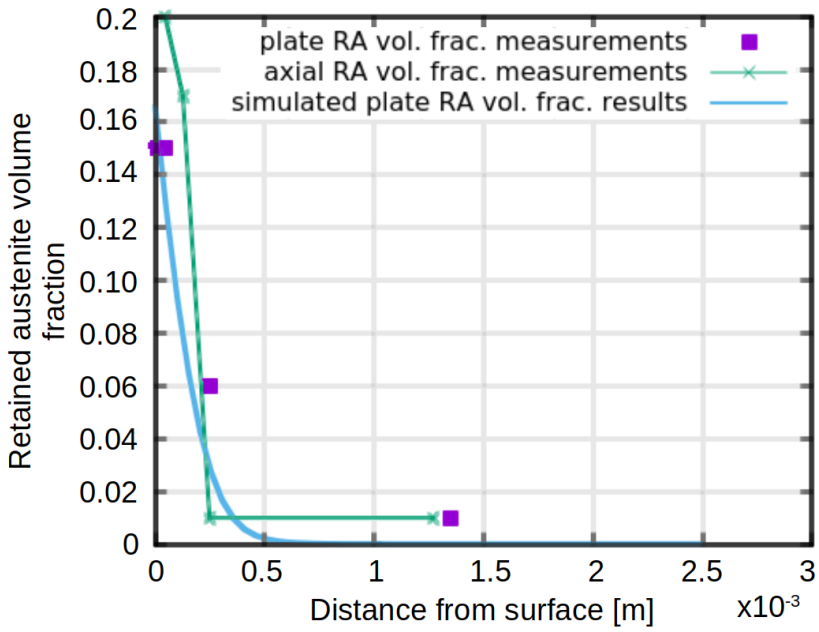

Figure 5.10: Simulated and measured retained austenite volume fraction

expansion coefficients of martensite and austenite as stated in Equations 2.13 and 2.14 in layer i, and $\frac{\Delta V_{\gamma\to\alpha}}{V_\gamma}^i$ is the volume change caused by austenite to martensite transformation described in Equation 2.12.

The quenching strain profiles were generated for the plate and axial cross-sections in a 25-layer model. To convert them to the 3-layer models, the average strain across the depth of the layer was taken. The approximated 3-layer strain values used in the compatibility model for the plate and axial samples are plotted along with the 25-layer profile in Figure 5.11.

Figure 5.11 shows a greater shrinkage strain magnitude on the surface of the axial sample (Figure 5.11b) than that on the plate (Figure 5.11a). From Figure 2.13, one can observe that, austenite has a larger thermal expansion coefficient than martensite, thus, it shrinks more under cooling. Additionally, it was assumed in this analysis that, unlike martensite, RA does not expand during quenching. Combining the two factors mentioned above, a high RA volume fraction in the sample would result in a high shrinkage strain.

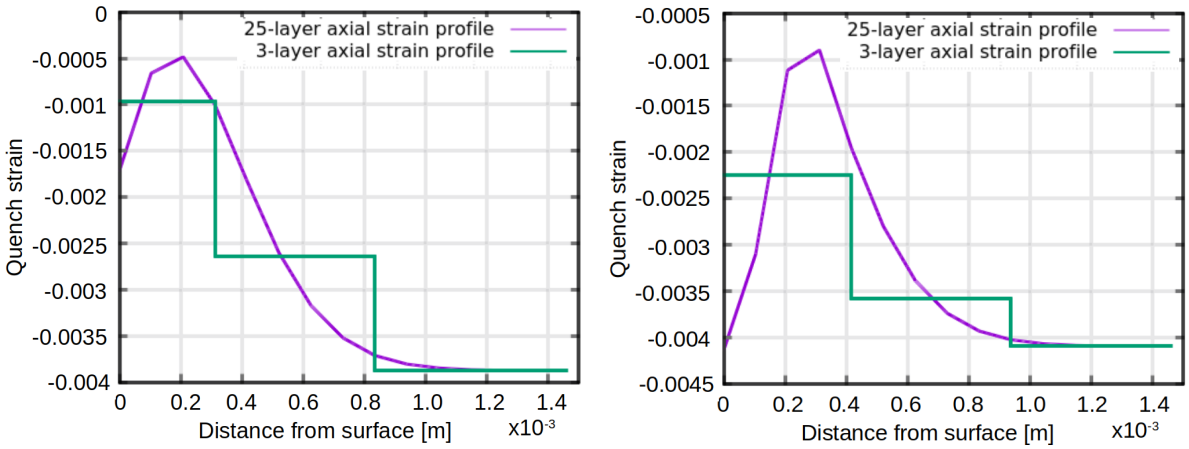

(a) Plate sample

(b) Axial sample

Figure 5.11: Quench strain profiles for the 3- and 25- layer models for the plate and axial samples

As shown in Figure 5.10, the retained austenite volume fraction in the surface layer of the axial sample is higher than that of the plate, which causes more shrinkage in the axial sample than the plate.

5.1.6 Finite element (FE) residual stress model

Three-layers ABAQUS models were used to estimate the residual stresses in the longitudinal and hoop directions in the axial and plate samples.

The stress-strain curves for the case, middle and core layers plotted in Figure 4.26 are the material inputs of the ABAQUS model.

In the plate model, the stress concentration zone near the centre notch was partitioned into multiple circles, so that the area of interest can be meshed with systematic hexahedral elements. The other sections were meshed with either hexahedral or tetrahedral elements, depending on the geometry complexity. On the other hand, the regularity of the 3-layer axial sample made it easy to mesh with hexahedron elements throughout the sample. All elements used in the FE models are quadratic.

The meshed samples and the boundary conditions are shown in Figure 5.12. An element size of 0.6 mm was applied to case and middle layers of the axial model, and 0.8 mm for the core layer. Near the stress concentration zone at a single layer of the plate sample, each meshed circle contain 48 elements. Tie constraints were employed between layers. The top surface is subjected to fixed boundary conditions in all directions.

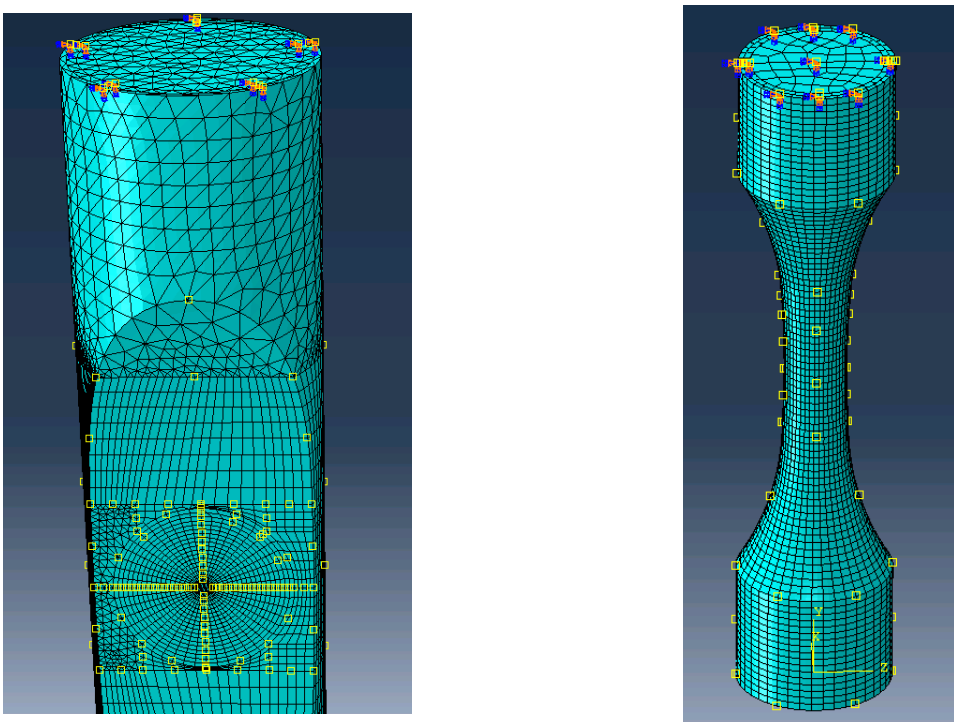

(a) Plate sample

(b) Axial sample

Figure 5.12: Meshed samples and their boundary conditions

Figure 5.13 depicts the cut sections of the analyzed models showing the longitudinal residual stress contour. To compare the simulated results with PROTO's measurements, the residual stress profiles were obtained along a path in each of the models. These paths are displayed in Figure 5.13.

Initially, the three-layer thermal strains shown in Figure 5.11 were used as the predefined input in the ABAQUS models. For each layer, a thermal expansion coefficient of 0.01 times

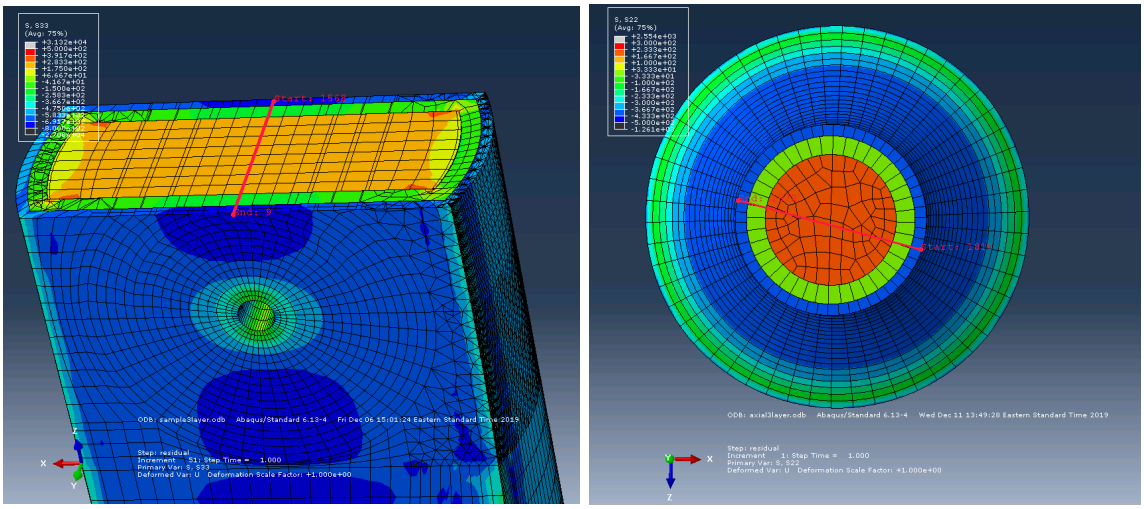

(a) Plate sample (b) Axial sample

Figure 5.13: Cross-section cut of the ABAQUS model showing the longitudinal residual stress in contour and the path taken (plotted in red) for the simulated stress profile

Table 5.4: Expansion coefficients and temperature change inputs for the ABAQUS models

	Layer 1	Layer 2	Layer 3
Plate expansion coefficients	-1.70E-05	-2.64E-05	-3.50E-05
Axial expansion coefficients	-2.54E-5	-3.58E-5	-3.90E-5
Temperature change	100	100	100

the quench strain was employed and a temperature change of 100 degree C was applied to generate the same resulting strain as the quench strain. However, as shown in Figure 5.14, the residual stresses generated from the 3-layer ABAQUS model do not reflect the measurements well. The simulated results over predicted the actual residual stress.

The thermal expansion coefficients in each layer were then manipulated until the initial residual stress profiles in the FE models match those from the compatibility models. The final thermal coefficients and other inputs of the ABAQUS models are listed in Table 5.4.

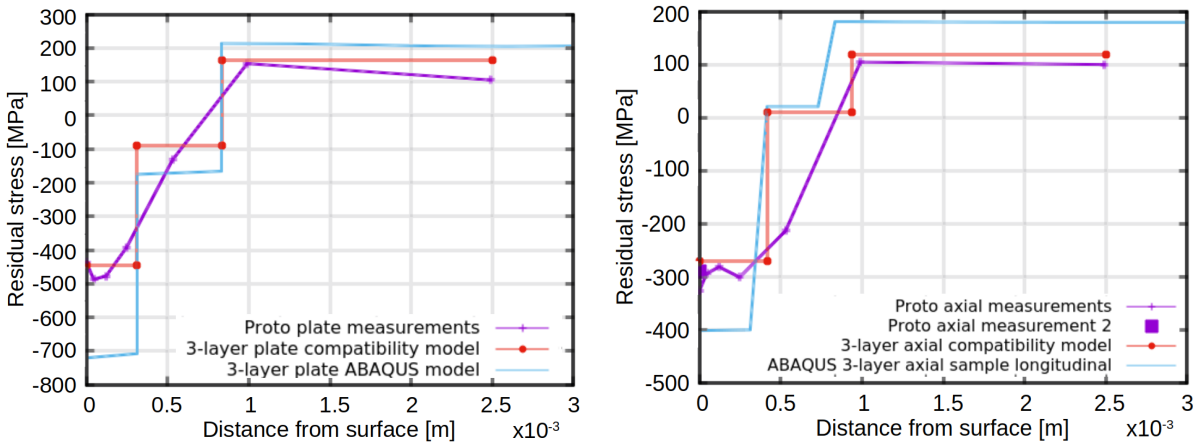

(a) Plate sample initial ABAQUS results

(b) Axial sample

Figure 5.14: Initial ABAQUS residual stress results using the quench strain plotted in Figure 5.11 as inputs for the plate and the axial models

5.1.7 Simulated initial residual stress results validation

By calculating the cross-sectional area for each of the 25 layers, and using the 25-layer quench strain profiles of the axial and the plate samples (Figure 5.11) as inputs for the compatibility model, the initial residual stress profiles plotted in Figure 5.15 were obtained.

In Figure 5.15, the plate residual stress profile of the 25-layer compatibility model matches that of the measurement results well. A drop in compressive residual stress on the surface can be observed in both profiles. The trend in the compatibility model is a replica of the quenched strain profile shown in Figure 5.11. The drop in the magnitude of shrinkage strain on the surface of the plate sample leads to the lower compressive residual stress value.

The axial compatibility model also predicted a drop of residual stress on the surface of the axial sample which differs from the measurement. The source of errors might come from the assumption of the same carbon profile in the plate and axial samples. Nevertheless, a three-layer model was later employed to estimate the residual stresses (Figure 5.16b).

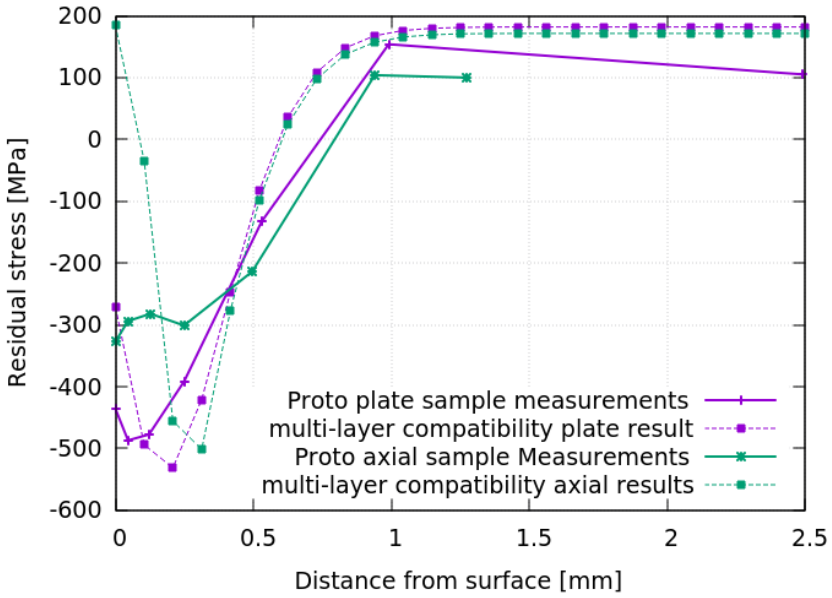

Figure 5.15: Results of the 25-layer axial and plate compatibility models and measured results

The results from the three-layer axial and plate compatibility models were obtained with the three-layer quenched strain profiles shown in Figure 5.11a and Figure 5.11b. The elastic modulus and the cross-sectional area inputs are listed in Table 5.1. The compatibility model methodology described in Section 2.4 was applied.

The three-layer ABAQUS model was simulated using the expansion coefficients and temperature changes listed in Table 5.4. After calibrating the longitudinal residual stress profiles of the axial and plate samples in the ABAQUS model with the compatibility model and the measurements, the ABAQUS model can then evaluate hoop stress in the sample and the longitudinal stress near the stress raiser zone.

The longitudinal residual stress results of the three-layer compatibility model and the FE models are compared with the measured residual stress profiles in Figure 5.16.

In addition to the longitudinal residual stress profile distance from the stress concentration zone, PROTO also measured the longitudinal and hoop residual stresses on the surface of the plate around the notch. The location of the measurements are drawn in

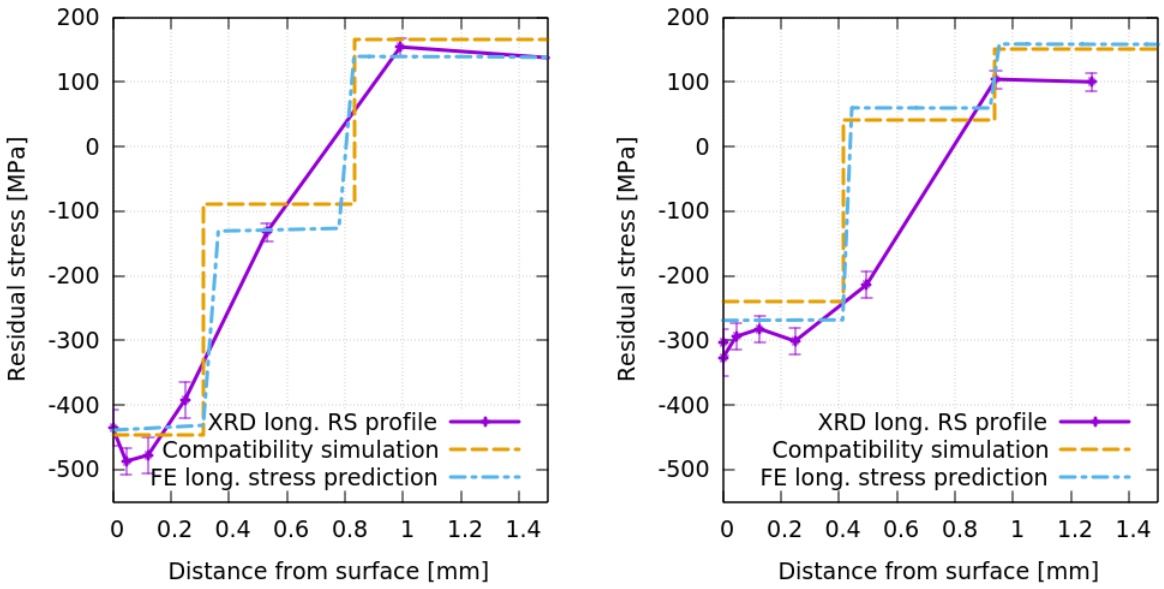

(a) Plate sample

(b) Axial sample

Figure 5.16: Longitudinal residual stress profile comparison of the three-layer compatibility and ABAQUS models for the axial and plate samples

Figure 5.17.

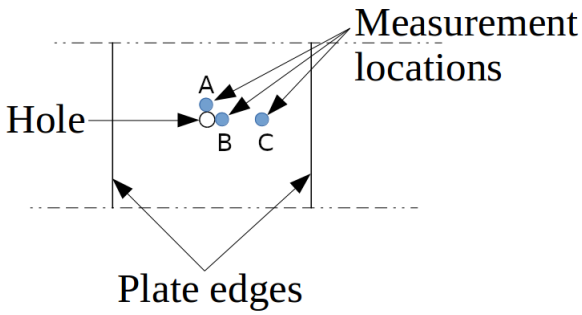

Figure 5.17: Residual stress measurement locations in the plate surface

The residual stresses in the longitudinal and hoop directions at these locations of the plate were obtained from the ABAQUS model. Figure 5.18 shows a comparison between the residual stress profiles generated in ABAQUS and the XRD measurements. Also included

is the hoop residual stress in the axial sample.

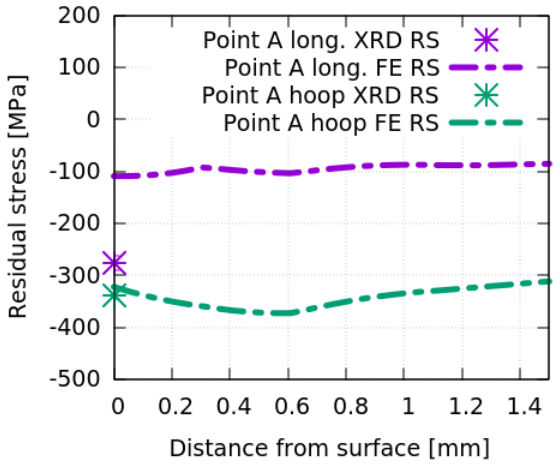

(a) RS profile along plate thickness at Point A in Figure 5.17

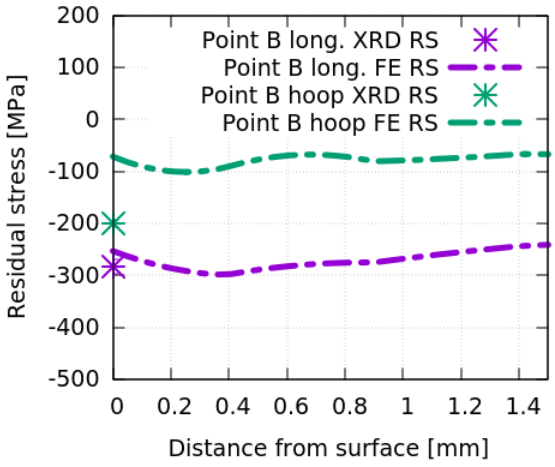

(b) RS at profile along plate thickness Point B in Figure 5.17

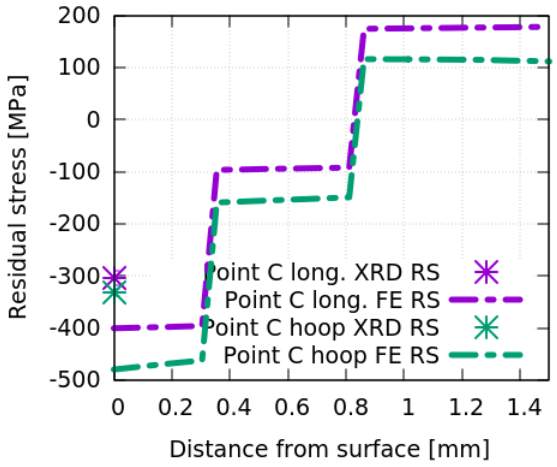

(c) RS profile along plate thickness at Point C in Figure 5.17

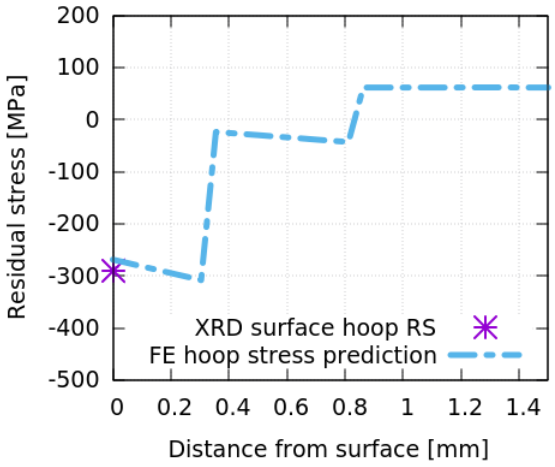

(d) Hoop RS profile along the diameter in the axial samples

Figure 5.18: Comparison between ABAQUS and measurement results of the longitudinal and hoop residual stresses at the stress-concentration zone in the notched plate and the hoop residual stress in the axial sample

Comparing Figures 5.18a and 5.18b for the residual stresses above and on the right of

the notch, the longitudinal residual stress at Point A has a lower magnitude than the hoop stress at this point, and vice versa for Point B. This can be explained by the location of the measured points. Point A is near the top of the notch, free of longitudinal constraint, thus resulting in a lower longitudinal residual stress. Point B is on the right side of the notch, where the lateral constraint could be minimal.

Figure 5.18d shows that the hoop stress on the surface of the axial sample was accurately estimated from the ABAQUS model. The FE estimates of residual stress near the notch of the composite plate, shown in Figures 5.18a to 5.18c, are also reasonably close to the measurements. The relativity of the longitudinal and hoop residual stresses were accurately predicted in the ABAQUS model.

5.2 Strain-induced RA transformation studies

Tension and compression tests were performed on the case and the composite specimens. To obtain the amount of RA transformed under different loading cases, the RA was measured on several tested and untested samples.

The transformation of RA induces a volume expansion that is reflected in the stress-strain curves. Under tensile loading, the sample with an RA transformation shows a higher strain at the same stress level compared to the one without an RA transformation and vice versa, a smaller strain was observed under compression in the sample with RA transformation .

5.2.1 RA transformation in the through-carburized case material

A through-carburized case sample was strained to 0.7% in tension, and another to -1.0% strain in compression. The stress-strain curves of those two tests are plotted in Figure 5.19 along with the tensile curve from a deep-freeze sample, which was cold treated in dry ice at approximately -78^{o}C and contains minimal austenite. Similar to Neu's [111] and Richman's [128] results, an asymmetry was observed in the tension and the compression

stress-strain curves in the through-carburized material with the tension curve lying below the compression curve.

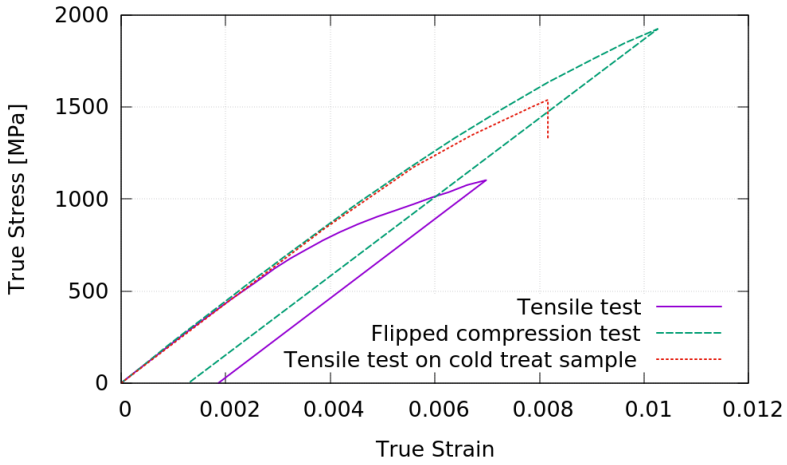

Figure 5.19: Tensile (0.7% strain) and compressive (-1.0% strain) stress-strain curves for the through-carburized case sample and that for the tensile test of a deep-freeze case sample

Using the tensile test of the deep-freeze sample which has no RA transformation as a reference, the tensile stress-strain curve of the normal through-carburized case sample shows a lower yield stress, and that for the compressive test shows a slightly higher yield stress. This suggests that as reported in [111] much more RA transforms under tension straining than under compression straining. Moreover, all three curves overlap in the elastic region but deviate with the onset of plastic straining. This indicates that the RA transformation was induced by plastic deformation [116, 135, 147, 103, 137, 48] in the through-carburized case sample.

Figure 5.20 shows the RA content in two of the through-carburized samples. One was loaded to 0.7% strain and the other was untested. The measurements were taken at a depth of 0.5 mm and at the center of the specimens to eliminate the effect of the IGO zone.

It is shown that the RA content in the case sample dropped from 16.1% to 11.2% at the depth of 0.5 mm after the 0.7% tensile strain loading.

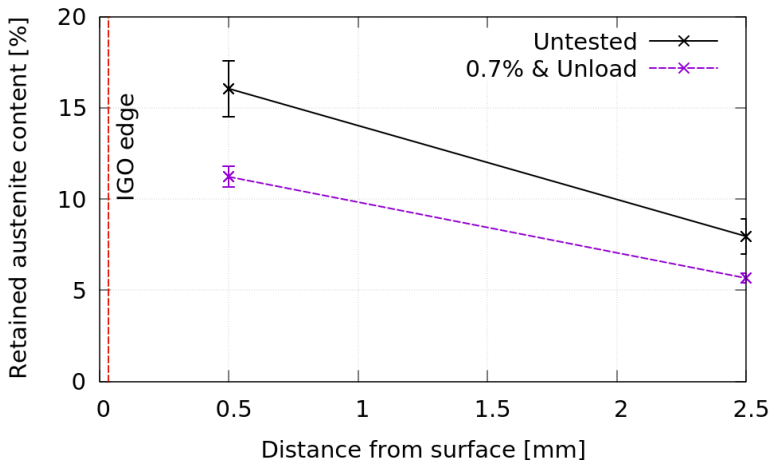

Figure 5.20: RA content measured after a tensile (0.7% strain) load compared to an untested sample in the through-carburized case axial samples

5.2.2 RA transformation in the case-hardened composite material

For the smooth case-hardened composite specimen, the tension and compression tests were strained to 1.0% and -1.0%, respectively. Figure 5.21 shows the stress-strain curves of the two tests together with the tensile test of a deep-freeze sample.

For the case carburized composite sample, the tensile stress-strain curve falls below the curve for the deep-freeze sample while the compressive stress-strain curve lies a little above that for the deep-freeze sample.

Figure 5.22 shows the initial RA content profile and the RA profiles after the tension and compression tests of the composite samples. The measurements show that an RA transformation occurred in both the tension and compression tests and a greater amount of RA decomposed under tensile loading than under compressive loading.

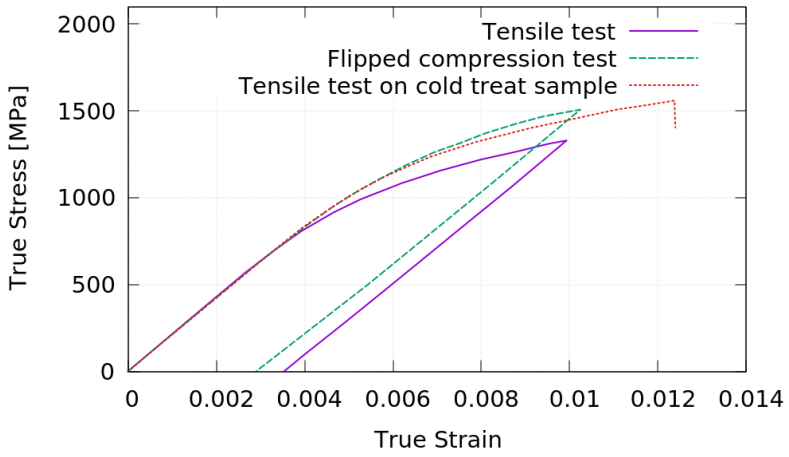

Figure 5.21: Tensile (1.0% strain) and compressive (-1.0% strain) stress-strain curves for the case-hardened composite sample and that for the tensile test of a deep-freeze composite sample

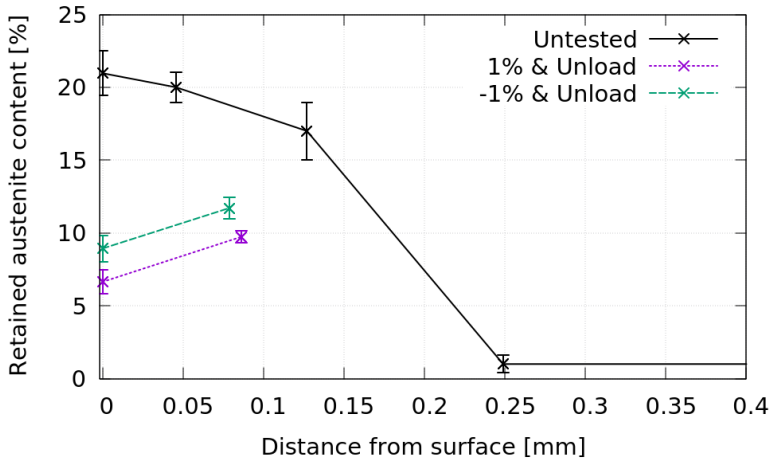

Figure 5.22: RA content measured after tensile and compressive loads compared to the initial values in the case-hardened axial composite samples

5.2.3 Discussion of test results

The stress-strain curves in Figures 5.19 and 5.21 show that the RA transformation begins with the onset of plastic deformation as was reported by a number of other researchers

[116, 135, 147, 103, 137, 48].

By comparing the differences between the RA content in the untested and the tensile loaded samples in Figures 5.20 and 5.22, one can observe that more RA transformed in the composite sample ($\sim 10\%$) than in the case sample ($\sim 5\%$).

The carburization process and the strain-induced RA transformation cause compressive residual stresses in the case layer of the composite specimens. This compressive residual stress exists both in the longitudinal direction and in the hoop direction. These biaxial stresses result in a higher shear stress in the case layer of the composite specimen than in the through-carburized specimen. When both are strained in the longitudinal direction a higher shear stress is exerted upon the case layer of the composite sample compared to that exerted on the through-carburized case sample due to the compressive residual stress in the hoop direction. Since an RA transformation is related to the amount of plasticity the material undergoes, the high shear that causes an early yield could explain the high RA transformation in the case layer of the composite sample.

5.3 Stress-strain behaviour and the post-loading residual stress of the composite sample

Smooth case-hardened samples were subjected to one of four strain controlled histories, as displayed in Figure 5.23, to study the changes in the RA and residual stress due to fatigue cycling.

5.3.1 FE model description

A three-layer FE model similar to that described in Section 5.1.6 was applied here with the same material inputs and initial boundary conditions.

However, in this simulation, only a quarter of the axial sample was modeled using the symmetric boundary conditions to save computation time. Quadratic hexahedral elements

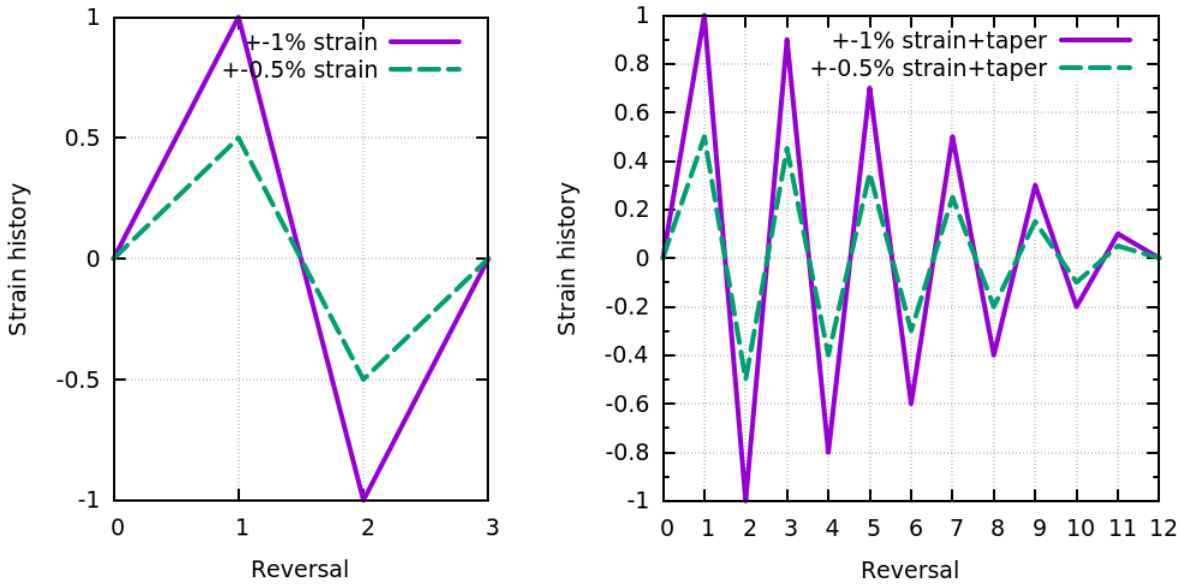

(a) The one cycle loading cases

(b) The one cycle plus taper loading cases

Figure 5.23: Strain histories of four load cases

were used in the 3D FE model. The edges of the elements in the outer layers are less than 0.6-mm long, and those in the middle and inner layers are up to 0.8 mm. Tie constraints were employed between layers. Displacements are assigned on one of the two grip end surfaces, while the other surface is fixed. The constrained fields are remote from the gauge section so that the stress concentration zone induced by the boundary conditions does not affect the simulated results in the gauge section. Iterative trials were run to determine the displacement values to achieve the proper strain change in the gauge section. Figure 5.24 shows a screenshot of the ABAQUS model.

To obtain an equivalent strain of the composite sample measured by the extensometer with a gauge length of 8 mm, two points that are 8 mm apart in the ABAQUS model were used to calculate the relative displacements for the strain calculations. The surface strains, at points A and B in Figure 5.25a, are identical and used to plot the simulated stress-strain curves. The simulated stress was acquired as the average stress along the y-axis of the cross-section at the middle of the gauge section. The residual stress profiles

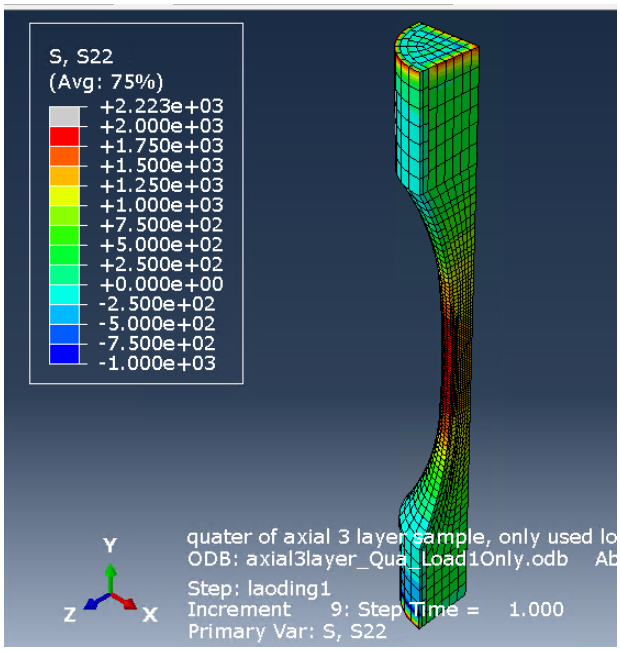

Figure 5.24: ABAQUS model

were collected along the path illustrated in Figure 5.25b

To simulate the volume expansion caused by the stress-induced RA transformation, the temperature in the case layer was altered in the first loading reversal to achieve the desired final longitudinal residual stress profile. Since negative coefficients of expansion were used initially (listed in Table 5.4), negative temperature changes correspond to expansion. The temperatures in each layer during the four different loading scenarios are listed in Table 5.5.

5.3.2 Compatibility model description

The same three-layer compatibility described in Section 5.1.4 was employed to predict the stress-strain behaviour and the post-loading residual stress profile in the composite axial sample. In the compatibility MATLAB model, the total force in the composite sample was calculated using Equation 2.15, knowing the mechanically loaded strain.

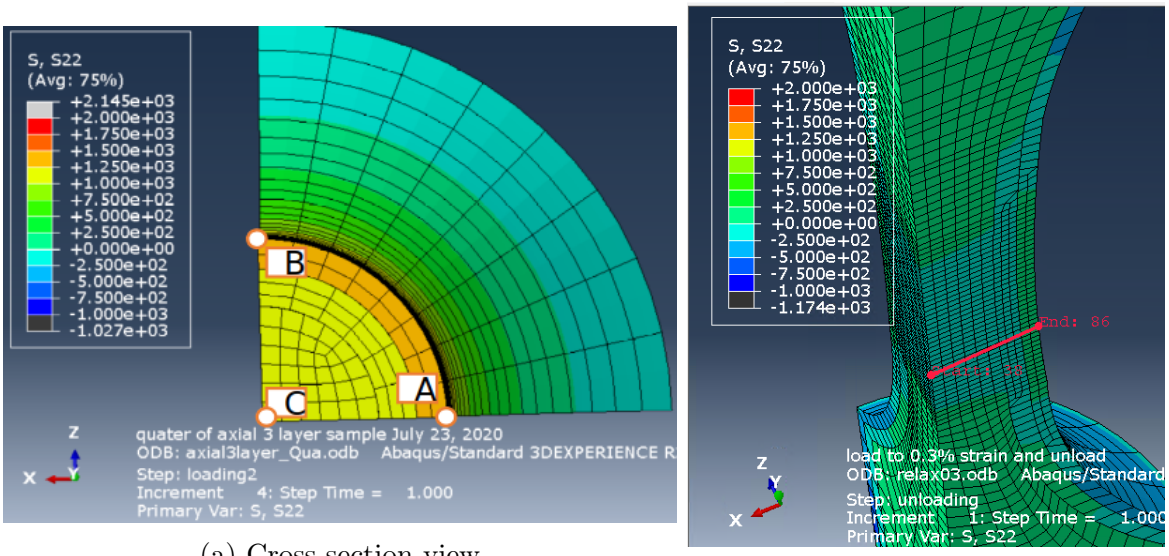

(a) Cross-section view

(b) Residual stress path

Figure 5.25: Details of the ABAQUS model of composite axial sample (legends show the contour palettes for longitudinal stress in MPa)

Table 5.5: Temperatures assigned to account for the RA transformation induced strain under loading in the ABAQUS model

	Temperature $[^oC]$		
Load case	Case	Middle	Core
±1% strain	-90	100	100
±0.5% strain	10	100	100
±1% strain +taper	-120 [a]	100	100
±0.5% strain +taper	10	100	100

[a] Temperature was set at -90^oC in the 1st cycle and -120^oC in the 2nd cycle

The effect of RA transformations is included in the compatibility model by extrapolating the measured data. PROTO used XRD to obtain the RA content in the case layer of the composite sample after each of the loading scenarios. With these measurements, the amount of RA decomposed under each loading sequence can be determined.

The transformation induced strain was calculated assuming an isotropic face-centered

cubic (FCC) to body-centered cubic (BCC) structure change during the austenite to martensite transformation. The transformation strain in the case layer was then converted to a modified initial residual stress as a material input.

Both the FE model and the compatibility model have some advantages and drawbacks. The FE ABAQUS model accounts for the multi-axial stress and predicts the material yield using the Mises yield surface. It also applies a kinematic hardening model while simulating the cyclic behaviour. However, an iterative process was needed to determine the appropriate combination of the temperature with the expansion coefficient inputs in each layer, in order to obtain the residual stress caused by RA transformation.

On the other hand, the compatibility model also predicted reasonably accurate longitudinal residual stress results. The inputs of the model are purely derived from measurements. Moreover, the model is based only on basic mechanics theories. Nonetheless, this simplified model only considers the stress in the loading direction.

5.3.3 Evaluating the RA transformation induced strain change for the compatibility model

Austenite has an FCC crystal structure. When austenite transforms to martensite under stress, a body-centred tetragonal structure (BCT) forms. The change in crystal structure during the transformation leads to a volume expansion and alters the residual stress in the case-hardened composite sample.

The RA content before and after the four load cases, presented in Figure 5.23, were measured using XRD and plotted in Figure 5.26.

A greater amount of RA transformed under the +-1% strain cycle than the +-0.5% cycle. The tapered history following the initial load cycle further decomposed the RA. Yet, the amount of austenite transformed under the tapered loading following the first cycle is trivial compared to the amount transformed during the first cycle.

The predicted carbon content on the surface of the case-hardened sample is about 0.75% after carburization (Figure 5.1b). With such a low carbon percentage, the c/a ratio

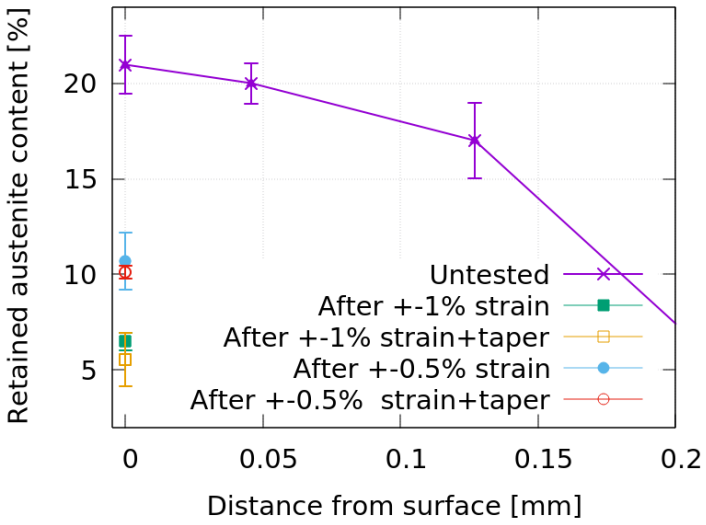

Figure 5.26: Initial and post-loading RA content measured by XRD

of the BCT approximates to 1.0, which is almost equivalent to a BCC structure [138, 32]. Therefore, in this analysis, a crystal structure change from FCC to BCC is assumed in the volume expansion calculation.

The amount of RA transformed during the corresponding load case can be determined from Figure 5.26 by subtracting the post-loading RA content from the initial value. Figure 5.22 indicates that the initial RA content in the composite sample drops to a negligible amount at the a depth of 0.25 mm. The case layer in the model is about 0.4 mm thick (Figure 4.2). Therefore, the strain change due to RA transformation is assumed to only occur in the case layer.

The transformation induced strain changes for each load case are listed in Table 5.6. These strains were added to the initial quench strain in the case layer of -0.224% (Figure 5.11b); so that, the initial residual stress is modified to account for the RA transformation.

Table 5.6: Transformation induced strain in the case layer for each load case

Load case	Transformed RA [%]	$\Delta\epsilon$ [%]
±1% strain	13.5	0.37
±0.5% strain	9.3	0.25
±1% strain +taper	14.4	0.39
±0.5% strain +taper	9.9	0.27

5.3.4 Stress-strain behaviour of the case-hardened sample

Figure 5.27 compares the measured and simulated stress-strain curves for one cycle of +-1% and +-0.5% strain loading for the two axial samples.

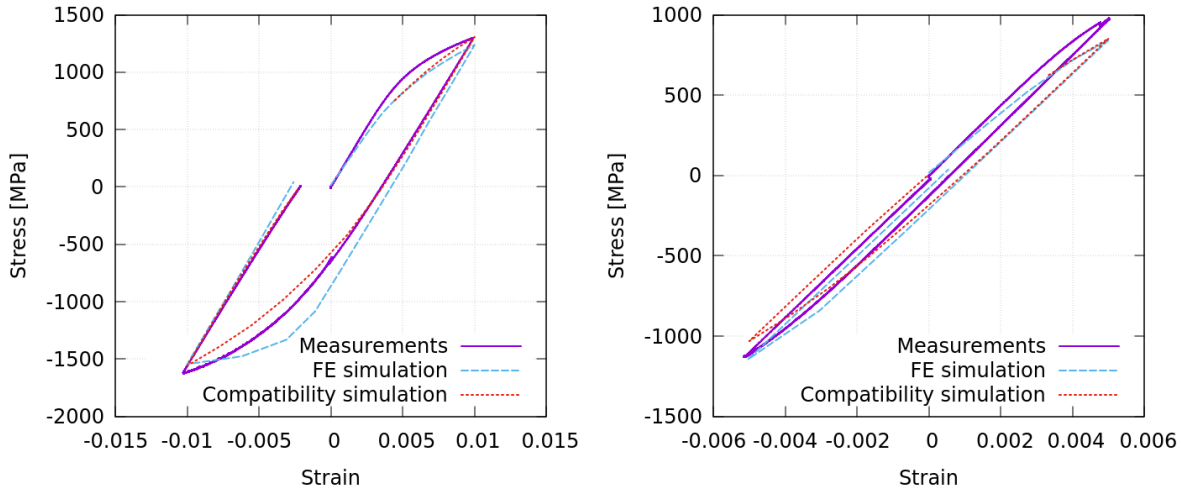

(a) +-1% stress-strain curve

(b) +-0.5% stress-strain curve

Figure 5.27: Comparison of the simulated and measured stress-strain behaviour for +-1% and +-0.5% strain cycles of the smooth composite sample

Asymmetric behaviour, with a higher peak stress in compression than in tension, was predicted by the models in both tests. In the models, the input material stress-strain behaviours are symmetric. Therefore, the asymmetric behaviour, in terms of peak maximum or minimum stresses, predicted from the models is caused by the residual stresses in these case-hardened samples.

For the +-1.0% strain test, the compressive peak stress measured in the experiment is higher than that of the simulated results. This is likely owing to the biased stress-strain behaviour in the case material.

In the +-0.5% strain test, the FE and compatibility models overlap each other on the tensile side, but the FE model shows a higher stress on the compressive side and predicts a behaviour closer to the experimental results. By considering the residual stress in the hoop direction, the FE model predicts a higher yield stress under compression.

The stress vs reversal data for loading histories with a taper (strain sequences shown in Figure 5.23b) are plotted in Figure 5.28. The results indicate that the uniaxial com-

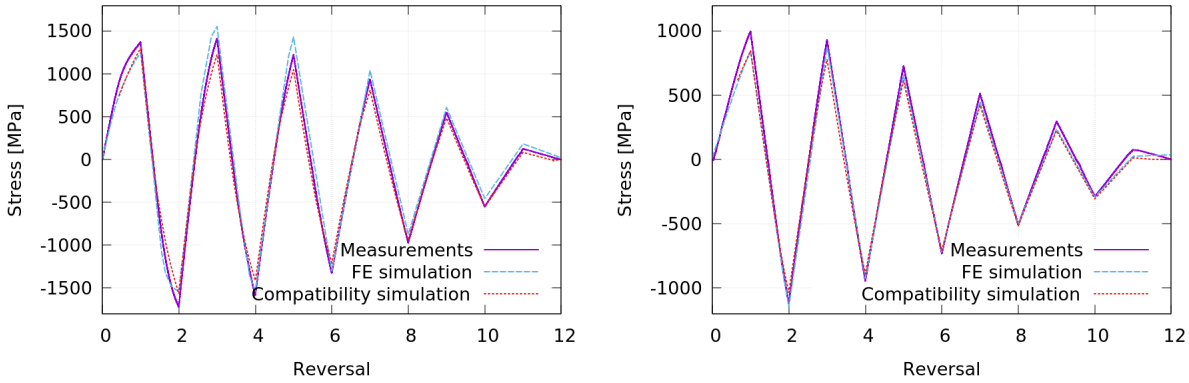

(a) +-1% strain cycle + taper

(b) +-0.5% strain cycle + taper

Figure 5.28: Stress and strain vs reversal graphs for loading histories with taper

patibility model underestimated the peak stresses. In contrast, the FE model is able to capture the hardening behaviour after the 1st load cycle. Yet, the difference in peak stresses between the two models and the experimental results are not significant.

5.3.5 Post-loading residual stresses

Due to the different stress-strain behaviours in the case, core and middle layers, residual stresses would be generated once the core layer deformed plastically, even without an initial

residual stress [162]. Therefore, the loading sequences shown in Figure 5.23 will alter the initial residual stress.

After each of the four tests (Figure 5.23), residual stresses across the gauge section were measured by XRD. Figure 5.29 shows a comparison between the measured and the simulated longitudinal residual stress profiles. The initial residual stress profile was also plotted in the same figure for reference purposes.

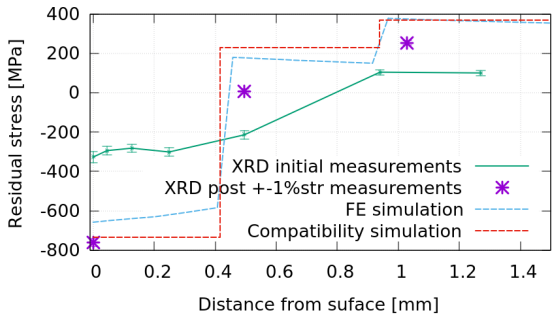

(a) After +-1% strain

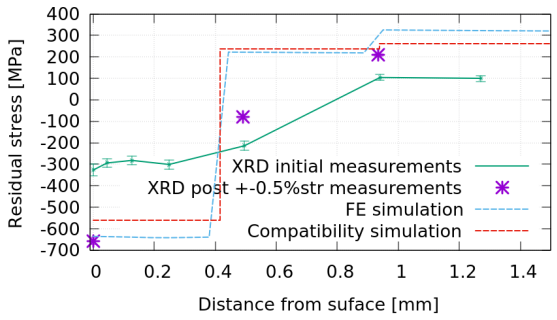

(b) After +-0.5% strain

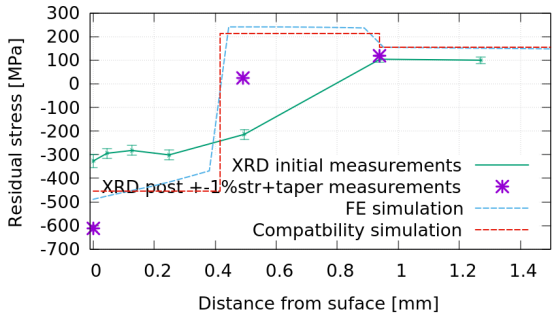

(c) After +-1% strain +taper

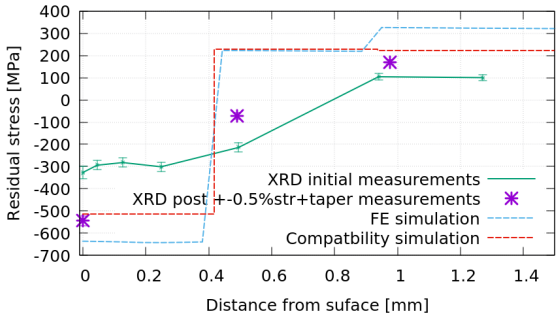

(d) After +-0.5% strain +taper

Figure 5.29: Comparison of the simulated and tested residual stress profiles after loading

As the RA in the case layer of the composite sample transformed under stress, the compressive residual stress on the surface of the sample increased in magnitude. This phenomenon is similar to what Morris and Jeddi [101, 65] found in other case-hardened materials.

The residual stress results shown in Figure 5.29 demonstrate that the compatibility model is able to capture most of the features in the change of longitudinal residual stresses.

This means that accounting for the strain change induced by RA transformation as modified initial residual stresses is feasible.

5.4 RA transformations under cyclic load

RA content was measured in multiple composite axial samples to determine the RA transformation after different loading sequences. The RA measurements were made after the loading sequences listed below:

- Unloaded
- 1 cycle of ±1% strain
- 1 cycle of ±0.5% strain
- 13 cycles of ±1% strain (around a quarter of the estimated final fatigue life)
- 10,000 cycles of ±0.5% strain (around a quarter of the estimated final fatigue life)
- ±0.90% strain until failure
- ±0.34% strain until failure

Figure 5.30 reveals the RA content in the composite samples loaded under the above sequences.

A significant amount of RA was transformed under the loading sequences mentioned above. By comparing the RA in the samples loaded to 1 cycle of the 0.5% and the 1.0% strain amplitudes to that loaded to a quarter of their fatigue lives, one could conclude that most of the RA transformed in the first few cycles, while the following cycles still contribute to minor amount of RA transformation.

The remaining RA contents in the fractured 0.9% and 0.34% samples are higher than those in specimens loaded to quarter lives at 1.0% and 0.5%, respectively. This proves that

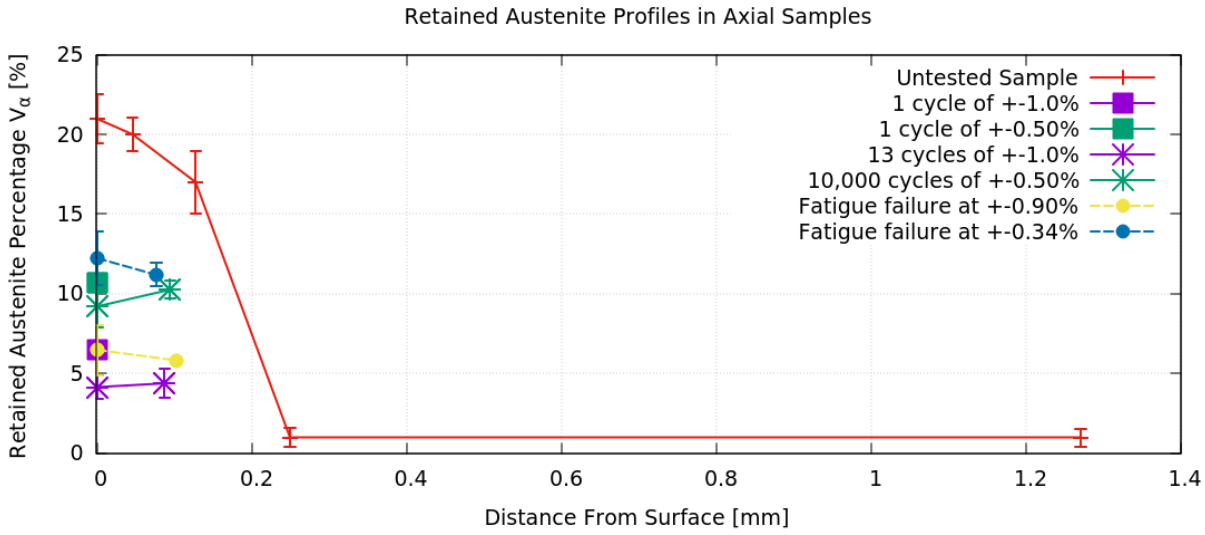

Figure 5.30: RA profile for samples loaded under different histories

the strain amplitude is a major factor in the RA transformation. In order to determine the change in residual stress caused by RA transformation under cyclic loading, the relationship between the RA transformed and the applied load needs to be established.

The amount of RA transformed under cyclic loading can be better visualized in Figure 5.31, in which the RA content vs the number of cycles is plotted for 1% and 0.5% strain amplitude loading. The RA content measured after one cycle and a quarter-life of CA loading are shown.

It is more evident in this figure that most RA transformed in the first cycle of loading, especially at 0.5% strain amplitude.

The carburizing and quenching procedure induces a hoop residual stress in addition to the longitudinal stress in the case layer of the composite sample. The compressive hoop residual stress caused early yielding in the case layer under a tensile load, promoting an RA transformation. Therefore, Von Mises stresses and the equivalent plastic strain (PEEQ) are considered as the independent variables for RA transformation in this study.

The Von-Mises stress and the PEEQ in the case layer of the composite sample were

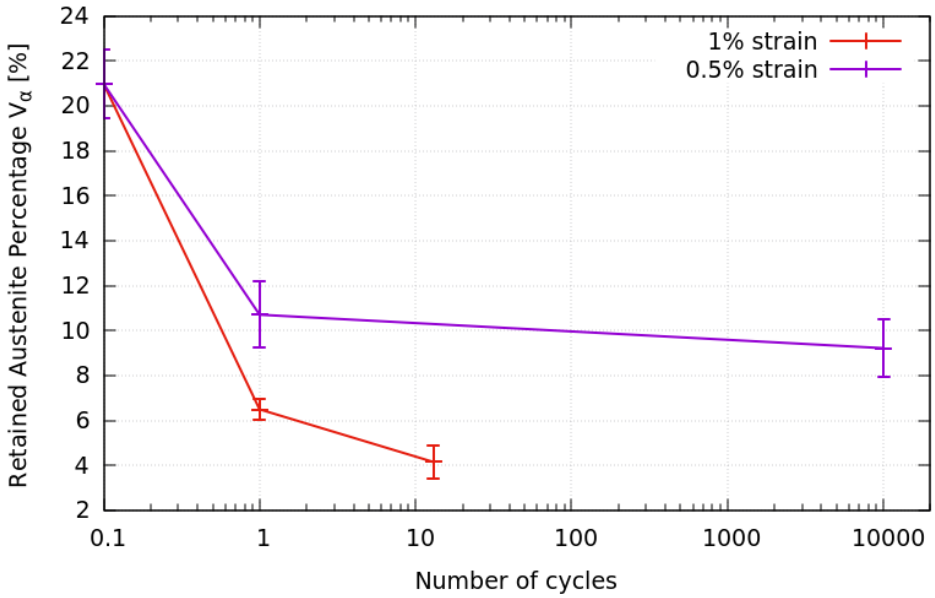

Figure 5.31: RA content vs number of cycle under 1% and 0.5% strain loading

obtained from ABAQUS models, in which the temperature expansion input only accounts for the initial residual stresses without the effect of RA transformation. In the ABAQUS models, the composite sample is loaded to the desired strain amplitudes under displacement constraints. Since most RA transformed under tensile loading, the Von Mises stress and PEEQ were acquired at the tensile peaks as the average value across the case layer of the composite sample.

The RA transformed percentage was calculated as the change in RA content over the initial RA content. If RA is measured at more than one depth in the tested samples, the average of the two measurements was used. Figure 5.32 shows the data for the percent RA transformation vs the Von Mises stress or PEEQ in the case layer of the composite samples shown in Figure 5.30.

It is worth noting that the data point for the fractured fatigue test under 0.34% strain amplitude is missing in the log-log scale plot in Figure 5.32b since no equivalent plastic strain was predicted in the ABAQUS model. The hysteresis loops for the composite samples loaded at strain amplitudes of 0.34% and 0.9% are plotted in Figure 5.33.

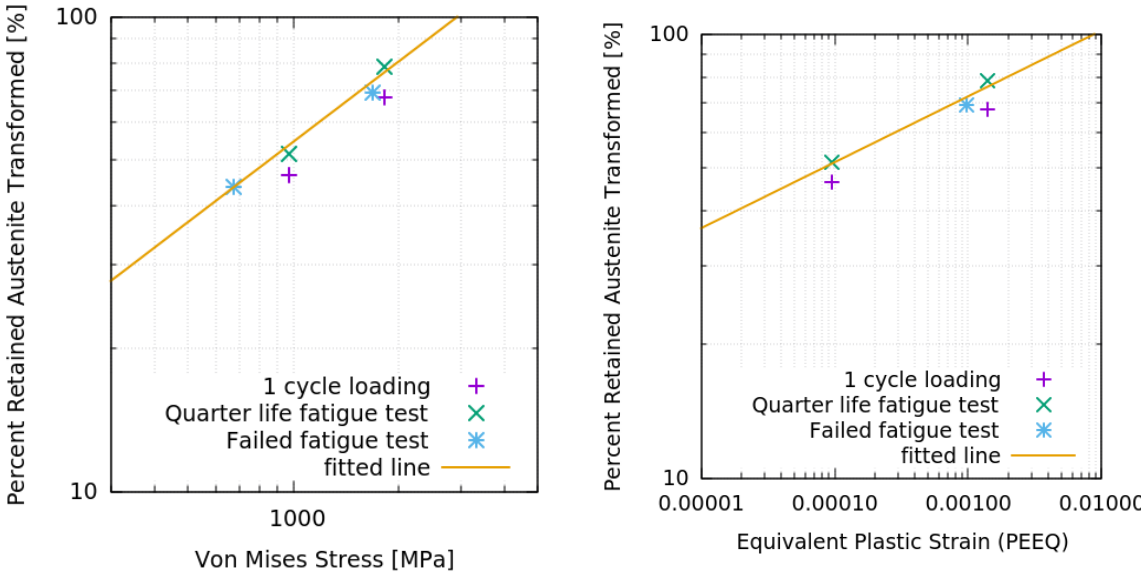

(a) Von Mises stress

(b) Equivalent plastic strain (PEEQ)

Figure 5.32: Relationship between stress or strain and percent RA transformed

A small amount of plasticity can be observed in the first tensile reversal of the composite sample loaded under 0.34% strain in Figure 5.33a, the remaining cycles are fully elastic. The ABAQUS model does not show any PEEQ at the 0.34% strain amplitude because cyclic material properties were used as the inputs instead of the monotonic properties, and the yield stress for the tensile curve in the case sample is much lower than that for the cyclic curve.

Figure 5.32 shows that the RA transformed after one cycle of loading (shown in purple points) is less than that transformed after the partial and fractured fatigue tests (green and blue points). Only data from the full and partial fatigue tests were considered in the fitting process to determine the RA transformed in the CA and VA cyclic tests. Linear relationships can be observed in the log-scale plots between the Von Mises stress and the percentage RA transformed, as well as the PEEQ vs RA transformation if the zero plastic strain point is excluded.

The ABAQUS models predict no PEEQ in the case layer of the composite sample at

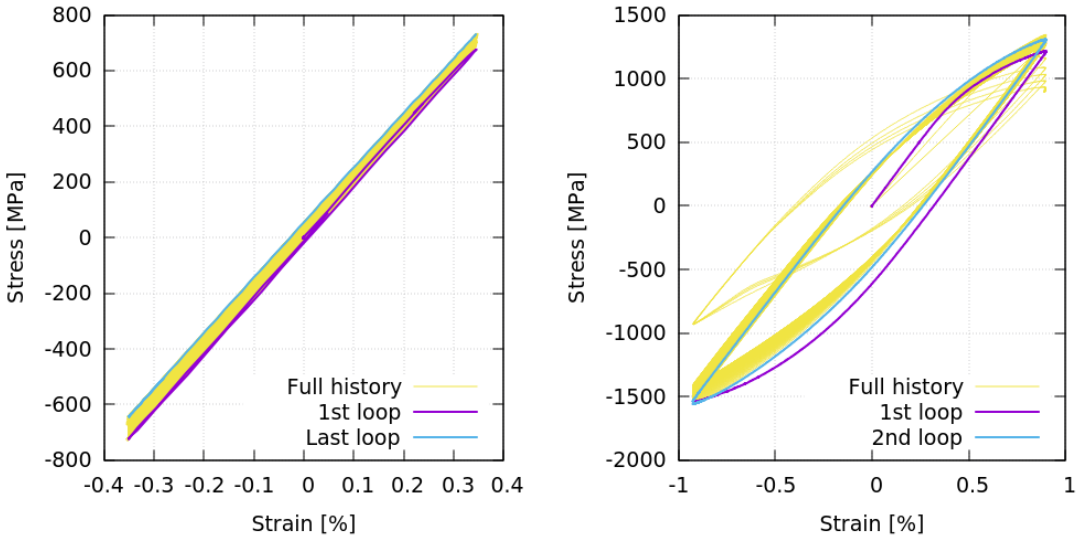

(a) Strain amplitude of 0.34%

(b) Strain amplitude of 0.90%

Figure 5.33: Hysteresis loops of two composites samples

strain amplitudes smaller than 0.5%. Therefore, the PEEQ fitting could generate inaccurate RA transformation predictions at a low strain amplitude loading. Von Mises stress is selected as the independent variable for the transformed RA estimation in this project. The equation for the fitted line in Figure 5.32a is:

$$\%RA \quad Transformed = 0.013\sigma_v^{0.56} \tag{5.2}$$

where σ_v is the Von Mises stress in the case layer of the composite sample.

To predict the percent RA transformed in cyclic tests loaded under other strain amplitudes, the ABAQUS model for the composite axial sample was run to simulate strain amplitudes ranging from 0.1% to 1.4%, and the Von Mises stresses were recorded. The amount of RA transformed in the case layer of the composite sample was then estimated using Equation 5.2 and converted to strain expansion for future residual stress calculations. A relationship between the loaded strain amplitude in the composite sample and the strain expansion in the case layer was established and plotted in Figure 5.34.

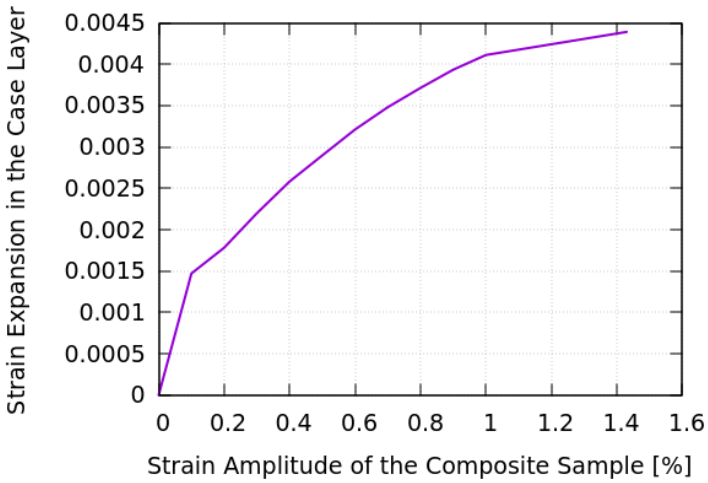

Figure 5.34: Relationship between the strain expansion due to RA transformation in the case layer and the composite strain amplitude

5.5 Residual stress estimation including RA transformation under CA and VA loading

The initial residual stress was modified based on the loading history of the test to account for the residual stress changes induced by the RA transformation. The strains generated during the carburization and quenching procedure in the case, middle, and core layers are -0.224%, -0.358% and -0.410%, respectively (Figure 5.11b). To include the RA transformation in the residual stress calculation, the strain expansion caused by RA transformation at the specific strain amplitude, as plotted in Figure 5.34, was added to the initial strain in the case layer. Then, the new residual stress was calculated using compatibility conditions.

The initial residual stresses in each layer, including the RA transformation effect at different strain amplitudes, are listed in Table 5.7.

For the CA loading histories, the initial residual stresses in Table 5.7 are used to predict the crack initiation location (case or core or transition layer) and fatigue life.

Since RA transforms under a tensile loading, the tensile peak stress in the VA load

Table 5.7: Residual stresses in the case, middle and core layers at different strain amplitudes including the effect of RA transformation

Strain amplitude	Residual stress in each layer		
	Case MPa	Middle MPa	Core MPa
1.00%	-844	302	410
0.90%	-818	291	399
0.80%	-785	277	385
0.70%	-751	262	370
0.60%	-712	245	353
0.50%	-666	226	333
0.40%	-619	205	313
0.30%	-563	181	289
0.20%	-501	155	262
0.10%	-455	135	243
0.00%	-240	42	150

history was used to estimate the residual stress changes due to the RA transformation by the following steps: 1) Find the maximum stress in the VA load history and convert it to strain using the composite cyclic stress-strain curve; 2) determine the RA transformation contributed strain expansion in the case layer of the tensile peak strain from Figure 5.34; 3) add the case strain expansion to the carburization residual strain and calculate the post RA transformation residual stress; 4) convert the updated residual stress to a residual strain assuming elastic material behaviour.

The residual strains obtained from the above procedure were added to the VA strain histories for fatigue predictions.

The simulated hysteresis loops from the FE model and the compatibility models are compared with the measured stress and strain in Figure 5.35.

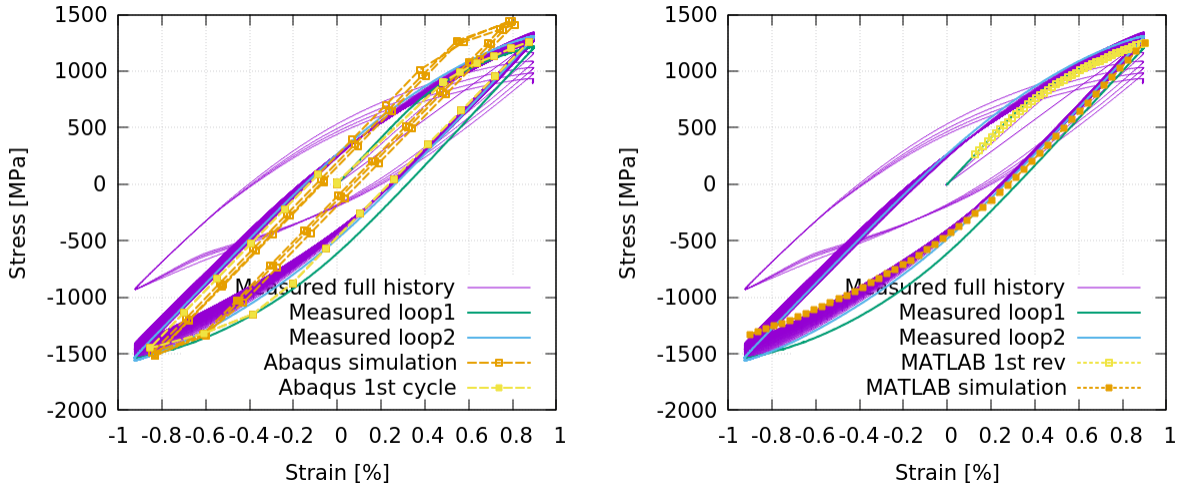

(a) ABAQUS output

(b) MATLAB output

Figure 5.35: Measured hysteresis loops compared to the simulations of composite axial sample

5.5.1 Cyclic stress-strain behaviour

Figure 5.35a shows that the peak tensile stress in the first reversal generated in the ABAQUS model matches the measurement well. However, the consecutive cycles yield higher tensile peaks. Even though the experimental measurements also revealed some hardening in the second reversal, it is less severe than that predicted by the ABAQUS model. The compressive peaks predicted by the ABAQUS model match the measurements.

The MATLAB model, as shown in Figure 5.35b, only generates one hysteresis loop. Because the same material inputs were used in all cycles, no hardening rules were employed in this model. The simulated tensile peak stress agrees with the measurements. However, this model underpredicts the compressive peak stress. One possible cause of the low estimated compressive yield and peak stress is that the transverse compressive residual stress in the case layer is neglected in the compatibility model.

5.5.2 Residual stress relaxation

Some literature [162, 29] suggests that the softest layer in a case-hardened component dominates the residual stress in a component. Once a part of the specimen experiences plastic deformation, the residual stress across the sample relaxes to achieve a new force balance condition. The amount that the residual stress relaxes under cyclic loading in the composite samples needs further investigation.

Unlike the shot-peened or cold-worked components, the material properties in a carburized sample vary between the case and the core layers. Consequently, residual stresses in a carburized sample can be developed under plastic deformation even without any initial residual stresses.

In this study, the residual stresses were measured at four depths in the composite samples after loading under fully reversed CA straining at $\pm 1.0\%$ and $\pm 0.5\%$ strain after one cycle and a quarter of the expected fatigue life. The measurements are plotted in Figure 5.36 with the initial residual stress. Also drawn in the figure are the three residual stress profiles predicted by the compatibility models with three residual stress assumptions:
1) the initial residual stress was calculated including both the carburization and the RA transformation effects; 2) initial residual stress was generated from the carburization process only; 3) without any initial residual stress.

The difference between the red and black points in Figure 5.36 suggests that some relaxation occurred between the first loading cycle and the quarter life cycle. More so under the $\pm 0.5\%$ strain loading than under the $\pm 1.0\%$ loading.

The yellow lines in Figure 5.36 show that, even if the carburized sample started with no initial residual stress, some of it would be generated after loading. The amount of residual stress generated in this case increases with the loading range. As expected, the magnitude of the predicted post-loading residual stress in the three models can be sorted from the least to the most in the following order: start with no initial residual stress, with only carburization residual stress, with RA and carburization residual stress.

Comparing the measured and the estimated post-loading residual stress profiles in Figures 5.36a and 5.36b, the stress in the case layer after cyclic straining for one quarter of the

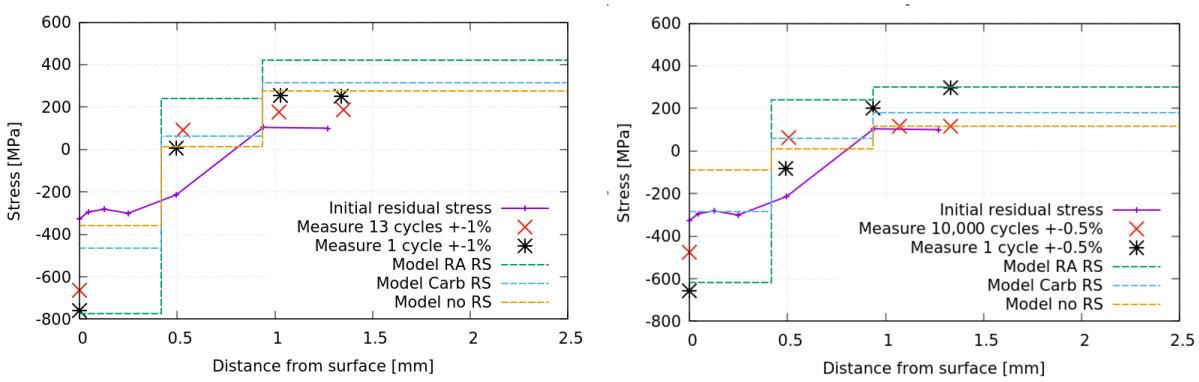

(a) ±1% strain (b) ±0.5% strain

Figure 5.36: Measured residual stresses before loading (purple line), after 1 cycle of loading (black points), and after a quarter of life (red points) are compared with residual stress profiles generated from compatibility models with an initial residual stress considering RA transformation (green line), without RA transformation (blue line), and no initial residual stress (yellow line)

fatigue life is in between the estimated results from the model including RA transformation and the model that only includes carburization. While in the core layer, the remaining residual stresses after relaxation are below or near the estimated value without any initial residual stress.

5.6 Cyclic stress-strain curve of the composite samples

Asymmetric stress-strain behaviour was observed in the composite samples, which is likely caused by the initial residual stress in the sample. Due to the initial tensile residual stresses in the core layer, an early yielding in the core layer can occur and consequently cause a lower yield stress in the tensile part of the composite sample compared to the compressive region. Simulations were conducted to examine the effect of initial residual stress on the tensile and compressive stress asymmetry of the composite sample.

The three residual stress conditions mentioned in Section 5.5.2 were studied. In order to better visualize the difference between the tensile and compressive stress-strain curve in the cyclically stabilized composite samples after some fatigue loading, the tensile and compressive peak stresses were plotted separately with the simulated results in Figure 5.37.

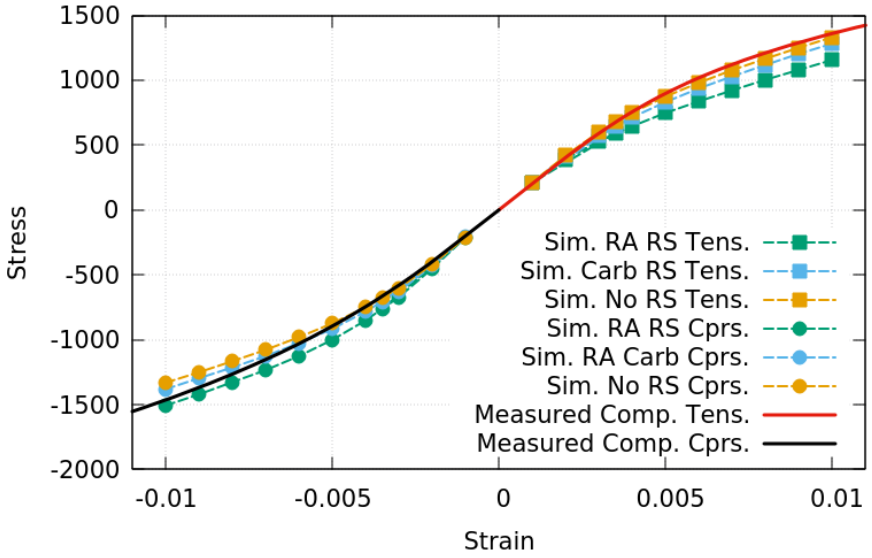

Figure 5.37: Simulated cyclic stress-strain curves with the 3 residual stress conditions compared with the measurements

The yellow curve in Figure 5.37 shows the simulated result without any initial residual stresses, and it is symmetric. While the green and the blue curves, which started with different initial residual stresses, show some asymmetry. The green curve modelled with carburization and RA transformation residual stresses is the most biased of all.

On the tensile side, the yellow curve without any initial residual stress is the closest to the experimental results; while under compression, the simulation with both RA transformation and carburization residual stresses (green curve) best correlates to the tests. Figure 5.36 shows that the residual stress in the core layer of the composite sample has relaxed significantly after cyclic straining for one quarter of the estimated fatigue life. This could explain why the model without any initial residual stress predicted the actual tensile cyclic behaviour of the composite sample.

Chapter 6

Fatigue analysis

This chapter presents the models used to predict the crack initiation location and the total fatigue life of the composite axial and notched samples under CA and VA loadings.

The strain/stress-based fatigue approach was applied to anticipate the crack initiation location in the three-layer models for the axial and notched composite samples while accounting for the residual stresses.

Subsurface crack propagation models were developed to estimate the crack propagation life in the axial samples where subsurface failures were expected and observed.

A through-crack model and a corner-crack model were implemented to assess the crack growth life in the interior layer of the notched sample after the case failed at the notch.

6.1 Initiation model for the axial composite sample

The cyclic stress-strain behaviour and the fatigue properties of the case, middle and core layers are the inputs for the initiation model, which was applied to predict the initiation location and the crack initiation life of the composite axial sample under CA and VA loadings.

6.1.1 Methodology

The stress-strain fatigue life data for the simulated core material may not be appropriate for the prediction of the life of the core layer in composite specimens for the following reasons: 1) the subsurface core layer is under constraint in all directions, while the surface of the simulated core only samples have no constraint normal to the surface and are prone to cross-slip crack initiation; 2) the interior of the composite sample is in a vacuum environment, while the core samples were tested in air; 3) the decarburized layer on the surface of the simulated core samples could contribute to early crack initiation.

Studies have shown that running fatigue tests in a vacuum environment lengthen the fatigue lives by a factor of 10 [156] and a factor of 2 [82] compared to those run in air at the stress levels above the fatigue limit. In order to account for the improvement in fatigue performance for cracks initiated from the subsurface core and middle layers, the calculated initiation lives in the core and middle were doubled in the initiation prediction as suggested by the reference's data [82], for a conservative estimate.

Since the CA and the SWT modified POL fatigue test data are close to each other for the through-carburized case and simulated core materials (Figure 4.13 and 4.12), the fatigue properties obtained under CA loading were applied for all initiation simulations. Additionally, the composite samples loaded under the full and the filtered bracket VA histories have similar lives, meaning that the small load cycles impose little damage to the fatigue life. This evidence shows that overloads do not cause cycles below the CA fatigue limit to do damage. The material properties for the case, middle and core were described in Sections 4.3 and 4.7.

A SWT mean stress correction was employed to account for the positive mean stress in the middle and core layers when predicting the initiation life. For the case layer, the negative mean stress rule suggested by Gaia Da Silva et al. [47] was applied as follows:

1. For hard and mostly elastic materials, if the mean stress is positive, damage is computed using a stress-based approach. The equivalent stress amplitude in a reversal

was estimated using Morrow's rule:

$$\sigma_{eq} = \frac{\sigma_{amp}}{1 - \frac{\sigma_m}{\sigma_f}} \tag{6.1}$$

where σ_{amp} is the stress amplitude of the load cycle, σ_m is the mean stress in the cycle, σ_f is the fatigue strength coefficient;

2. if the mean stress is negative, the equivalent stress amplitude is set equal to the maximum stress in the reversal;

3. if the maximum stress in the reversal is less than 90% of the fatigue limit, it was assumed that no damage was generated.

The shortest predicted life among the three layers of the composite sample indicates the crack initiation location. Due to the high hardness of the case material, if the crack initiated in the case layer, the crack propagation life was assumed to be negligible compared to that spent on initiation.

Therefore, if the initiation life of the case layer is the shortest of all in the axial composite sample, the final fatigue life equals the predicted case initiation life. If the crack was initiated in the middle or the core layer, subsurface failure is predicted. The fatigue life of the sample is set equal to the shorter of the case initiation life or the subsurface crack propagation life. It is assumed that, for subsurface failure, inclusions pre-exist in the middle or core layer of the composite sample. Therefore, the subsurface propagation life can be estimated by assuming an initial crack length similar to the inclusion radius and propagating the small inclusion crack to the case layer.

For the CA load histories, predictions were made at different strain levels ranging from 1.0% strain amplitude to the predicted fatigue limit at 0.3% strain amplitude. The compatibility model was used to determine the maximum and minimum stresses and strains at each of the case, middle, and core layers under the applied strain in the composite sample. As discussed earlier, the initiation prediction for the core layer of the composite sample using the simulated core material fatigue properties is expected to under estimate

the fatigue strength of the core material encased in a carburized core. The R=-0.5 and R=-1 curves of the the Hasegawa1 da/dN lines were applied to estimate the subsurface crack propagation life in the smooth specimen under CA loading. The three residual stress conditions mentioned in Section 5.5.2 were simulated.

Figure 6.1 shows the procedure for predicting the fatigue initiation life under VA loading.

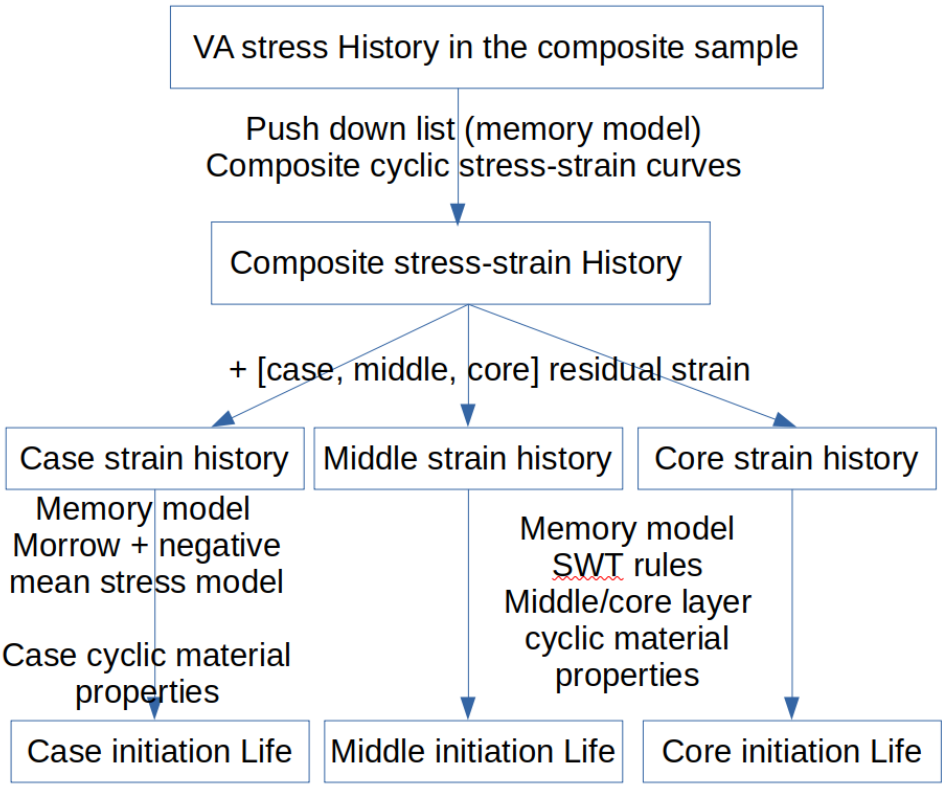

Figure 6.1: Initiation prediction flow chart for VA loading history

Firstly, the VA stress history was converted to a strain history using the memory model with the cyclic stress-strain curve of the composite material. The residual strain in each layer caused by RA transformation and the carburization process was then added to the composite strain history to obtain the strain history for each layer.

The residual strain instead of the stress was added to the original VA history to calculate the damage because the core layer often experiences plastic deformation. The model could produce unbalanced forces if stress were added to the load history. Additionally, the sum of the applied stress and the residual stress in the core layer, calculated assuming elastic deformation, could be large and lead to a predicted fracture in a ductile material like the core.

After the strain histories in the three layers were determined, they were used to calculate the stress and strains in each reversal with the corresponding cyclic stress-strain curves as inputs. Knowing the stresses and strains in each layer, the damage resulting from each loading reversal can be predicted by applying the models mentioned earlier. The push-down list method described in detail in Chapter 3 was employed here for calculating the accumulated damage under the VA loading history.

For demonstration purposes, a short VA load history with a minimum stress of -1100 MPa is plotted in Figure 6.2a. This history is extracted from the bracket history by keeping its maximum and minimum stresses with a few random points in between. The simulated hysteresis loop for the composite sample under this loading history is plotted in Figure 6.2b.

The hysteresis loop in Figure 6.2b shows how the stress and strain in each reversal were estimated in the memory model. The smaller loops are hung on the top or the bottom of the bigger loops, depending on the loading history.

Figure 6.3a shows the strain histories for the case, middle and core layers with the residual strain that includes both the carburization and RA transformation effects. As displayed, the case layer experiences a significant amount of compressive mean strain, while the core and middle layers experience tensile mean strains.

Using the same memory model and the cyclic stress-strain curves for the material in each layer, the strain histories plotted in Figure 6.3a were converted to the stress histories in Figure 6.3b.

At the absolute tensile peak in Figure 6.3b, the stresses at the core and middle layers almost overlap with the composite stress, which indicates a large amount of plastic

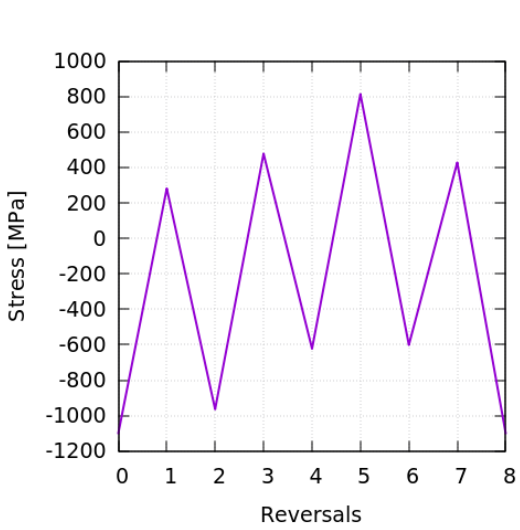

(a) Stress history

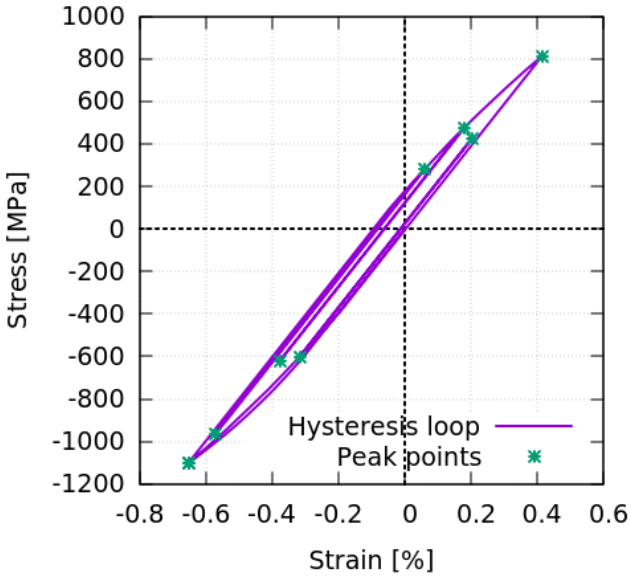

(b) Simulated composite hysteresis loop

Figure 6.2: A short VA history for the composite sample

deformation in both the middle and the core layers.

The predicted composite stress at the maximum point using the three-layer model is about 15% higher than that simulated using the cyclic stress-strain curve for the composite sample. This issue will be further illustrated in the force balance discussion in a later part of this section.

Figure 6.4 displays the simulated hysteresis loops for the composite and the three layers.

The hysteresis loops clearly show the plastic deformations in the middle and the core materials; while little plasticity was observed in the case layer.

6.1.2 Initiation location for CA loading

In this section, the initiation lives in the case, middle and core layers were predicted using smooth specimen fatigue-life curves for the three residual stress cases. If the shortest

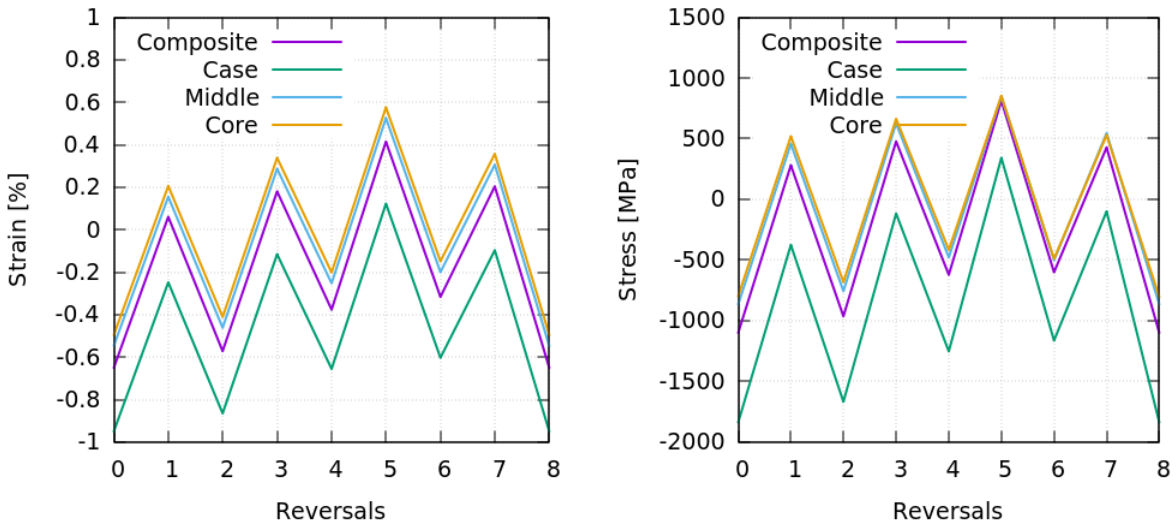

(a) Strain histories

(b) Stress histories

Figure 6.3: Strain and simulated stress histories for all three layers and the composite material with residual stress including RA transformation and carburization effects

initiation life is predicted in the case layer, the total life is the initiation life. However, if the middle or the core layer has a shorter initiation life than the case, the total life at this stress level is chosen as the shorter of the case initiation life or the subsurface core or middle layer crack propagation lives. It should be noted that the core initiation prediction using the simulated core material fatigue properties is conservative due to the vacuum environment, physical constraints in the subsurface and the absence of IGO shown on the surface of the simulated core sample.

The strain- and stress-life curves for the initiation only predictions for the three layers with residual stress, including both the carburization and the RA transformation effects under CA loading, are plotted in Figure 6.5. The analyses for residual stress with only the carburization effect and without initial residual stresses are shown in Figures 6.6 and 6.7. Note that the red line in the figures, for overall initiation life, follows the shortest initiation prediction at each simulated stress level.

As shown in Figures 6.5, 6.6 and 6.7, the initiation location shifts from the case layer

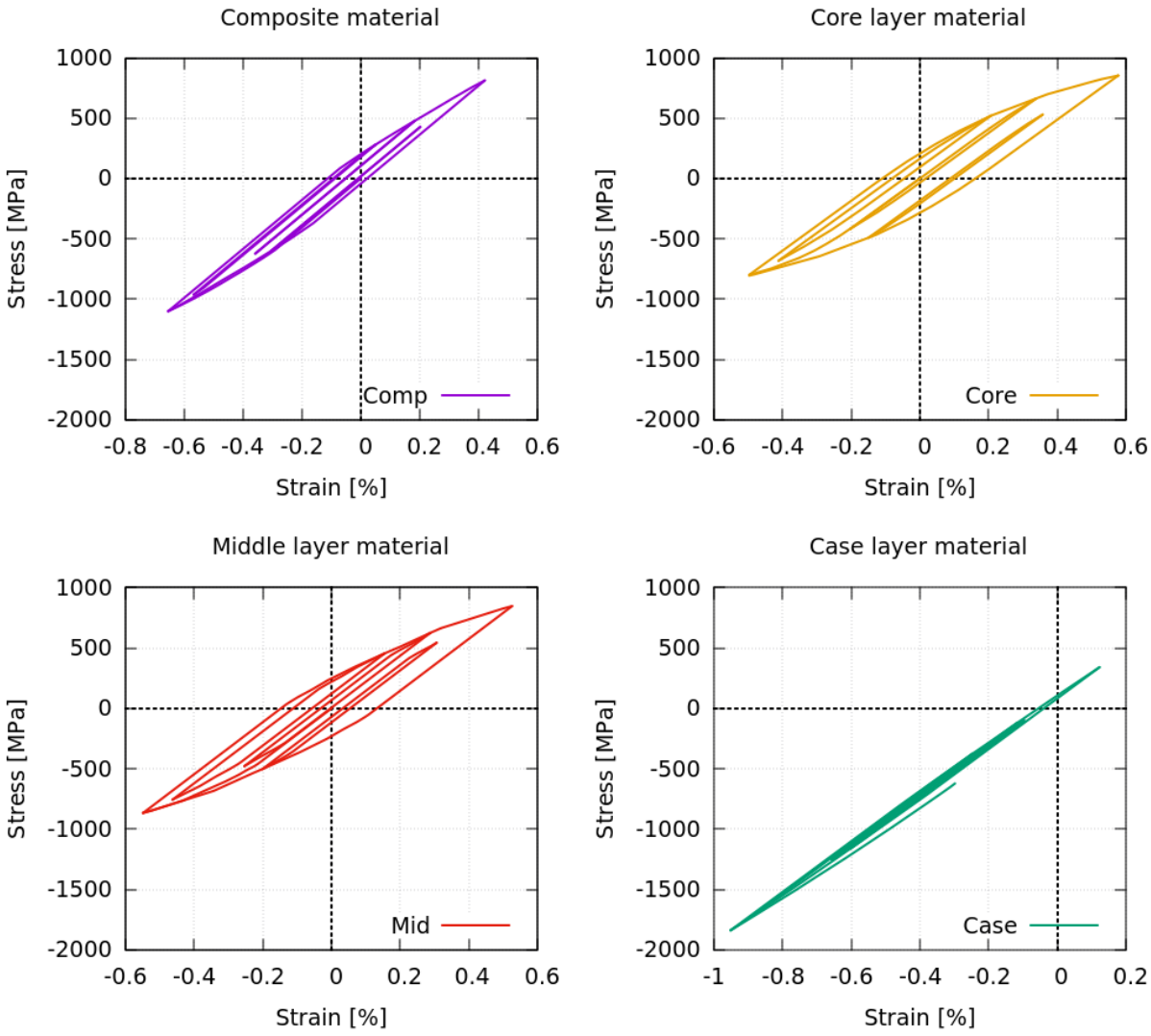

Figure 6.4: Hysteresis loops for all layers under the short VA history

to subsurface layers at lower stress levels as the magnitude of the residual stress in each layer drops. This is because the compressive residual stress in the case layer lengthens the initiation life, while the tensile residual stresses in the subsurface layers diminish it. The initial mean stresses are notably beneficial when the deformation is mostly elastic at low-stress levels since the plasticity diminishes the initial mean stress at a high strain

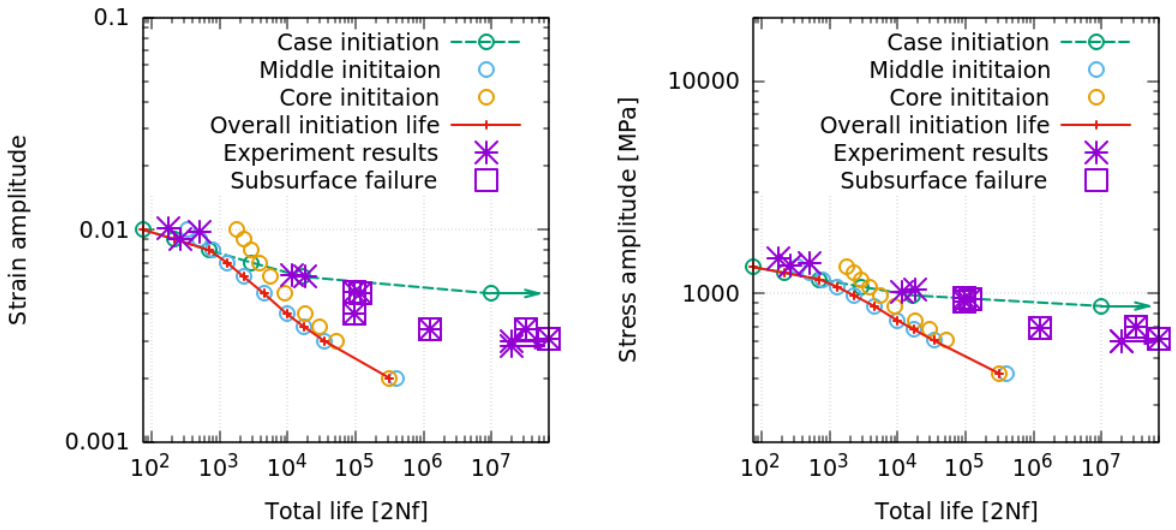

(a) Strain-life (b) Stress-life

Figure 6.5: Initiation predictions for case, middle and core layers with initial residual stress including both the carburization and the RA transformation effects compared with experiment data under CA loading of smooth specimens

amplitude.

The initial mean stress has a more prominent effect in the initiation life prediction for the case layer than for the subsurface layers. This can be attributed to the high yield stress in the case cyclic stress-strain curve so that the stress due to strain changes caused by austenite transformations is elastic and not reduced by yielding.

6.1.3 Force balance check under VA loading in composite axial sample

To check the force balance in the simulations, the overall stress simulated in the case, middle and core layers of the composite axial samples were compared with the maximum and minimum applied loading stresses in the VA history. Figure 6.8 shows the calculated composite stress from the three simulated layers with the inputs for the three different

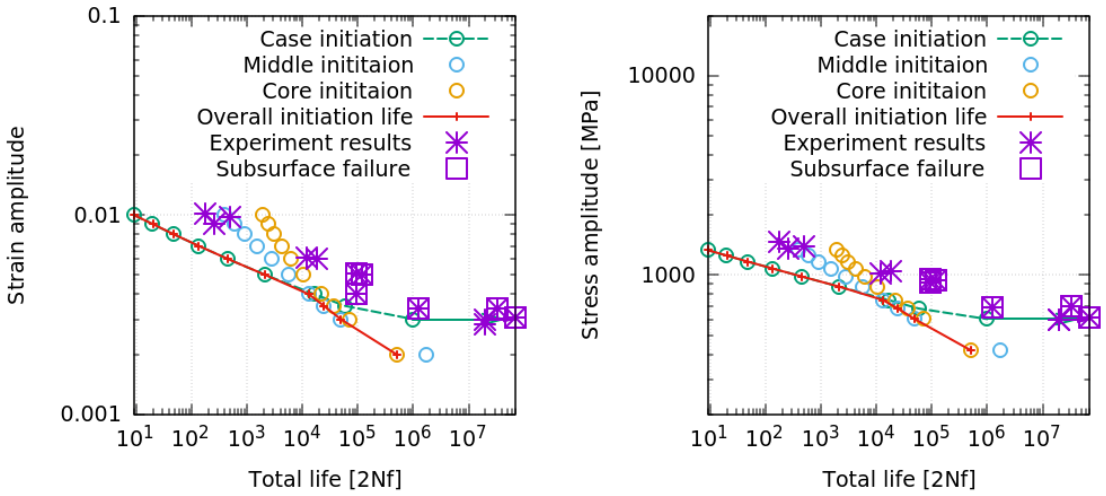

(a) Strain-life (b) Stress-life

Figure 6.6: Initiation predictions for case, middle and core layers with residual stress including only carburization effect compared with the experiment data under CA loading of smooth specimens

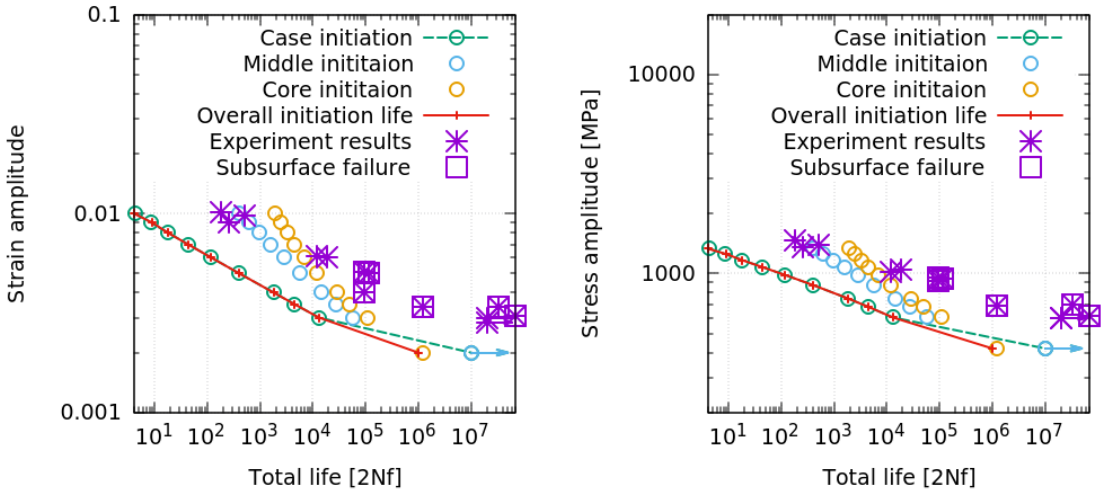

(a) Strain-life (b) Stress-life

Figure 6.7: Initiation predictions for case, middle and core layers without initial residual stress compared with the experiment data under a CA loading of smooth specimens

residual stress cases.

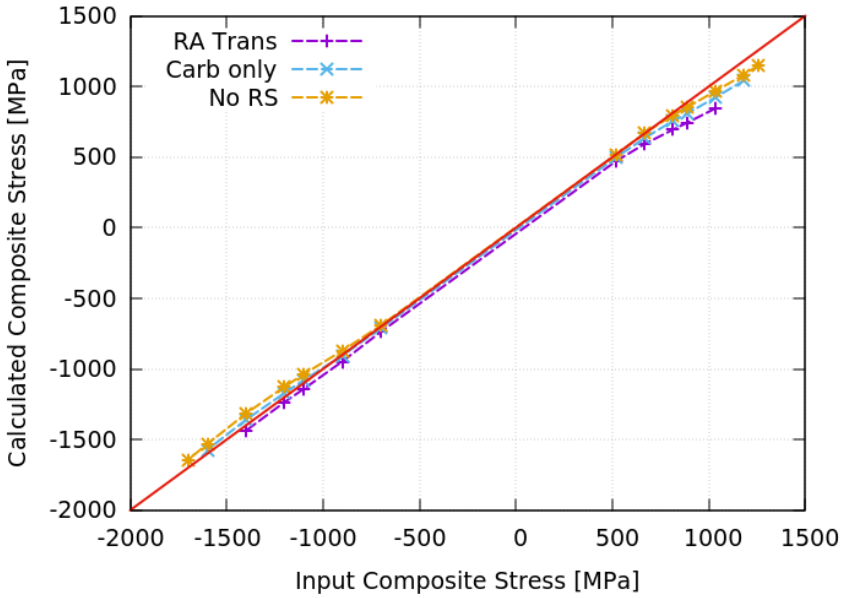

Figure 6.8: Force balance check for the three residual stress cases under VA loading

The force balance result under VA shows a similar trend to the cyclic stress-strain curve simulations for the CA loading (Figure 5.37). The RA Trans model predicts the most asymmetry between the tension and compression loading and predicts relatively accurate compressive results while underpredicting the stress on the tensile side. The other two residual stress models predict more symmetric tension-compression results. Overall the simulated stresses are marginally less than the input stress on the tensile side. This issue could be solved by regenerating a middle layer curve with a higher stress-strain curve.

6.1.4 Initiation location prediction for VA loading

The initiation lives for the case, middle and core layers loaded under bracket VA histories scaled to different maximum stresses were predicted using the model described in Section 6.1.1. The simulated results are plotted in Figures 6.9, 6.10 and 6.11 for residual stress considering both carburization and RA transformation, carburization only and no

residual stresses, respectively. Again, the core initiation lives predicted in these simulations are conservative since the core material does not represent the subsurface core layer in the composite, as mentioned earlier.

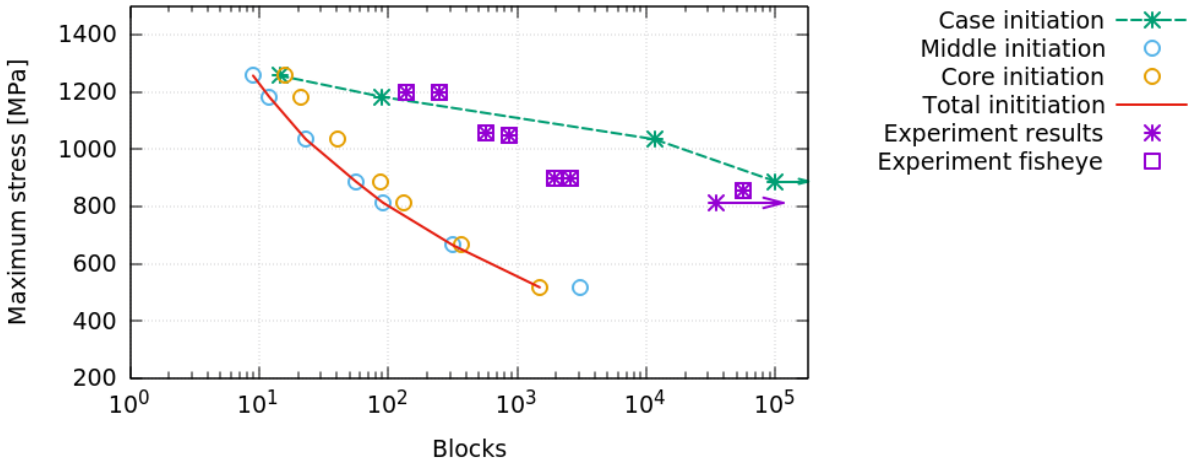

Figure 6.9: Initiation predictions for case, middle and core layers with residual stress including both the carburization and the RA transformation effects compared with experiment data loaded under VA history using smooth specimens

Again, the subsurface crack propagation life from the initial flaw size to the fracture length was taken to be the fatigue life when the crack initiated in the subsurface.

In the CA predictions, the initiation location shifts to the interior at lower stress levels as each layer's residual stress drops in the different assumptions. For the two simulations that included initial residual stresses in Figures 6.9 and 6.10, failures were predicted to initiate from the subsurface. This matches the test results that all the fractured surfaces of the axial samples failed under VA loading displaying one or two fisheyes.

In the simulation without any initial residual stresses (Figure 6.11), the initiation location follows the case prediction at high-stress levels and switches to the core prediction at low stresses.

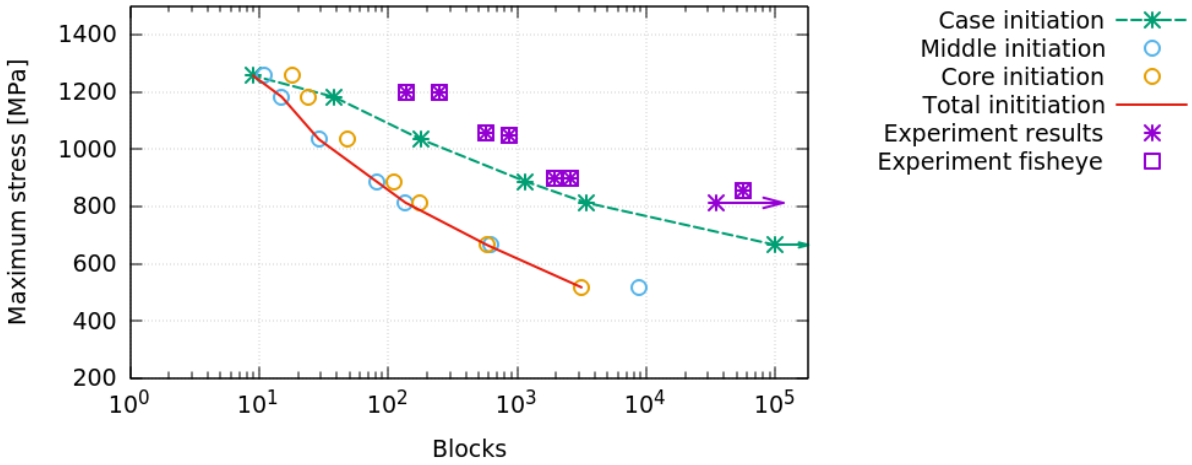

Figure 6.10: Initiation predictions for case, middle and core layers with carburization residual stress compared with experiment data loaded under VA history using smooth specimens

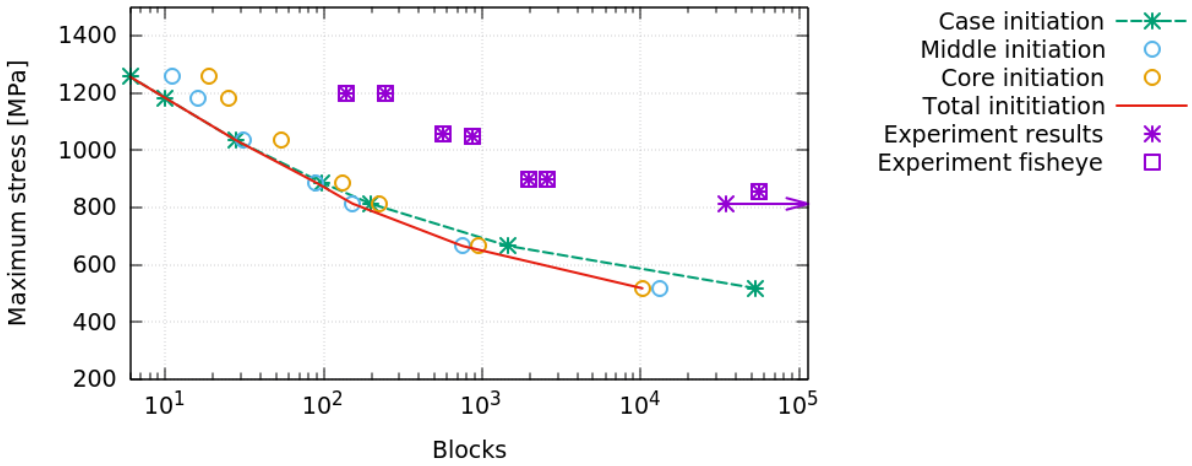

Figure 6.11: Initiation predictions for case, middle and core layers without residual stress compared with experiment data loaded under VA history using smooth specimens

6.1.5 Using composite CA data to predict fatigue life under VA loading

As previously mentioned, the CA fatigue properties of the simulated core material are not representative of those in the core layer of the composite sample due to the vacuum environment and the constraints in the core of the composite as well as the IGO zone on the surface of the simulated core samples. Therefore, an attempt was made to derive the core layer fatigue properties from the composite CA fitted curve so that the subsurface failure condition is considered.

To derive the subsurface fatigue properties, residual stress, including both the RA transformation and carburization effects, was assumed to exist in the composite sample under CA. For each CA strain amplitude applied on the composite sample, the maximum and minimum stresses and strains in the middle and core layers of the composite sample were calculated using the cyclic stress-strain curves for these layers, including the residual stresses, with the three-layer compatibility model.

The SWT parameter ($\epsilon_{amp} \times \sigma_{max}$) vs fatigue life data for the newly derived subsurface layers are plotted with the experimentally fitted data in Figure 6.12.

The newly derived middle and core layer curves lay very close to the composite curve. In the long life region the derived curves, representing fully revered stress cycles without a mean stress, lie slightly above the composite curve.

These subsurface layer fatigue properties were applied to predict the fatigue life of the composite sample under VA loading. The predictions from the derived middle and core curves yield almost the same result.

Moreover, the CA composite fitted curve was also used to predict the composite sample life under the VA.

The predicted results for the composite axial sample under VA loading using the two approaches mentioned above are plotted in Figure 6.13. The composite material test data under VA loading are also plotted in the figure.

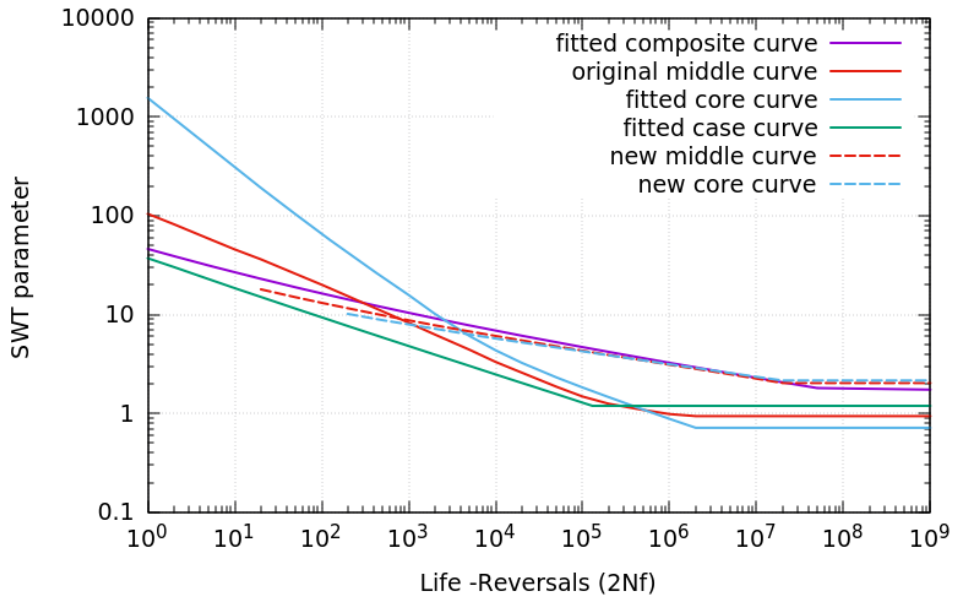

Figure 6.12: Derived material curves for the core and the middle layers from the composite CA curve of the smooth specimens compared with the fitted curves

The two approaches introduced in this section produced the same VA prediction, which matches the test results well. The reasons that the CA curve could be used for VA predictions include: 1) the tests were run on axial samples, where the applied stress across the sample is uniformly distributed; 2) the subsurface material seems to be insensitive to the periodic overload effects.

6.2 Subsurface crack propagation model

The three approaches, i.e. ASME [7], BS7910 [14] and Murakami [104], for estimating the SIF of subsurface elliptical cracks introduced in the Section 2.12 were investigated. The fatigue life of an axial composite sample loaded under CA histories was predicted using the three approaches, and the results were compared.

The SIF estimation adopted by BS7910 was applied to predict the subsurface crack

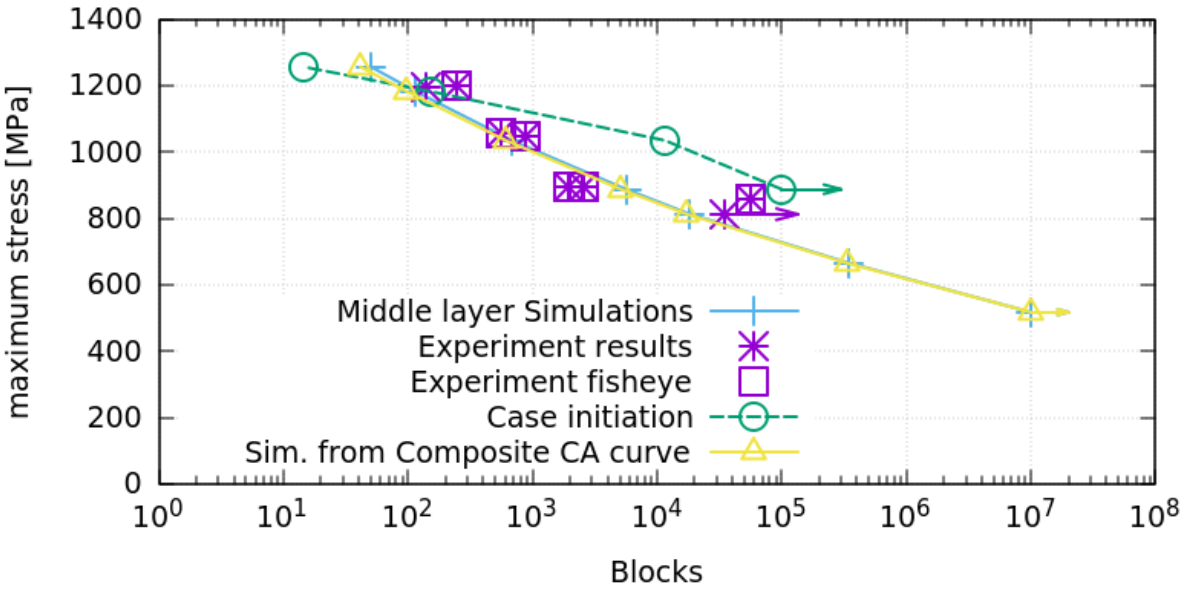

Figure 6.13: VA life prediction with middle layer properties derived from CA composite curve comparing with predictions using the CA composite curve and the experimental results for smooth specimens

propagation life of the axial composite sample loaded under VA histories. Different sets of da/dN curves were used in the simulations, and the predicted fatigue lives were compared with the experimental results.

6.2.1 Comparison of BS7910, ASME and Murakami's subsurface crack SIF models and constant amplitude simulations

The three approaches for estimating mode I SIF for subsurface cracks, i.e. ASME [7], BS7910 [14] and Murakami [104] were compared by applying the same assumptions listed below:

- the membrane stress governing the subsurface cracks is constant;
- the shape of the crack stays circular as it grows ($a = c$ in BS7910 or $l = 2a$ in ASME);

- the crack growth is dominated by the maximum SIF at the point closest to the surface ($\theta = \pi/2$ in BS7910; Point 1 in ASME);
- the cross-section geometry of the fictitious plate is as shown in Figure 6.14;
- the crack is located at the centre of the plate (for ASME, $d = \frac{t}{2}$);
- the yield stress of the material is 1000 MPa for the ASME model.

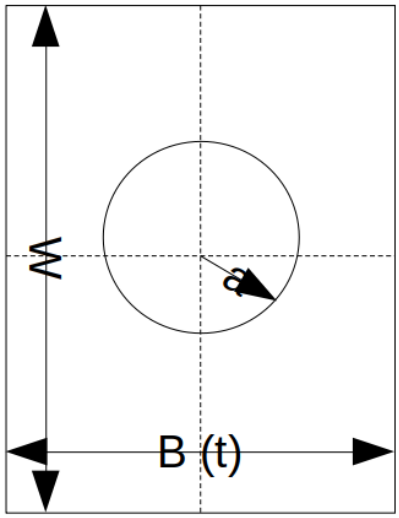

Figure 6.14: Subsurface circular crack in a plate assumption demonstration

The assumptions generated based on the loading conditions and the fracture surface of specimen cComp4, as demonstrated in Figure 6.15, for the comparison models include:

- the width of plate is 2.26 mm (B in BS7910 and t in ASME), calculated as the sum of the fisheye diameter and twice the case depth;
- the length of the plate is 5.5 mm (applicable in BS7910), and is set to satisfy the condition $2c/w < 0.5$;

- initial crack length, a_o, equals 0.0185 mm, which is the radius of the inclusion measured from the SEM of cComp4;
- the stress range applied in the core layer is 1281 MPa, as simulated in the compatibility model for residual stresses.

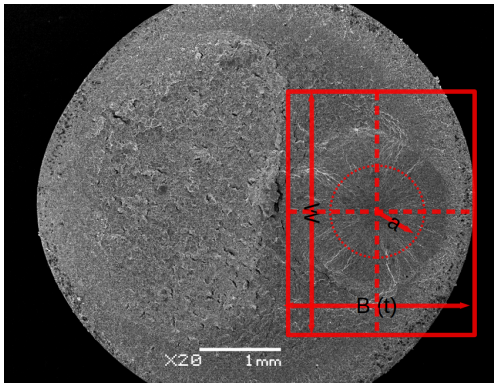

Figure 6.15: Specimen cComp4 subsurface growth crack model demonstration

For the three residual stress conditions examined in this study, the stress ratios in the core layer loaded under $\pm 0.34\%$ strain in cComp4 are -1, -0.78 and -0.64 for the no residual stress, the carburization only residual stress, and the RA transformation included residual stress conditions, respectively. Therefore, to be conservative, the ASME da/dN curve for $R = -0.5$ was applied to determine the crack growth in the CA simulations with the assumed plate plate shape for the smooth specimens.

It is assumed that the fracture of the specimen occurs when: 1) the subsurface crack length reaches 0.8 mm, which is approximately the fisheye radius; 2) the calculated SIF approaches $59MPa\sqrt{m}$, the core material fracture toughness measured by Zhang et al. [165].

Figure 6.16 shows the simulated results for specimen cComp4 under CA loading by applying the subsurface crack SIF calculated from ASME [7], BS7910 [14] and Murakami [104].

The failure for the cComp4 simulation was dominated by the crack length reaching $0.8mm$ in all three models, and they predicted similar crack propagation behaviour. Among

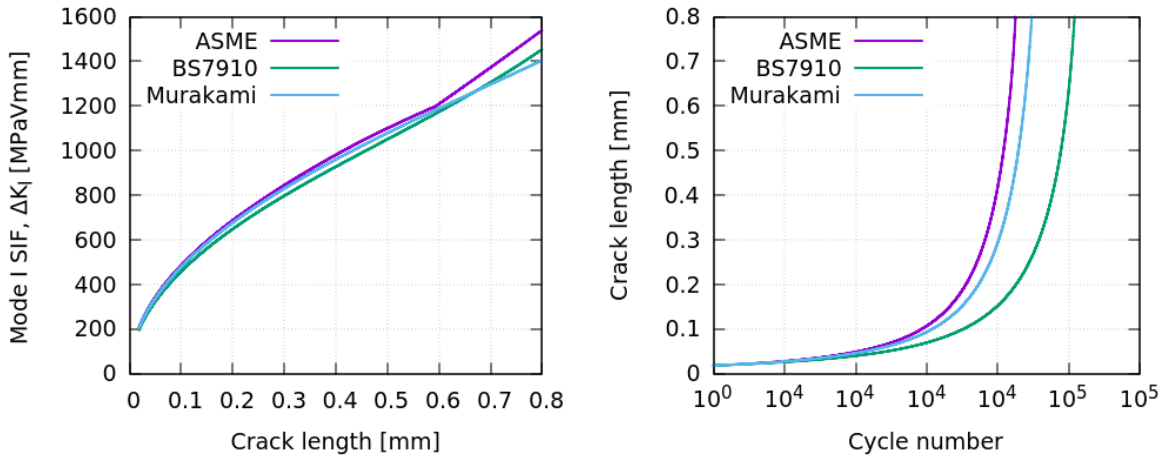

(a) SIF vs. crack length

(b) Crack length vs. number of cycles

Figure 6.16: Crack propagation simulations for cComp4 smooth specimen using ASME [7], BS7910 [14] and Murakami [104] subsurface crack SIF

the three models, the ASME [7] predicted the most conservative results, followed by Murakami's inclusion area theory [104], and the results evaluated from the BS7910 code [14] is the least conservative. The difference in life prediction between the three models is less than 20%.

To examine the effect of an eccentric subsurface crack on fatigue life prediction, some of the parameters in the ASME model were altered to represent the actual inclusion location in the plate. The plate width, t, was changed from 2.26 mm to 5.0 mm (diameter of the sample); and the distance from the center of the inclusion to the surface is 1.13 mm. A comparison of the simulation, including the eccentricity effect, is compared with the original ASME results in Figure 6.17.

The two curves overlap, indicating that the effect of eccentricity is marginal. After accounting for the eccentricity, the final life is shortened by less than 1% in this simulation.

The total life for CA tests at various strain ranges was simulated to further compare the three models for calculating the SIF of subsurface elliptical cracks. In addition to the general assumptions mentioned earlier, some parameters were set based on the measurements

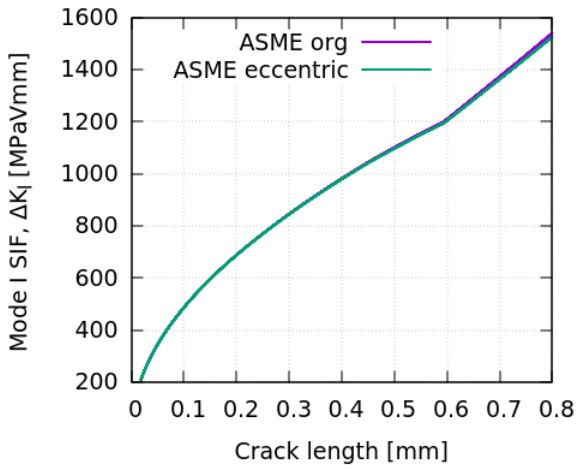

(a) SIF vs. crack length

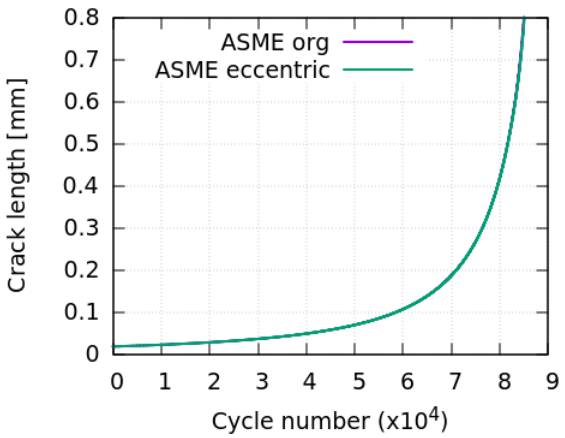

(b) Crack length vs. number of cycles

Figure 6.17: Crack propagation simulations for cComp4 smooth specimen using ASME [7] with and without eccentric subsurface crack location

on the SEM from cComp3 and cComp4 listed in Table 4.4:

- the initial crack size ,a_o, is 0.015 mm, which equals the assumed radius of the of the inclusion;
- the plate width, B in BS7910 or t in ASME, is two-thirds of the diameter, which is 3.3 mm;
- the same failure criteria were applied.

The stress ranges in the core layer, estimated with residual stresses including RA transformation and the assumptions mentioned above, were used as inputs for the propagation simulations. The simulations were run for composite strain amplitudes ranging from 1.0% to 0.3%, where all three propagation models predicted non-propagating cracks. The crack initiation predictions are those with residual stress including RA transformation. The CA simulated results from BS7910 [14], ASME [7] and Murakami's [104] propagation approaches with the "Hasegawa1" da/dN curve for R=-0.5 are plotted in Figure 6.18, and those with the R=-1 da/dN curve are plotted in Figure 6.19.

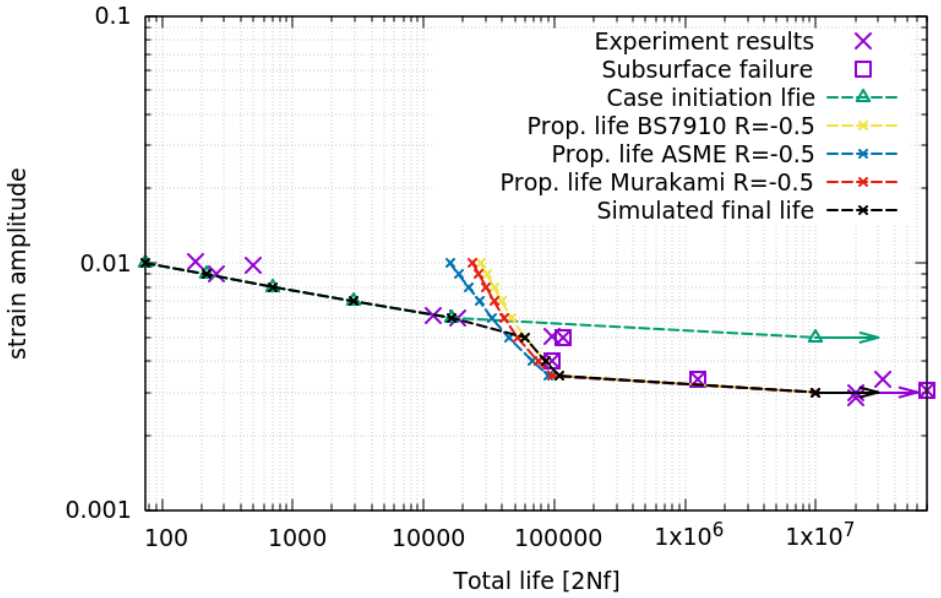

Figure 6.18: Crack propagation simulation results from the three models using ASME da/dN curve for R=-0.5 compared with experimental data for CA smooth samples

From Figures 6.18 and 6.19, one can observe that the three SIF calculations predict similar propagation lives and a similar runout limit for the CA loading.

The final life follows the case layer initiation prediction in the short-life region. In the region with a fatigue life longer than 100,000 reversals, the subsurface crack propagation dominates the fatigue life. The same surface to subsurface switch in failure mode was found in the experiments. The fisheyes observed in the fracture surface indicate a subsurface failure.

It is worth mentioning that, in the crack propagation simulations, the failure was controlled by the fracture toughness, ΔK_{max}, at high-stress levels, and by the pre-determined fracture length, a_f, of 0.8 mm at low-stress levels. The propagation results predicted using the R=-1 da/dN curve are 2.4 times longer than those with the R=-0.5 curve. The total life prediction is relatively accurate in the long-life region.

The investigation in this section indicates that the three SIF calculation approaches generate similar results. BS7910 is chosen to conduct the VA predictions.

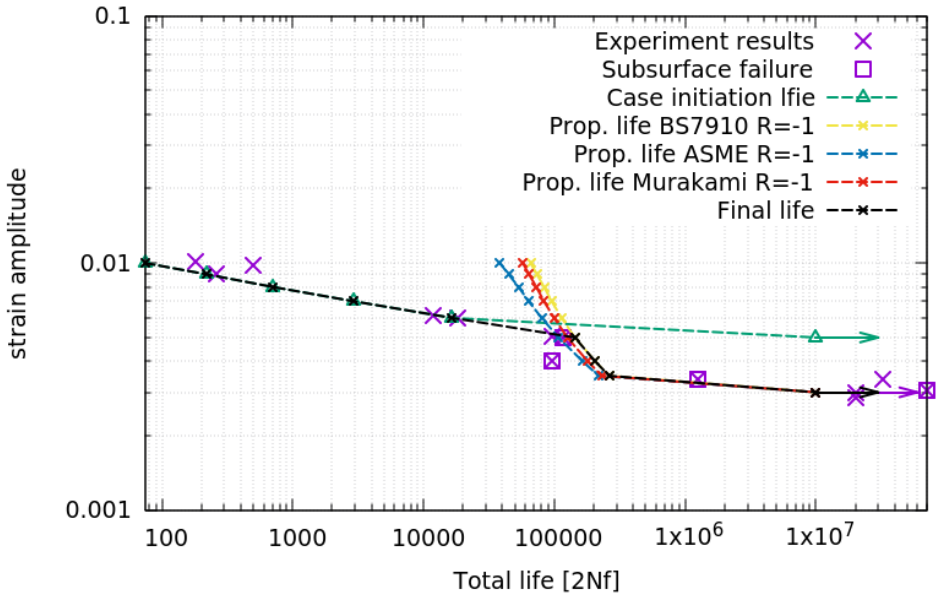

Figure 6.19: Crack propagation simulation results from the three models using ASME da/dN curve for R=-1 compared with experimental data for CA smooth samples

6.2.2 VA loading subsurface crack propagation simulations

Simulations were run to predict the fatigue life of the case-hardened axial samples loaded under bracket VA histories at multiple stress levels. The stress histories at different layers were obtained by following the procedure described in Section 6.1 and plotted in Figure 6.3.

Figure 6.9 shows that the crack was predicted to initiate at subsurface under the bracket loading history at all stress levels except for the maximum level simulated. The subsurface crack propagation model for an interior initiation was applied using the middle layer material properties and stress histories. The total life is chosen as the shorter of the case initiation life and the middle layer crack propagation lives.

In this study, it is assumed that inclusions, 0.15 mm in radius, exist in the subsurface, thus the subsurface crack propagation life equals to the total fatigue life if it starts from a flaw in the subsurface.

To account for the varying stress-ratios in the VA histories, the "Hasegawa1" da/dN curves shown in Figure 2.22 were used for estimating the crack growth rate after each reversal.

Due to the tensile mean residual stress in the subsurface layers, the crack growth curves for R=-0.5 and R=-1 were frequently applied during the simulation. The crack growth rate of R=-0.5 is around three times that of R=-1. To be conservative, in the crack growth simulation, when an R-ratio fell between two of the "Hasegawa1" da/dN lines, the R-value was taken as the higher da/dN line. Two crack growth rate curves for R=-0.65 and R=-0.8 were interpolated and used in the simulations to achieve a better resolution for da/dN computation. The enhanced da/dN curves are plotted in Figure 6.20.

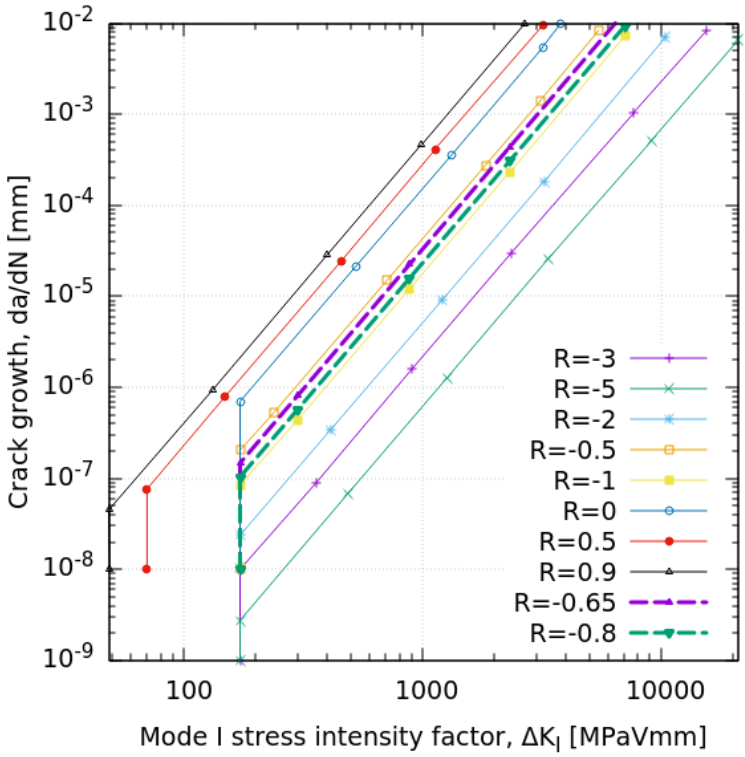

Figure 6.20: Crack growth curves with interpolated lines for R=-0.65 and R=-0.8 based on the "Hasegawa1" da/dN curves (10 ASME da/dN curves)

The simulated VA results from the original (Figure 2.22) and the enhanced "Hasegawa1" da/dN curves with the two extra stress ratios (Figure 6.20) are shown with experimental results in Figure 6.21.

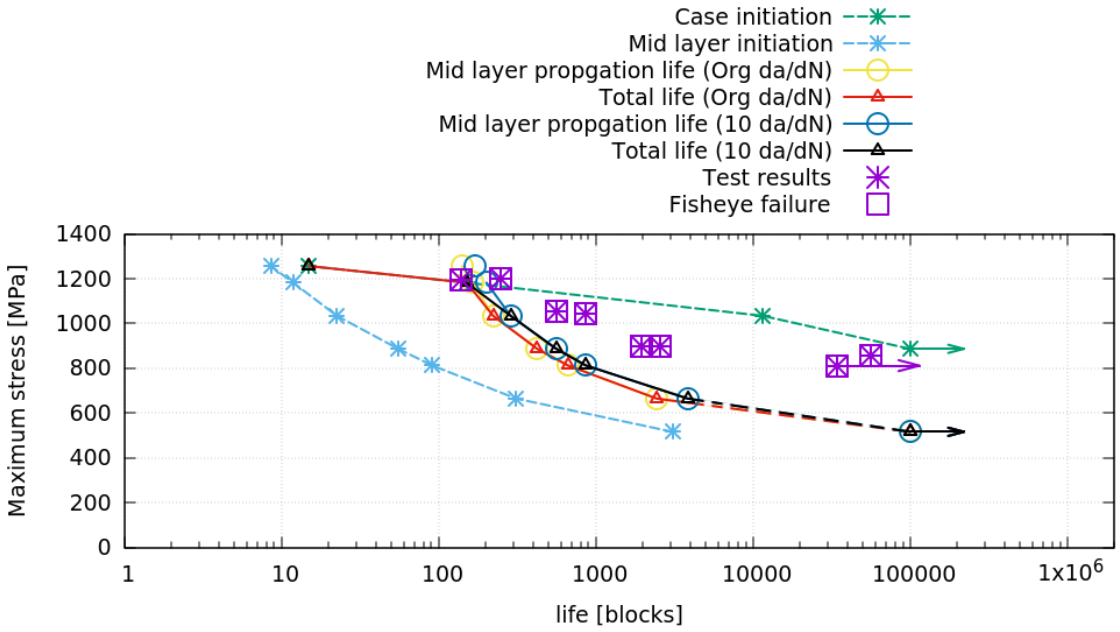

Figure 6.21: Smooth specimen subsurface crack propagation simulation results for VA bracket history with the original and the enhanced "Hasegawa1" da/dN curves

As mentioned earlier, the predicted middle layer initiation life is much shorter than that of the case layer. Therefore, the shorter of the middle layer crack propagation life or the case initiation is taken to be the total predicted life.

The total life predicted using the original and the enhanced "Hasegawa1" da/dN curves (the red and black lines in Figure 6.21) are conservative. The enhanced "Hasegawa1" da/dN curves extended the crack propagation lives slightly. However, the predicted life is still much shorter than the test results. The threshold region of the "Hasegawa1" crack growth curves is conservative, which probably contributed to the short predicted life in the subsurface crack growth model.

Hasegawa et al. [54] proposed Equation 2.60 to calculate ΔK_{th} for different stress ratios.

This set of da/dN curves were named "Hasegawa2" in this thesis, and plotted in Figure 2.24. They were employed in the middle layer crack propagation model. The fatigue life predictions for the composite axial samples loaded under CA and VA histories are shown in Figure 6.22 and 6.23.

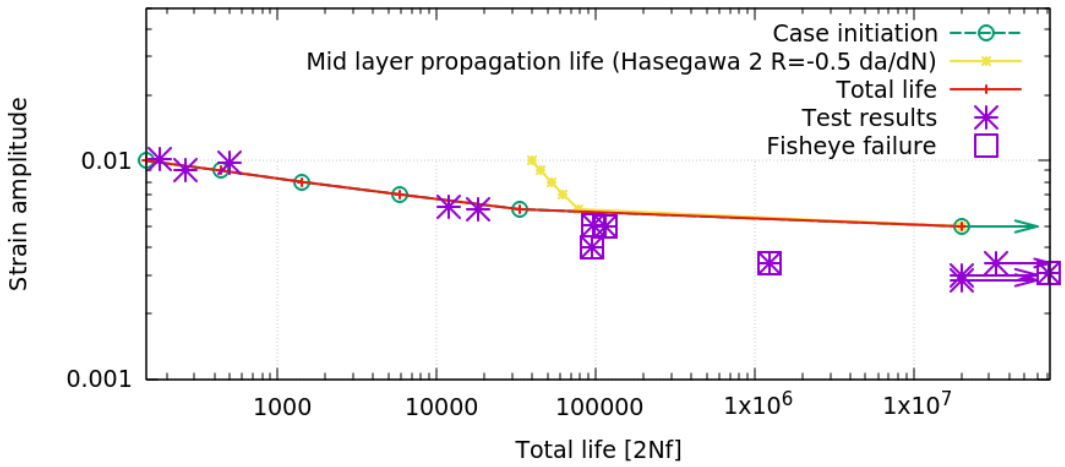

Figure 6.22: Smooth specimen subsurface crack propagation simulation results for CA loading history with the "Hasegawa2" R=-0.5 da/dN curve

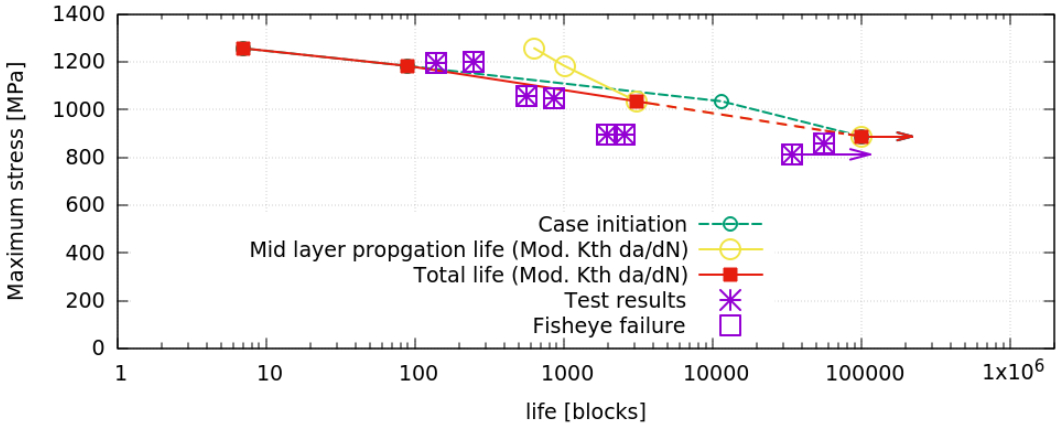

Figure 6.23: Smooth specimen subsurface crack propagation simulation results for VA bracket history with the "Hasegawa2" da/dN curves

The middle layer crack propagation life predicted using the "Hasegawa2" da/dN curves

for both the CA and VA loadings are slightly non-conservative. This is probably caused by the high SIF threshold values at the negative stress ratios.

The simulations using the "Hasegawa1" and the "Hasegawa2" da/dN curves predicted conservative and unconservative fatigue lives for the smooth specimen under VA loading, respectively. The difference in ΔK_{th} between the two sets of da/dN curves leads to the variation in the fatigue life prediction.

The collected vacuum crack growth data [136, 141, 51, 131] plotted in Figure 2.26 indicates that in the vacuum environment, the stress ratios have little effect on crack growth rate. A da/dN curve is fitted through the vacuum crack growth data. This curve is plotted in Figure 6.24 with the collected data and the "Hasegawa1" da/dN curves in the background as a reference.

Most of the collected vacuum data are very close to the R=-0.5 curve, except those near the threshold region which have a slightly slower crack growth rate. Therefore, the R=-0.5 curve in the multi-R-ratio da/dN with an adjusted threshold value is used as the vacuum crack growth curve (plotted in black in Figure 6.24).

The CA simulations were run using the same parameters and the fitted vacuum da/dN curve. The results are plotted in Figure 6.25 with the experimental data. Under CA loading, the model predicts a higher runout limit than the experimental data.

The crack propagation results simulated using the fitted vacuum crack growth curve for VA histories are plotted in Figure 6.26.

Using the fitted vacuum da/dN curve, the simulated results are less conservative and closer to the test results than those simulated using the "Hasegawa1" da/dN curves, especially at low-stress levels. The higher ΔK_{th} in the vacuum fitted curve contributed to this change. The maximum stress at the simulated runout level increased from 517 MPa to 665 MPa. Nevertheless, the prediction is still conservative. This could be attributed to the bi-linear shape of the applied da/dN curves, which could yield a faster crack growth rate than a rounded da/dN curve near the threshold region. In this region, all the low SIF vacuum data lay on the right side of the fitted curve (shown as the black line in Figure 6.24).

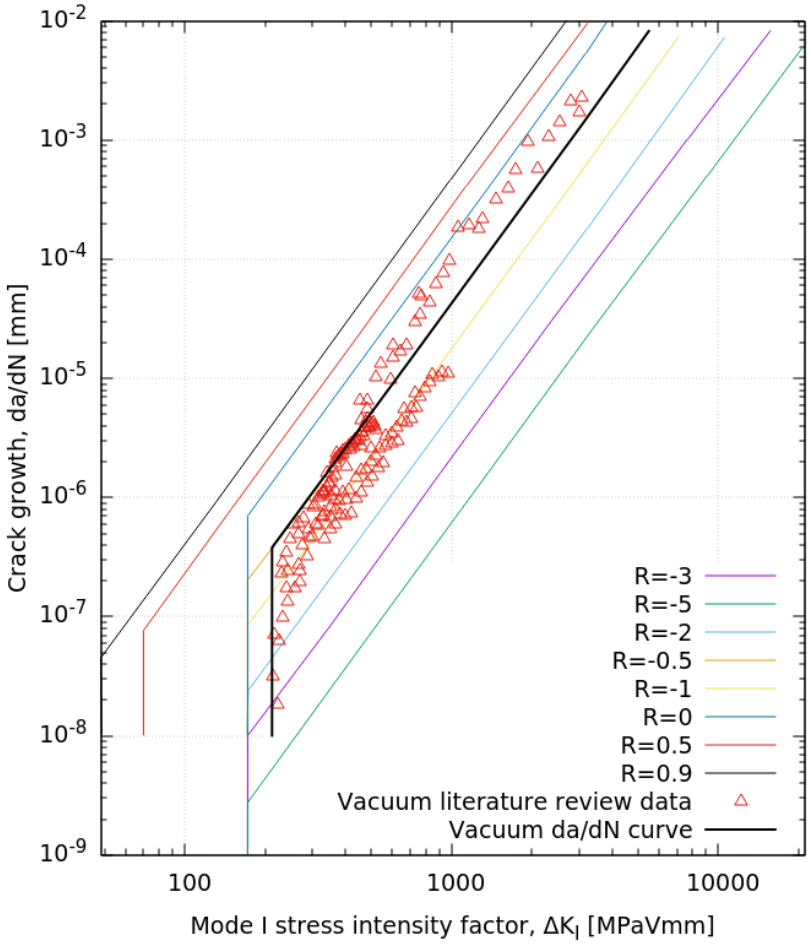

Figure 6.24: Crack growth curves fitted through the collected vacuum data [136, 141, 51, 131] with the "Hasegawa1" da/dN curves included as reference

The predicted threshold stress under VA loading is lower than the experiment's, yet, the reverse is true under CA loading. If mean stress affects the crack growth rate in the subsurface layer, the relaxation of the initial tensile mean residual stress in the middle and core layers could contribute to this phenomenon.

A theoretical intrinsic crack length, depending on the threshold SIF and the stress range at the fatigue limit, can be calculated using Equation 2.51. The fitted vacuum

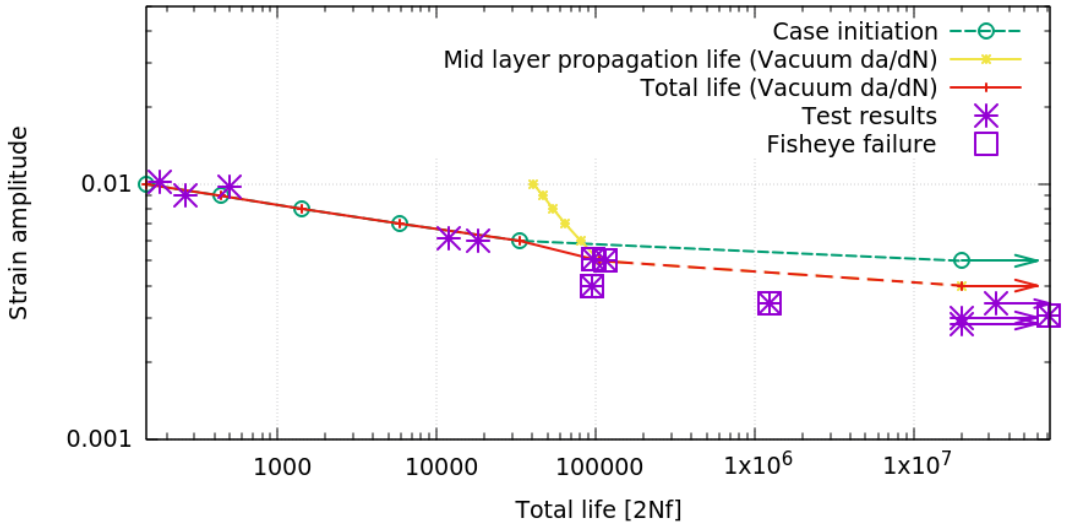

Figure 6.25: Smooth specimen subsurface crack propagation simulation results for CA loading history with the fitted Vacuum da/dN curve

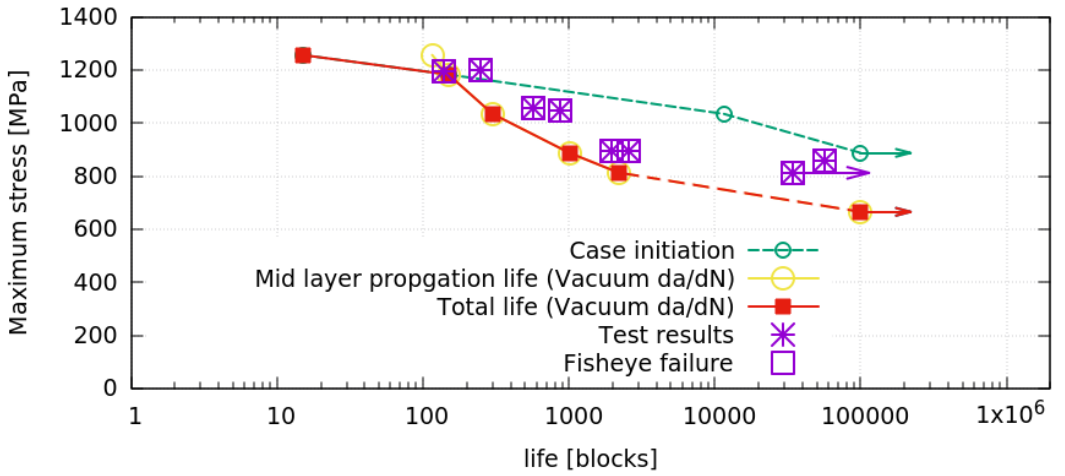

Figure 6.26: Smooth specimen subsurface crack propagation simulation results for VA bracket history with the fitted Vacuum da/dN curve

da/dN curve consists of a threshold SIF, ΔK_{th}, of $212MPa\sqrt{mm}$. The core stress-life curve yields a fatigue limit stress range, $\Delta\sigma_f$, of 1293 MPa. The crack geometry factor,

F, for subsurface elliptical crack determined from BS7910 [14] is 0.637. By substituting the above parameters in the Equation 2.51, an intrinsic crack length, a_o, of $0.0211mm$ was calculated.

The measured inclusion diameter, which is considered to be the initial crack length, is $0.015mm$. This is slightly shorter than the calculated intrinsic value. The $\Delta\sigma_f$ of the core material was measured in an air testing environment, which has shown to be lower than that in the subsurface. The lower $\Delta\sigma_f$ parameter used in the calculation would contribute to the longer calculated intrinsic crack length compared to the measurement.

6.3 Fatigue life prediction for composite notched plate

The fatigue life of the composite notched sample was investigated to study a scenario comparable to a case-hardened component design in real life.

The conservative predicted fatigue life curves for the core and the composite notched samples shown in Figure 4.11 suggest that crack propagation in the core takes up a significant portion of the total life in those notched samples. Therefore, the fatigue life of the composite notched sample was calculated as the sum of the notch case layer initiation life and the subsequent core layer crack propagation life.

6.3.1 Initiation prediction in the composite notched sample

The crack initiation lives of the case and the core layers of the composite notched sample were estimated. The shorter of the two indicates the initiation life and location in the composite notched sample.

Case layer cracks will initiate at the stress raiser in the composite notched sample. Therefore, to estimate the case layer initiation life, Neuber's rule was applied to calculate the local stress at the notch while accounting for the stress concentration factor. The case layer strain history, including the residual stress developed during the carburization process and stress-induced RA transformation, was generated following the procedure described

in Figure 6.1. Then the strain history was converted to the corresponding nominal stress history using the fitted cyclic stress-strain curve of the case material.

The K_t factor for a circular notched in a finite plate can be calculated using Equation 2.21. The K_t in the composite notched plate sample was determined to be 3.02, which was approximated to 3 while estimating the local stress and strain using the Neuber's rule for the case initiation life prediction. The case layer material properties used in this simulation are plotted in Figure 4.7 and 4.8.

Because the core layer in the composite sample is outside of the stress concentration zone (as shown in Figure 2.18), the stress applied in the core layer equals the nominal stress. Since the core layer lies inside a carburized case, a crack can start internally or after the case has been cracked. With internal initiation, initiating from a flaw underneath the case layer, the stress-life curve equals to that of the composite smooth specimen, shown as the purple points in Figure 6.27. If the crack initiates in the case layer at the notch, the initiation life is predicted by the smooth specimen case curve adjusted by the stress concentration factor, which is plotted in black.

Three case initiation predictions are plotted in Figure 6.27. The green dashed line is the prediction for the composite axial sample without any stress raiser effect. The blue dashed line was obtained by dividing the stress levels in the green dashed line by a factor of 3. The black dashed line was determined using a K_t of 3 and Neuber's rule as described earlier in this section.

The difference between the dashed blue and black lines is negligible, which can be explained by the mostly elastic cyclic stress-strain curves of the case material.

The predicted case initiation life is shorter than the composite notched sample test results, especially in the short-life region. Crack propagation in the core after the failure of the case could increase the predicted fatigue lives.

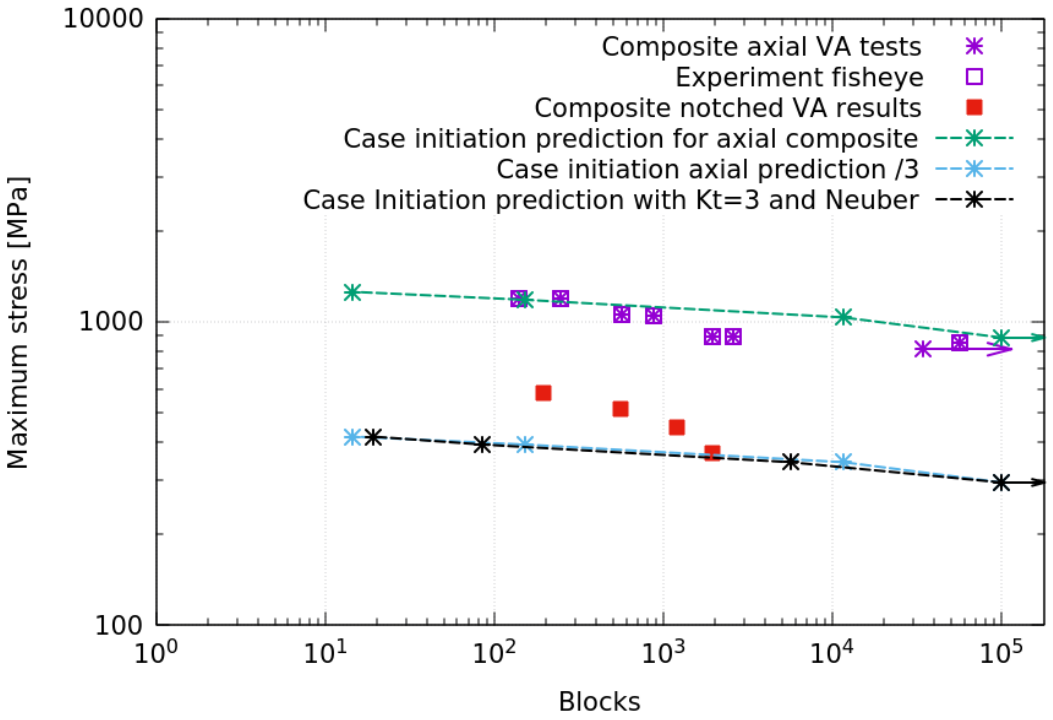

Figure 6.27: Initiation predictions for composite notched samples compared with axial and notched samples test results

6.3.2 Core layer crack propagation simulation

Two crack propagation models, a through-thickness centre crack model and a corner crack model at a hole, were run to determine the propagation life in the core layer of the composite notched sample. Since the case layer of the notched composite sample has cracked, it is assumed that no residual stress remains in the core layer due to force balance. The original bracket loading histories at different nominal stress levels were used in the core layer crack propagation life estimate. The core material properties were applied in these simulations.

Through-width centre crack

Figure 6.28a shows the through-thickness centre crack geometry defined by BS7910. Figure 6.28b demonstrates the assumed plate geometry on the composite notched sample fracture surface, where the initial half centre crack length, a_0, is the sum of the notch radius and the case depth.

The case depth of the plate along the notch was measured on its fracture surface via ImageJ, since the case layer can be visually distinguished by the discoloration. Before the measurement, the scale was calibrated based on the 1 mm notch diameter. The case depth was found to be 0.52 mm, which matches the residual stress and the micro-hardness profiles of the notched composite sample.

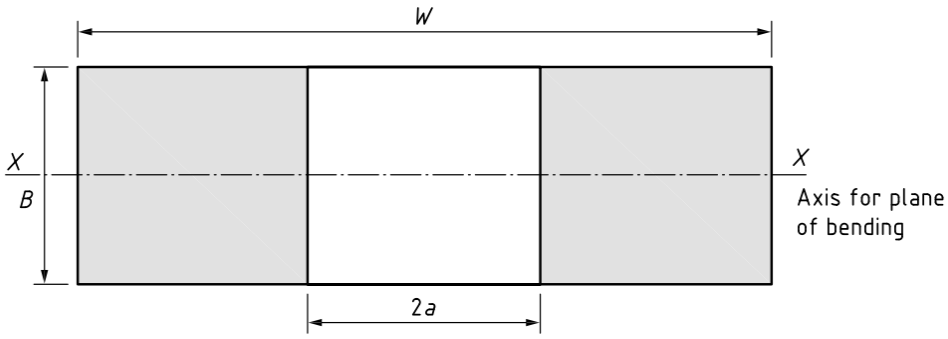

(a) BS7910 through-thickness flaw geometry [14]

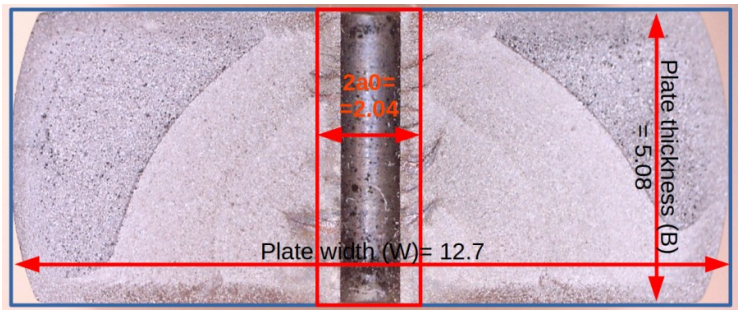

(b) Fracture surface of the composite sample with through crack parameters

Figure 6.28: Centre through-thickness flaw demonstration

Equation 2.37 was applied to determine the ΔK_I of the crack, and F_w was determined

using Equation 2.29.

To account for the crack growth rate at different stress ratios, the "Hasegawa1" da/dN, plotted in Figure 2.22, were employed in the crack growth calculations.

The predicted total fatigue lives, defined as the sum of the case initiation and the through-crack core propagation lives, of the composite notched sample are plotted with the experimental data in Figure 6.29.

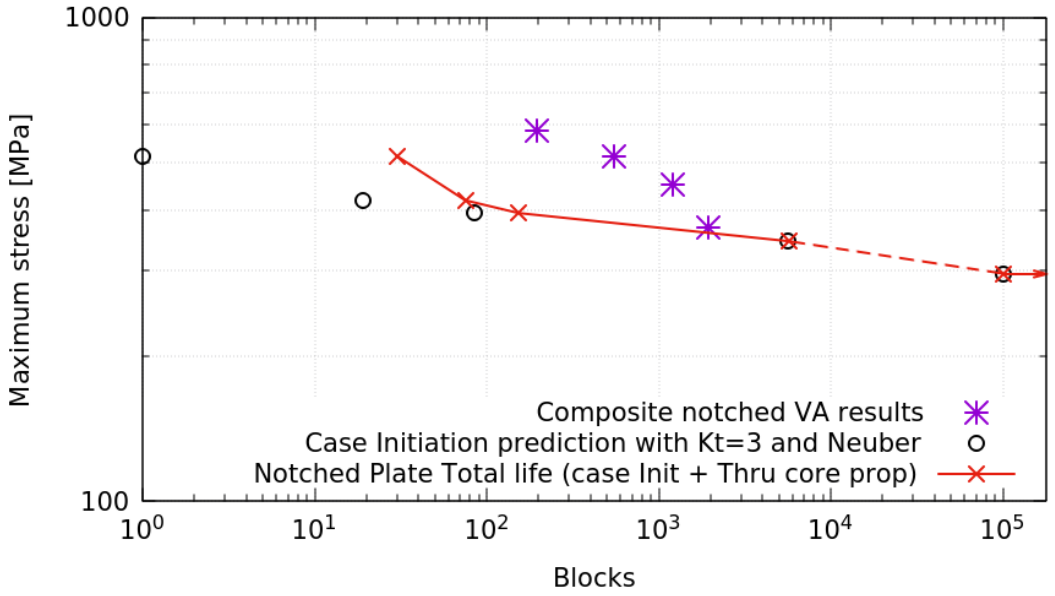

Figure 6.29: Total fatigue life (initiation + propagation) prediction for composite notched samples assuming full through crack at centre of plate

Due to the short predicted initiation life, it is probable that crack propagation takes up a significant portion of the total fatigue life at the high-stress levels. However, in the long-life region, the crack propagation life has a negligible effect on the total life.

The predicted total life is still substantially conservative at the high-stress levels.

The crack propagation life predictions, prolonged by running the simulations with the crack growth curves plotted in Figure 2.24, is negligible at the high-stress levels, since most of the crack growth occurs above the threshold region.

Corner cracks at a hole

The ΔK_I for corner cracks at a hole was calculated using the methodology described in Section 2.13. The indicative geometry of the cracks on the plate is demonstrated in Figure 6.30.

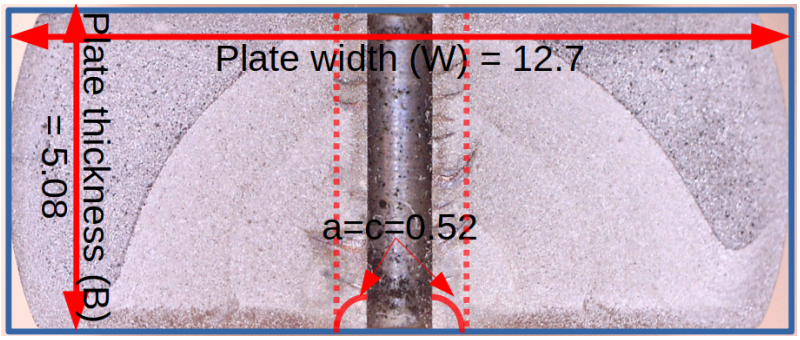

Figure 6.30: Fracture surface of the composite sample with corner flaws parameters

The width (W) and thickness (B) of the composite notched plate are 12.7 mm and 5.08 mm, respectively. The notched radius (r) is 0.5 mm. The initial cracks growing into the thickness (crack a) and along the width (crack c) of the plate are both assumed to be 0.52 mm long, which is the case layer depth. Since there is one corner crack on each side of the symmetrical plate, n in Equation 2.53 equals 2. The crack propagation simulations for the core layer were conducted using "Hasegawa1" da/dN curves shown in Figure 2.22.

Unfortunately, the specimen design of the composite notched plate sample does not satisfy the applicable condition of $0.5 \leq r/B \leq 2$ listed in BS7910 for corner cracks ($r = 0.5$ and $B = 5.08$). The samples used in the study are too thick for the designed notch radius; alternatively, a larger notch should be drilled for the existing plate size. Regardless of the out-of-range situation, the simulation was run to obtain propagation results.

In the corner crack growth program, the f_w and M_m values for cracks a and c were pre-calculated for the specified range, and an array was generated as an output. This predetermined array was then fed into the main crack propagation program, and the nearest a and c cracks values in the array were chosen to determine the corresponding M_m and f_w factors. In this approach, the original M_m and f_w calculations (which involve calculations,

including the power of factors and large numbers) do not have to be conducted at each reversal. The computation time can be significantly shortened using this approach rather than directly calculating the M_m and f_w at each reversal from the equations.

The output array consists of 75 crack a and 75 crack c values in this simulation. Constant factors, k_a and k_c, determined using Equation 6.2, were applied to calculate the next a and c values based on the previous ones.

$$k_a = (\frac{a_n}{a_0})^{(\frac{1}{n_a})} \tag{6.2}$$

where a_n and a_o are the upper and lower bounds of the a crack length, and n_a is the number of points in the array for crack a values (75 in this case). The same equation was applied to determine k_c using the c crack boundaries. By applying the scaled interval instead of the evenly spaced interval, more data points were generated at the small crack lengths region, where most of the propagation life was spent.

The applicable range for M_m listed in BS7910 [14] is $0.2 \leq a/c \leq 2$. However, in this simulation, it was found that the crack ratio grows out of the applicable range in a relatively early stage. Therefore, if the crack ratios are outside the defined range in the simulation, the last valid M_m values were reapplied.

The M_m values at $\theta = 90$ (along crack a) generated from the corner crack propagation simulation with a maximum stress of 517 MPa are plotted with the predetermined array for the corresponding M_m in a 3D plot, in which the x and y axes are the a and c crack lengths, respectively. Figure 6.31 shows two views of the 3D plot at different angles.

The M_m values at $\theta = 00$ (along crack c) are plotted in Figure 6.32 with the pre-calculated M_m array.

The simulated M_m values, plotted in green, follow along the predetermined M_m array surface before reaching beyond the boundary of $a/c = 2$. In the simulation with a max stress of 517 MPa, the M_m for both cracks a and c diverge from the surface at $a = 1.89mm$ and $c = 0.945mm$, and the M_m values for crack a and crack c stay constant at $M_m90 = 0.889$ and $M_m00 = 0.878$, respectively, as the cracks grow further.

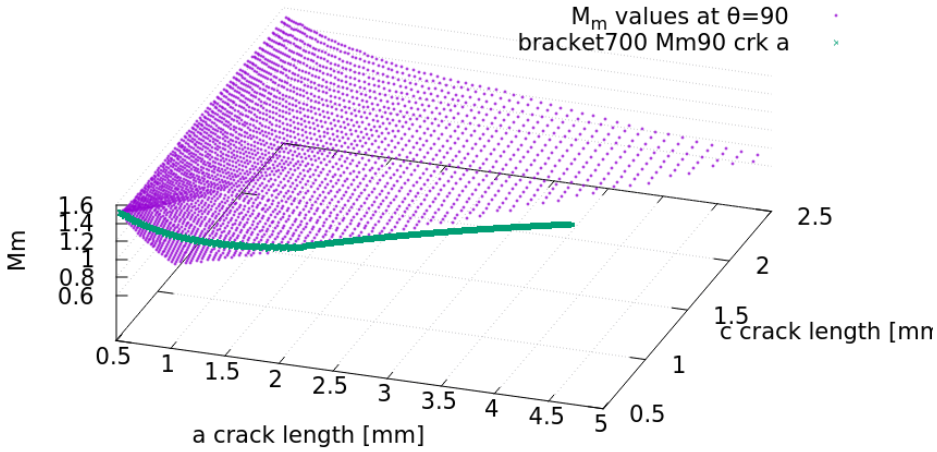

(a) Orientation 1

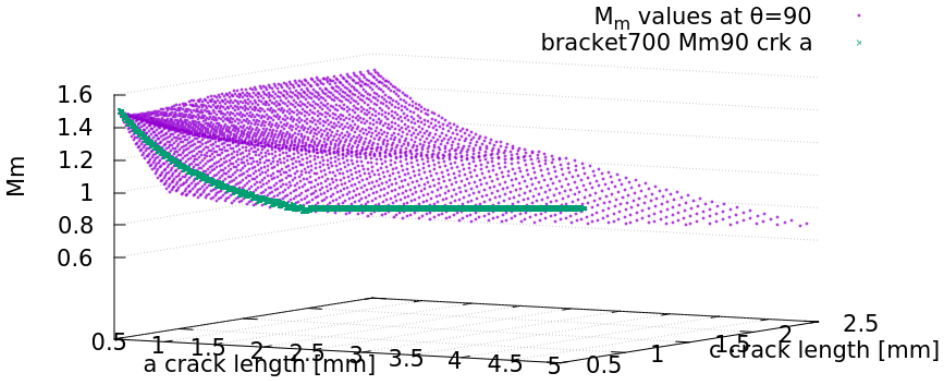

(b) Orientation 2

Figure 6.31: Simulated Mm values for crack a on the predetermined grid

Since the stress concentration factor for membrane load, M_m, dwindles as the cracks grow away from the stress raiser, keeping the M_m values constant at a short crack length would generate a relatively conservative prediction. The M_m values in the array along

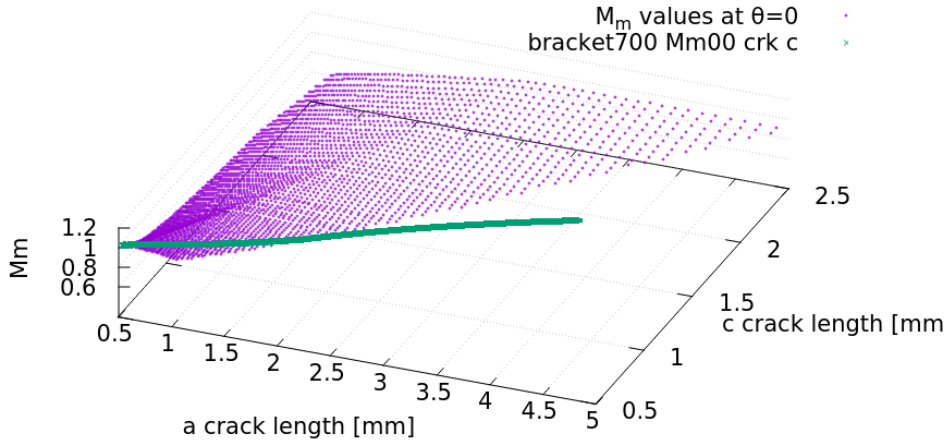

(a) Orientation 1

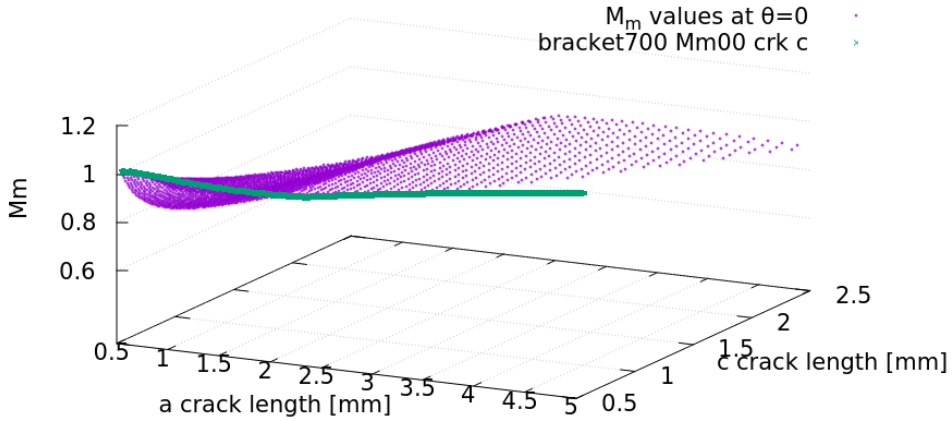

(b) Orientation 2

Figure 6.32: Simulated Mm values for crack c on the predetermined grid

the axis for crack c seem to be relatively stable after the point M_m was switched to a constant along the boundary of $a/c = 2$. While for crack a, the M_m values continue to drop moderately as the crack grows.

For the corner crack propagation simulation with a maximum stress of 517 MPa, the da/dN vs ΔK data points along both crack a and crack c were extracted and plotted with the "Hasegawa1" da/dN curves in Figure 6.33.

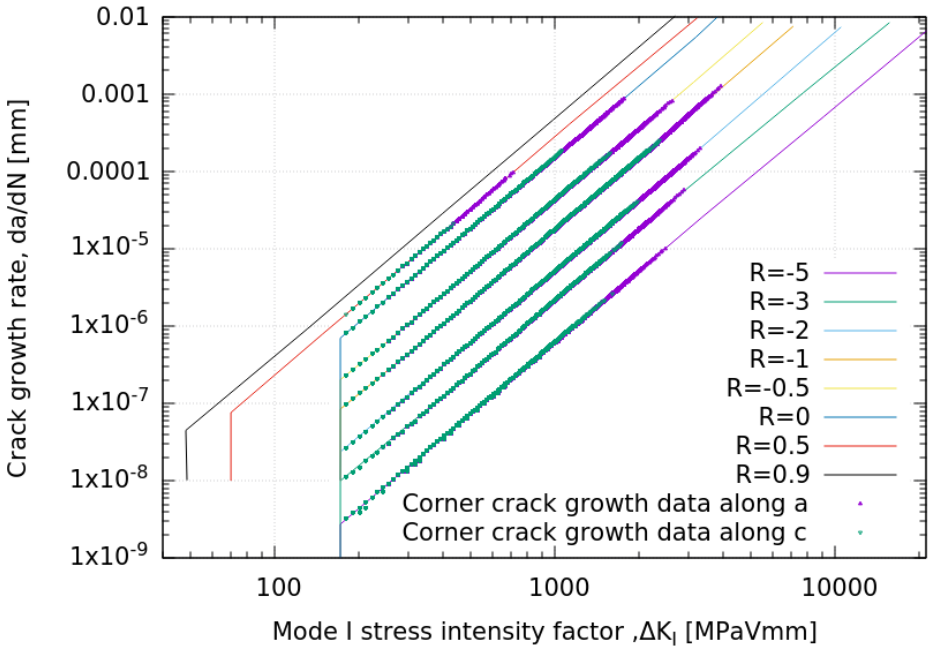

Figure 6.33: Crack growth data for cracks a and c in the corner crack simulation with maximum stress of 517 MPa plotted with the "Hasegawa1" da/dN curves

A higher crack growth rate along crack a (purple points) than crack c (green points) can be observed in this plot, which means that the corner crack propagates faster into the thickness than along the width. Therefore, a through-thickness crack could form at a relatively early stage of the fatigue life .

The crack growth data in the same simulation are plotted with colours that indicate the number of times a specific growth rate was applied along the da/dN curves in Figure 6.34a. While, in Figure 6.34b, the colour denotes the total damage, calculated as the number of points multiplied by da/dN, generated at each point of the curve. The growth rates for both cracks a and c are included in these plots.

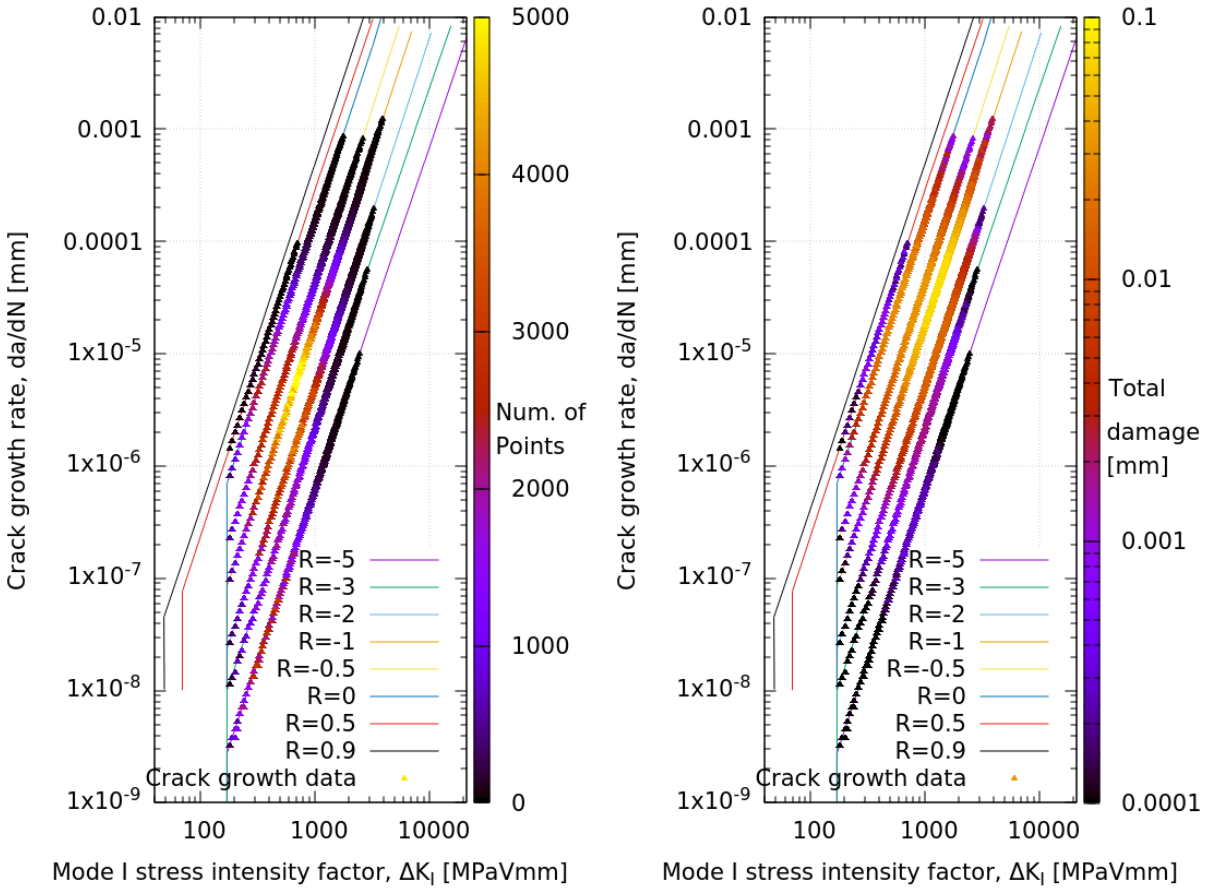

(a) Palette for number of points

(b) Palette for damage caused

Figure 6.34: Crack growth data plotted with palette in the corner crack simulation with a Bracket history maximum stress of 517 MPa on the "Hasegawa1" da/dN curves

The yellow and red zones on the curve on Figure 6.34a indicate that the crack growth curves for R between -0.5 to -2 were employed the most in this simulation with a ΔK_I in between $400MPa\sqrt{mm}$ and $2000MPa\sqrt{mm}$. Due to the fast growth rate in the high ΔK region, the cracks grow to a fracture in very few cycles; and only a handful of points are located in this region. However, Figure 6.34b shows that the high K_I points on the crack growth curves at $R > -2$ generated some substantial damage in the simulation. In contrast, little damage was caused by the near threshold region when $R < -0.5$.

The predicted total fatigue life results using the corner cracks model and the "Hasegawa1" da/dN curves are plotted in Figure 6.35. The initiation points and the predictions using the through-thickness crack model are also included for reference.

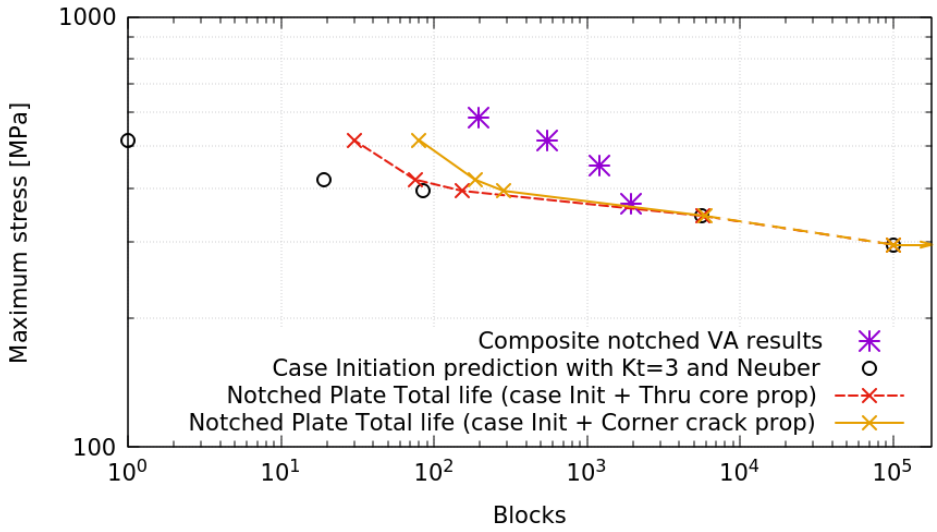

Figure 6.35: Total fatigue life (initiation + propagation) prediction for composite notched samples with corner crack propagation life using the "Hasegawa1" da/dN curves with constant K_{th} at $R < 0$

The total life predicted using the corner crack propagation model in the short-life region is considerably longer than the through-width crack model, while the difference in the low-stress region becomes negligible. Even though the corner crack propagation model predicted a longer life than the through crack model, the simulated total fatigue life is still conservative compared to the test data in the high-stress region.

Another simulation was conducted with the same corner crack propagation model but using the "Hasegawa2" crack growth curves as shown in Figure 2.24. The predicted results are plotted in Figure 6.36 with those from the "Hasegawa1" da/dN curves.

Using higher thresholds, ΔK_{th}, for crack growth at negative stress-ratios almost made no difference in the predicted propagation life. The propagation lives in the two highest stress levels lengthened by one block, yet, the change is imperceptible on the plot.

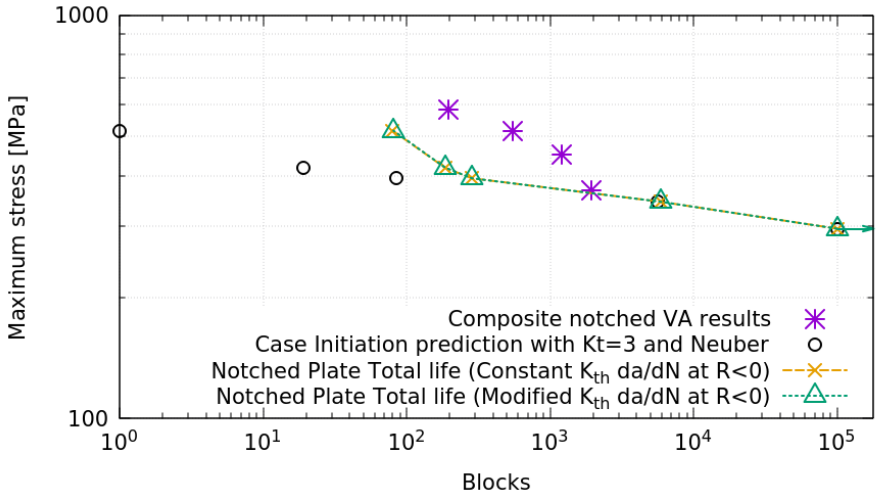

Figure 6.36: Comparison of the total life predictions (initiation+propagation) for the composite notched samples with corner cracks at a hole using the "Hasegawa1" and "Hasegawa2" da/dN curves

6.3.3 Discussion

The total life predictions for the composite notched samples under VA are conservative. The potential reasons that have contributed to this are:

- The stress concentration factor at high-stress levels could be smaller than the constant K_t applied in this simulation [21];
- Neuber's approach is conservative for local stress and strain estimates compared to the energy method proposed by Molski and Glinka [100];
- The M_m values for the crack decrease as the crack elongates; however, due to the applicable range issue, a constant and conservative M_m was used, especially for the crack growing into the thickness.
- The coaxing effect in the case layer of the composite notched sample could lengthen the initiation life under VA loading;

Chapter 7

Discussion, conclusions and recommendations

This chapter includes discussion of the previously-presented research, conclusions of the research and some recommendations for future investigation.

7.1 Discussion

7.1.1 Effective-strain based and multi-R-ratio model comparison

The effective-strain based model and the multi-R-ratio model with Hasegawa1 growth curves were reviewed and the simulation results obtained by applying the two models to predict the fatigue life of G40.21-50A notched plates are compared in this study.

A large amount of test results were collected for the effective stress intensity factor vs. crack growth rate. The collected data plot shows that, unlike the traditional crack growth curves, the effective growth curves are independent of R-ratio, sample thickness and material hardness. Some scatter can be observed at the threshold region of the da/dN vs. ΔK_{eff} data.

Both the initiation plus Hasegawa1 crack growth simulations and the effective-strain based simulations predicted the final life within a factor of two of the G40.21 steel experimental results, except for those under the suspension history. The reasonable predictions indicate that the assumptions for the effective-strain based material inputs are appropriate. Nevertheless, improvements can be made by conducting POL tests on smooth specimens to produce a fully effective strain-life curve, and enhance the accuracy of the steady-state crack opening stress fitting.

Errors in the long fatigue life predicted by the multi-R-ratio model with the Hasegawa1 crack growth curves may be due to the unconservative assumption that zero damage is caused by the fully compressive half cycles. The lack of load level interaction in the multi-R-ratio approach can be another factor that causes the unconservative prediction for the G40.21 steel, especially under the suspension load history.

Due to the unconservative life predictions for the suspension load history, crack growth behaviour under fully compressive loads with occasional overloads should be further investigated.

Due to the complexity of the strain-based method, it was not implemented to predict the the crack propagation life in the case-hardened samples.

7.1.2 Experiments

In this study, extensive experiments were conducted to understand the material behaviour of the different layers in the case-hardened 16MnCr5 steel samples. The through-carburized case, simulated core and case-hardened composite samples were subjected to fully reversed CA loading to obtain their fatigue properties. Negative mean stress CA tests were conducted on case axial samples, and the results confirmed the accuracy of the negative mean stress rule for very hard steel proposed by Diogo et al. [47]. The CA and POL tests on the case and the core material indicate that overloads have little detrimental impact on the fatigue performance of these two materials. On the other hand, an increase in fatigue strength due to the coaxing effect was observed in the through-carburized case samples.

The stress-life data obtained from the full and the filtered bracket VA history tests on the composite axial samples overlapped, suggesting that the eliminated small cycles in the unfiltered VA tests do not cause damage. The eliminated small cycles were all below the fatigue limit of the composite sample under CA fully reversed load.

Several CA tests were conducted on the notched plates for the case, core and composite materials to study the notch effect. The notch in the case material lowered the fatigue curve by a factor of 3 (K_t of the notch) compared to the axial samples. However, directly applying the K_t factor for the core and composite axial fatigue life produces a conservative prediction for the notched samples. The crack propagation phase in the core and composite notched samples was thought to contribute to this difference. The fatigue life for the case and composite notched plates loaded under full bracket VA histories were also obtained, and were used to evaluate the accuracy of the simulation results.

Composite axial samples loaded under a VA at all the ranges examined failed from the subsurface, as well as those at the long-life region under CA load. However, no fisheye cracks were found on the fracture surface of the composite notched plates. The fracture surfaces with a subsurface failure in the axial composite samples were examined by taking SEM images and zoomed-in pictures. Inclusion and fisheye sizes of two composite axial samples were measured and used as inputs for the subsurface crack propagation model.

The crack growth results collected at stress ratios of -1 and -3 from the core notched plate are reasonably close to the Hasegawa1 da/dN curves at the corresponding stress ratios.

The fatigue and cyclic stress-strain properties of the transition layer of the composite sample were derived based on those of the case and the core materials, and the properties were used in the three-layer model for residual stress estimation and fatigue life prediction.

Mean stress relaxation, which consistently increases with the strain amplitude in a single sample, was observed in simulated core material. However, variations were found between samples under strain control. In the through-carburized case sample while in strain control, RA transformed at the beginning of the tests, which caused the initially negative mean stress to shift towards more negative values. Relaxation occurred after the

RA transformation was completed. It is hard to study the mean stress relaxation in the case material because of interference from the RA transformation effect.

7.1.3 Residual stress and RA studies

The initial residual stresses of the case-hardened composite plate and axial samples generated during the carburization and quenching process were estimated using both a three-layer FE model and a compatibility model. The stress-strain curves of the case and the core materials are the inputs for the FE model, while elastic behaviour was assumed in the compatibility model. The compatibility model predicted a reasonable longitudinal residual stress profile for the composite samples, and the FE model was able to simulate the residual stress in the hoop direction.

The influence of RA transformations on residual stress on case-hardened 16MnCr5 steel under axial load was examined. An asymmetry of stress-strain behaviour was observed in both the through-carburized case material and the case-hardened material. In both types of samples, the tensile stress-strain curves of the deep-freeze samples lay in between the normal tensile and compressive curves, which indicates an RA transformation under both the tensile and the compressive loads. This observation was confirmed by the RA measurements made in each of the loading cases.

In order to study the changes of RA and residual stress due to loading, case-hardened axial samples were strained under four loading histories. The RA content and the RS were measured using XRD after each of the tests. The compatibility model and the FE model were applied to simulate the stress-strain behavior and the residual stress profiles of the case-hardened material. The inputs of the model include the stress-strain curves of the case and the core materials, as well as the amount of RA transformed in the case layer of the composite sample. The results of the residual stress predictions from the two models are reasonably accurate. The compatibility model generates reliable post-loading longitudinal residual stress profiles of the case-hardened sample; however, it tends to underestimate both the tensile and compressive stress peaks in the strain-controlled

loading histories. Neglecting the effect of residual stress in the hoop direction on yield stress probably contributes to this error.

Based on the amount of RA measured after the four (2 partial life and 2 full life) fatigue tests, the relationship between the Von Mises stresses in the case layer and the percentage of RA transformed was determined. This enabled calculation of the RA transformation induced strain expansion in the case layer due to the strain amplitude imposed on the composite sample.

Residual stresses remaining in the composite axial samples after several types of loading were estimated and compared with measurements. Three residual stress models were considered: 1) with initial residual stress including both the carburization and RA transformation effect; 2) with initial residual stress due to the carburization effect; 3) a sample with no initial residual stress. The measured residual stress in the case layer after some loading is closer to the prediction generated by Model 1), and that in the middle and core layer are closer to the measurement using Models 2) and 3).

7.1.4 Fatigue analysis

The crack initiation locations in the composite axial samples loaded under CA and VA histories were predicted using a three-layer model with the strain-life curves of each layer while considering the three residual stress conditions mentioned above. The initiation location predicted with residual stress Model 1) matches the experimental results the best.

The composite material fatigue properties obtained from the CA tests were used to predict the fatigue life of the composite axial samples loaded under VA histories. The obtained results are within a factor of two of the experimental fatigue lives.

The BS7910, ASME and Murakami's SIF estimation for subsurface elliptical crack propagation were compared. All three models produced similar results. The approach adopted by BS7910 was applied to predict the subsurface crack propagation life of the composite axial sample under CA and VA loading. The Hasegawa1 da/dN curves generated accurate CA loading history predictions but conservative results under VA loadings. Using

the Hasegawa2 da/dN curves, the crack propagation lives became unconservative even under VA loading.

The da/dN curve fitted to the collected vacuum crack growth data generated the best-matching results for VA loading histories, while the predicted fatigue limit under CA load is unconservative. This choice of the vacuum da/dN curve is thought to be reasonable since the collected vacuum crack growth data seem to be independent of R-ratio, but more vacuum fatigue data would be useful.

In the composite notched sample VA tests, no fisheyes were found on the fracture surface. In the predictions, the case layer initiation model that includes the stress raiser effect predicted a much shorter initiation life than the core layer with nominal stresses. Both the experiments and the simulations indicate case layer crack initiation at the notch. The total fatigue life estimates for the composite notched sample are conservative, when the core propagation life and the total propagation life were predicted using the through-thickness crack and corner crack models with nominal stresses.

7.2 Conclusions

The comparison between the effective-strain based model and the multi-R-ratio model using Hasegawa1 crack growth curves shows that both models produced adequate results for a centre notched sample loaded under random VA histories with positive or near-zero mean stresses. The multi-R-ratio model was chosen to run the crack propagation simulation in the carburized steel analysis due to its simplicity in implementation and the abundantly available crack growth data.

This study indicates that fatigue lives of the case-hardened composite smooth and notched samples under VA loading are best estimated by taking the following steps:

- estimate the initial residual stress in the composite sample generated during the carburization process;

- determine the amount of RA transformed under cyclic loading and evaluate the residual stress in each layer of the composite sample including this effect;
- estimate the initiation life in the case layer of the composite sample;
- apply the subsurface elliptical crack propagation model adopted by BS7910 to calculate the core layer crack propagation life from the inclusion to failure in the smooth sample; use through-crack or corner crack models to determine the core layer propagation life in the notched sample.
- the final fatigue life of the smooth composite sample should be taken as the shorter of the case initiation and the core propagation lives; while the final life of the notched sample is best calculated as the sum of the case initiation life considering the stress raiser effect and the core propagation life.

The properties for the through-carburized case and the simulated core materials, the inputs of the models, were obtained from experiments.

Three crack growth curves, Hasegawa1, Hasegawa2 and the vacuum da/dN curves, were used to predict the subsurface crack propagation life in the core layer of the composite sample in the smooth samples. The simulations ran using the Hasegawa1 curves predicted conservative fatigue life, and those using Hasegawa2 produced unconservative results. The fitted vacuum crack growth curve gave the best estimate of the fatigue life among the three, which is reasonable since the crack in the core layer of the composite axial sample is subsurface and in a vacuum environment.

For the notched samples, using the Hasegawa1 and the Hasegawa2 da/dN curves to predict the crack propagation life for the core layer does not make a difference in the results. This is because of the relatively long initial crack length assumed in this simulation, and most of the damage was generated in the ΔK region away from the threshold.

The fatigue models accurately predict the crack initiation location in the composite samples. By simulating the fatigue lives with these techniques reasonably accurate predictions are obtained when compared to the experimental results.

7.3 Recommendations for future studies

A limited amount of analysis was conducted on RA transformation under cyclic loading since the focus of the study was on fatigue performance. In future studies, more RA measurements could be collected at different load levels at various cycles to fill in the curve on the RA content vs. load cycle plot.

The effective-strain based model that counts damage after each reversal could be implemented to predict subsurface and corner crack growths to predict the crack propagation life in the composite samples.

Additional subsurface crack growth measurements at different R-ratios, especially near the threshold region, could benefit the subsurface crack, propagation model. The subsurface crack growth rate could be measured by conducting two-step stress amplitude tests, described by Masuda et al. [96], and observing the fracture surface for the crack growth at each stress amplitude. Another possible alternative for obtaining the subsurface crack growth rate is using the X-ray or ultrasound to measure the subsurface crack size during the test.

The XRD measurements in the composite samples after cyclic loading show that the residual stress relaxed more severely in the core layer compared to the case layer. Further studies could be conducted to investigate the mechanism responsible for relaxation.

Additional negative R-ratio da/dN vs. SIF tests could also be conducted as very little data of this kind is available in the literature.

References

[1] AISI Bar Steel Fatigue Group. AISI Bar Steel Fatigue Database, Project 16,18, 20, 22. https://fde.uwaterloo.ca/Fde/Materials/SMDIdbase/Steel/projectIndex.html, 2020.

[2] Akira, O. The Effect of Coaxing in 18 Cr-8 Ni Austenitic Stainless Steel. *Research reports of the Ariake Technical College 12*, 25 (1973), 25–31.

[3] Akita, M., Nakajima, M., Tokaji, K., and Uematsu, Y. Fatigue behaviour of pre-strained type 316 stainless steel. In *Fracture of Nano and Engineering Materials and Structures - Proceedings of the 16th European Conference of Fracture* (2005), pp. 229–230.

[4] Allen, R. J., Booth, G. S., and Jutla, T. A Review of Fatigue Crack Growth Characterisation By Linear Elastic Fracture Mechanics (LEFM). Part I—Principles and Methods of Data Generation. *Fatigue & Fracture of Engineering Materials & Structures 11*, 1 (1988), 45–69.

[5] Arcari, A., and Dowling, N. E. Modeling mean stress relaxation in variable amplitude loading for 7075-T6511 and 7249-T76511 high strength aluminum alloys. *International Journal of Fatigue 42* (2012), 238–247.

[6] ASM Handbook Committee. *Heat Treating*, 9 ed., vol. 4. The Materials Information Company, 1991.

[7] ASME. Rules for In Service Inspection of Nuclear Power Plan Components. In *ASME Boiler and Pressure Vessel Code*, 2017 ed. ASME, New York, 2017, ch. XI, pp. 329–414.

[8] ASTM International. *American Society for Testing and Materials*, vol. 03.01. 2014, ch. E647 Standard Test Method for Measurement of Fatigue Crack Growth Rates, pp. 1–50.

[9] Bao, H., and McEvily, A. J. On plane stress-plane strain interactions in fatigue crack growth. *International Journal of Fatigue 20*, 6 (1998), 441–448.

[10] Baumel jr., A., and Seeger, T. Thick surface layer model- life calculation for specimens with residual stress distribution and different material zones. *International Conference on Residual stresses 53*, 9 (1989), 809–814.

[11] Beretta, S., and Carboni, M. Variable amplitude fatigue crack growth in a mild steel for railway axles: Experiments and predictive models. *Engineering Fracture Mechanics 78*, 5 (2011), 848–862.

[12] Bloom, J. M. An approach to account for negative R-ratio effects in fatigue crack growth calculations for pressure vessels based on crack closure concepts. *Journal of Pressure Vessel Technology, Transactions of the ASME 116*, 1 (1994), 30.

[13] Bloom, J. M., and Hechmer, J. L. High stress crack growth - Part II predictive methodology using a crack closure model. *American Society of Mechanical Engineers, Pressure Vessels and Piping Division (Publication) PVP 350* (1997), 351–357.

[14] BS 7910. BSI Standards Publication Guide to methods for assessing the acceptability of flaws in metallic structures. In *BSI Standards Publication*, vol. 1. 2015, p. 490.

[15] Carbonni, M., Patriarca, L., and Regazzi, D. Determination of Delta Kth by compression pre-cracking in a structural steel. *Journal of ASTM International 6*, 9 (2009), 1–13.

[16] Christodoulou, P. I., Kermanidis, A. T., and Krizan, D. Fatigue behavior and retained austenite transformation of Al-containing TRIP steels. *International Journal of Fatigue 91*, June (2016), 220–231.

[17] Cohen, M. The Strengthening of Steel. *Trans. TMS-AIME 224* (1962), 638–656.

[18] Conle, F. A. *An Examination of Variable Amplitude Histories in Fatigue*. Doctor of philosophy, University of Waterloo, 1979.

[19] Conle, F. A. A Collection of Cyclic Mean Stress Relaxation Data. In *F.D.E. Spring 2019 Meeting* (Detroit, 2019).

[20] Conle, F. A., and Liang, W. F.D.+E. Steels Crack Propagation Charts. https://fde.uwaterloo.ca/Fde/CrackDB/startCrkPropDB.html, 2021.

[21] Conle, F. A., and Nowack, H. Verification of a neuber-based notch analysis by the companion-specimen method. *Experimental Mechanics 17*, 2 (1977), 57–63.

[22] Conle, F. A., Oxland, T. R., and Topper, T. H. Computer-Based Prediction of Cyclic Deformation and Fatigue Behavior. *ASTM Special Technical Publication* (1987), 1218–1236.

[23] Conle, F. A., and Topper, T. H. Overstrain effects during variable amplitude service history testing. *International Journal of Fatigue 2*, 3 (1980), 130–136.

[24] Costa, J. D., and Ferreira, J. A. Effect of stress ratio and specimen thickness on fatigue crack growth of CK45 steel. *Theoretical and Applied Fracture Mechanics 30*, 1 (1998), 65–73.

[25] Crooker, T. W., and Lange, E. A. Fatigue Crack Propagation in a High-Strength Steel Under Constant Cyclic Load with Variable Mean Loads. *NAVAL RESEARCH LAB 6805* (1968), 1–17.

[26] Davis, J. R. *Surface Hardening of Steels*. ASM International, 2002, ch. Gas Carburizing, pp. 23–24.

[27] de Diego-Calderón, I., Rodriguez-Calvillo, P., Lara, A., Molina-Aldareguia, J. M., Petrov, R. H., De Knijf, D., and Sabirov, I. Effect of microstructure on fatigue behavior of advanced high strength steels produced by quenching and partitioning and the role of retained austenite. *Materials Science and Engineering A 641* (2015), 215–224.

[28] Deng, H. L., Liu, H., Liu, Q. C., Guo, Y. P., and Yu, H. Fatigue strength prediction of carburized 12Cr steel alloy: Effects of evaluation of maximum crack sizes and residual stress distribution. *Fatigue and Fracture of Engineering Materials and Structures 43*, 2 (2020), 342–354.

[29] Dindinger, P., Kurath, P., and Langner, M. Summary of the experimental program: induction hardened notch shaft. *Multiaxial Fatigue of an Induction Hardened Shaft, No. AE-28. Warrendale, PA: Society of Automotive Engineers* (1999), 3–21.

[30] Dowling, N. E. Crack Growth During Low-Cycle Fatigue of Smooth Axial Specimens. *American Society for Testing and Materials* (1977), 97–121.

[31] Dowling, N. E., and Thangjitham, S. An overview and discussion of basic methodology for fatigue. *ASTM special technical publication 1389* (2000), 3–38.

[32] Dunlap, R. A. The Symmetry and Packing Fraction of The Body Centered Tetragonal Structure. *European J. of Physics Education 3*, 3 (2012), 19–24. https://files.eric.ed.gov/fulltext/EJ1052041.pdf.

[33] DuQuesnay, D. L., Topper, T. H., Yu, M. T., and Pompetzki, M. A. The effective stress range as a mean stress parameter. *International Journal of Fatigue 14*, 1 (1992), 45–50.

[34] Eason, E. D., Nelson, E. E., and Gilman, J. D. Technical basis for a revised fatigue crack growth rate reference curve for ferritic steels in light water reactor environments. *American Society of Mechanical Engineers, Pressure Vessels and Piping Division (Publication) PVP 286*, February 1992 (1994), 81–95.

[35] El-Haddad, M. H. Fatigue strength of welded components. Masters thesis, University of Waterloo, Waterloo, Ontario, 1975.

[36] El-Haddad, M. H. *Study of the growth of short fatigue cracks based on fracture mechanics*. Ph.d. thesis, University of Waterloo, Waterloo, Ontario, 1978.

[37] El-Haddad, M. H., Smith, K. N., and Topper, T. H. A strain based intensity factor solution for short fatigue cracks initiating from notches. *Fracture Mechanics* (1979), 274–289.

[38] El-Haddad, M. H., Smith, K. N., and Topper, T. H. Fatigue crack propagation of short cracks. *Journal of Engineering Materials and Technology, Transactions of the ASME 101*, 1 (1979), 42–46.

[39] El Malki Alaoui, A., Thevenet, D., and Zeghloul, A. Experimental investigations on the growth of small fatigue cracks in naval steel. *Fatigue and Fracture of Engineering Materials and Structures 30*, 6 (2007), 489–498.

[40] El-Zeghayar, M., Topper, T. H., and Bonnen, J. J. Derivation of effective strain-life data, crack closure parameters and effective crack growth data from smooth specimen fatigue tests. *SAE International Journal of Materials and Manufacturing 6*, 3 (2013), 576–588.

[41] Elber, W. The significance of fatigue crack closure. *ASTM International, Damage Tolerance in Aircraft Structures* (1971), 230–242.

[42] Farrahi, G. H., Majzoobi, G. H., Hosseinzadeh, F., and Harati, S. M. Experimental evaluation of the effect of residual stress field on crack growth behaviour in C(T) specimen. *Engineering Fracture Mechanics 73*, 13 (2006), 1772–1782.

[43] Feddersen, C. E. Discussion to plane strain crack toughness testing. *ASTM STP 410* (1966), 77.

[44] Fitch, Bennett. Eight Lubrication Failure Mechanisms for Rolling-Element Bearings. https://www.machinerylubrication.com/Read/31068/bearing-failure-mechanisms, 2003.

[45] Fleck, N. A., and Smith, R. A. Fatigue life prediction of a structural steel under service loading. *International Journal of Fatigue 6*, 4 (1984), 203–210.

[46] Fonte, M., Romeiro, F., and Freitas, M. Environment effects and surface roughness on fatigue crack growth at negative R-ratios. *International Journal of Fatigue 29*, 9-11 (2007), 1971–1977.

[47] Gaia da Silva, D., Lockwood, J. T., Liang, W., and Topper, T. H. Mean stress effect in stress-life for hard steels. *International Journal of Fatigue 146*, September 2020 (2021), 106101.

[48] García-Mateo, C., and Caballero, F. G. The role of retained austenite on tensile properties of steels with bainitic microstructures. *Materials Transactions 46*, 8 (2005), 1839–1846.

[49] Gergely, M., Somogyi, S., and Buza, G. Calculation of transformation sequences in quenched steel components to help predict internal stress distribution. *Material Science and Technologyrials Science and Technology 1*, October (1985), 893–897.

[50] Ghahremani, K., Walbridge, S., and Topper, T. H. A methodology for variable amplitude fatigue analysis of HFMI treated welds based on fracture mechanics and small-scale experiments. *Engineering Fracture Mechanics 163* (2016), 348–365.

[51] Grinberg, N. The effect of vacuum on fatigue crack growth. *International Journal of Fatigue 1777*, April (1982), 83–95.

[52] Haidemenopoulos, G. N., Kermanidis, A. T., Malliaros, C., Dickert, H. H., Kucharzyk, P., and Bleck, W. On the effect of austenite stability on high cycle fatigue of TRIP 700 steel. *Materials Science and Engineering A 573* (2013), 7–11.

[53] Hasan, H. S. *Evaluation of Heat Transfer Coefficient during Quenching of Steels*. Ph.d. thesis, University of Technology, Iraq, 2009.

[54] Hasegawa, K., Dvořák, D., Mareš, V., Strnadel, B., and Usami, S. Suitability of fatigue crack growth thresholds at negative stress ratios for ferritic steels and aluminum alloys in flaw evaluation procedures. *Engineering Fracture Mechanics 248*, January (2021).

[55] Hasegawa, K., Mares, V., Yamaguchi, Y., Li, Y., Vratislav, M., Yamaguchi, Y., and Li, Y. Fatigue Crack Growth Rates for Ferritic Steels Under Negative R Ratio. *ASME 2016 Pressure Vessels and Piping Conference 50350* (2016), V01AT01A007.

[56] Hechmer, J. L., Bloom, J. M., and Van Der Sluys, W. A. High stress crack growth, part I, testing program and data assessment. *American Society of Mechanical Engineers, Pressure Vessels and Piping Division (Publication) PVP 350* (1997), 337–345.

[57] Hénaff, G., Petit, J., and Bouchet, B. Environmental influence on the near-threshold fatigue crack propagation behaviour of a high-strength steel. *International Journal of Fatigue 14*, 4 (1992), 211–218.

[58] Heywood, R. B. *Designing by photoelasticity*, 1st ed. Chapman and Hall, Londo, 1952.

[59] Holzapfel, H., Schulze, V., Vöhringer, O., and MacHerauch, E. Residual stress relaxation in an AISI 4140 steel due to quasistatic and cyclic loading at higher temperatures. *Materials Science and Engineering A 248*, 1-2 (1998), 9–18.

[60] Howland, R. C. J. On the Stresses in the Neighbourhood of a Circular Hole in a Strip under Tension. *Philosophical Transactions of the Royal Society A: Mathematical, Physical and Engineering Sciences 229*, 670-680 (1930), 49–86.

[61] Hudak Jr., S. J., Saxena, A., Bucci, R. J., and Malcolm, R. C. Development of standard methods of testing and analyzing fatigue crack growth rate data. *Westinghouse Research and Developmenet Center* (1978).

[62] Şimşir, C., and Gür, C. H. 3D FEM simulation of steel quenching and investigation of the effect of asymmetric geometry on residual stress distribution. *Journal of Materials Processing Technology 207*, 1-3 (2008), 211–221.

[63] Ishihara, S., Yoshifuji, S., McEvily, A. J., Kawamoto, M., Sawai, M., and Takata, M. Study of the fatigue lifetimes and crack propagation behaviour of a high speed steel as a function of the R value. *Fatigue and Fracture of Engineering Materials and Structures 33*, 5 (2010), 294–302.

[64] Itoh, Y. Z., Suruga, S., and Kashiwaya, H. Prediction of fatigue crack growth rate in welding residual stress field. *Engineering Fracture Mechanics 33*, 3 (1989), 397–407.

[65] Jeddi, D., Sidhom, H., and Lieurade, H.-P. Effect of retained austenite on high cycle fatigue behaviour of carburized 14NiCr11 steel. *ICEM 2008: International Conference on Experimental Mechanics 2008 7375* (2008), 73751J.

[66] Johnson, J. A., Krauss, G., and Matlock, D. K. Fatigue of Microalloyed Bar Steels. *SAE Technical Paper Series 1*, 724 (2000).

[67] Jones, D., Hoppe, R., Hechmer, J. L., and James, B. A. An Experimental Study on the Effects of Compressive Stress on the Fatigue Crack Growth of Low-Alloy Steel. *Journal of Pressure Vessel Technology 116*, August 1994 (1994), 317–323.

[68] Jono, M., Song, J., Mikami, S., and Ohgaki, M. Fatigue Crack Growth and Crack Closure Behavior of Structural Materials. *The societry of materials Science, Japan 33*, 367 (1984), 98–104.

[69] Kang, K. J., Song, H., and Earmme, Y. Y. Fatigue crack growth and closure through a tensile residual stress field under compressive applied loading. *Fatigue & Fracture of Engineering Materials & Structures 12*, 5 (1989), 363–376.

[70] Karabelchtchikova, O. *Gas Carburizing Fundamentals: Kinetics and Thermodynamics of Mass Transfer in the Carburizing Atmosphere, Gas-Steel Interface and Carbon Diffusion in Steel.* PhD thesis, Worcester Polytechnic Institute, 2007.

[71] Karlsson, A., and Bäcklund, J. Summary of SIF design graphs for cracks emanating from circular holes. *International Journal of Fracture 14*, 6 (1978), 585–596.

[72] Klesnil, M., and Lukáš, P. Influence of strength and stress history on growth and stabilisation of fatigue cracks. *Engineering Fracture Mechanics 4*, 1 (1972), 77–92.

[73] Knop, M., Jones, R., Molent, L., and Wang, C. On the Glinka and Neuber methods for calculating notch tip strains under cyclic load spectra. *International Journal of Fatigue 22*, 9 (2000), 743–755.

[74] Kobayashi, H., Ogawa, T., Nakamura, H., and Nakazawa, H. Evaluation of fatigue crack growth and crack closure under spectrum loading. [SFVV3 steel]. *Chemical Pharmaceutical Bulletin*, 43 (1984), 2091.

[75] Kobayashi, H., and Todoroki, A. Effect of Weld-Induced Residual Stress on Fatigue Crack Growth in Compact Specimen. *The Iron and Steel Institute of Japan 11*, 103 (1986), 1984.

[76] Koistinen, D., and Marburger, R. A general equation prescribing the extent of the austenite-martensite transformation in pure iron-carbon alloys and plain carbon steels. *Acta Metallurgica 7*, 1 (1959), 59–60.

[77] Kondo, Y., Sakae, C., Kubota, M., and Kashiwagi, M. Interpretation of material hardness, stress ratio, and crack size effects on the ΔKth of small cracks based on crack closure measurement. *Journal of ASTM International 2*, 4 (2005), 69–83.

[78] Kondo, Y., Sakae, C., Kubota, M., and Kudou, T. The effect of material hardness and mean stress on the fatigue limit of steels containing small defects. *Fatigue and Fracture of Engineering Materials and Structures 26*, 8 (2003), 675–682.

[79] Kondo, Y., Sudo, T., and Kubota, M. Critical crack size that causes retardation of short fatigue crack by single overload. *Fatigue and Fracture of Engineering Materials and Structures 32*, 10 (2009), 856–864.

[80] Korda, A. A., Mutoh, Y., Miyashita, Y., and Sadasue, T. Effects of pearlite morphology and specimen thickness on fatigue crack growth resistance in ferritic-pearlitic steels. *Materials Science and Engineering A 428*, 1-2 (2006), 262–269.

[81] Kujawski, D. Estimations of stress intensity factors for small cracks at notches. *Fatigue & Fracture of Engineering Materials & Structures 14*, 10 (1991), 953–965.

[82] Kujawski, D., and Ellyin, F. Crack initiation and total fatigue life of a carbon steel in vacuum and air. *Journal of Testing and Evaluation 20*, 6 (1992), 391–395.

[83] Kurihara, M., Katoh, A., and Kawahara, M. Analysis on fatigue crack growth rates under a wide range of stress ratios. *Journal of Pressure Vessel Technology, Transactions of the ASME 108*, 2 (1986), 209–213.

[84] Lam, T. S., Topper, T. H., and Conle, F. A. Derivation of crack closure and crack growth rate data from effective-strain fatigue life data for fracture mechanics fatigue life predictions. *International Journal of Fatigue 20*, 10 (1998), 703–710.

[85] Landgraf, R. W., and Chernenkoff, R. A. Residual Stress Effects on Fatigue of Surface Processed Steels. *Analytical and Experimental Methods for Residual Stress Effects in Fatigue* (1988), 1–12.

[86] Lee, S. J., Lusk, M. T., and Lee, Y. K. Conversional model of transformation strain to phase fraction in low alloy steels. *Acta Materialia 55*, 3 (2007), 875–882.

[87] Li, W., Deng, H., and Liu, P. Interior fracture mechanism analysis and fatigue life prediction of surface-hardened gear steel under axial loading. *Materials 9*, 10 (2016).

[88] Li, Z. C., and Ferguson, B. L. Computer modeling and validations of steel gear heat treatment processes using commercial software DANTE. *Journal of Shanghai Jiaotong University (Science) 16*, 2 (2011), 152–156.

[89] Lingamanaik, S. N., and Chen, B. K. The effects of carburising and quenching process on the formation of residual stresses in automotive gears. *Computational Materials Science 62* (2012), 99–104.

[90] Liscic, B., Tensi, H. M., and Luty, W. *Theory and technology of quenching: a handbook*. Springer Science & Business Media, 2013.

[91] Lu, J., Flavenot, J., and Turbat, A. Prediction of Residual Stress Relaxation During Fatigue. *Mechanical Relaxation of Residual Stresses* (1988), 75–90.

[92] Lu, X., and Zheng, S. Strengthening and damaging under low-amplitude loads below the fatigue limit. *International Journal of Fatigue 31*, 2 (2009), 341–345.

[93] Lukas, P. Stress intensity factor for small notch-emanated cracks. *Engineering fracture mechanics 26*, 3 (1987), 471–473.

[94] Marines-Garcia, I., Paris, P. C., Tada, H., Bathias, C., and Lados, D. Fatigue crack growth from small to large cracks on very high cycle fatigue with fish-eye failures. *Engineering Fracture Mechanics 75*, 6 (2008), 1657–1665.

[95] Masing, G. Eigenspannumyen und verfeshungung beim messing. In *Proc. Inter. Congress for Applied Mechanics* (1926), pp. 332–335.

[96] Masuda, K., Oguma, N., Ishihara, S., and McEvily, A. J. Investigation of subsurface fatigue crack growth behavior of D2 tool steel (JIS SKD11) based on a novel measurement method. *International Journal of Fatigue 133*, August 2019 (2020), 105395.

[97] Miettinen, J. Calculation of solidification-related thermophysical properties for steels. *Metallurgical and Materials Transactions B: Process Metallurgy and Materials Processing Science 28*, 2 (1997), 281–297.

[98] Minagi, A., and Tokaji, K. Fatigue crack propagation of laser welded butt joints. *Journal of the Iron and Steel Institute of Japan 86*, 1 (2000), 51–56.

[99] Miner, M. A. Cumulative damage in fatigue. *American Society of Mechanical Engineers* (1945).

[100] Molski, K., and Glinka, G. A method of elastic-plastic stress and strain calculation at a notch root. *Materials Science and Engineering 50*, 1 (1981), 93–100.

[101] Morris, D., Sadeghi, F., Singh, K., and Voothaluru, R. Residual stress formation and stability in bearing steels due to fatigue induced retained austenite transformation. *International Journal of Fatigue 136*, March (2020), 105610.

[102] Moyer, J. M., and Ansell, G. S. The volume expansion accompanying the martensite transformation in iron-carbon alloys. *Metallurgical Transactions A 6*, 9 (1975), 1785–1791.

[103] Müller-Bollenhagen, C., Zimmermann, M., and Christ, H. J. Very high cycle fatigue behaviour of austenitic stainless steel and the effect of strain-induced martensite. *International Journal of Fatigue 32*, 6 (2010), 936–942.

[104] Murakami, Y., Kodama, S., and Konuma, S. Quantitative evaluation of effects of non-metallic inclusions on fatigue strength of high strength steels. I: Basic fatigue mechanism and evaluation of correlation between the fatigue fracture stress and the size and location of non-metallic inclusions. *International Journal of Fatigue 11*, 5 (1989), 291–298.

[105] Nakai, Y., Tanaka, K., and Kawashima, R. Stress-ratio effect on fatigue crack growth treshold in steels. *Journal of the Society of Materials Science, Japan 33*, 371 (1984), 1045–1051.

[106] Nakai, Y., Tanaka, K., and Nakanishi, T. The effects of stress ratio and grain size on near-threshold fatigue crack propagation in low-carbon steel. *Engineering Fracture Mechanics 15*, 3-4 (1981), 291–302.

[107] Nakajima, M., Nakamura, Y., Shimizu, T., and Mochizuki, Y. Coaxing effect of high strength steels with different strength levels. *Zairyo/Journal of the Society of Materials Science, Japan 62*, 9 (2013), 547–553.

[108] Nakajima, M., Uematsu, Y., Tokaji, K., and Jung, J.-W. Fatigue Behavior of Type 304N2 High-Nitrogen Austenitic Stainless Steel. *Journal of the Society of Materials Science, Japan 58*, 12 (2009), 956–961.

[109] Nakatani, M., Fujihara, H., Sakihara, M., and Minoshima, K. Fatigue crack growth acceleration caused by irreversible hydrogen desorption in high-strength steel and its mechanical condition. *Materials Science and Engineering A 528*, 25-26 (2011), 7729–7738.

[110] National Research Institute for Metals. NRIM Fatigue Data Sheets No. 65. Data Sheets on Fatigue Properties for Weld and Base Metals of SUS304-HP (18Cr-8Ni) Hot Rolled Stainless Steel Plate, 1990.

[111] Neu, R. W., and Sehitoglu, H. Stress-induced transformation in a carburized steel-Experiments and analysis. *Acta Metallurgica Et Materialia 40*, 9 (1992), 2257–2268.

[112] Neuber, H. Theory of stress concentration for shear-strained prismatical bodies with arbitrary nonlinear stress-strain law. *Journal of Applied Mechanics, Transactions ASME 28*, 4 (1960), 544–550.

[113] Newman, J. C., and Raju, I. S. Stress-Intensity factor equations for cracks in three-dimensional finite bodies subjected to tension and bending loads, 1984.

[114] Newman, J. C., Ziegler, B. M., Shaw, J. W., Cordes, T. S., and Lingenfelser, D. J. Fatigue Crack Growth Rate Behavior of A36 Steel using ASTM Load-Reduction and Compression Precracking Test Methods. *Journal of ASTM International 9*, 4 (2012), 103966.

[115] Nguyen, H. Q., Gallimard, L., and Bathias, C. Numerical simulation of fish-eye fatigue crack growth in very high cycle fatigue. *Engineering Fracture Mechanics 135* (2015), 81–93.

[116] Olson, G., and Cohen, M. Kinetics of strain-induced martensitic nucleation. *Metallurgical transactions A 6*, 4 (1975), 791.

[117] Paris, P. C., and Erdogan, F. A Critical Analysis of Crack Propagation Laws. *Journal of Basic Engineering 85*, 4 (1963), 528–533.

[118] Paulo. The basics of oil quenching in heat treating. https://www.paulo.com/basics-oil-quenching-heat-treating/, 2017.

[119] Pearson, S. Initiation of fatigue cracks in commercial aluminium alloys and the subsequent propagation of very short cracks. *Engineering Fracture Mechanics 7*, 2 (1975).

[120] Peet, M. J., Hasan, H. S., and Bhadeshia, H. K. D. H. Prediction of thermal conductivity of steel. *International Journal of Heat and Mass Transfer 54*, 11-12 (2011), 2602–2608.

[121] Peterson, R. *Stress Concentration Factors*, 1st ed. John Wiley & Sons, Inc, New York, 1974.

[122] Pippan, R. Threshold and effective threshold of fatigue crack propagation in ARMCO iron II: The influence of environment. *Materials Science and Engineering A 138*, 1 (1991), 15–22.

[123] Pippan, R., Plöchl, L., Klanner, F., and Stüwe, H. The Use of Fatigue Specimens Precracked in Compression for Measuring Threshold Values and Crack Growth. *Journal of Testing and Evaluation 22*, 2 (1994), 98.

[124] Proto Manufacturing. Measurement Services. https://www.protoxrd.com/measurement-services, 2020.

[125] Radon, J. C., and Woodtli, J. Influence of microstructure on the cyclic crack growth in a low-alloy steel. *International Journal of Fatigue 6*, 4 (1984), 221–227.

[126] Rangaswamy, P., Garcia, F. P., Prime, D. M. B., and Prantil, V. C. Residual Stress Measurment and Prediction in. *Materials Science 836* (2000).

[127] Reti, T. Residual stresses in carburized, carbonitrided, and case-hardened components. *Handbook of residual stress and deformation of steel* (2002), 189–208.

[128] Richman, R. H., and Landgraf, R. W. Some effects of retained austenite on the fatigue resistance of carburized steel. *Metallurgical Transactions A 6*, 5 (1975), 955–964.

[129] Rooke, D. P. Asymptotic stress intensity factors for fatigue crack-growth calculations. *International Journal of Fatigue 2*, 2 (1980), 69–75.

[130] Roy, A., Manna, I., and Chattoraj, I. Anomalies in hydrogen enhanced fatigue of a high strength steel. *International Journal of Fatigue 59* (2014), 14–22.

[131] Sarazin-Baudoux, C., Gardin, C., Pham, T. H., Chrétien, G., Petit, J., Tran, V. X., and Benoit, G. Fatigue Crack Propagation in Gaseous Hydrogen Environment in Low Alloy Steel. In *Procedia Engineering* (2015), vol. 114, Elsevier B.V., pp. 354–360.

[132] Schijve, J. Significance of Fatigue Cracks in Micro-Range and Macro-Range. *ASTM* (1967), 415.

[133] Schijve, J. The Stress Intensity Factor of Small Cracks At Notches. *Fatigue & Fracture of Engineering Materials & Structures 5*, 1 (1982), 77–90.

[134] Schijve, J. Fatigue Crack Closure: Observations and Technical Significance. *Mechanics of Fatigue Crack Closure* (1988), 5–5–30.

[135] Sherif, M. Y., Mateo, C. G., Sourmail, T., and Bhadeshia, H. K. D. H. Stability of retained austenite in trip-assisted steels. *Materials Science and Technology 20*, 3 (2004), 319–322.

[136] Shinko, T., Hénaff, G., Halm, D., Benoit, G., Bilotta, G., and Arzaghi, M. Hydrogen-affected fatigue crack propagation at various loading frequencies and gaseous hydrogen pressures in commercially pure iron. *International Journal of Fatigue 121*, September 2018 (2019), 197–207.

[137] Smaga, M., Walther, F., and Eifler, D. Deformation-induced martensitic transformation in metastable austenitic steels. *Materials Science and Engineering A 483-484*, 1-2 C (2008), 394–397.

[138] Smallman, R. E., and Ngan, A. H. *Modern Physical Metallurgy: Eighth Edition*, eigth edit ed. Butterworth-Heinemann, Oxford, 2013.

[139] Smith, K. N., Topper, T. H., and Watson, P. A stress–strain function for the fatigue of metals. *Journal of Materials 5*, January 1970 (1970), 767–778.

[140] Smith, R. A., and Miller, K. J. Fatigue cracks at notches. *International Journal of mechanical sciences 19*, 1 (1977), 11–22.

[141] Stewart, A. T., Region, S. W., and Down, B. The Influence of Environment and Stress Ratio on Fatigue Crack Growth At Near Threshold Stress Intensities in Low-Alloy Steels. *Engineering Fracture Mechanics 13* (1980), 463–478.

[142] Sudo, T., Kubota, M., and Kondo, Y. Investigation of critical crack size that causes retardation of fatigue crack propagation by single overload. *Zairyo/Journal of the Society of Materials Science, Japan 58*, 12 (2009), 1023–1029.

[143] Suwanpinij, P., Togobytska, N., Keul, C., Weiss, W., Prahl, U., Homberg, D., and Bleck, W. Phase Transformation Modelling and Parameter Identification from Dilatometric Investigations. *Steel Research International 79*, 10 (2008), 793–799.

[144] Tanaka, Y., and Soya, I. Effects of Stress Ratio and Stress Intensity Factor Range on Fatigue Crack Closure in Steel Plate. *Quarterly Journal of the Japan Welding Society 5*, 1 (1987), 119–126.

[145] Taylor, D., and Knott, J. F. Fatigue Crack Propagation Behaviour of Short Cracks; the Effect of Microstructure. *Fatigue & Fracture of Engineering Materials & Structures 4*, 2 (1981), 147–155.

[146] Thelning, K. E. *Steel and its Heat Treatment*. Butterworth-heinemann, 2013.

[147] Thibaud, S., Boudeau, N., and Gelin, J. C. TRIP steel: Plastic behaviour modelling and influence on functional behaviour. *Journal of Materials Processing Technology 177*, 1-3 (2006), 433–438.

[148] Tibbetts, G. G. Diffusivity of carbon in iron and steels at high temperatures. *Journal of Applied Physics 51*, 9 (1980), 4813–4816.

[149] Topper, T. H., and Duquesnay, D. L. The effects of overloads in service load histories on crack closure and fatigue damage. *SAE Technical Papers*, 2001-01-4079 (2001).

[150] Topper, T. H., and El-Haddad, M. H. Fatigue strength prediction of notches based on fracture mechanics. In *Int. Symposium on Fatigue Thresholds* (1981), vol. 2, pp. 777–798.

[151] Tsay, L. W., Young, M. C., Shin, C. S., and Chan, S. L. Hydrogen-enhanced cracking of 2205 duplex stainless steel. *Fatigue and Fracture of Engineering Materials and Structures 30*, 12 (2007), 1228–1236.

[152] Tucker, L., and Bussa, S. The SAE cumulative fatigue damage test program. *SAE Congress*, SAE paper 750038 (Feb 1975), 198–248.

[153] van Bohemen, S. M. C. Bainite and martensite start temperature calculated with exponential carbon dependence. *Materials Science and Technology 28*, 4 (2012), 487–495.

[154] Varvani-Farahani, A., Topper, T. H., and Plumtree, A. Confocal scanning laser microscopy measurements of the growth and morphology of microstructurally

short fatigue cracks in Al 2024-T351 alloy. *Fatigue and Fracture of Engineering Materials and Structures 19*, 9 (1996), 1153–1159.

[155] Vormwald, M., and Seeger, T. The Consequences of Short Crack Closure on Fatigue Crack Growth Under Variable Amplitude Loading. *Fatigue & Fracture of Engineering Materials & Structures 14*, 2-3 (1991), 205–225.

[156] Wadsworth, N. J. The influence of atmospheric corrosion on the fatigue limit of iron-0.5% carbon. *Philosophical Magazine 6*, 63 (1961), 397–401.

[157] Warke, V. S., Sisson, R. D., and Makhlouf, M. M. A model for converting dilatometric strain measurements to the fraction of phase formed during the transformation of austenite to martensite in powder metallurgy steels. *Metallurgical and Materials Transactions A: Physical Metallurgy and Materials Science 40*, 3 (2009), 569–572.

[158] Xu, R. X., Topper, T. H., and Thompson, J. C. Mode I stress intensity factor equations for cracks at notches and cavities. *Fatigue and Fracture of Engineering Materials and Structures 20*, 9 (1997), 1351–1361.

[159] Yamabe, J., and Matsui, T. Influences of Hardness, Defect Size and Retained Austenite on Fatigue Strength at N= 107 for Carburized Steels. *Journal of the Society of Materials Science, Japan 56*, 3 (2007), 236–243.

[160] Yamada, Y., and Newman, J. C. Crack closure behavior on a variety of materials under high stress ratios and K max test conditions. *Journal of ASTM International 9*, 2 (2012), 109–125.

[161] Yin, F., and Fatemi, A. Fatigue behaviour and life predictions of case-hardened steels. *Fatigue and Fracture of Engineering Materials and Structures 32*, 3 (2009), 197–213.

[162] Yin, F., and Fatemi, A. Monotonic and cyclic deformations of case-hardened steels including residual stress effects. *Strain 47*, SUPPL. 1 (2011), 74–83.

[163] Yin, F., Fatemi, A., and Bonnen, J. Variable amplitude fatigue behavior and life predictions of case-hardened steels. *International Journal of Fatigue 32*, 7 (2010), 1126–1135.

[164] Zerbst, U., Vormwald, M., Andersch, C., Mädler, K., and Pfuff, M. The development of a damage tolerance concept for railway components and its demonstration for a railway axle. *Engineering Fracture Mechanics 72*, 2 (2005), 209–239.

[165] Zhang, H.-Y., Stephens, R. I., and Glinka, G. Subsurface fatigue crack initiation and propagation behavior of induction-hardened shafts under the effect of residual and applied bending stress. *American Society for Testing and Materials 30*, 1360 (2000), 240–260.

[166] Zhao, L. H., Li, J. X., Yu, W. Y., Ma, J., and Zheng, S. L. Experimental Study on the Coaxing Effect of Multi-Level Stresses with Different Sequences. *Strength of Materials 49*, 1 (2017), 55–60.

[167] Zhuang, W. Z., and Halford, G. R. Investigation of residual stress relaxation under cyclic load. *International Journal of Fatigue 23*, SUPPL. 1 (2001), 31–37.

Appendix A: Tables for experimental data

Table A1: Case sample constant amplitude test data

Strain Ampl.	2Nf	Sts Ampl. MPa	Mean Stress MPa	Plastic Strain Ampl.	Inital Emod MPa	Neuber Stress Ampl. MPa	Sample ID	
0.01026	4	1900	-430	0.00100	205186	2000	4	
0.00508	1242	1045	-291	0.00005	207924	1051	5	
0.00360	9658	719	-43	0.00004	201994	723	7	
0.00300	17124	660	80	-0.00028	201023	631	9	
0.00272	8132	644	60	-0.00044	203928	598	10	
0.00272	51072	605	3	-0.00015	211064	589	11	
0.00260	22666	544	-13	-0.00014	198370	530	12	
0.00256	20662	515	-24	0.00002	202462	517	13	
0.00630	884	1253	-410	0.00013	203037	1266	14	
0.00836	22	1671	-343	0.00027	206618	1699	16	
0.00301	73572	610	0	0.00001	203638	612	33	
0.00215	10000000	413	0	0.00018	209143	431	6	#runout
0.00246	10000000	508	8	-0.00013	195891	495	8	#runout

Table A2: Core sample constant amplitude test data

Strain Ampl.	2Nf	Sts Ampl. MPa	Mean Stress MPa	Plastic Strain Ampl.	Inital Emod MPa	Neuber Stress Ampl. MPa	Sample ID	
0.00912	2002	976	-29	0.00437	205297	1352	3	
0.00456	14032	829	-25	0.00104	206352	931	4	
0.00303	101574	623	32	0.00008	211201	631	5	
0.00260	153900	536	-12	0.00011	215243	547	6	
0.00198	807576	421	0	-0.00006	206617	415	7	
0.00400	32894	822	-53	0.00007	209169	830	9	
0.00180	10000000	375	0	0.00002	210302	377	8	#runout

Table A3: Composite sample constant amplitude test data

Strain Ampl.	2Nf	Sts Ampl. MPa	Mean Stress MPa	Plastic Strain Ampl.	Inital Emod MPa	Neuber Stress Ampl. MPa	Sample ID	
0.00612	11836	1016	-57	0.00099	197977	1109	2	
0.00904	262	1365	-94	0.00272	215986	1632	6	
0.01016	180	1462	-92	0.00308	206595	1752	14	
0.00982	500	1399	-137	0.00292	202758	1669	21	
0.00600	18308	1051	0	0.00111	214736	1164	22	
0.00400	95510	914	67	-0.00066	195908	846	3	#fisheye
0.00340	1241888	689	40	-0.00004	200405	685	4	#fisheye
0.00500	116352	942	45	0.00052	210432	996	17	#fisheye
0.00306	71302922	613	0	0.00011	207600	624	19	#fisheye
0.00506	96208	960	-4	0.00057	213584	1018	23	#fisheye
0.00340	32820360	698	-1	-0.00001	204917	698	24	#fisheye
0.00284	20000000	597	0	0.00000	210432	597	20	#runout
0.00300	20000000	596	-13	0.00005	201798	601	5	#runout

Table A4: Case material negative mean stress tests

Test type	Maximum Stress MPa	Minimum Stress MPa	Life	Sample ID	
CA tests	410	-410	5000000	6	#runout
	513	-497	5000000	8	#runout
Negative mean stress tests	392	-797	5000000	39	#runout
	401	-1057	5000000	44	#runout
	396	-1536	5000000	45	#runout
Positive mean stress tests	580	0	5000000	47	#runout
	722	-2	369372	46	

Table A5: Case notched sample constant amplitude tests

Nominal Stress Ampl. MPa	Fatigue Life Reversals	Mean Stress MPa	Sample ID
426	13	21	1
203	90028	0	2
278	15752	0	4

Table A6: Core material periodic overload tests

Maximum Stress MPa	POL Min. Stress MPa	Small cyc. Min. Stress MPa	Small cyc. Stress Ampl. MPa	Overload Stress Ampl. MPa	Num of sml. Cyc. per overload Cycles	Overload Damage %	Fatigue Life Cycles	Equivalenet Small cyc. life Reversals	Sample ID	
746	-745	37	354	745	80	12.99%	103952	235967	10	
748	-746	209	269	747	150	11.66%	174835	393165	11	
747	-746	316	215	746	300	12.02%	360595	816986	12	
744	-745	388	178	744	550	14.84%	816322	1913713	13	
747	-746	461	143	746	900	27.24%	2451615	6731436	14	
746	-745	514	116	745	900	55.56%	5000000	22475000	15	#runout

Table A7: Case material period overload tests

Maximum Stress MPa	POL Min. Stress MPa	Small cyc. Min. Stress MPa	Small cyc. Stress Ampl. MPa	Overload Stress Ampl. MPa	Num of sml. Cyc. per overload Cycles	Overload Damage %	Fatigue Life Cycles	Equivalenet Small cyc. life Reversals	Sample ID	
582	-571	92	245	576	100	24.47%	374593	981970	28	
585	-584	244	170	584	2000	16.59%	5000000	11982673	29	#runout
589	-588	137	226	588	2000	16.93%	5000000	12032277	30	#runout
589	-587	98	246	588	2000	16.93%	5000000	12032277	31	#runout
620	-618	-125	373	619	70	1152.20%	10000000	N.A.	34	#runout
580	-802	0	290	691	200	3.40%	170160	350548	48	
589	-588	-110	349	588	500	84.66%	5000000	65021192	31B	#runout
589	-588	-280	434	588	500	90.00%	5000000	99550000	31C	#runout
589	-588	-280	434	588	2000	50.00%	5000000	19980000	30B	#runout
589	-588	-392	490	588	2000	75.00%	5000000	39940000	30C	#runout
589	-588	-504	546	588	2000	66.67%	5000000	29940000	30D	#runout
580	-763	0	290	672	200	96.15%	5000000	258700000	47B	#runout

Table A8: Composite axial sample variable amplitude tests

Nominal Max. Stress MPa	Nominal Min. Stress MPa	Fatigue Life Blocks	Sample ID	
812	998	34395	25	#runout
1197	1619	139	26	
1046	1418	869	27	
896	1217	1957	28	
1198	1628	247	29	
1055	1429	565	30	
897	1219	2568	31	
856	1157	56189	32	
Filtered VA History				
898	-1211	2216	33	
856	-1158	58741	34	
824	-1114	14490	35	
1055	-1427	1140	36	
821	-1111	46223	37	
1197	-1619	166	38	

Table A9: Composite notched plate variable amplitude tests

Nominal Max. Stress MPa	Nominal Min. Stress MPa	Fatigue Life Blocks	Sample ID
451	-606	1205	1
584	-785	194	4
514	-692	553	5
368	-498	1955	6

Table A10: Case notched plate variable amplitude tests

Nominal Max. Stress MPa	Nominal Min. Stress MPa	Fatigue Life Blocks	Sample ID
453	-612	7	5
320	-431	275	6
222	-298	3483	7
281	-378	64	8

Appendix B: Coffin-Manson and Ramberg-Osgood fitting for the fatigue data

Stabilized stress-strain data obtained from strain-life fatigue tests were used to construct the material's cyclic stress-strain curve shown in Figure 4.8. The cyclic stress-strain curve is described by the following equation:

$$\varepsilon = \frac{\sigma}{E} + \frac{\sigma}{K'}^{\frac{1}{n'}} \tag{B1}$$

Where ε is the true total strain amplitude, σ is the cyclically stable true stress amplitude, E is the average observed modulus of elasticity, K' is the cyclic strength coefficient, and n' is the cyclic strain hardening exponent. All of these values were obtained from a best fit of the above equation to the test data.

The stress amplitude corresponding to the peak strain amplitude at the CA tests was calculated from the peak load amplitude at one half of the specimen's fatigue life. A constant strain amplitude fatigue life curve for the case, core and composite materials are given in Figure B1 and is described by the following equations:

$$\frac{\triangle\varepsilon_e}{2} = \frac{\sigma'_f}{E}(2N_f)^b \tag{B2a}$$

$$\frac{\triangle\varepsilon_p}{2} = \varepsilon'_f(2N_f)^c \tag{B2b}$$

Since $\Delta\varepsilon = \Delta\varepsilon_e + \Delta\varepsilon_p$,

$$\frac{\Delta\varepsilon}{2} = \frac{\sigma'_f}{E}(2N_f)^b + \varepsilon'_f(2N_f)^c \tag{B3}$$

Where $\frac{\Delta\varepsilon}{2}$ is the total strain amplitude,
$\frac{\Delta\varepsilon_e}{2}$ is the elastic strain amplitude ($\frac{\Delta\varepsilon_e}{2} = \frac{\Delta\sigma_{measured}}{2E}$) ,
$\frac{\Delta\varepsilon_p}{2}$ is the plastic strain amplitude ($\frac{\Delta\varepsilon_p}{2} = \frac{\Delta\varepsilon_{measured}}{2} - \frac{\Delta\varepsilon_e}{2}$) ,
$2N_f$ is the number of reversals to failure,
σ'_f is the fatigue strength coefficient,
b is the fatigue strength exponent,
ε'_f is the fatigue ductility coefficient,
c is the fatigue ductility exponent.

The values of the strain-life parameters determined from a best fit of strain life data to Equations B2 are given in Table B1. Run-out tests (run 10,000,000 reversals without failure) were not included in the least squares fitting process.

The fitted strain-life and Neuber stress vs life curves for the three materials are plotted in Figures B1.

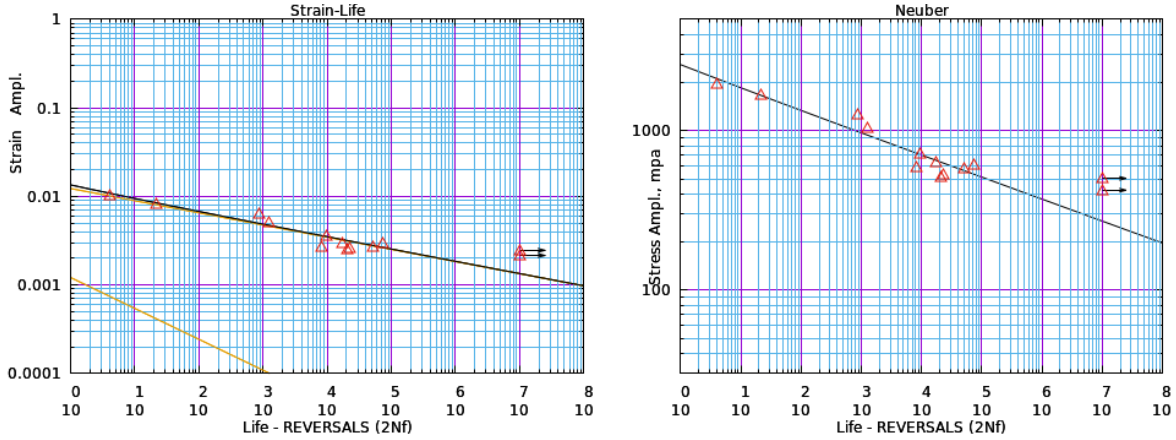

(a) Through-carburized Case

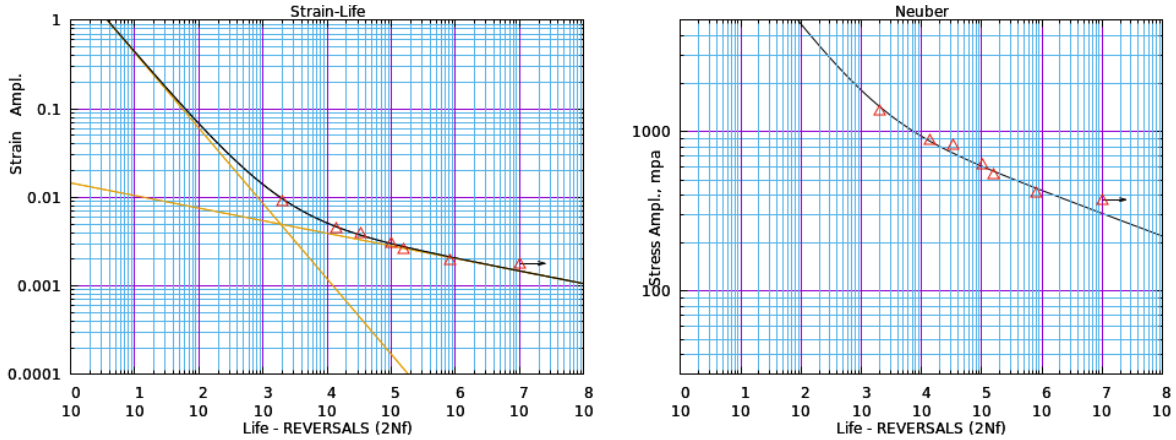

(b) Simulated Core

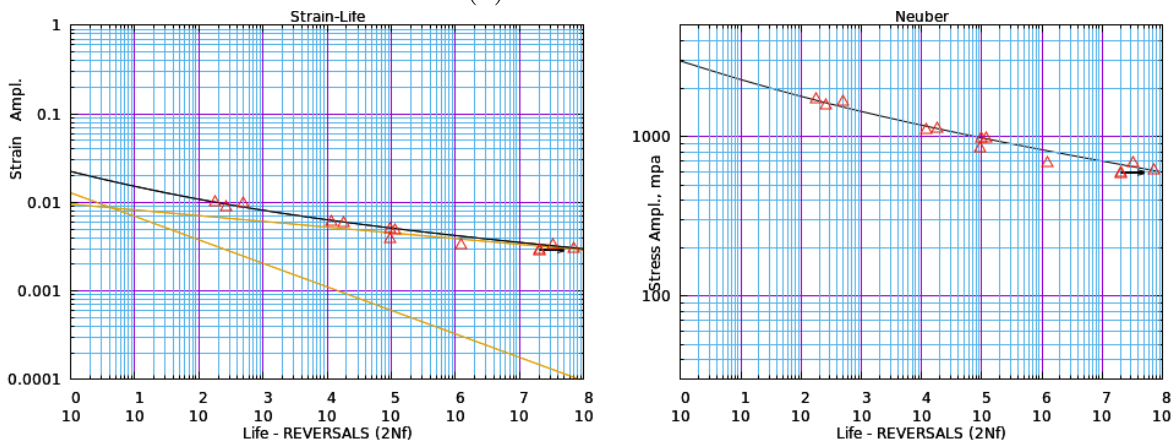

(c) Case-hardened composite

Figure B1: CA fatigue data fitted by Equation B3 with the parameters listed in Table B1

Table B1: Constant Strain Amplitude Fatigue Parameters for the case, core and composite 16MnCr5 samples

Name	Unit	Case	Core	Composite
Monotonic Strength Coefficient, K		7836	2574	3804
Monotonic Strain hardening Exponent, n		0.32	0.14	0.19
Cyclic Strength Coefficient, K'	MPa	34839	2518	5660
Cyclic Strain Hardening exponent n'	-	0.3936	0.1669	0.2443
Fatigue Strength Coefficient,σ'_f	MPa	2479	3035	1953
Fatigue Strength Exponent, b	-	-0.1374	0.1421	-0.0649
Fatigue Ductility Coefficient, ϵ'_f	-	0.0012	3.059	0.0128
Fatigue Ductility Exponent, c	-	-0.349	-0.8514	-0.2656